Producing Ruthenium and Palladium Doped Stainless Steel by Field Assisted Sintering

Natasha Sweeney Fort

A thesis submitted to the School of Chemical, Materials and Biological Engineering at the University of Sheffield for the degree of Doctor of Engineering

March 2025

"Ignis aurum probat, miseria fortes homines."

— Lucius Annaeus Seneca

Abstract

Stainless steels are generally corrosion resistant, however, in reducing acidic environments passive film dissolution can occur. Though studies have shown alloying with platinum group metals (PGMs) benefits stainless steel corrosion resistance, cost and performance issues have limited the commercial success of this strategy. This project explored the production of stainless steel-PGM alloys via powder metallurgy to address these challenges.

Using the field assisted sintering technique (FAST), bulk alloyed and functionally graded materials (FGM) were successfully produced using water atomised 316L and 17-4PH stainless steel doped with 0.5 wt.% Ru and Pd, respectively. Sintering optimisation was carried out by varying the processing temperature and time. Corrosion performance was evaluated by electrochemical testing in H_2SO_4 and immersion testing in NaCl. The performance of cast and sintered PGM-doped 316L was also compared.

Increasing the sintering temperature enhanced the density of the 17-4PH samples but had little effect on the 316L specimens. In contrast, increasing the sintering time had minimal impact on either alloy's density. Regarding the effect of PGM doping on corrosion performance, no clear trend emerged in H_2SO_4. In NaCl, however, immersion testing revealed PGM doping benefitted the corrosion resistance of 316L. The cast samples outperformed the sintered samples exhibiting wider passive regions and a greater ease of passivation. In the FGMs, it was observed that PGM presence had a positive effect on pitting resistance in a chloride environment.

This study demonstrated the feasibility of powder metallurgical PGM-doped stainless steels. While mixed corrosion performances were observed, further research could render more consistency. Future studies should focus on investigating the effect of different atomisation techniques or sintering conditions.

Acknowledgements

First and foremost I'd like to thank the EPSRC, Johnson Matthey and Globus Metal Powders for their funding and technical support. A special thanks to Richard Thackray, my academic supervisor, for his support and guidance throughout my EngD journey and for challenging me to grow as a researcher. I want to extend my thanks to Tes Monaghan for her invaluable metallographic preparation help and kindness. I am grateful to the Royce Discovery Centre (Henry Royce Institute) for providing the opportunity to use world-class equipment. I express my gratitude to Dirk Engelberg, who acted as my corrosion supervisor, for his indispensable recommendations and for allowing me to work alongside his corrosion group at the University of Manchester. A special thanks goes to Sharon Brown, the senior programme manager of the Advanced Metallic Systems Centre for Doctoral Training, for her incredible work in the smooth running of the centre and pastoral care, your time and effort doesn't go unnoticed. Finally, I want to give my appreciation to my sister, Kylee, for her unfaltering support of my academic pursuits.

Contents

List of Figures

List of Tables

Acronyms

Acronym	Definition
AM	Additively manufactured
CRP	Cu-rich precipitates
CTE	Coefficient of thermal expansion
EBSD	Electron backscatter diffraction
EDS	Energy-dispersive X-ray spectroscopy
FAST	Field assisted sintering technique
FG	Functionally graded
FGM	Functionally graded materials
FIB	Focused ion beam
GA	Gas atomisation
HIP	Hot isostatic pressing
HP	Hot pressing
HT	Heat treatment
LPBF	Laser powder bed fusion
LSA	Laser surface alloying
MIM	Metal injection moulding
OCP	Open circuit potential
OM	Optical microscopy
PIM	Powder injection moulding
PGM	Platinum group metals
PH	Precipitation hardening
PM	Powder metallurgy
SEM	Scanning electron microscopy
SLM	Selective laser melted
SS	Stainless steels
TEM	Transmission electron microscopy
VIGA	Vacuum induction gas atomisation
WA	Water atomisation
XPS	X-ray photoelectron spectroscopy

CHAPTER

1 Introduction and Aims

1.1 Background

Steels are a widely implemented and generally cost-effective group of materials comprised of Fe alloying with various elements[1]. SS are a subcategory of Fe alloys which contain more than 10.5 wt.% Cr[2]. As illustrated in Figure 1.1, the stainless steel alloys are grouped into five different families. 316L is a stainless steel grade that is austenitic in its microstructure and is characterised by its excellent resistance to general and intergranular corrosion and good high-temperature strength[1,3,4]. Referred to as the workhorse of stainless steel alloys, austenitic stainless steels find applications within the petrochemical, pharmaceutical and nuclear industries[5,6]. 17-4PH is another grade of SS belonging to the precipitation hardening (PH) martensitic family. It is described as an alloy with good corrosion resistance and mechanical properties[7]. Precipitation-hardenable stainless steels are used in various applications, including fuel tanks, pump shafting and expansion joints[7].

Corrosion resistance is a principal feature of stainless steels. The Cr content in stainless steels improves their corrosion resistance by forming an adherent passive layer of chromium oxide[8]. Increasing the Cr content of SS steels improves corrosion resistance but compromises mechanical properties[8]. When operating in reducing acidic environments, such as those found in fuel cells, electrowinning cells and waste-water treatment applications, SS are subject to degradation by corrosion due to the dissolution of the passive oxide layer[9,10]. As a result, the SS part may perform poorly and have limited durability, necessitating premature replacement or repair[9]. Cathodic modification is a technique which can improve the corrosion resistance of stainless steels in reducing acid environments. The process involves alloying stainless steels with PGMs which enhances

corrosion resistance by two different mechanisms[11]:

- Altering corrosion thermodynamics so the passive state, whereby corrosion rates are low, is easier to achieve
- Inhibiting metal dissolution by blocking active sites on the stainless steel surface exposed to the corrosive medium

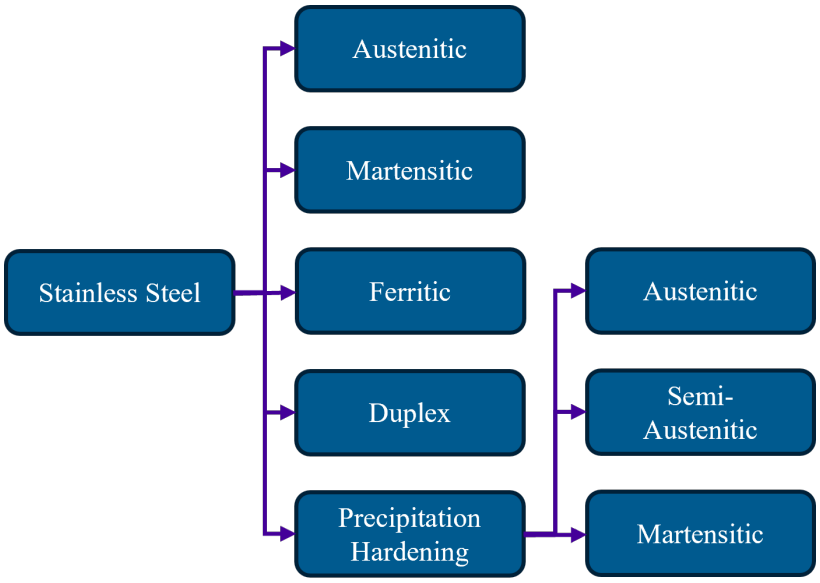

Figure 1.1: Schematic diagram illustrating the stainless steels (SS) family. Precipitation hardening SS are divided into three subtypes which describe the phase composition in their precipitation hardened state

The cathodic modification phenomenon was first noted by Monnartz[12] in 1911, who observed that winding platinum wire around iron-chromium alloys reduced corrosion rates in acids. Since then, numerous studies have shown that bulk alloying and coating steels with PGMs improves corrosion resistance through cathodic modification[13–19]. Despite the demonstrations of the cathodic modification of stainless steels by PGMs[13–19], this technique has not achieved commercial success[9]. A significant reason bulk alloying with PGMs is not a widely implemented solution to corrosion is that it is a expensive technique due to the volume of PGMs required[17,20,21]. Coating SS with PGMs is a less expensive option[17,21]. However, research has shown that this technique also has limitations, including spalling and unpredictable corrosion performance, meaning it is unlikely to provide effective long-term corrosion protection[9,10,16,22].

Despite the advantages presented by powder metallurgical routes, the topic of powder processed cathodically modified stainless steels has received limited research attention. To the best of the author's knowledge, the subject has been explored solely by Peled and Itzhak[18,23,24], who studied the corrosion behaviour of sintered bulk alloyed PGM-doped 316 stainless steel in sulphuric acid. However, these studies did not account for critical variables affecting the corrosion behaviour of sintered stainless steel. Parameter optimisation is of utmost importance when dealing with powder metallurgical processes. Selecting ideal processing conditions means that characteristics such as phase composition, grain size and density can be tailored to render the performance the best it can be. The corrosion properties of sintered materials are influenced by density; as a general rule, in acidic environments, high density sintered stainless steels possess better corrosion resistance than their low density counterparts[25]. In their work, Peled and Itzhak[18,23,24] did not evaluate the impact of density on the corrosion behaviour of the samples studied nor was parameter optimisation explored. Additionally, the corrosion behaviour of the sintered samples was not compared to cast equivalents, so it is difficult to assess the corrosion performance of samples produced by Peled and Itzhak.

Functional grading by powder processing is an as-yet unexplored approach to enhancing stainless steels using PGMs which may overcome some of the issues associated with cathodic modification by bulk alloying and coating. Functionally graded materials are characterised by the continuous change in phase composition as a function of position[26]. Incorporating PGMs into stainless steels by functional grading means the cathodic modifiers can be concentrated where corrosion resistance is needed: at the interface between the component and the environment. As a result, a lower volume of PGMs would be required to impart the same corrosion resistance when compared with bulk alloying, improving the cost-to-benefit ratio of cathodic modification. Functional grading can also overcome the spalling issues associated with coatings by facilitating gradual microstructural changes.

FAST is a powder consolidation method that can be used to produce high density parts from metallic and non-metallic powder feedstock by applying uniaxial pressure and a pulsed direct current[27]. Compared with conventional sintering techniques, FAST can use lower sintering temperatures, shorter sintering times and higher heating rates[28]. The literature demonstrates that FAST can be used to successfully create functionally graded materials[26,29–33].

The research on powder processed PGM-doped stainless steels is limited. To the best of the author's knowledge, no publications have explored the use of FAST to produce functionally graded PGM-doped stainless steels. This thesis aims to expand the knowledge of cathodically modified stainless steels produced by powder metallurgy in addition to investigating the feasibility of FAST to produce novel FGM cathodically modified stainless steels.

1.2 Industrial Context

It is imperative to understand the industrial context in which this EngD project fits. This section explores the predicted PGM market trends and how this will effect the economic viability of industrially utilised cathodically modified stainless steels.

1.2.1 PGM Availability

Ru doping dominates recent publications on the topic of stainless steel cathodic modification[9]. The primary reason why ruthenium is the research focus of stainless steel cathodic alloying is its cost. According to the latest market report published by Johnson Matthey, currently, the price of Ru is the lowest of all the PGMs, as has historically been the case for the last 25 years[34]. However, the share price of PGMs fluctuates with time, owing to supply and demand trends which accompany the development of new technologies. At present, the demand for Pd exceeds the supply due to their critical status in the production of catalytic converters for internal combustion engines[35]. The majority of Pd is used in automotive applications (83%), though its distributional usage across different sectors is set to change in the future[36]. Increasingly ambitious global emission targets are a strong driver for the change in the consumption of PGMs since it prompts internal combustion engines to be phased out in favour of battery and fuel cell powered vehicles[37]. In September 2023, it was announced that from 2035 all new vehicles sold in the UK must be zero emission[38]. Globally, 27 countries have signed targets to aim for fully electric bus and lorry sales by 2040[39]. These policies will lead to reduced demand for catalytic converters and, therefore, the reduced consumption of Pd in the automotive industry[36]. With this demand reduction, a fall in price will likely follow[36]. This market trend makes the cathodic modification of stainless steel more economically viable in the future than it currently is.

1.3 Problem Definition

The cathodic modification of stainless steels has been widely researched over the last 100 years. Despite this, the technique has not achieved commercial success. The high cost and unpredictable long-term behaviour are the main obstacles to the industrial roll-out of cathodically modified materials. At present, research on powder metallurgical approaches to cathodic modification remains lacking despite the evident potential cost-saving benefits of functional grading. An understanding of the processing-microstructure-properties relationship of such materials is crucial to the progression of research into powder processed cathodically modified stainless steels. The research presented in this thesis aims to address the highlighted gaps in knowledge and contribute to the discipline of corrosion and materials science.

1.4 Project Aims

This project aims to produce Ru- and Pd-doped 316L and 17-4PH stainless steels by powder metallurgical processing. Through characterisation, this research seeks to understand the effect of the processing technique and PGM additions on microstructure and corrosion. In powder metallurgy, parameter optimisation is a fundamental step in producing materials with the desired characteristics. As a result, varying the processing conditions is a necessary step within the scope of this EngD project.

1.5 Project Objectives

The following bullet points detail the steps which should be taken to achieve the project aims.

- Use FAST to produce bulk alloyed samples and work towards parameter optimisation for each of the compositions studied. Near-optimal conditions will be achieved by varying sintering temperature and time
- Investigate the relationship between sintering conditions, microstructure, mechanical and corrosion properties
- Assess the feasibility of using FAST to produce functionally graded PGM-doped materials. Characterise elemental distribution and assess the corrosion performance

of these samples

- Explore the effect of conventional heat treatment cycles on the corrosion performance of sintered PGM-doped 17-4PH stainless steel

1.6 Thesis Outline

In the present chapter, the background is presented, the current literature on the topic of the study is disseminated and the need for the current study is highlighted. The industrial context is also established here.

Chapter 2 presents a review of literature pertinent to this study. The chapter begins by introducing stainless steels and exploring their chemical composition and typical properties. It then presents an overview of powder metallurgical processing with a focus on the production and consolidation of metal powders. Special attention is given to the consolidation technique of primary interest to this study, field assisted sintering technique (FAST). The operation of FAST is explained and its capabilities are compared to similar sintering techniques. Following this, the general principles of metallurgical corrosion are presented before honing in on the corrosion of conventionally and powder processed stainless steel. The cathodic modification mechanism is described and an overview of relevant literature on the cathodic modification of stainless steels is given.

Chapter 3 explains the experimental techniques used in this study. It includes a description of the analytical processes used to characterise the powder feedstock and the sintered samples. In addition, the chapter explains how FAST was used to produce bulk alloyed and functionally graded samples. Lastly, the methods used to assess the corrosion performance of the doped and undoped stainless steel samples are outlined.

This thesis consists of four combined results and discussion chapters. The first of which, Chapter 4, presents the characterisation of the stainless steel powders used in this study. The impact of powder composition, morphology and size on corrosion resistance is explored. Chapter 5 presents the characterisation of the bulk alloyed stainless steel samples, with a focus on the effects of sintering conditions on material microstructure and physical properties. The impact of the atomisation technique on the microstructure and hardness behaviour of 316L stainless steel is also discussed here. Following this is the assessment of the functionally graded material produced using FAST. The impact of heat treatment on powder processed PGM-doped 17-4PH is studied in Chapter 6.

Finally, the effect of atomisation technique, consolidation approach, heat treatment and PGM doping on corrosion performance is investigated in Chapter 7.

The findings and industrial implications of this project are summarised in Chapter 8. In light of this study's conclusions, potential areas for future research are identified here.

CHAPTER

2

Literature Review

2.1 Stainless Steel

Stainless steels are iron alloys which contain between 10.5 wt.% to 30 wt.% Cr[2,40]. It is the Cr content of stainless steels which is a major proponent of their corrosion resistance. Upon exposure to the environment, stainless steel will form a 1 - 5 nm surface layer primarily composed of Cr_2O_3 which inhibits further chemical changes and degradation to the bulk material[2,40]. The passive film found on stainless steels is chemically dynamic with Cr, O and Fe bonds which form the film continually breaking and remaking[2]. It is because of this self-healing behaviour the passive film of stainless steels can reform within seconds once damaged[1]. Due to their ability to operate in corrosive environments, stainless steels are considered an integral group of materials and can be found in a variety of domestic, artistic, architectural and industrial applications, as illustrated in Figure 2.1[7].

Based on their alloy chemistry and resulting phase composition, stainless steels can be classified as being either austenitic, martensitic, ferritic, duplex or precipitation hardening with each type possessing unique mechanical and corrosion resistance characteristics (Figure 1.1). The two stainless steel grades of interest to this study are 316L and 17-4PH, which belong to the austenitic and martensitic precipitation hardening families, respectively. Within this section, the general behaviour of stainless steels belonging to these two families will be explored before presenting the uses, behaviour and processing of the two stainless steel grades relevant to this study: 316L and 17-4PH.

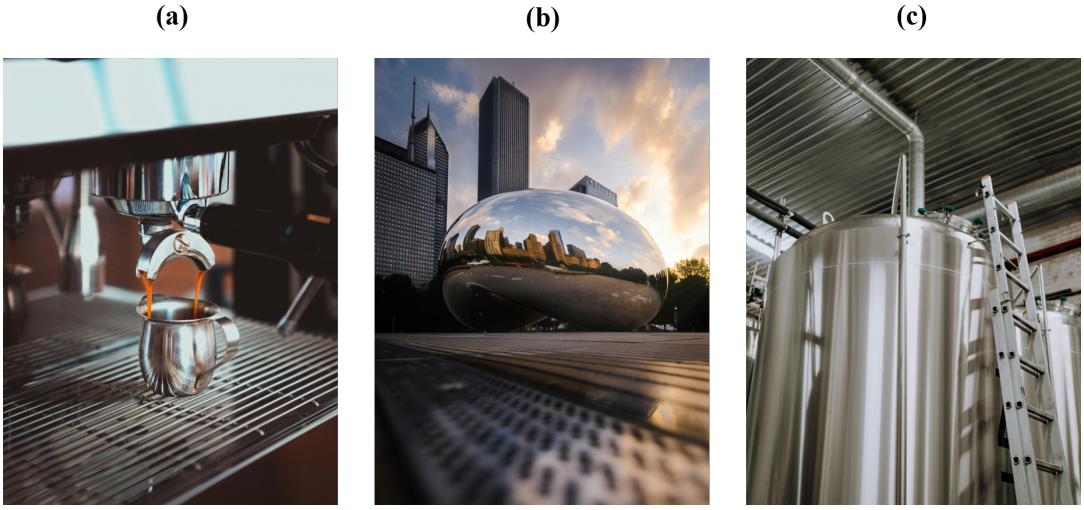

Figure 2.1: Examples of stainless steel usage. Photograph (a) shows a domestic coffee machine, (b) shows *Cloud Gate* a sculpture in Chicago and (c) shows a fermentation tank used in brewing. Images are royalty-free and obtained from pexels.com

Austenitic Stainless Steels

Of all the stainless steel families, austenitic stainless steels are the most prevalent owing to their useful combination of high strength, ease of fabrication and excellent corrosion resistance[41]. Austenitic stainless steels possess face-centred cubic austenite as the majority phase at ambient temperatures[42]. Regarding corrosion resistance, austenitic stainless steels typically outperform their martensitic and ferritic counterparts[42].

316L is an austenitic stainless steel which contains Cr to improve corrosion resistance, Ni to stabilise austenite and Mo to improve corrosion pitting resistance[43]. The 'L' designation in *316L* signifies that it is a low-carbon stainless steel grade and is less susceptible to sensitisation[44].

Precipitation Hardening Stainless Steels

Precipitation hardening (PH) stainless steels are characterised by their hardenability. These alloys are subjected to a two-step heat treatment process. The thermal processing causes the precipitation of nano-sized particles which impede the motion of dislocations, strain the crystal lattice and produce a strengthening effect[45]. The PH stainless steel family can be further divided into three categories depending on which major phase is present in the material in the heat treated condition. One such subcategory of

PH stainless steels is the martensitic PH steels, characterised by their body-centred tetragonal crystal structure, this group is the most widely used of the PH family[42,45].

17-4PH is a martensitic precipitation hardenable alloy. After the two-step heat treatment, the resultant 17-4PH microstructure possesses material-strengthening Cu-rich precipitates, making the heat treated condition the preferred condition[4,7]. In its heat treated condition, 17-4PH has corrosion resistance comparable to the austenitic grades in most media[7,44]. The heat treatment of 17-4PH is further discussed in Section 3.3.

2.1.1 Elemental Composition

Compared to other widely used metals, stainless steels are highly alloyed[46]. Stainless steels are designed so that the type and amount of each alloying element influences chemical or mechanical behaviour in a specific way. Their chemical complexity, however, means that care must be taken to maintain the fine-tuned balance of elements in stainless steels to give rise to the desired properties[46]. Though the main focus of this EngD is the impact of PGM elemental additions on corrosion performance, the role and influence of each element present in the undoped stainless steel compositions cannot be ignored. Here, the effect of each major alloying element in 316L and 17-4PH is investigated.

Chromium

The protective oxide film which imparts the characteristic corrosion resistance to stainless steels is Cr-rich. As a result, a minimum of around 10.5 wt.% Cr must be present to facilitate the formation and stability of the passive film[2]. Increasing the Cr content enhances corrosion resistance by improving the stability of the film[47]. However, this comes at a cost to mechanical performance and so Cr content cannot be increased indefinitely[48]. Therefore, alternative ways to improve the corrosion behaviour of stainless steels are sought.

Generally, martensitic stainless steels contain less Cr than austenitic grades since Cr is a δ-ferrite stabiliser[44,45]. Rapid cooling can contribute to the formation of δ-ferrite since it restricts diffusion, inhibiting the formation of austenite from δ-ferrite. The presence of δ-ferrite has a reported adverse effect on the corrosion performance of SS as it causes sensitisation, depleting adjacent regions of Cr leaving it more susceptible to corrosive attack due to the decreased stability of the passive oxide layer[49,50]. Lower δ-ferrite

amounts are often desired since δ-ferrite is typically associated with the deterioration of the mechanical performance of stainless steels[51–53].

Nickel

Nickel is an austenetising element and so it is added in large amounts to 316L stainless steel to retain austenite at room temperature, enhancing toughness and weldability by doing so[1,48]. Compressibility is an important characteristic of materials used in powder metallurgy because it is intrinsically linked to final part density - a highly compressible powder can achieve high density compacts with lower applied pressure[54]. Nickel has a beneficial effect on the compressibility of steel powders and its content, therefore, approaches the upper limits of the standardised material compositions[46]. Regarding corrosion resistance in stainless steels, Ni aids repassivation and improves pitting resistance[2,47].

Molybdenum

The presence of Mo helps to stabilise the passive film increasing the pitting and crevice corrosion resistance of stainless steels when working in conjunction with Cr[2,48]. While the exact mechanism by which Mo improves pitting resistance is unknown[47], Mo may block active sites in stainless steels and facilitate homogeneity in the passive film[55]. Mo reportedly helps to reduce the pit depth and diameter growth rates[56].

Manganese

Mn is added to stainless steels to form MnS inclusions which improve the machinability of the material[57]. However, MnS inclusions also play a central role in pitting corrosion in stainless steels since they act as pit nucleation sites[58,59].

During conventional stainless steel processing, some Mn will be removed during the deoxidation stage, whereby Mn reacts with oxygen, slag forms and is subsequently removed[60]. Atomisation has reduced abilities for oxidation and slag removal. As a result, the Mn content must be carefully tailored to the chosen melting and atomisation technique. Lower Mn contents are typically prescribed to WA stainless steels compared with their GA counterparts[61–63]. This is because, as a strong oxidising agent, Mn readily reacts with oxygen in the air[64]. Owing to the conditions under which the metals are atomised, the risk of Mn oxidising in WA is higher than in VIGA[60,63]. As a result, the

Mn content of the feedstock used to produce WA 316L is typically lower than that of VIGA 316L[60,63]. It is desirable to have control over the manganese content of stainless steels since, similar to MnS inclusions, manganese oxide inclusions are also reported to act as pit initiation sites[65,66]

Silicon

Similar to Mn, Si is an oxidising agent. However, the careful control of the concentration of Si is of greater importance than Mn because the majority of the oxidation which occurs during the water atomisation of stainless steels is that of silicon[60]. Silicon is added to stainless steel melts during water atomisation so that a protective layer of SiO_2 forms on the powder surface limiting further oxidation and controlling the total oxygen content of the alloy[67,68]. However, SiO_2 is not easily reduced and will often remain in powder metallurgy (PM) parts after sintering[60]. This is undesirable since SiO_2 powder coverage can retard coarsening mechanisms during the intermediate stage of sintering, preventing the formation of necks between adjacent powder particles[62,69].

Additionally, SiO_2 inclusions can impede the formation of a stable chromium oxide film and impair corrosion behaviour as a result[60]. Due to its strong affinity for oxygen, excessive Si can contribute to higher overall oxygen in water atomised stainless steels[46]. Therefore it is imperative that the Si content be carefully controlled in the precursor material used to produce WA atomised stainless steel.

The atomisation fluid used in gas atomisation can be air or can be an inert alternative such as argon[60]. Using an argon atomisation fluid enables you to beneficially limit the amount of oxidation occurring[60]. GA powders produced in this way typically oxidise less and possess smaller oxides than their WA counterparts[68,70]. The atomisation fluid used also has an influence on the chemistry and surface coverage of the oxides which form on the powder particles. Bracconi and Gasc[71] found that nitrogen atomised 304L stainless steel possessed Mn, Fe and Cr-based oxides on the surface of powder particles. These findings were supported by Nyborg and Olefjord[72] who found the same oxides on nitrogen atomised martensitic Fe12Cr stainless steel. Meanwhile, Tunberg and Nyborg[73] characterised the surface oxides of water atomised 304L stainless steel and found that the oxides on the surface were predominantly Si-based with lesser amounts of Cr, Fe and Mn. SiO_2 has a deleterious effect on corrosion performance and so where possible it is desirable to minimise its presence[74]. The effect of atomisation fluid on corrosion

performance is explored in greater detail in Section 2.4.3.

Copper

Copper is present in 17-4PH stainless steel to increase strength and toughness by the precipitation of nano-sized precipitates throughout the martensitic matrix[46]. This strengthening mechanism is achieved by a two-step heat treatment[45].

Niobium

Niobium is added to stainless steel as a measure against intergranular corrosion[75]. As a strong carbide former, niobium carbides will preferentially form rather than chromium carbides[41]. By suppressing the formation of chromium carbides, Nb helps to prevent sensitisation[76].

Carbon

Carbon is an important component of stainless steel as it improves mechanical properties via interstitial strengthening by impeding the motion of dislocations[1]. However, the amount of carbon in stainless steels must be carefully controlled owing to its detrimental influence on corrosion performance. When present in solid solution, C does not affect pitting resistance and will only reduce pitting corrosion resistance when in the form of carbides[47]. The formation of carbides plays a pivotal factor in whether *intergranular corrosion* will occur. The exact nature of intergranular corrosion and how it can be avoided is discussed in the following paragraphs.

Intergranular Corrosion

The composition and processing of austenitic stainless steels must be carefully controlled to avoid intergranular corrosion (also known as intergranular embrittlement). The mechanism proceeds in austenitic stainless steels exposed to moderate temperatures (371 - 760°C)[75]. Powder metallurgical processing can place materials at risk of sensitisation due to the slow heating and cooling rates typically employed[46]. Processing at these temperatures can lead to the precipitation of $M_{23}C_6$ carbides, usually Cr-rich, on the grain boundaries of austenitic stainless steels[1,41]. As a result, the volume of material surrounding grain boundaries can become Cr-depleted, a process known as *sensitisation*[75]. If the depleted regions contain less Cr than is needed to form a stable, dynamic passive

film then as a result of this chemical and microstructural change intergranular corrosion may proceed[1]. The propensity for sensitisation is reduced by *stabilisation*[75]. To stabilise a stainless steel the following material design approaches may be taken[1]:

- Reduce carbon content
- Alloy with strong carbide-forming elements such as Nb and Ti, so that they will preferentially react with carbon
- Alloy with elements which increase the time taken for Cr carbides to form, such as Mo

The carbon content in stainless steels affects phase composition owing to it being a strong austenite former[41]. The Fe-C phase diagram can be used to explain the impact of C content on phase stability (Figure 2.2). The solubility limit of carbon in austenite is a function of the carbon content[1]. As such, when the concentration of C exceeds the solubility limit, C will precipitate from austenite and form carbides[41]. Though the diagram presented in Figure 2.2 illustrates the general effect of C on phase stability, it specifically describes a plain carbon steel and is therefore a simplification of the elemental complexity of stainless steel. As a result, the diagram doesn't accurately capture the phase transformations which would occur in austenitic grades. In austenitic stainless steels, as opposed to cementite formation described in Figure 2.2, $M_{23}C_6$ would form instead[41]. The tendency of stainless steels to form undesirable carbides mean that alloy contamination must be carefully avoided at each step of its processing.

2.1.2 Heat Treatment

The heat treatment of 17-4PH comprises of three steps: solution treatment, rapid cooling and ageing (illustrated in Figure 2.3)[45]. Typically, 17-4PH is supplied from the mill in what is known as *Condition A*[7]. This refers to the standardised material produced by solution treatment during hot rolling[45]. During solution treatment, the dissolved Cu forms a supersaturated solution with the stainless steel and ensures that the microstructure is fully austenitic[45]. Since the solubility of Cu decreases with a decrease in temperature, rapid cooling is required to maintain the Cu in a supersaturated solution[45]. From Condition A, 17-4PH is aged to produce fine Cu-rich precipitates (CRP)s[7,77]. By straining the crystal lattice, CRPs impede the motion of dislocations and produce a strengthening effect[45].

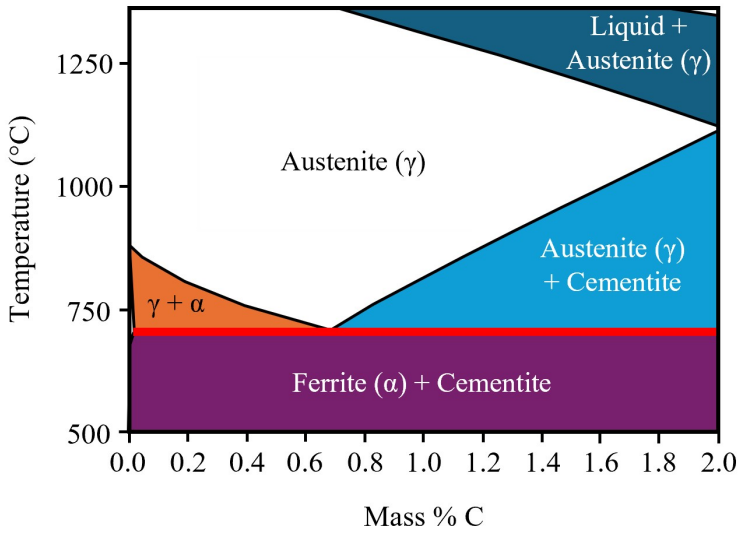

Figure 2.2: The Fe-C phase diagram illustrating the solubility limits of carbon in austenite. Reprinted from Steels: Microstructure and Properties (Fourth edition), Bhadeshia, H. and Honeycombe, R., Chapter 3 - Iron-Carbon Equilibrium and Plain Carbon Steels, Pages 59 - 100, Copyright (2017), with permission from Elsevier [1]

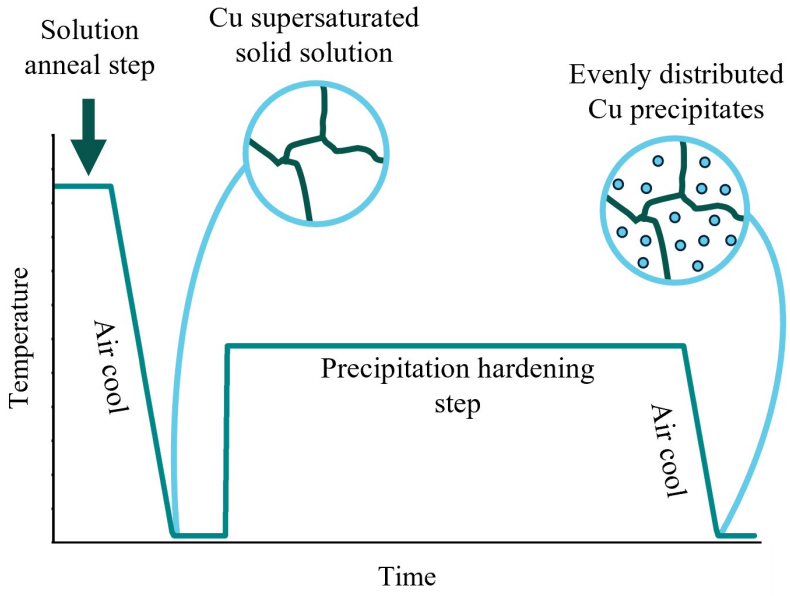

Figure 2.3: Schematic diagram illustrating the solution anneal and precipitation hardening steps in the thermal processing of 17-4PH. The solution anneal step produces a matrix that is supersaturated with Cu. The precipitation hardening (also known as the ageing step) nucleates nano-sized Cu-rich particles [46]

In terms of morphology, during the process of ageing the microstructure of the Cu precipitates evolves from spheroidal particles and can eventually form elongated rod-like precipitates with prolonged ageing[78]. At the end of the ageing step the material is cooled and it is during this step that martensite forms[1]. Owing to the material property enhancement generated by CRP presence, heat treated 17-4PH is the preferred form for critical applications[7,77].

The heat treatment conditions used for processing 17-4PH are designated a code of the following format: 'H' followed by a number which describes the temperature at which the ageing is carried out at in °F. For example, H1075 describes a heat treatment process whereby ageing is at 1075°F.

2.2 Powder Metallurgy

Powder metallurgy is the method by which near-net-shape components are formed from powdered materials at temperatures below their melting points[27,79]. Due to their relatively low processing temperatures compared with casting, powder metallurgy can have reduced energy costs and minimise component-mould reactions[27]. The powder processing route is suitable for the mass production of metal components of widely varying shapes and sizes, though high start-up costs render powder metallurgy only economically feasible in large-scale production runs (more than 100,000 parts)[27,80]. Melt casting remains the chief metallurgical processing technique, though powder metallurgy has developed a large global market throughout the aerospace, automotive and medical industries[27,79,81]. While powder metallurgy can produce parts from a wide range of materials, in terms of tonnes produced, ferrous-based metals dominate, examples of which are given in Figure 2.4[80].

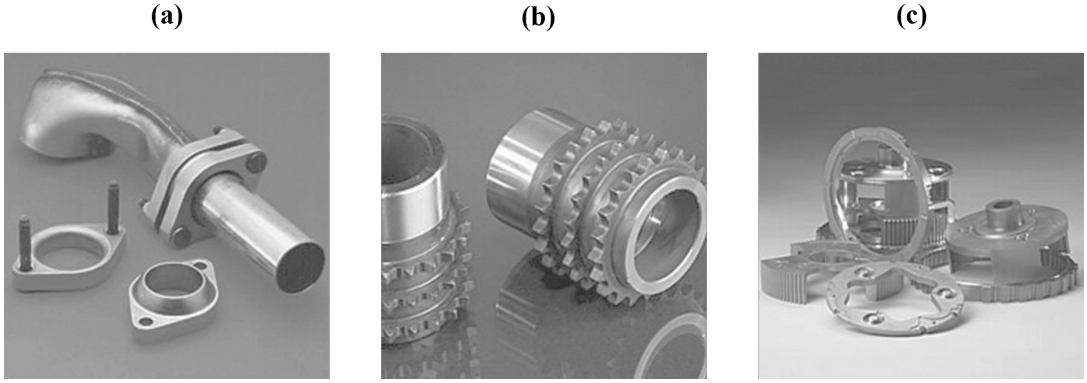

Figure 2.4: Examples of various ferrous powder metallurgy components. Photograph (a) shows a stainless steel manifold flange and exhaust converter outlet flange, (b) shows a steel crankshaft sprocket for an automotive engine and (c) shows a five component carrier and one-way rocker clutch assembly for automatic transmission. Reprinted from Advances in Powder Metallurgy, Ramakrishnan, P., Chapter 17 - Automotive Applications of Powder Metallurgy, Pages 493 - 519, Copyright (2013), with permission from Elsevier[82]

Before exploring the facets of powder metallurgy, it is useful to define what is considered a *powder*. Dunkley[83] explains that a powder is usually a granular solid which is less than 1000 µm in size; powders larger than 150 µm are described as being coarse while those smaller are considered fine. Powdered metals can also vary in terms of their morphology (Figure 2.5).

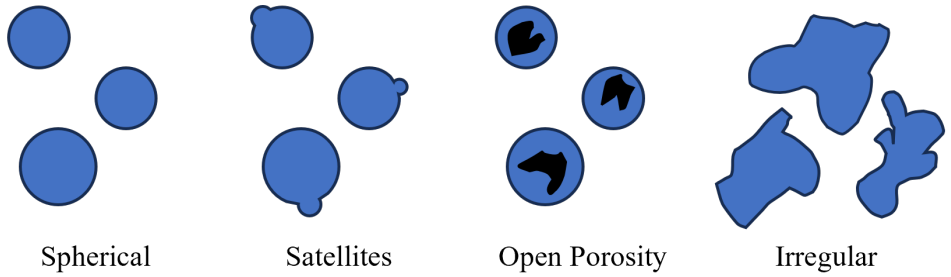

Figure 2.5: Schematic representation of four common metal powder morphologies

2.2.1 Atomisation

The first step in powder metallurgy is the production of the metal powder. On an industrial scale, atomisation is the preferred process for producing metal powders[84]. To atomise metals, first large ingots comprising of the chosen alloying elements alongside the base metal must be produced[85]. The process of atomisation by the two most widely used atomisation techniques, GA and WA, is shown in Figure 2.6[79].

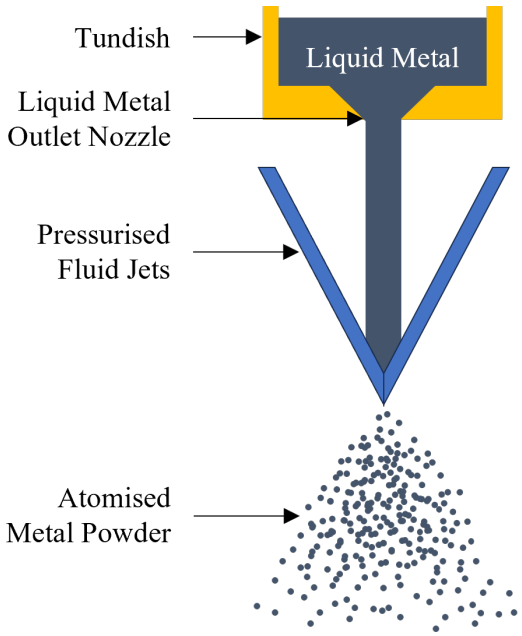

Figure 2.6: Schematic showing the production of metal powders by the gas or water atomisation technique. The stream of liquid metal is impinged by jets of either gas or water causing the formation of molten metal droplets which form powder particles upon cooling. Adapted from Fundamentals of Metallurgy, Lemoisson F. and Froyen, L., Chapter 12 - Understanding and improving powder metallurgical processes, Pages 471 - 502, Copyright (2005), with permission from Elsevier[79]

Compared with other powder production methods, atomisation produces powders with sizes varying between a few to several hundred microns in size with high packing density and low specific surface area, resulting in a powder with good flow characteristics and compressibility[79]. The specific combination of characteristics that a metal powder possesses is governed by the atomisation technique used, the operating conditions and the material to be atomised[79].

WA is the cheapest of the atomisation techniques and so is more widely used than GA[84]. The purity of WA powders is often limited, so where low oxygen contents are required, such as in aerospace applications, GA techniques are used instead[84,86]. The oxygen content of GA powders depends on the type of gas impinging the molten metal and the type of atmosphere in which the powder is produced[87]. GA carried out in air using compressed air for atomisation results in a high oxygen content of around 1000 ppm[87]. Using jets of inert gas rather than compressed air prevents the oxidation of the melt and powders produced have a lower oxygen content, typically around 100 - 500 ppm[87]. Performing inert gas atomisation within a vacuum chamber, a technique known as VIGA, further reduces the oxygen content of produced powders to as low as 50 ppm and allows for the production of reactive metal powders[87].

Water atomised powders tend to be more irregular in shape than GA powders, which are typically spherical (Figure 2.7)[88]. The resultant particle shape is the product of competing solidification and spheroidisation mechanisms[84]. The oxide films found on water atomised powders reduces droplet surface tension meaning that particles solidify before they can spherodise[84].

Powder characteristics are also influenced by the selected atomisation conditions. Employing higher water pressures in WA result in smaller powder particles[79]. Similarly, the particle size produced by GA can be minimised by increasing gas pressure and decreasing melt flow rate[79,84]. The particle size distribution of WA powders is typically large with a median particle size of 100 µm while GA powders tend to have a median particle size between 50 - 300 µm and a smaller particle size distribution[84]. Finer powders are desired since they minimise initial defect size; however, they are costlier than coarse powders as yields are reduced through the process of sieving[85].

Depending on the type of atomisation used, the operating conditions and the material used, the resulting metal powders will have varying morphology, purity, size and size distribution[79]. These characteristics will influence how the powder is used in later

processes and the resulting consolidated part properties and behaviour[84]. Atomisation produces particles of a range of sizes, these form a log-normal distribution[83]. Powder size and shape are important considerations since they control the ways in which the powder can be used in future processes[84]. Issues are associated with both small and large powder particles. Smaller particles are at risk of agglomeration as a result. Ma and Lim[89] states that the optimal particle size distribution is dependent on the composition being used, the consolidation technique and the conditions applied. Larger powder size distributions can be beneficial to final density as it means that any small gaps between larger powder particles can be filled by the smaller powder particles, leading to better packing density and better overall part densification. To the best of the author's knowledge, the optimal particle size distribution for FAST processing of 316L has not been researched, though the influence of particle size on FAST stainless steel has been investigated[90,91].

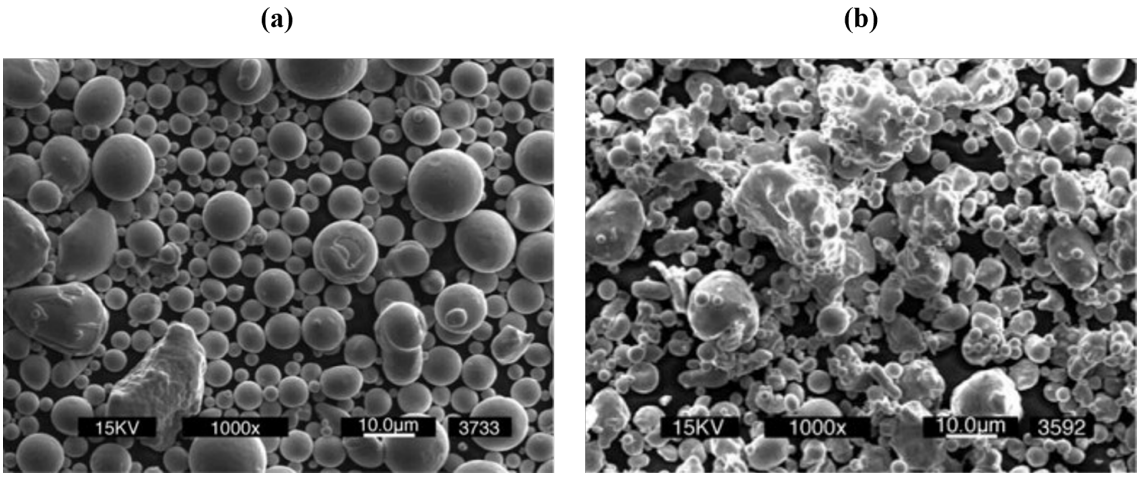

Figure 2.7: Scanning electron micrographs of (a) spherical stainless steel powder typical of GA and (b) irregular stainless steel powder typical of WA. Reprinted from Handbook of Metal Injection Molding, German, R. M., Chapter 3 - Powders for Metal Injection Molding (MIM), Pages 50 - 63, Copyright (2012), with permission from Elsevier[88]

2.2.2 Powder Consolidation

Consolidation is the process of forming a solid from powders. Figure 2.8[92] depicts the three main metal powder consolidation approaches.

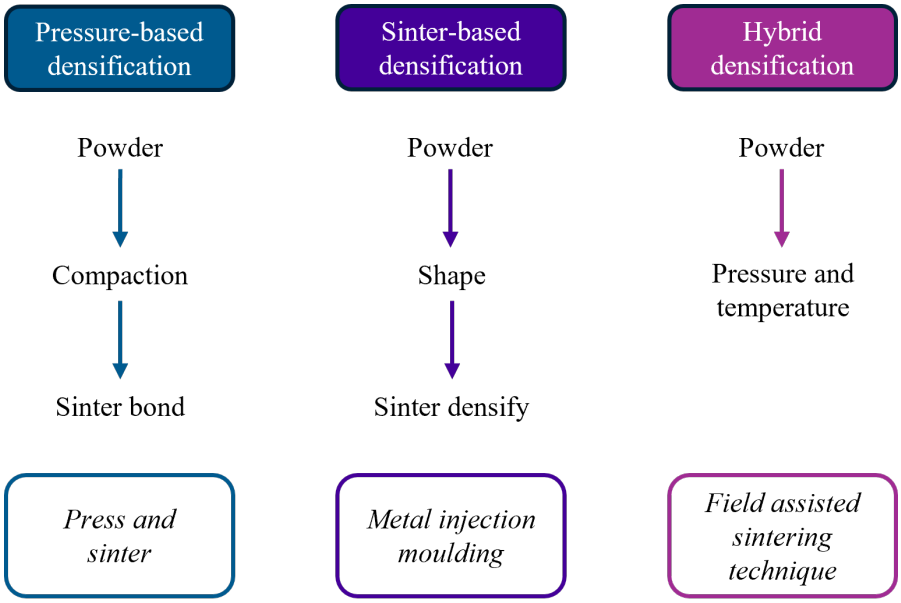

Figure 2.8: Diagram illustrating the three main types of compaction processes, the main steps involved and an example technique for each category of process in powder metallurgical processing. Adapted with permission of ASM International, from Powder Metallurgy Methods and Applications in Powder Metallurgy, James, W. B., 2015; permission conveyed through Copyright Clearance Center, Inc[92]

Pressure-based densification is characterised by the application of high pressure to achieve compaction followed by sintering to develop part strength[92]. Lubricants are often combined with powders to reduce interparticle friction and assist in particle rearrangement though this does limit the final density[92].

Metal injection moulding (MIM) is a sinter-based densification technique which uses high temperatures and fine powders to produce samples[92]. Binders and plasticisers are added to metal powders to improve the mouldability of the mixture, though these must be removed before the sintering step[92]. Samples shrink isotropically during sinter-based densification and as a result, the shrinkage should be accounted for when designing the process so the desired geometry tolerances are still achievable[92].

Pressure and elevated temperatures are employed simultaneously in hybrid densification techniques[92]. Vacuum conditions can also be used in hybrid densification operations

to minimise the oxygen content of sintered samples[92]. FAST is a form of hybrid densification and as the consolidation technique selected for use in this project, it will be further explored.

2.2.3 Sintering Phenomena

Before exploring FAST, the phenomena underpinning the process of sintering will be discussed. Sintering is characterised by the formation of chemical bonds between adjacent particles, often facilitated by the application of heat and pressure. The first stage of sintering is where the powder is loosely packed (Figure 2.9 (a)), individual powder particles are identifiable and a complex pore network can be observed[93]. With the application of pressure, physical particle-particle contacts form (Figure 2.9 (b)). As sintering proceeds, mass transport of atoms means that adjacent particles become bonded at their contact points and compact strength increases (Figure 2.9 (c))[93]. Later on in sintering, necks increase in size, the pore network becomes closed due to matter transport and pores begin to spherodise. The density of the compact begins to markedly increase (Figure 2.9 (d))[93]. As sintering proceeds further, porosity is reduced until maximum densification is attained.

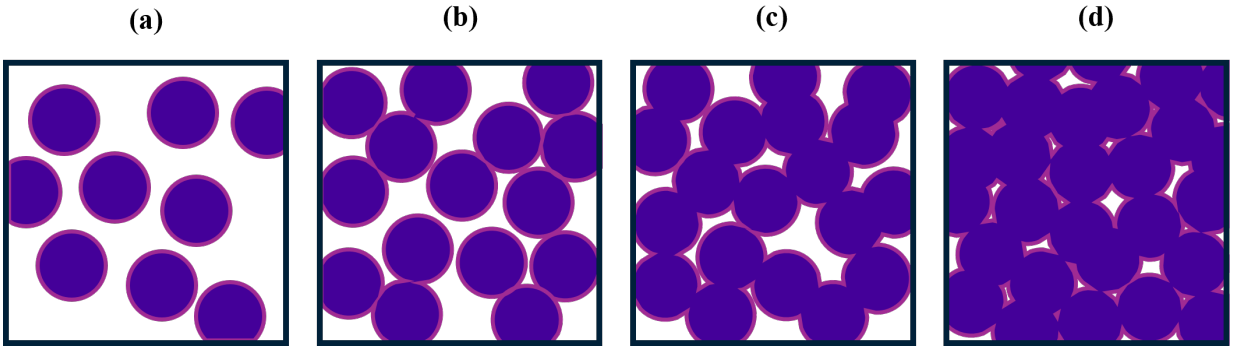

Figure 2.9: Schematic diagram showing the morphological changes in the pore structure which occur during sintering

As described by German[94], sintering is a phenomenon characterised by the reduction of energy of a system. One of the ways in which this is accomplished is by the elimination of surface area by bond growth between contacting particles[94]. The necking that results leads to the formation of grain boundaries, a microstructural feature which is necessary to accommodate crystallographic misorientation and enable the annihilation of pores[94]. Although the formation of new grain boundaries increases grain boundary area (leading

to an increased system energy), the new grain boundaries facilitate further densification by grain boundary diffusion mechanisms[94].

Grain growth is another energy reduction process as it decreases grain boundary area[94]. Grain size changes as sintering proceeds by the coalescing and coarsening mechanisms facilitated by the mass transport of atoms[95]. Coalescence is the process by which larger grains absorb smaller grains while coarsening is a diffusion-regulated process whereby atoms are exchanged between two different grains, with atoms flowing from a smaller grain to a larger grain[95]. Coarsening is also influenced by composition, strain and crystal orientation of the microstructure. The changes to grain shape and size occur because the system is thermodynamically driven to reduce interfacial energy[95]. As sintering proceeds, the number of grains decreases as the size of the grains increases. Pores must be close to grain boundaries to shrink during sintering. Pore annihilation is necessary for densification to proceed. Grain growth causes the distance between pores and grain boundaries to increase. Therefore, grain growth can be detrimental to the progression of sintering as it can prevent the annihilation of pores and prevent higher densities from being achieved. Additionally, grain coarsening will proceed even after the final part density is achieved and coarsened grains can negatively impact properties, it is imperative that samples are not overprocessed[95].

In general, literature reports that increasing sintering temperature improves mechanical properties, increases density and decreases porosity due to densification processes[96–100]. Since densification and grain coarsening are thermally activated processes they proceed at higher rates with increased sintering temperature[93,101]. Similarly, extended sintering times provide greater opportunities for the mass transport mechanisms associated with densification and grain coarsening to proceed[94]. While grain size increases during densification and after maximum density has been achieved, coarsening does not proceed linearly. Grain growth is rapid at first, but decelerates once the grain size matches that of the powder particle size[94]. The presence of pores also work to retard grain growth but once eliminated, grain coarsening proceeds rapidly[94]. Over-sintering is the phenomenon whereby a sample is sintered at overly high temperatures for excessive periods of time which can result in excessive grain coarsening[94].

2.2.4 Field Assisted Sintering Technique

FAST is a rapid powder consolidation technique which works by applying a pulsed direct current to a conductive graphite die containing the powder to be sintered (shown in Figure 2.10)[102]. The electric field generated by the applied current enhances densification by the Joule effect which causes local temperature elevation when the current discharges between powder particles[28]. The application of uniaxial force in FAST increases the contact area between powder particles promoting densification mechanisms[28].

Sintering using FAST often proceeds under near-vacuum conditions with a small volume of Ar used to backfill the vacuum chamber[103]. This is done to raise the partial pressure within the vacuum chamber so it exceeds the vapour pressure of elements within the stainless steel to minimise compositional changes[103]. An element that is known to evaporate during the sintering of stainless steels is Cr, however this element will only evaporate from the outer surfaces of sintered materials and is not believed to affect bulk composition[70].

The primary disadvantages of FAST are that only simple geometries can be produced, using fine powders less than 100 nm in size can result in non-uniform densification and that it can be an expensive technique due to the need for a pulse DC generator[28]. In terms of the advantages associated with FAST, the process employs lower temperatures and higher heating rates and produces parts quicker than conventional powder metallurgy techniques, such as hot pressing (HP) and hot isostatic pressing (HIP)[99]. The relatively high heating rates of FAST restrict grain coarsening and inhibit the formation of undesirable phases[28]. FAST can produce uniform sintering without the need for binders and its precise control over processing parameters enables significant control over the resulting microstructure[28]. The technique is also highly tolerant to particle shape and size, unlike additive manufacture (AM) techniques, enabling cheaper powder feedstock use[102]. Additionally, FAST is a versatile processing technique capable of consolidating powders and joining metal parts, sintering coatings and producing functionally graded materials - a concept which will be further explored in the following section[29,104–109].

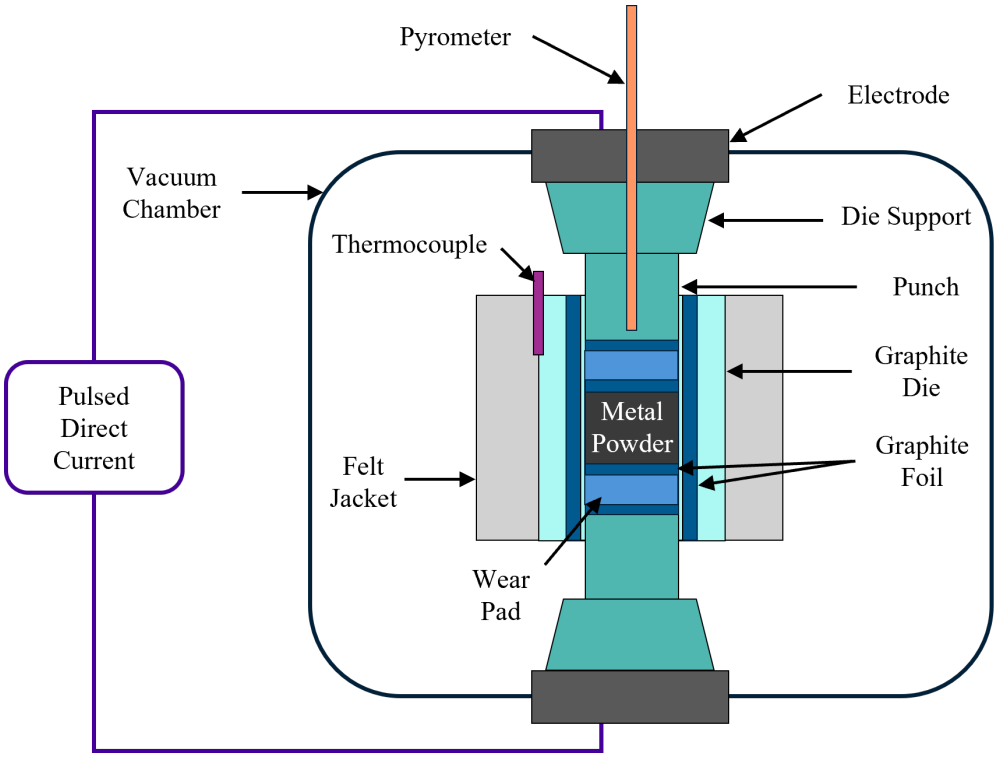

Figure 2.10: Schematic of the FAST apparatus depicting the arrangement of the metal powder in a felt jacket clad graphite die which is placed within a vacuum chamber. The positioning of the thermocouple and pyrometer are also represented

2.3 Functionally Graded Materials

FGMs are characterised by the spatial change of composition, microstructure or porosity for the purpose of tailoring the material properties to a specific application. Functional grading can be achieved by a variety of different processing routes, as shown in Figure 2.11. However, the versatility of powder metallurgy in particular lends itself well to the production of FGMs by enabling a level of control over microstructure that simply cannot be achieved by wrought or cast manufacturing approaches. Over the past two decades, the development of powder metallurgy and additive manufacturing technologies has enabled continuous growth of research in the area of FGMs (Figure 2.12).

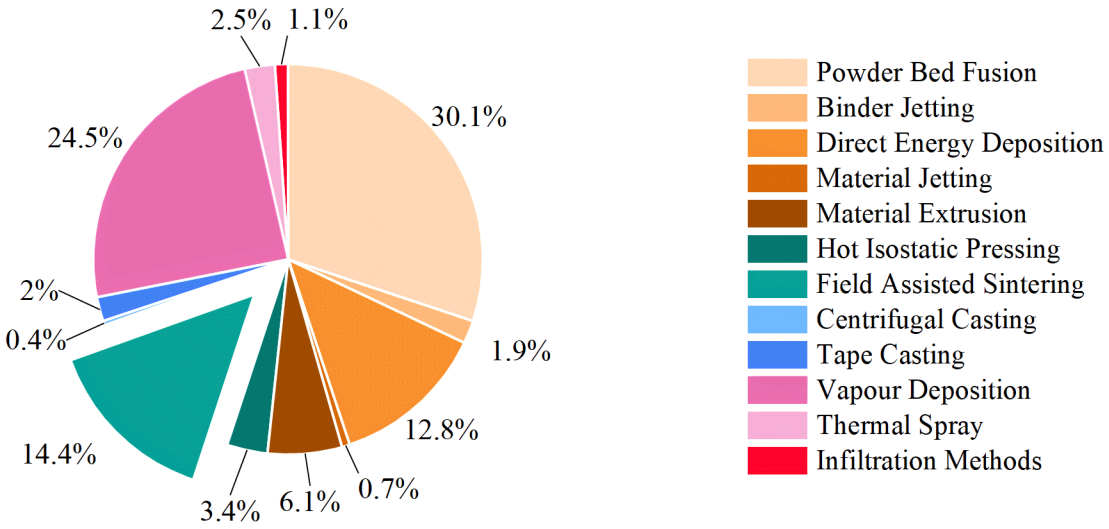

Figure 2.11: Pie chart showing the proportions of articles published in 2024 on the subject of different FGM processing routes. This search was conducted on 5th January 2025 using *ScienceDirect.com*. The wedge representing FAST publications has been exploded

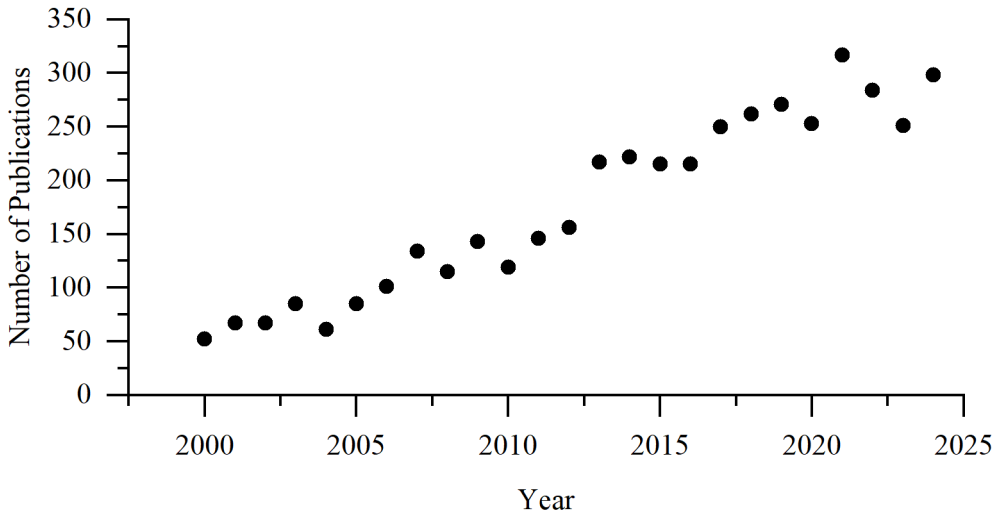

Figure 2.12: Graph showing the number of articles published each year. The search was conducted using the search term "functionally graded materials". This search was conducted on 5th January 2025 using *ScienceDirect.com*

Powder Processed Functionally Graded Materials

Presently, PM stainless steels find widespread use in automotive, medical and industrial sectors[110]. The primary reason for the use of powder metallurgy in these industries lies in its capacity to create complex geometries. However, a key motivation driving the future use of powder metallurgy (PM) is the desire to produce components with graded material properties - a characteristic unattainable by cast or wrought techniques alone[111]. This manufacturing approach means that novel application-specific materials can be designed and produced furthering the range of applications stainless steels can be used in. For example, Tan et al.[29] suggested a 316L/W FGM for use in fusion reactors, taking advantage of tungsten properties such as low tritium retention alongside the structural properties of 316L to produce an ideal material property combination for this application.

The current study explores the synthesis of stainless steel-platinum group metal FGMs to maintain the advantageous mechanical properties of SS while enhancing the corrosion resistance and minimising the total volume of PGMs used. This may enable the material to be employed in more aggressive environments, opening up new opportunities for its usage.

FAST FGMs

Research has shown that FAST can be used to produce compositionally graded samples with various potential applications, as Figure 2.13 illustrates.

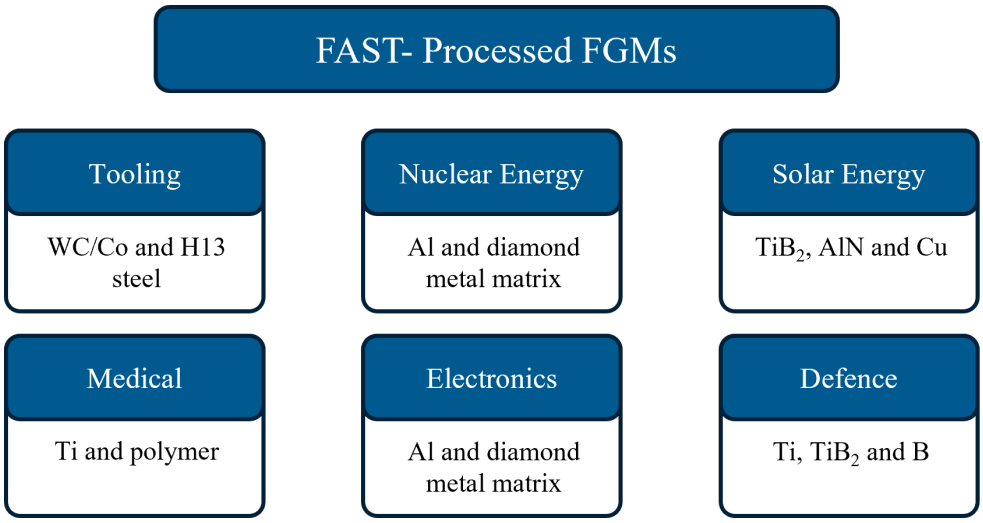

Figure 2.13: List of examples of applications and compositions of FGMs produced by FAST reported in literature[31,112–116]

Figure 2.14 illustrates the two ways in which FAST has been used to produce compositionally graded materials. The *layering approach* (Figure 2.14 (a)) involves initially filling the graphite die with the first powder composition and then levelling out by the powder by tapping the die assembly on a flat surface. Subsequently, the second powder composition is then poured on top of the first powder and levelled out by the same method. The sample is then sintered in the usual fashion to produce a functionally graded specimen.

The layering approach has been used to successfully produce FGMs made from various combinations of materials (Table 2.1). Using the layering approach and a modified die, Jajarmi and Sajjadi[30] successfully produced a six layer 316L/3Y-PSZ FGM. The modified die was necessary since the different layers in the 316L/3YPSZ FGM require different sintering temperatures due to their varying melting temperatures. The varied die diameter ensured a temperature gradient developed within the powders. As a result, homogeneous sintering behaviour proceeded and a higher density material was produced than if an unmodified die was used. The use of a modified die to produce FGMs by FAST was also demonstrated by Jin et al.[31] successfully producing a TiB_2/AlN/Cu FGM.

(a) Layering Approach

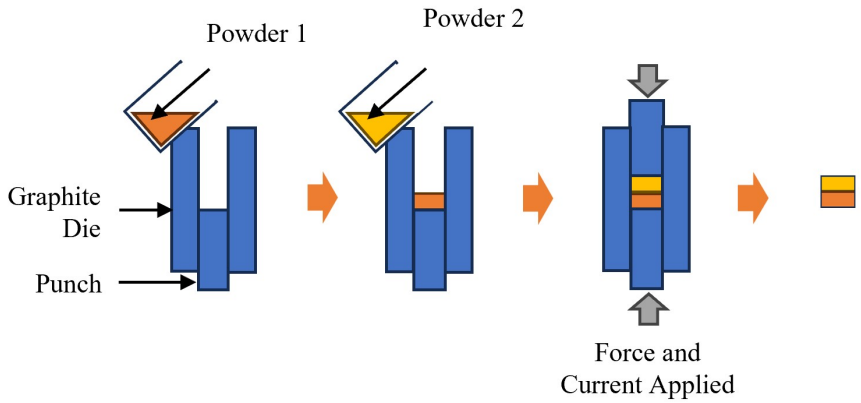

(b) Embedding Approach

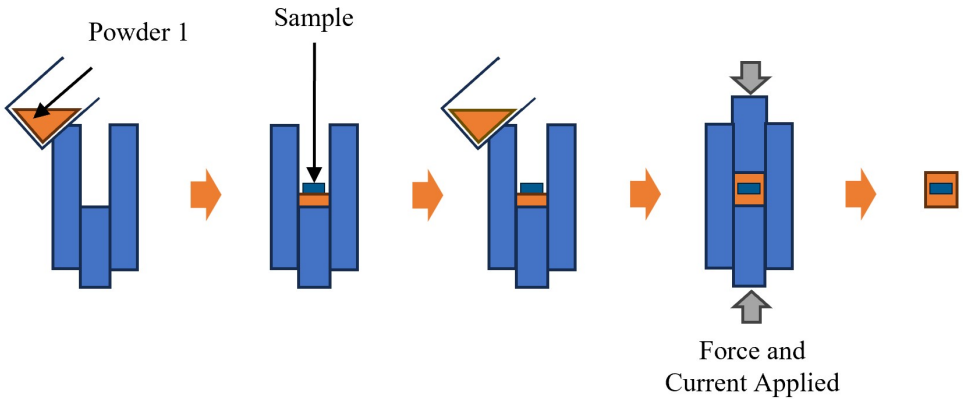

Figure 2.14: Schematic diagram showing how FAST can be used to produce compositionally graded materials via the (a) layering and embedding (b) approaches

Table 2.1: Summary of the different layered functionally graded materials which have been successfully produced using FAST as reported in literature

Description of Layered FGM Composition	Source
Six layer 316L/3Y-PSZ	Jajarmi and Sajjadi [30]
TiB_2/AlN/Cu	Jin et al. [31]
Distaloy SE-carbon	Zarebski and Putyra [32]
WC, Co and H13 steel	Machado et al. [33]
316L-2205 duplex stainless steel	Obadele et al. [26]
316L-tungsten	Tan et al. [29]

Various stainless steel FGMs have been produced using the layering approach. Zarebski and Putyra [32] successfully produced Distaloy SE-carbon graded samples using FAST and the layered approach. Machado et al. [33] has also shown it is feasible to produce FGMs made from combinations of WC, Co and H13 steel using FAST. Obadele et al. [26] and Tan et al. [29] demonstrated FAST can be used to produce 316L-2205 duplex stainless steel and 316L-tungsten FGMs respectively. The published research indicates that FGM stainless steel parts can be produced using FAST.

An alternative way of producing FGMs using FAST is the *embedding approach* and is illustrated in Figure 2.14 (b). It involves adding a powder to the graphite die and then levelling out by the powder by tapping the die assembly on a flat surface. Then the material to be embedded is inserted into the die. More powder is then added to the die to fully cover the embedded part. The sample is then sintered by the usual technique.

Almathami and Brochu [108] used the embedding approach to sinter fully dense 316L SS coatings containing 0, 2 and 6 wt.% Al onto SS substrates. Zhu et al. [105] reported the successful use of FAST to produce a dense, crack-free $MoSi_2$-MoB- ZrO_2 coating onto a Mo substrate. Both Pakseresht et al. [107] and Nozahic et al. [106] have shown that FAST can be used to successfully apply complex, multi-layer thermal barrier coatings (TBC) to superalloy substrates.

2.4 Corrosion

2.4.1 Principles of Corrosion

Corrosion is the thermodynamic process by which a material changes to attain its most stable state due to chemical, biochemical and electrochemical interactions[7,117]. The changes in the material due to corrosion can take the form of degradation of properties, serviceability and aesthetics and the formation of oxide or sulphide products[7,118]. The significant economic impact of corrosion is a strong driver for research into improving corrosion resistance. In the US alone, the annual cost of corrosion is estimated to be up to $90 billion[7]. Improving a material's resistance to corrosion imparts savings through reduced maintenance needs and improved part longevity[118]. Another major driver for the improved corrosion resistance of steels is the possibility of widening their range of applications[118].

As previously mentioned, corrosion can proceed due to electrochemical or chemical reactions. Electrochemical corrosion is often characterised by the presence of an electrolyte. Conversely, chemical corrosion relies on there being direct contact between the reactants[117].

Corrosion in an aqueous environment is often an electrochemical process. It involves at least one anodic oxidation partial reaction (Equation 2.1) and at least one cathodic reduction partial reaction (Equation 2.2), where M is the corroding metal[10,119,120]. The anodic reaction describes the dissolution of the metal while the cathodic reaction describes the reduction of water[117]. These reactions are illustrated in Figure 2.15. Note the corrosion process described here is a simplification of reality; corrosion often proceeds as a result of several different reactions occurring concurrently.

The dominant corrosion reaction is determined by the energy change associated with each of these partial reactions, the dominating reaction gives way to a net flow of electrons with an associated current[117]. If the rate of the oxidation reactions exceed that of the reduction reactions, then an anodic current will flow; if the opposite is true, then the current will be cathodic[10].

$$Anodic\ Reaction : M(s) \rightarrow\ M^{n+}\ (aq) + ne^{-} \tag{2.1}$$

$$Cathodic\ Reaction : 2H^{+} + 2e^{-} \rightarrow\ H_2 \tag{2.2}$$

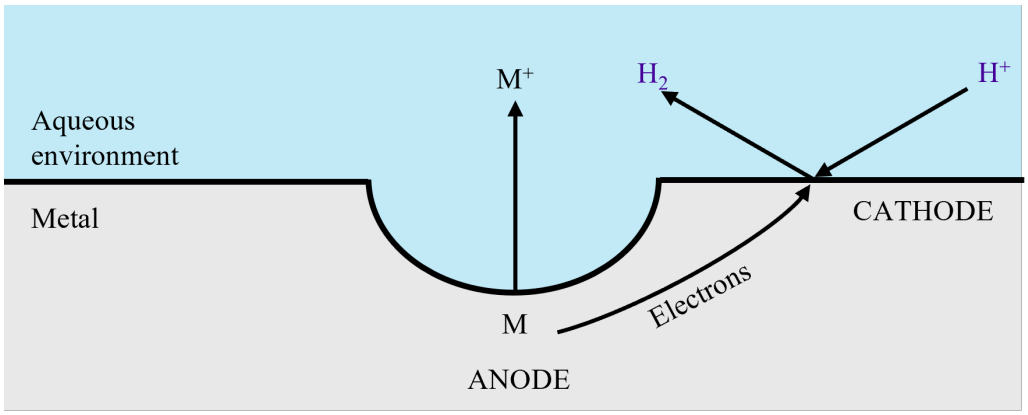

Figure 2.15: Schematic diagram illustrating anodic and cathodic corrosion reactions. The cathodic reaction represented is the formation of hydrogen from hydrogen ions while the anodic reaction shown is the dissociation of metal into metal ions and electrons. Adapted from Plant Engineer's Handbook, Schofield, M. J., Chapter 53 - Corrosion, Pages 961 - 985, Copyright (2001), with permission from Elsevier[121]

Whether or not corrosion can proceed in a particular situation is a question of thermodynamics. Equation 2.3[10] can be used to describe corrosion, where ΔG is the Gibbs free energy, n is the number of electrons exchanged during corrosion, F is the Faraday constant and E is the corrosion potential with respect to a standard reference electrode.

$$\Delta G = -nFE \tag{2.3}$$

When ΔG is negative, it indicates a reaction can take place, the more negative ΔG is the higher the possibility of a reaction occurring[122]. Contrastingly, when the change in Gibbs free energy is positive, the corrosion reaction cannot occur[122]. Thermodynamics cannot fully explain corrosion processes, nor can it indicate whether a reaction will actually occur and at what rate it will do so[10]. To further understand corrosion, kinetics must also be considered.

Corrosion Kinetics

At equilibrium, the net current is zero and the rates of the anodic and cathodic reactions are equal (illustrated in the Evans diagram in Figure 2.16). The potential at which equilibrium is achieved is known as the corrosion potential E_{corr} or as the OCP[10]. The corresponding current is known as the corrosion current I_{corr}[10]. When normalised to the exposed surface area the corrosion current becomes the corrosion current density i_{corr}[10].

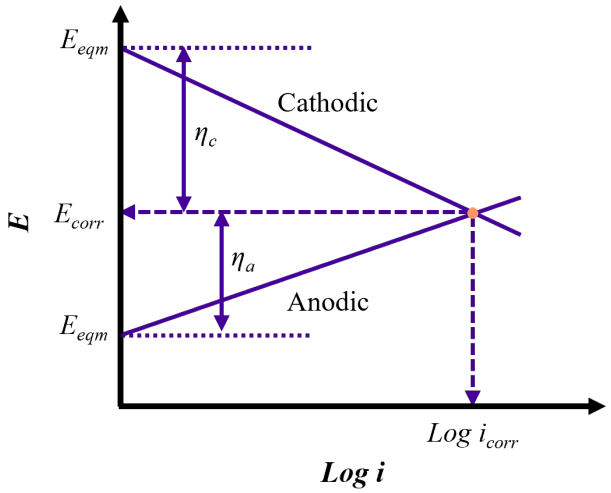

Figure 2.16: Schematic of an Evans diagram. The point at which the anodic and cathodic curves intersect represents equilibrium conditions. Adapted from Corrosion Failures, K. Elayaperumal, K. and Raja, V. S., Thermodynamics and Kinetics of Electrochemical Corrosion, Pages 9 - 28, Copyright (2015), with permission from John Wiley and Sons[123]

Since i_{corr} cannot be directly experimentally determined as it represents the point at which no net current flows, a potential known as the *overvoltage* η is applied to the metal to *polarise* it[10]. The value of overvoltage is given by the difference between E_{corr} and the anodic and cathodic values of E_{eqm}, as shown in Figure 2.16. Corrosion current density, i_{corr}, represents the flow of current during corrosion and is directly proportional to corrosion rates hence higher values are indicative of more metallic dissolution[10].

As seen by Figure 2.16, the larger the value of η the higher i_{corr} will be. The corrosion current density can then be determined using Equation 2.4 and 2.5[123] which calculate the anodic and cathodic overvoltages respectively.

$$n_a = -a + \beta_a log \cdot i \tag{2.4}$$

$$n_c = -a - \beta_c log \cdot i \tag{2.5}$$

Passivation

As shown by Figure 2.16, increasing ηa is expected to increase the anodic current, thereby increasing the dissolution of the metal[123]. In reality, some metals will exhibit an increase followed by a decrease in anodic dissolution due to passivation. When a material passivates, a film forms on the exposed surface which resists further corrosion[7]. The passive film must have good adhesion to the metal surface; if spalling occurs this exposes the underlying metal leaving it prone to further corrosion and material loss[7].

In the following sections, the general corrosion behaviour of stainless steels will be examined. Additionally, the experimental methods by which corrosion performance is tested is discussed.

2.4.2 Corrosion of Stainless Steels

The corrosion resistance of stainless steels is owing to the presence of a dynamic and self-healing Cr-rich oxide film[47]. The film provides a barrier which prevents further oxidation of the stainless steel. The exact nature of the passive film varies depending on environmental conditions (pH, temperature and solution) and in response to the alloy composition[10].

The chemical speciation and therefore the stability of the passive film is determined in part by environmental potential[48]. When operating in a potential range in which passivation is achieved, stainless steel will form an adherent passive film primarily comprised of trivalent chromium species[10]. However, operating outside this potential range renders this form of Cr unstable, meaning the passive film is susceptible to dissolution and cannot provide adequate protection against material degradation[10]. At such potentials other forms of less protective metal oxide species may be present which can be detrimental to corrosion performance as they are not able to adhere to the stainless steel surface and provide the same protection as trivalent Cr[10].

The corrosion behaviour of stainless steel can be characterised by *potentiodynamic polarisation* testing. This test entails applying a potential to the metal which changes

at a constant rate and measuring the current response. An example curve produced from this technique is shown in Figure 2.17[123]. Several useful parameters and trends can be extracted from polarisation data and used to understand a material's corrosion behaviour. These are discussed in the paragraphs below.

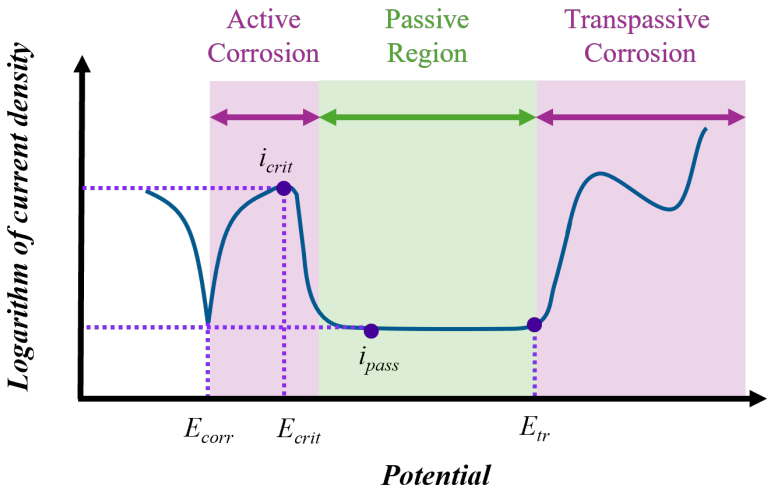

Figure 2.17: Schematic polarisation curve of stainless steel with parameters and features of interest highlighted

The general polarisation behaviour exhibited by stainless steel is described as active-passive. This means that the polarisation curve presents an observable distinction when the material is protected by the passive film in the *passive* region, when the passive films begins to dissolve in the *transpassive* region and when the material is dissolving in the *active* phase[117]. The first parameter of interest which will be discussed here is the critical corrosion current i_{crit}, the value of current at the point of inflexion. The critical current describes the ease with which passivation can be achieved for the material under the particular conditions of the corrosion experiment[10]. The potential corresponding to i_{crit} is known as E_{crit} and it marks the potential below which the sample is active and is subject to dissolution. At potentials above E_{crit} the material begins to passivate and corrosion rates are reduced (Figure 2.17). The potential range over which stainless steel is considered to be passive can typically be identified from the polarisation curve by the region of plateaued and/or relatively low current known as i_{pass}. Increasing the applied potential to higher values causes the passive film to become unstable and no longer capable of protecting the underlying stainless steel. The stainless steel is said to be transpassively corroding and it can be characterised by the rapid increase of the

current. The onset of transpassive corrosion is signified by E_{tr}.

The corrosion resistance of stainless steels is considered excellent and is one of the primary reasons for its widespread use[124]. However, in reducing acid and chloride-containing environments the material is susceptible to corrosion which can render the performance of stainless steels less than satisfactory[10,125]. Since the current study focused on the corrosion of stainless steel in sulphuric acid and sodium chloride solutions, the following sections are focused on the corrosion behaviour, namely general and pitting corrosion, that the alloy exhibits in these environments.

Corrosion in Sulphuric Acid

Before exploring the effect of H_2SO_4 solutions on stainless steels it is imperative to first define the terms *strength* and *concentration* when discussing acids. These two independent characteristics of acids are often confused so here the two terms will be clarified. The strength of an acid is the degree to which the acid will react in a solution with water to dissociate into ions. The electronegativity of the atom to which hydrogen is bonded in the acid will determine how readily the acid molecule dissociates in water[126]. It is owing to the bonding structure of sulphuric acid molecules, whereby H atoms are bonded to O atoms, that it is considered a strong acid (Figure 2.18[126]. Conversely, acid concentration is related to how much acid is present in a solution. The concentration of an acid is typically given in one of the following units: mass percentage %, molarity M or normality N.

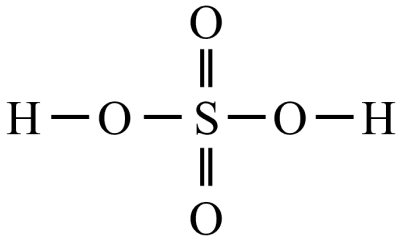

Figure 2.18: Chemical bonding of sulphuric acid molecules. The hydrogen atoms are bonded to O, the second-most electronegative element of the periodic table

An interesting point to note is that the degree of corrosion occurring in stainless steels exposed to H_2SO_4 is not necessarily directly proportional to concentration[127]. This is owing to the concentration of H^+ ions present in H_2SO_4 of different concentrations[128].

Water is required for the sulphuric acid molecules to dissociate into sulphate and hydrogen ions. At acid concentrations greater than 70% (12 M) little water remains in the solution and as a result the sulphuric acid molecules remain undissociated. This gives rise to the decrease in corrosion rates associated with high sulphuric acid concentrations (Figure 2.19).

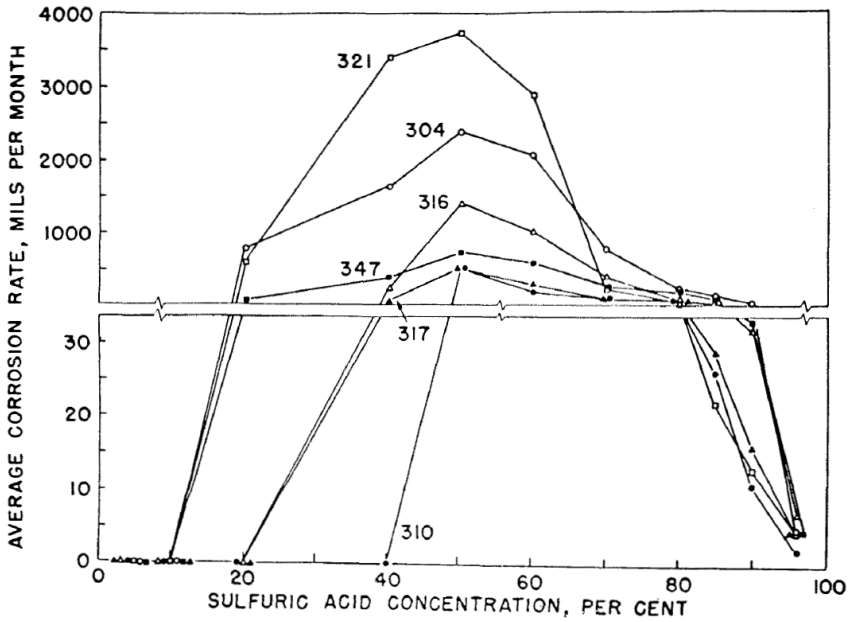

Figure 2.19: Mean corrosion rates of different stainless steel grades in various concentrations of aerated H_2SO_4 at 70°C. Used with permission of AMPP GLOBAL CENTER, INC, from Corrosion of Austenitic Stainless Steels in Sulfuric Acid, Phelps, E. H. and Vreeland, D. C., 1957; permission conveyed through Copyright Clearance Center, Inc[127]

Depending on temperature and concentration, H_2SO_4 can behave as either a reducing or an oxidising acid[128]. If exposed to H_2SO_4 when it is behaving as an oxidising solution, the passive film on stainless steels can form[128]. Contrastingly, when operating as a reducing agent, H_2SO_4 can impair the ability of the Cr-rich passive film to form and self-heal, often leading to reduced corrosion resistance[128]. Equation 2.2 describes the hydrogen evolution reaction which underpins the cathodic activity of reducing acids. Reducing acids typically cause general corrosion in stainless steels. This is because sulphate ions are not expected to initiate pitting and so pitting corrosion is not typically observed[10].

Uniform corrosion, also known as *general corrosion*, is the most common and simplest form of corrosion which results in the even loss of material thickness across the exposed

surface (depicted in Figure 2.20 (a-b))[7]. As the most predictable form of corrosion, the material loss rate can be expressed in millimetres per year[7]. This type of corrosion attack can lead to component failure by the loss of material thickness over time, leading to the part no longer being able to perform as designed[128]. However, catastrophic failure by this corrosion mechanism can be avoided by inspection, monitoring and maintenance.

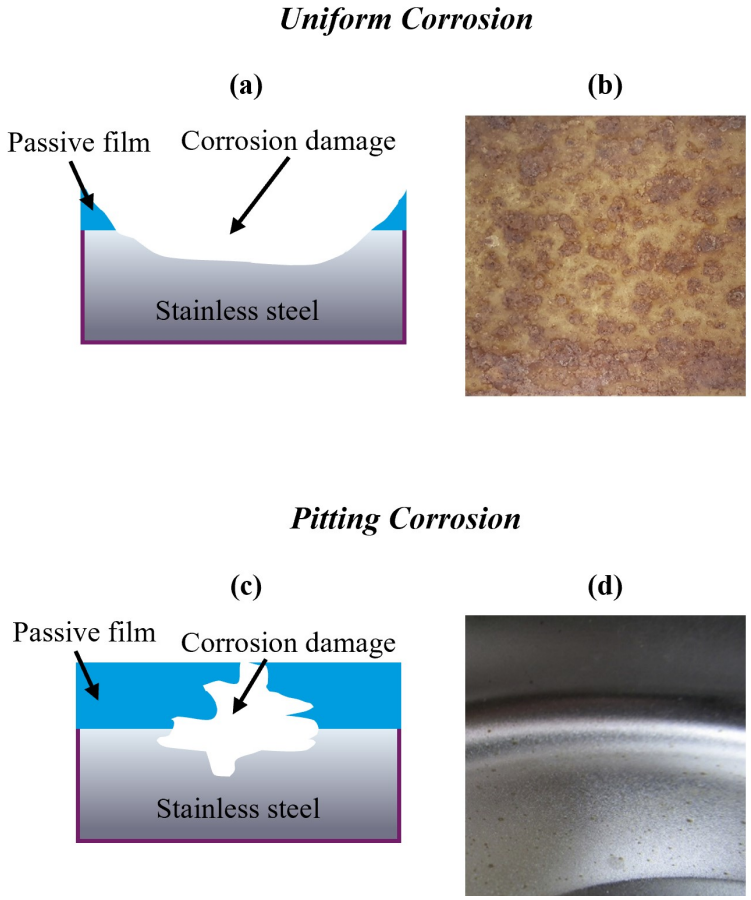

Figure 2.20: Schematic diagrams of (a) general and (c) pitting corrosion. Photographs of (b) general corrosion in ferritic stainless steel test coupon and (d) pitting corrosion in 304L stainless steel. Photographs reprinted from Corrosion Atlas Case Studies (2019 Edition), Corrosion Atlas Series, Pages 97 - 151, Copyright (2020) with permission from Elsevier[129]

Uniform corrosion can be characterised by electrochemical techniques or by weight loss method[117]. The way these techniques work will be discussed in greater detail in Section 2.4.4.

Corrosion in Sodium Chloride Solutions

The ions of the group 17 elements of the periodic table, the halogens, are known as halides. These ions can severely harm the corrosion performance of stainless steels since they can interact with and damage the passive film[47]. The exact mechanism by which halides interact with the passive film is unknown[130]. Though they will not be discussed here several different theories exist which may explain the mechanism of pitting by the action of halides[47]. What is agreed upon is that halide penetration generally occurs at microstructural heterogeneities, such as inclusions, secondary phase precipitates, grain boundaries or breaks in the passive film[47].

As a member of the halide family of chemical species, chlorides can be devastating to stainless steel leading to corrosion in the form of pitting. In contrast to general corrosion, pitting corrosion is characterised by highly localised metal loss (Figure 2.20 (c-d))[7]. Pitting corrosion is facilitated by the initiation of microscopic holes, which occur where the passive film breaks down and metal dissolution proceeds[7,47]. Due to its highly localised nature and small scale, little evidence of pitting corrosion may be observed during routine inspections (Figure 2.21). To make the identification of pitting corrosion even more difficult, corrosion products may accumulate in the pit opening obscuring the pit from the observer[7].

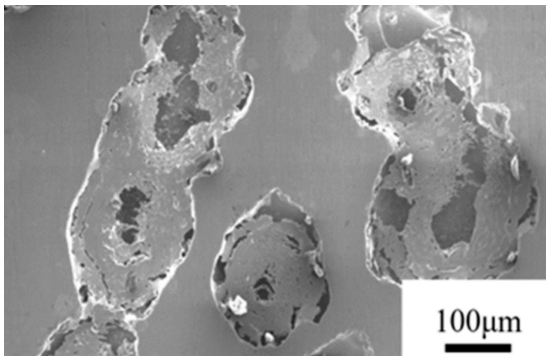

Figure 2.21: Surface morphology of 316L stainless steel following potentiodynamic polarisation in 3.5% NaCl solution. Reproduced from Liao et al.[131]

Chloride solution pitting is an *autocatalytic* process; this means that once a pit is initiated the conditions within the pit facilitate the self-propagation of further pit growth[7,125]. The process of pitting corrosion is illustrated in Figure 2.22.

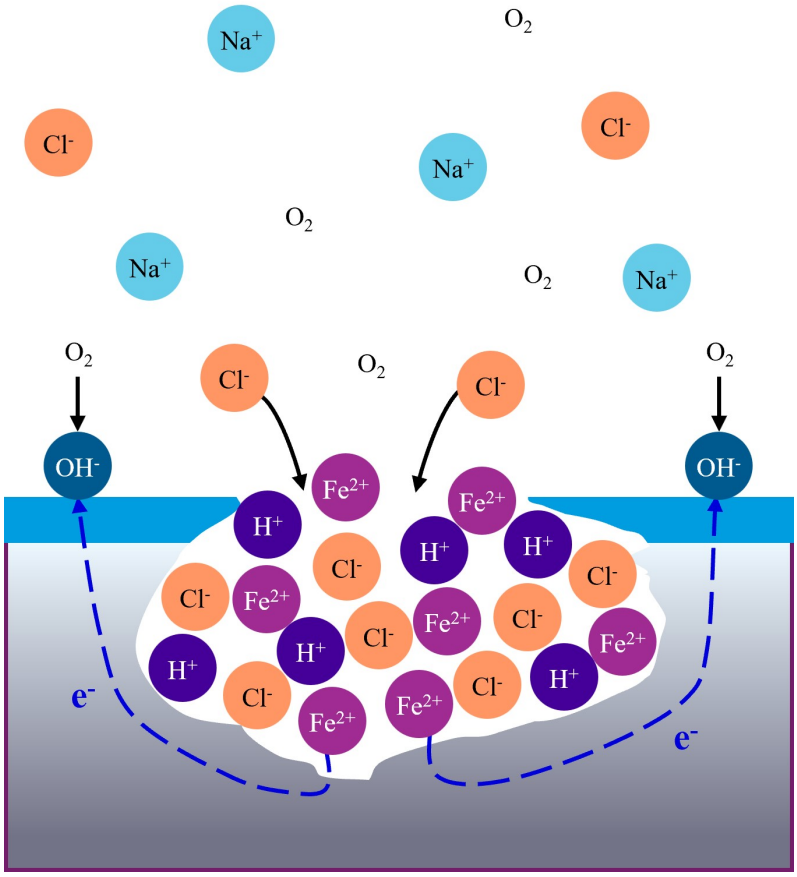

Figure 2.22: Schematic diagram of pitting corrosion of stainless steel in an aerated NaCl solution. Dissolution of the metal occurs within the pit while the reduction of O proceeds on the outer metal surface. Adapted with permission of ASM International, from Pitting Corrosion in Corrosion: Fundamentals, Testing, and Protection, Frankel, G. S., 2003; permission conveyed through Copyright Clearance Center, Inc.[125]

The reduction of oxygen and the dissolution of metal ions are the two reactions which underpin stainless steel corrosion in sodium chloride (described by Equation 2.6 and Equation 2.1, respectively)[25].

$$O_2 + 2H_2O + 4e^- \rightarrow 4OH^- \tag{2.6}$$

Metal ions produced by Equation 2.1 cause an electrical imbalance between the pit and the outer metal surface[10]. As a result, chloride ions migrate into the pit where they react with metal ions to form metal chlorides[47]. These metal chlorides are then hydrolysed by water to form metal hydroxides and free acid which increase acidity at the site; increased metal dissolution rates result (Equation 2.7)[47,130]. There then exists a differential in pH between the solution in the pit and the bulk solution, which will remain neutral[130].

$$FeCl_2 + 2H_2O \rightarrow Fe(OH)_2 + 2HCl \tag{2.7}$$

When water and oxygen are available, the ferrous hydroxide can then oxidise (Equation 2.8).

$$4Fe(OH)_2 + 2H_2O + O_2 \rightarrow 4Fe(OH)_3 \tag{2.8}$$

Pitting corrosion can be devastating for part performance since a single pit can propagate to the degree that it perforates the entire thickness of the material leading to the inability of the part to perform as desired with little overall material loss[7]. The possibility of pitting in stainless steels can be mitigated in several ways: by ensuring the part does not come into contact with halides, altering alloy content, adjusting environment temperature or by using cathodic or anodic protection[117].

2.4.3 Powder Processed Stainless Steels

Powder processed steels often exhibit worse corrosion resistance than their cast and wrought counterparts[2]. This is owing in part to chemical changes brought about by the atomisation process which can alter the stability of the chromium oxide film and the formation of inclusions[2]. Other factors reported to affect the corrosion resistance of

powder processed stainless steel include the degree and nature of porosity[2]. With careful consideration of the selected atomisation process, sintering method and post-processing a sintered stainless steel part can be produced which has adequate corrosion performance.

Before analysing the studies on powder processed stainless steels, a summary of the general effect of porosity and inclusions on corrosion resistance of these alloys is presented.

Porosity in Stainless Steels

A feature of sintered stainless steels which can affect their corrosion resistance is porosity. The corrosion performance of stainless steel is strongly influenced by part density, a feature which is intrinsically linked to porosity. Pores can be detrimental to corrosion behaviour because they can provide a site for pitting and crevice corrosion to proceed. Crevice corrosion can occur in a blind pore, illustrated in Figure 2.23. The solution within the pore can become stagnant and the reactions which proceed can result in damage to the passive film and dissolution of the metal[2,132]. Within pores a lack of passivation can also occur, leaving areas of the material susceptible to corrosive attack which can lead to pitting corrosion[25,133].

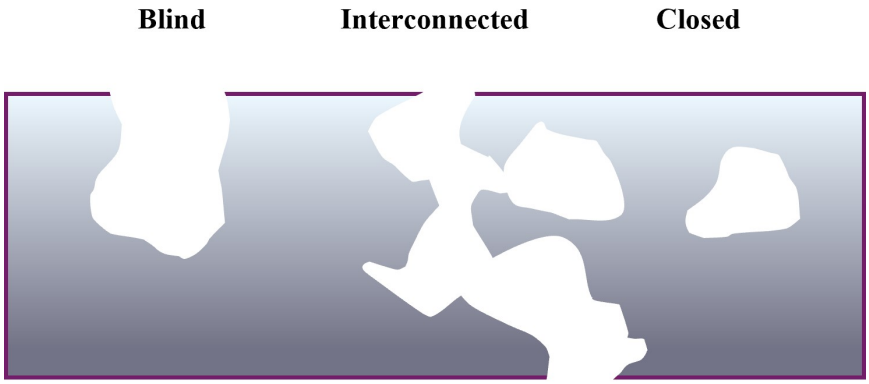

Figure 2.23: Schematic diagram of three primary types of pore morphology: (a) blind, (b) interconnected and (c) closed. Both blind and interconnected pore types are considered forms of *open* porosity

Pore type, shape and size can affect the corrosion mechanisms which proceed in stainless steels. Pore type is linked to the optimisation of sintering parameters as well as the feedstock powder size[134]. As Verlee et al.[97] explains, achieving densities above 90% means that most pores found within the sample will be of the blind type. Pore shape

is linked to the morphology of the feedstock material which itself is dictated by the atomisation technique used. Pores tend to spherodise as sintering proceeds, however, due to their spheroidal geometry, sintering gas atomised powders can result in the formation of spheroidal pores earlier in the sintering process then sintering WA powders[70]. In terms of the effect of pore shape on corrosion resistance, Samal[2] explains that interconnected pores are not likely to contribute to crevice corrosion but long and narrow blind pores are more prone to this corrosion phenomenon[2].

Pore size can also impact the corrosion mechanism that proceeds. Raghu et al.[135] found that general and localised corrosion proceeded in pores between 10 to 20 µm in diameter while in larger pores the attack was primarily localised. Additionally, it was reported that repassivation of fine pores was more difficult to achieve since the sample with the fine pores had a greater number of pores which therefore accounted for a greater number of discontinuities in the passive film[135]. The propensity for micron-scale crevice corrosion is linked to pore size. While larger pores (those > 10 µm) are more likely to cause to crevice corrosion, smaller pores also risk crevice corrosion[136,137]. Furthermore, Otero et al.[132] explains that the width of a pore opening can influence corrosion performance. Otero et al.[132] link a smaller volume pore with severe crevice corrosion, since the volume of electrolyte which fills the smaller pore is lower, the pore can more quickly become deoxygenated and acidified to crevice corrosion levels leading to the dissolution of the passive film and the attack of the stainless steel. Meanwhile, Lou et al.[62] states that finer pores are associated with accelerated general corrosion. However, what constitutes a fine pore and what constitutes a large pore isn't agreed upon. Additional challenges arise in the research of pores since pore size can be difficult to accurately determine due to its three-dimensional nature.

Inclusions in Stainless Steels

Inclusions are another characteristic of sintered stainless steels which can effect corrosion performance. An inclusion is defined as a non-metallic particle which typically features elements such as C, N, S and O[138]. Silicon dioxide is an example of an inclusion particle which forms during the process of water atomisation[139]. Inclusions such as this can act as pit initiation sites and negatively affect corrosion performance[47,74]. It is therefore desirable to eliminate or minimise inclusions during the processing of sintered stainless steel.

SiO_2 can be removed by the process of reduction during sintering if the sintering conditions are suitable. The ease with which oxides can be reduced can be understood by the Ellingham diagram presented in Figure 2.24. Oxides which are unstable and are easily reduced are represented by lines found near the top of the diagram, while the reverse is true for harder to reduce oxides. Since the line representing the formation of SiO_2 is lower relative to other oxides it can be inferred that it is a relatively hard to reduce oxide.

Sintering can be carried out under near-vacuum conditions or in an atmosphere such as dissociated ammonia. Although sintering in dissociated ammonia can reduce SiO_2 [73], this process gas can have an unwanted nitriding effect on stainless steels [2]. Sintering in dissociated ammonia can facilitate the formation of chromium nitride near the surface of the part which can render the material more susceptible to corrosion [2]. Vacuum sintering is primarily used in sintering stainless steels as it avoids unwanted reactions occurring between the powder and the atoms in the sintering atmosphere [140]. Additionally, sintering in a vacuum rather than in a process gas enables greater control of inputs such as temperature and heating and cooling rates [103]. When it comes to corrosion performance, parameter control is of great importance since it has a profound impact on the microstructure and physical properties which are intrinsically linked to corrosion resistance.

Having explored the effect of porosity and inclusions on corrosion performance, an assessment of the literature pertaining to the corrosion resistance of PM stainless steels will now be presented. The study most similar to this EngD was carried out by Peled and Itzhak [18] who investigated corrosion performance of sintered Pd-doped 316 SS. However, this study did not include potentiodynamic polarisation graphs nor mention corrosion parameters, results which are necessary for the reader to interpret the corrosion behaviour of the studied samples. As a result, to the best of the author's knowledge no literature is available to directly compare to the observations in this study to. Instead, parallels will be drawn between the samples in this study and PM and conventionally processed stainless steels in the literature. This literature review focused on the behaviour of these materials when exposed to acidic and chloride containing environments.

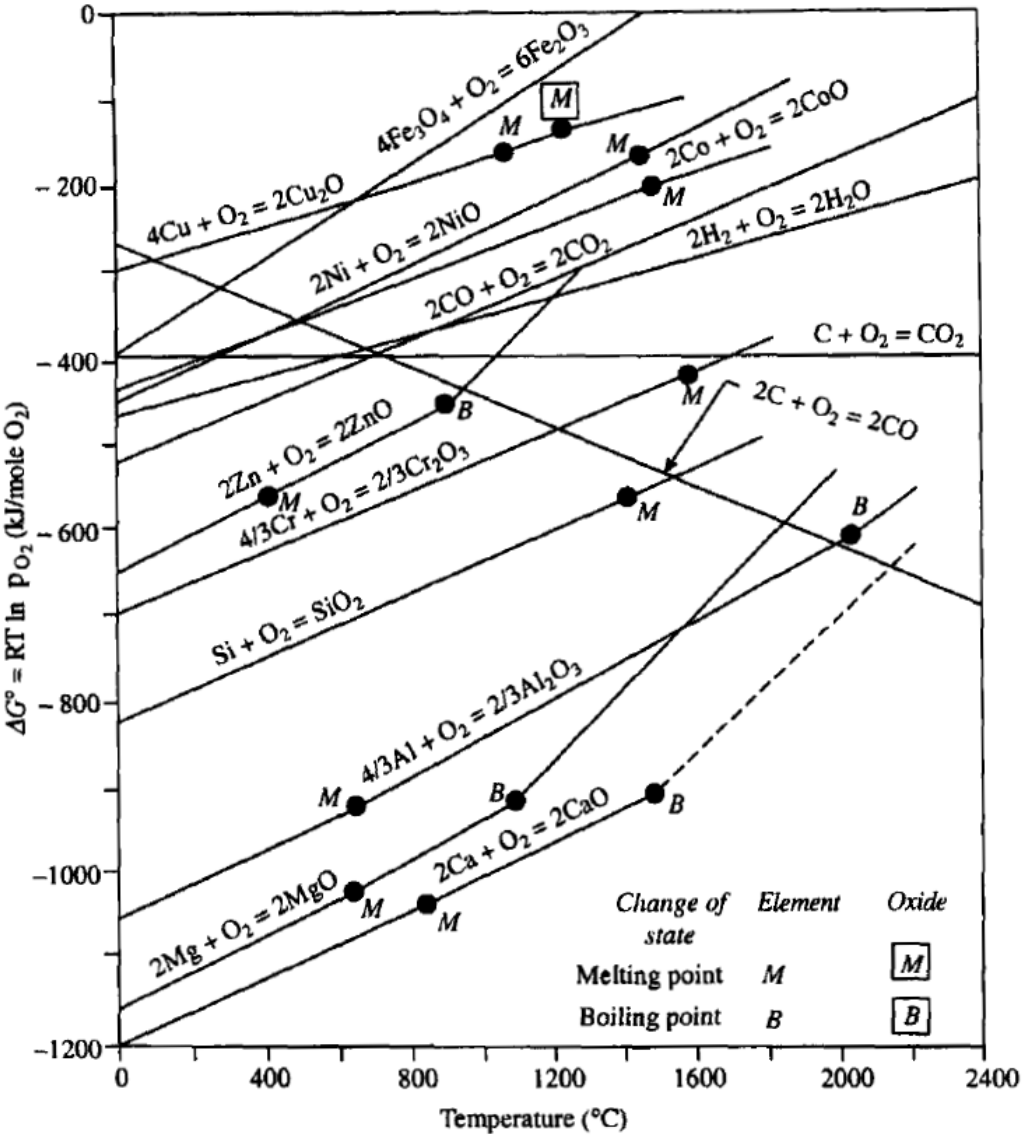

Figure 2.24: Ellingham diagram showing the standard free energy of formation of selected oxides at varying temperatures. The stability of oxides can be determined from the relative height of their lines, with more stable oxides being found at the bottom of the diagram. Reprinted from Corrosion of Austenitic Stainless Steels, Pillai, S. R., Chapter 11 - High Temperature Corrosion of Austenitic Stainless Steels, Page 1 - 36, Copyright (2002), with permission from Elsevier[141]

Effect of Processing Technique

In 1988, Raghu et al.[142] compared the corrosion behaviour of sintered and wrought 316L stainless steel in 0.5 - 5 M H_2SO_4 and observed significant differences. The sintered sample resisted corrosion poorly and exhibited i_{crit} and i_{pass} values three to four orders of magnitude higher than wrought. This behaviour was attributed to the entrapment of electrolyte and the subsequent formation of a hydrogen ion concentration cell in the pores which drove the corrosion mechanism. Discontinuities in the passive film were also thought to contribute to the inferior properties of the sintered stainless steel. It is worth noting here that the samples studied by Raghu et al.[142] were considerably porous (29 - 63% porosity) owing to the relatively low compaction pressures used. Raghu et al.[142] highlights that while it is reasonable to assume that reducing the porosity will improve corrosion performance, it is important to also consider the impact of transitioning from a network of interconnected to isolated pores. This transition is reported to occur at relative densities above 90% and may contribute to the formation of crevice corrosion susceptible morphologies[97].

A subsequent study by Otero et al.[132] compared the corrosion performance of sintered and cast 316L stainless steel in H_2SO_4 solutions. Similar to the earlier study by Raghu et al.[142], here it was also observed that the PM samples possessed worse corrosion resistance and higher corrosion rates than the cast samples. This was despite the samples produced by Otero et al.[132] possessing 87.9% relative density which higher than samples used by Raghu et al.[142]. The work of Raghu et al.[142] and Otero et al.[132] suggest that lower porosity levels are needed for PM 316L stainless steels to possess corrosion resistance similar to their cast equivalents. They present the theory that corrosion attack in sintered steels is initiated in pores as illustrated in Figure 2.25.

An investigation by Geenen et al.[143] presented evidence which supports the corrosion mechanism theory of Raghu et al.[142] and Otero et al.[132]. Geenen et al.[143] compared cast and fully-dense, HIP-processed 316L stainless steel in 0.5 M H_2SO_4 and found that both samples possessed similar corrosion performance. This observation was attributed to the lack of pores in the powder processed sample. This evidence paired with the findings of Raghu et al.[142] and Otero et al.[132] suggest that pores have considerable influence over the corrosion behaviour of sintered stainless steels in H_2SO_4.

Comparative studies have assessed the corrosion resistance of conventionally and powder processed stainless steels in NaCl solutions. For example, Raghu et al.[135] compared the corrosion resistance of porous sintered and wrought 316L stainless steel in 3% NaCl solution. Their investigation revealed that the passivation range was broader for the wrought sample compared to the sintered samples. Additionally, the wrought sample rapidly stabilised upon immersion within the electrolyte. In contrast, the sintered samples did not stabilise within the solution and instead exhibited a progressively decreasing OCP with time. This behaviour is indicative of passive film dissolution leading to increased exposure of the base metal to the electrolyte.

Irrinki et al.[144] carried out a similar study on wrought and laser powder bed fusion (LPBF) 17-4PH samples in a 0.5 M NaCl solution. Their study reported that GA LPBF samples with relative densities above 97% outperformed the wrought samples, a result which contrasts with the findings of Raghu et al.[135]. However, the study by Irrinki et al.[144] did not provide an explanation for the observed corrosion trends. The corrosion behaviour of the LPBF and wrought samples studied by Irrinki et al.[144] may stem from microstructural and chemical differences that evolve from the LPBF process which are known to affect corrosion resistance.

A study by Marnier et al.[99] compared the corrosion resistance of FAST-processed ultrafine 316L powder (mean particle size 2.3 µm) and cast 316L. The FAST samples were sintered under a range of different sintering temperature, time and pressures resulting in samples of relative densities ranging from 97.5 - 99.5%. Though the samples of both types passivated within the 3 wt.% NaCl test solution it was found that the lower density samples had slightly lower OCP compared with cast materials. Meanwhile the high density (99.6%) FAST-processed sample exhibited a wider passivation range and a lower passivation current than the cast sample. Owing to the ultrafine feedstock powder and the careful optimisation of the FAST process, fine grains (< 5 µm) were obtained in this study. Marnier et al.[99] suggested that its superior corrosion behaviour compared with the cast sample was because of the fine grain size obtained in the high density sintered sample. This conclusion was also drawn by Fredriksson et al.[145] who found that a finer grained HIP 316L sample possessed better pitting resistance than a more coarse grained cast sample. Both these studies show strong agreement with the findings of Ralston et al.[146] who linked finer grains to better corrosion resistance in passivating materials.

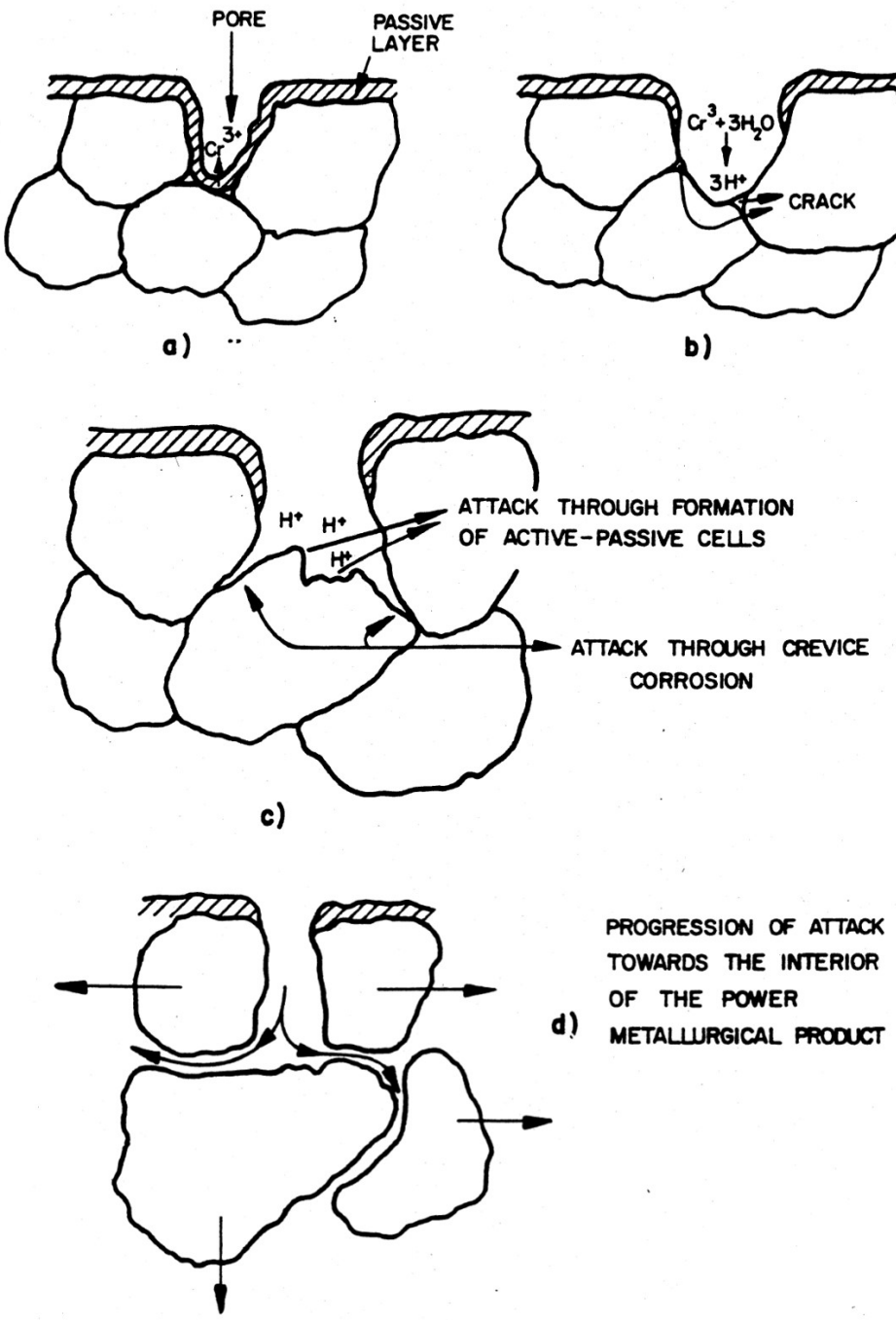

Figure 2.25: Diagram illustrating the proposed mechanism of powder processed stainless steel corrosion as conceived by Raghu et al.[142] and Otero et al.[132]. Used with permission of Elsevier Science & Technology Journals, from Corrosion Behaviour of AISI 304L and 316L Stainless Steels Prepared by Powder Metallurgy in the Presence of Sulphuric and Phosphoric Acid, Otero et al., 40, 8, 1998; permission conveyed through Copyright Clearance Center, Inc

Tobar et al.[63] compared laser deposited 316L with a wrought equivalent in a NaCl solution. The PM sample exhibited superior corrosion resistance and possessed a wider passive range than the wrought sample. Unlike in the studies by Marnier et al.[99] and Fredriksson et al.[145], which attributed similar observations to microstructural differences, Tobar et al.[63] identified discrepancies in Mn content of the wrought sample and the powder feedstock as responsible. The wrought sample possessed more Mn than the powder feedstock, leading to the formation of MnS inclusions. Tobar et al.[63] argued that this chemical discrepancy led to the formation of MnS inclusions which are known to be detrimental to the pitting resistance of stainless steels, providing a plausible explanation of the observed corrosion behaviour.

Kale et al.[124] compared the corrosion performance of FAST-processed and as-rolled 316L stainless steel in 3 wt.% NaCl. The FAST sample exhibited poor passivation behaviour compared with the as-rolled specimen. Consistent with findings reported by Raghu et al.[135],[142] and Otero et al.[132], the poor corrosion behaviour of the PM sample was attributed to the presence of porosity. Kale et al.[124] performed an analysis of the cross-section of the corroded samples to investigate the shape of the pores following corrosion attack (shown in Figure 2.26). They achieved this by filling the surface with epoxy resin to prevent mechanical damage to the surface and then sectioning the sample. The findings of Kale et al.[124] show good agreement with the corrosion mechanism theory presented by Otero et al.[132] in Figure 2.25.

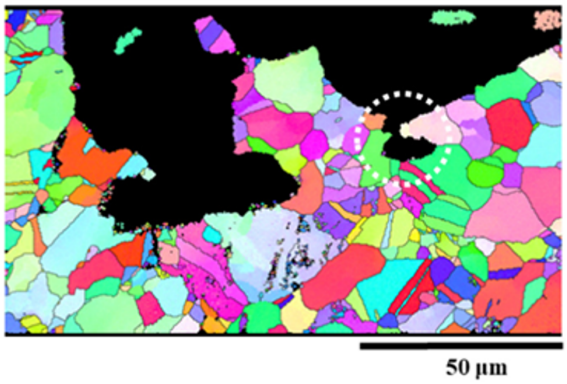

Figure 2.26: Inverse pole figure (IPF) maps of the cross-section of FAST 316L stainless steels which have been exposed to 3 wt.% NaCl. The dark regions of the map illustrate the corrosion which occurred in the pores due to exposure to NaCl. Reprinted from An Investigation of the Corrosion Behavior of 316L Stainless Steel Fabricated by SLM and SPS Techniques, Materials Characterization, 163, Kale, A. B.; Kim, B.; Kim, D.; Castle, E. G.; Reece, M.; Choi, S., Copyright (2020), with permission from Elsevier[124]

Saito et al.[147] also used FAST to produce 316L samples which were compared in terms of corrosion resistance to a wrought specimen in a 0.1 M NaCl solution. The sintered sample did not passivate in the solution and many pits were generated. The initiation of pitting was attributed to the presence of both MnS inclusions and porosity. This is because it was observed that reducing pore size and porosity improved corrosion resistance. To investigate the effect of MnS on the pitting resistance, the sintered samples were subjected to pulse electrolysis in 0.1 M $NaNO_3$ to dissolve the MnS inclusions. As a result, the pitting resistance was noted to significantly improve, showing good agreement with the studies of Tobar et al.[63] and Baker and Castle[58].

Summarised in Table 2.2 are the primary findings in the literature assessing the impact of metallurgical processing technique on the corrosion resistance of stainless steel in H_2SO_4 and chloride solutions. Overall the findings on the corrosion resistance of PM and conventionally processed stainless steels are mixed. This is owing to the range of different factors which can affect the corrosion performance of stainless steels. Among the factors affecting corrosion behaviour are:

- Porosity
- Grain size
- Inclusions

Since it has previously been established that the atomisation technique has a profound effect on the resulting metal powder, the following section explores the relationship between the selected atomisation fluid and the corrosion performance of the specimens produced. This section focuses specifically on comparing WA and GA powders since they are of greatest relevance to this EngD study.

Table 2.2: Summary of the literature comparing the corrosion performance of stainless steel samples made by conventional and powder metallurgical processing

Source	Material	Processing Techniques	Test Solution	Summary of Findings
Raghu et al. [142]	316L	Press and sinter, wrought	0.5 - 5 M H_2SO_4	Wrought samples outperform sintered samples. Attributed to porosity
Otero et al. [132]	316L	Press and sinter, cast	1 - 25% H_2SO_4	Cast samples outperform sintered samples. Attributed to porosity
Fredriksson et al. [145]	316L	HIP, cast	0.5 M H_2SO_4, 0.5 M HCl	HIP sample had better pitting resistance in HCl than cast. Attributed to finer grain size in former sample
Geenen et al. [143]	316L	HIP, cast	0.5 M H_2SO_4	Similar corrosion performance, attributed to lack of pores in HIP sample
Raghu et al. [135]	316L	Press and sinter, wrought	3 wt.% NaCl	Wrought outperformed sintered. No reason given
Marnier et al. [99]	316L	FAST, cast	3 wt.% NaCl	Sintered sample outperformed cast, attributed to fine grain size of the latter
Tobar et al. [63]	316L	Laser powder deposition, wrought	3.5% NaCl	PM sample outperformed the wrought. Attributed to MnS inclusions in wrought sample
Irrinki et al. [144]	17-4PH	LPBF, wrought	0.5 M NaCl	LPBF outperformed wrought, reason not given
Kale et al. [124]	316L	FAST, as-rolled	3 wt.% NaCl	FAST sample exhibited poor passivation behaviour. Attributed to surface porosity
Saito et al. [147]	316L	FAST, wrought	0.1 M NaCl	Pitting resistance worse in FAST sample. Attributed to porosity and MnS inclusions

Effect of Atomisation Fluid

Similar to the studies comparing PM and conventionally processed stainless steels, porosity is often a factor attributed to the behaviour of compacts produced from WA and GA powders. For example, Malhotra et al.[148] studied the corrosion behaviour of pressed and sintered GA and WA 316L samples in 3% NaCl and found that the GA sample outperformed the WA sample. Though no reasons for this behaviour were given by the author, it was found that the GA possessed lower porosity and a smaller mean pore size than the WA equivalent. This presents a potential reason for the observed behaviour.

Porosity was also found to influence corrosion behaviour by Bonato et al.[149]. In their study they compared the corrosion performance of powder injection moulding (PIM) WA and GA 316L in 3.5% NaCl. Higher pit density and corrosion rates were observed in the GA samples. This finding was attributed to the higher porosity observed in the GA samples which enabled electrolyte to penetrate the sample. The findings of Bonato et al.[149] and Malhotra et al.[148] suggest regardless of whether the powder used was produced by WA or GA the reduction of porosity is of great importance.

Further evidence was presented by Irrinki et al.[144] to support the idea that porosity is an influential factor in determining the corrosion resistance of sintered WA and GA stainless steel. Irrinki et al.[144] studied the corrosion resistance of samples produced by LPBF using GA and WA 17-4PH powders in a 0.5 M NaCl solution. They found sample density was the main factor influencing corrosion performance and samples of similar density had similar corrosion performance regardless of whether they were produced from WA or GA powders. This suggests that porosity played a critical role in the observed corrosion performance. They also proposed that at relative densities above 97% the availability of pores for pitting corrosion sites are reduced and so corrosion rates are lower.

Other researchers have concluded that the corrosion behaviour of sintered WA and GA differs because of powder chemistry discrepancies. Lou et al.[62] compared PIM specimens produced from WA and GA 316L powders. This investigation found that the corrosion rates were two times higher in the GA sample compared with the WA sample. According to Lou et al.[62] this observation can be accounted for by the presence of SiO_2 inclusions which they explain provide passivation in a similar way that Cr oxide does, an explanation which contradicts other research. Elsewhere it is reported that SiO_2

inclusions have a generally negative effect on corrosion performance[74,103]. In the study by Lou et al.[62], both samples had similar densities but their grain sizes were vastly different, with the mean grain size of the GA sample being 302 µm while the WA sample is 106 µm. In this study, the samples produced from GA powder also possessed higher Mn content than those produced from WA, a trend also observed by Tobar et al.[63] and Hedberg et al.[150]. As previously mentioned, other research has linked higher Mn content of SS to the formation of MnS inclusions leading to worsened pitting corrosion[63]. Since larger grain sizes can impact corrosion performance in a negative way[99,145,146], this factor alongside the higher Mn content may have contributed to the corrosion performance trends observed by Lou et al.[62].

Jandaghi et al.[61] used LPBF to produce samples made from WA and GA 316L powders. In corrosion testing in a 3.5% NaCl solution, the sample made from WA powder possessed better resistance to corrosion than specimens made from GA powders, though neither sample passivated. In this study, it was found that the WA specimens contained more Si-, Cr- and Mn-rich oxide inclusions. Like Lou et al.[62], Jandaghi et al.[61] also argued that the improved corrosion behaviour of the WA was due to the presence of inclusions. In their discussion, Jandaghi et al.[61] explained further that the inclusions helped to form a denser and more uniform passive layer by promoting the accumulation of dislocations in the adjacent metal matrix[61]. However, this conclusion lacked support, for example in the form of X-ray photoelectron spectroscopy (XPS) experimental data to verify passive layer thickness. As a result, further study may be required to further explore this idea in the context of PM stainless steels. Though other studies have found that inclusions can act as preferential nucleation sites facilitating pitting corrosion[58,63,147,151], Jandaghi et al.[61] argue that the observed inclusions and their associated dislocations lead to a more stable passive film which helps to prevent the formation and propagation of pits. Dislocations are also typically associated with higher corrosion rates. This is because electrons are more active in the vicinity of dislocations and as a result the energy barrier for corrosion to occur is lower[152]. Another explanation offered by Jandaghi et al.[61] for the improved corrosion resistance of the WA samples compared to the GA samples is differences in grain boundary density. Specifically, Jandaghi et al.[61] conclude that the lower grain boundary density of the WA sample contributed to its higher corrosion resistance. This is in agreement with the findings of Ralston et al.[146] who found that when a sample is not protected by a passive film, as the samples studied by Jandaghi et al.[61] were found to be, then decreased grain boundary densities were associated with

lower corrosion rates.

Tobar et al.[63] compared the corrosion resistance of laser deposited 316L WA and GA powders. They found that the samples passivated in 3.5 wt.% NaCl solution unlike Jandaghi et al.[61]. Additionally, they found that the WA derived samples outperformed the GA sample. This finding was attributed to chemical differences in the feedstock powders, namely Mn, which was higher in concentration in the GA powder compared with the WA powder. Mn is an element which, as previously explained, can form MnS inclusions that are highly detrimental to pitting resistance.

To the best of the author's knowledge, the comparative corrosion assessments of GA and WA powders were conducted exclusively in HCl and NaCl solutions, so it is not clear how compacts made from powders produced by these two atomisation techniques compare in sulphide containing environments, such as H_2SO_4.

Table 2.3 summarises the findings of the literature which compares the corrosion performance of samples made from WA and GA stainless steel powders. As found in the literature comparing cast and PM stainless steels, the literature which compares samples made from WA and GA also attributed corrosion trends to porosity and inclusions, with higher porosity being associated with worse corrosion performance. The reported effect of inclusions on corrosion performance of stainless steels is mixed. Overall, it appears that multiple different factors contribute to the corrosion resistance of GA and WA stainless steels making it difficult to determine the extent to which atomisation fluid influences electrochemical performance.

Table 2.3: Summary of the literature which compares the corrosion performance of samples made from WA and GA stainless steel powders

Source	Material	Powder Processing Technique	Test Solution	Summary of Findings
Malhotra et al.[148]	316L	Press and sinter	3% NaCl	GA sample showed a lesser tendency for localised corrosion. No reasons for this behaviour given but GA possessed lower porosity and a smaller mean pore size than the WA sample
Bonato et al.[149]	316L	PIM	3.5% NaCl	Higher corrosion rates in GA sample. Attributed to its higher porosity
Irrinki et al.[144]	17-4PH	LPBF	0.5 M NaCl	Samples of similar density had similar corrosion performance regardless of whether WA or GA
Lou et al.[62]	316L	PIM	5% HCl	Higher corrosion rates in GA sample. Attributed to the presence of SiO_2 in WA sample having a passivating effect
Tobar et al.[63]	316L	Laser powder deposition	3.5% NaCl	Higher corrosion rates in GA sample. Attributed to its higher Mn content
Jandaghi et al.[61]	316L	LPBF	3.5% NaCl	Higher corrosion rates in GA sample. Attributed to inclusions helping to form denser/more uniform passive layer

The following section focuses on the reported effect of heat treatment on the corrosion resistance of powder processed PH stainless steels since 17-4PH forms a part of this EngD study.

Effect of Heat Treatment

Precipitation hardening stainless steels, such as 17-4PH, develop mechanical property-enhancing precipitates by a two-step heat treatment[45]. Typically, the effect of this process on the corrosion resistance on powder processed steels has been reported to be positive. This is attributed to the homogenising effect of thermal processing on elemental distribution, a finding that Leo et al.[153] linked to the even development of the passive film in the selective laser melted (SLM) processed 17-4PH samples they studied. This finding was also confirmed by Wang et al.[154] in their study of the effect of heat treatment on 15-5PH also produced by SLM. However, it should be noted that excessive precipitation hardening treatment times were found to render the material less resistant to pit initiation - an observation Wang et al.[154] attributed in part to the coarsening of CRPs. If ageing is carried out for longer times and higher temperatures, the CRPs become more Cu-rich and expel elements such as Ni leaving the area depleted of Ni[155]. As a passive film stabilising element, the increased time and temperature of ageing can lead to the reduction in corrosion resistance[2,47].

2.4.4 Corrosion Measurement Techniques

The corrosion resistance of materials can be assessed in two major ways: electrochemical and non-electrochemical techniques.

Non-Electrochemical Techniques

Weight loss and salt spray are two examples of non-electrochemical methods for the characterisation of corrosion behaviour. Non-electrochemical techniques are the simplest and most common approach to corrosion performance analysis[156]. However, inaccuracies in corrosion rate estimates can result from the weight loss technique since all mass loss is attributed to general corrosion[7]. Additionally, non-electrochemical techniques may require long exposure times whereas electrochemical methods require relatively shorter times[157].

Electrochemical Techniques

OCP, potentiodynamic polarisation and electroimpedence spectroscopy are three examples of electrochemical corrosion characterisation techniques. These measurements typically involve the application of a potential to the specimen using a potentiostat to polarise the material from the corrosion potential, E_{corr}, to accelerate the corrosion process[10,158].

A potential limitation of electrochemical corrosion analysis is the resistance of the electrochemical solution itself. When employing electrochemical techniques, the resistance comprises both the polarisation resistance of the sample, R_p, and the resistance of the solution, R_s. Consequently, relying solely on the current as an indication of corrosion behaviour introduces inaccuracies. To reduce the error associated with solution resistance, the distance between the reference electrode and the working electrode (i.e. the specimen) must be minimised. This can be accomplished by incorporating glassware such as a capillary tube into the electrochemical cell.

Additional inaccuracies can be introduced by localised corrosion mechanisms such as pitting. Pitting chemically changes the solution in the region surrounding a pit[130]. Furthermore, it can change the geometry and surface area of the specimen which can affect accuracy of the data[158]. As potentiodynamic polarisation measures a material's general corrosion response, the effect of pitting cannot be accurately quantified. However pitting behaviour can be described by parameters measurable by electrochemical characterisation techniques. Pitting potential is a measure of the potential beyond which pitting will propagate[117]. The more positive the pitting potential E_p, the lower the likelihood of pit initiation[130]. Higher repassivation potentials E_{pass} signifies a lower likelihood of pit propagation[130]. Owing to the small amount of material loss which occurs during pitting corrosion, weight loss techniques are not useful in the characterisation of pitting behaviour.

Further limitations are associated with the electrochemical testing of PM parts. The first relates to the pores which are a typical feature of powder processed steels. Pores effectively increase the surface area of the material which is exposed to the corrosive medium[25]. However, owing to the difficulty associated with calculating the surface area of these pores, it means that measurements of exposed surfaces of PM parts will be an underestimation of the actual surface area. This becomes an issue in electrochemical testing since currents have to be normalised to the surface area of exposed material and

inaccuracies will ensue where PM materials are concerned[2]. Assumptions are therefore typically made when normalising the current of sintered materials since the impact of pores on surface area is ignored.

Another source of inaccuracy is that in potentiodynamic polarisation measurements it is assumed that only general corrosion is occurring. However, when testing PM materials crevice and pitting corrosion may also proceed leading to inaccuracies in the interpretation of the polarisation curves[2]. As a result of the aforementioned limitations of non-electrochemical and electrochemical characterisation, both techniques have been used to evaluate the corrosion behaviour of the materials in this study. An overview of the two electrochemical testing techniques used in this study, OCP and potentiodynamic polarisation, are discussed in the following pages. Greater explanation as to how these tests are carried out are presented in Section 3.7.

Open Circuit Potential

OCP measurements are carried out before potentiodynamic polarisation tests for two primary reasons: to permit specimen stability in the test solution and to characterise corrosion behaviour. The former is necessary for accurate data collection in the proceeding tests while the latter reveals the thermodynamic stability of the sample under the specified test conditions. This information can be gauged from the shape of the curve produced and by the potential at which the sample stabilises (Figure 2.27 (a)). A smooth curve which asymptotically approaches a certain potential value, like that illustrated in Figure 2.27 (a), suggests that the sample is stable in the test solution. Meanwhile, an irregular curve without asymptotic behaviour suggests that the sample is unstable in the test solution. A sample which exhibits gradually decreasing potential in the OCP test can be interpreted to be increasingly active[25]. The OCP test is carried out by measuring the sample potential over a predetermined amount of time or until stability of the corrosion potential E_{corr} is achieved.

Potentiodynamic Polarisation

Following the OCP test, potentiodynamic polarisation may be carried out. It is carried out by applying a potential to the sample which varies at a constant rate and measuring the current response. Several useful qualitative parameters can be extracted from the data produced by potentiodynamic polarisation tests. Two such parameters are the critical corrosion current density i_{crit} and the passivation current density i_{pass}. The

former provides information about the ease with which passivation can be achieved while the latter gives an indication of the corrosion rates exhibited by the specimen (Figure 2.27 (b)).

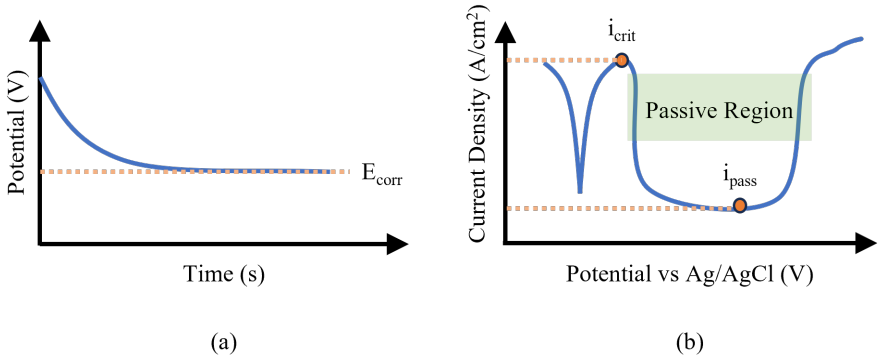

Figure 2.27: Schematic of (a) an OCP curve and (b) a potentiodynamic polarisation curve. Parameters of interest (corrosion potential E_{corr}, critical corrosion current density i_{crit} and passivation current density i_{pass}) are highlighted

The rate at which the applied potential changes is called the scan rate (or alternatively, the sweep rate). Using a low scan rate is imperative for the reduction in the distortion of the polarisation curve[159]. However, using a lower scan rate increases the time taken for the test to complete. Within the ASTM G59-23 standard[160], which describes the test method for conducting potentiodynamic polarisation tests, a scan rate of 0.167 mV/s is described. An analysis of the scanning rates used in 38 publications on the topic of the cathodic modification of stainless steels is presented in Figure 2.28. Despite the ASTM standard scan rate of 0.167 mV/s, many studies use scan rates exceeding this. The current study uses the higher scan rate of 0.5 mV/s, a figure which was selected to reduce the time taken to perform electrochemical tests, reduce any distortion in the polarisation measurements and maintain some comparability to other studies.

A final point of note is the convention applied when producing potentiodynamic polarisation graphs which differs depending on geographical location. In the United States, i_{corr} is plotted on the x-axis despite being the dependent variable and the independent variable E on the y-axis[158]. To present the results collected in this study, the British convention of E on the x-axis and i_{corr} on the y-axis will be used.

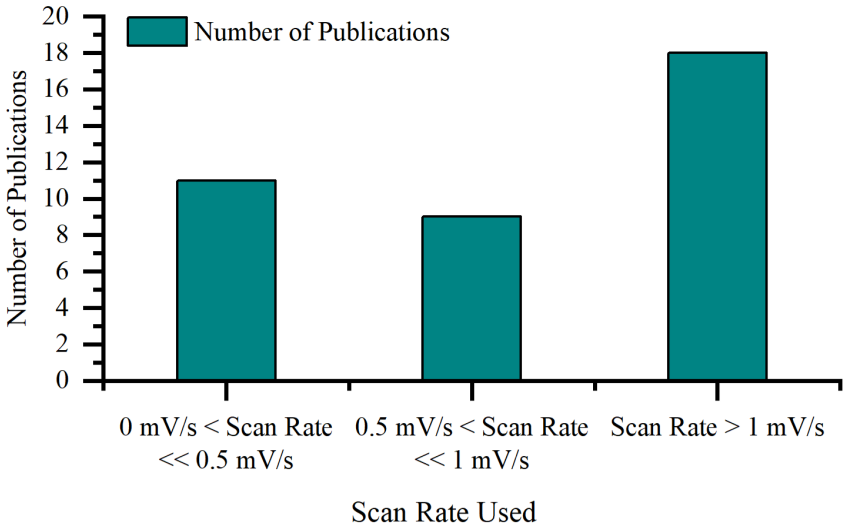

Figure 2.28: Scan rates used in potentiodynamic polarisation electrochemical studies presented in 38 papers on the cathodic modification of stainless steel[10,13–19,22–24,161–186]

2.4.5 Evaluating the Corrosion Performance of Functionally Graded Materials

Different methods have been used in the literature to investigate the corrosion performance of FGMs. Pütz et al.[187] performed cyclic polarisation testing on a three-layered compositionally graded steel sample. The method by which they sectioned the sample for corrosion performance evaluation involved extracting samples from each composition and the two composition transition zones. While this approach has the benefit of testing each composition in the FGM it requires more samples to be tested and so electrochemical testing will be a more time-intensive pursuit.

Senthil et al.[188] used a similar approach when investigating the corrosion performance of a two-layered Inconel 825/316L SS FGM. Senthil et al.[188] performed weight loss tests of three separate sections of the sample, so that each composition and the transition zone could be corrosion tested. Since this FGM is compositionally less complex than that produced by Pütz et al.[187] fewer sections were required to represent the unmixed alloys and the transition zone. Additionally, weight loss measurements as opposed to electrochemical evaluation requires less effort in terms of sample preparation and so can be a less time-intensive approach to the study of the corrosion performance of FGMs.

Jiang et al.[189] utilised another approach to understand the corrosion behaviour of a five-layered stainless steel/12CrNi2 FGM. In their study, Jiang et al.[189] sectioned a 1 cm^2 area off using paraffin wax. The region encompassed all layers of the FGM sample. The sample was then evaluated by potentiodynamic polarisation testing. While this approach minimises time spent performing electrochemical evaluation, it does mean that the corrosion data extracted will be an average of all of the compositions involved in the FGM. The compositional inhomogeneity in the sample corrosion tested by Jiang et al.[189] means that the extracted corrosion currents will be averaged over the entirety of the area of the working electrode.

Difficulties and inaccuracies arise when investigating the corrosion performance of FGMs because of their spatial complexity. Regardless of the approach there are associated challenges which must be considered.

2.5 Cathodic Modification

In some materials, the conditions in which passivity is achieved can be expanded through *cathodic modification*. Cathodic modification is whereby noble elements are introduced to a material to enhance its corrosion resistance[20]. A material's suitability for cathodic modification is dependent on three criteria[9]:

- Before cathodic modification, the material must display active-passive behaviour in acidic environments
- The range of potentials over which the material is passive must be wide enough to avoid transpassive or pitting corrosion
- The critical current density must be low enough to prevent the PGM-doped material from corroding at lower potentials

As a result of these criteria, only SS, Ti alloys and Cr-based alloys exhibit beneficial cathodic modification behaviour using PGMs[20].

2.5.1 Mechanism of Cathodic Modification

Alloying with PGMs improves the corrosion behaviour of SS via two different mechanisms[9]:

- Lowering hydrogen overvoltage
- Blocking active sites in the crystal lattice to reduce dissolution

Lowering the hydrogen overvoltage results in the catalysis of the hydrogen evolution reaction (Equation 2.2) and hence increasing the cathodic efficiency, enabling spontaneous passivation and a decrease in corrosion rates[9,20].

2.5.2 Cathodic Modification of Stainless Steels

The cathodic modification of SS has been extensively researched, demonstrating that the introduction of PGMs can improve corrosion resistance in a range of reducing acids at temperatures up to 100°C. The analysis of 40 journals relating to the cathodic modification of SS by PGMs has revealed that the majority of the research was carried out on ferritic and austenitic SS (Figure 2.29 (a)). Most of the cathodic modification was achieved via bulk alloying (Figure 2.29 (b)) and Ru was the most commonly used dopant (Figure 2.29 (c)). As the cheapest of the PGMs in recent history, it is likely the research into Ru doping was economically driven[9]. Of the articles analysed, none were found to study the effects of PGMs on martensitic SS. Since they are not of relevance to the current study, articles which investigate the oxidation behaviour of cathodically modified SS are not discussed below.

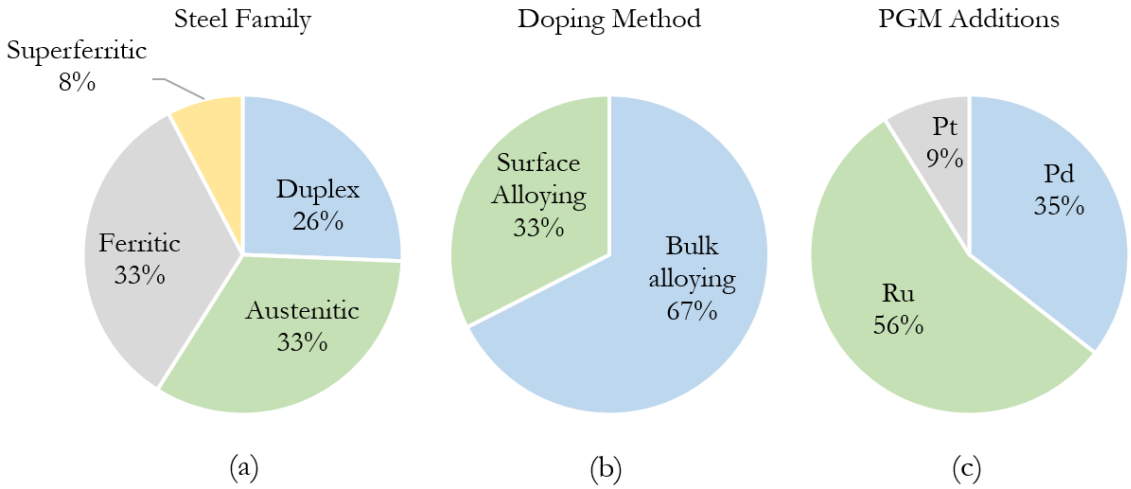

Figure 2.29: Analysis of research articles relating to the cathodic modification of SS showing the distribution of (a) steel families studied, (b) PGM doping methods used and (c) PGMs used to achieve cathodic modification

Bulk Alloyed

Studies on the effect of PGM doping on the corrosion performance of SS have been conducted under various test conditions and on different families of stainless steels. Potgieter et al.[173] studied the corrosion behaviour of duplex low Ni Fe-22Cr-9Ni-3Mo in 40% H_2SO_4 at 55°C and found that Ru additions improved corrosion behaviour by inhibiting anodic dissolution. These findings were also corroborated by Olubambi et al.[19]. Sherif[14] further examined this alloy, doped with up to 0.28 wt.% Ru, in 10% H_2SO_4 at room temperature. The corrosion rates decreased with the presence and increased amounts of Ru. Similar studies carried out in 2 M HCl and 3.5% NaCl reported consistent corrosion rate behaviour[13,174]. Pitting resistance was also reported to be improved by Ru doping in the research of Sherif et al.[13,174].

The impact of PGM doping on corrosion performance has been investigated across a range of temperatures. Olaseinde et al.[15] analysed the corrosion behaviour of 2101 lean duplex SS with 0.15 wt.% Ru in 1 M H_2SO_4 up to 80°C. It was reported that at 25°C, the corrosion rate of the doped alloy was lower than its undoped counterpart. Meanwhile, at higher temperatures the opposite was found to be true. However, it is important to note that the methodology for calculating the corrosion rate was not specified. Weight loss tests were not mentioned in the study, suggesting that corrosion rates were determined from electrochemical data. Such an approach to corrosion rate determination is complicated, especially for alloys as complex as stainless steel[190]. As a result, the corrosion rate data presented by Olaseinde et al.[15] should be interpreted with caution. The study did reveal that PGM doping lowered the passivation current density values and shifted the OCP values to higher values across the temperature range investigated, suggesting that the cathodic modification was successful.

Similar to Olaseinde et al.[15], Potgieter and Brookes[171] alloyed a duplex Fe-29Cr-14Ni-3Mo with up to 0.28 wt.% Ru and tested the corrosion performance in H_2SO_4 (10 - 50%) up to 90°C. In their study, Potgieter and Brookes[171] used weight loss tests to calculate corrosion rates. In contrast to Olaseinde et al.[15], Potgieter and Brookes[171] revealed that stainless steel doped with 0.28 wt.% exhibited corrosion rates lower than the undoped sample across the entire temperature and concentration range considered.

In general, Ru is reported to be a more effective cathodic modifier than Pd in reducing acids. Biefer[161] studied ferritic 430 SS in 5% H_2SO_4 and found that adding 0.46 - 1.91 wt.% Pd passivated the material. Biefer[161] found that alloying with 0.26 wt.% Pd was

insufficient to cause passivity. Compare this to the study carried out by Potgieter and Brookes[171] discussed in the previous paragraph, whereby alloying with the lower volume of 0.28 wt.% Ru effectively improved corrosion resistance. This is consistent with the data obtained by Chernova et al.[191] who compared Pd and Ru additions to Fe-25Cr in HCl and H_2SO_4. They found that Ru was more effective than Pd at lowering corrosion rates and causing faster passivation, though both improved the corrosion resistance of the SS in the acidic media.

The effect of increasing PGM content on corrosion performance was explored by Higginson et al.[192] and Tjong[179] who studied the effects of 0.1% and 0.2% Ru doping on ferritic Fe-40Cr at in 0.5 M H_2SO_4 and 0.5 M HCl up to temperatures of 92 and 85°C respectively. Higginson et al.[192] found that spontaneous passivation was achieved more rapidly with higher doping content. This is consistent with the findings of Potgieter and Brookes[171] who explored the effect of Ru doping between 0.06 - 0.28 wt.% and found that the highest content considered in the study, 0.28 wt.%, was the most effective at enhancing corrosion behaviour.

It is well established from a variety of studies that increasing solution strength is detrimental to the corrosion performance of PGM-doped stainless steel. In the study by Olubambi et al.[19], it was found that increasing the concentration of H_2SO_4 and HCl up to 2 M was detrimental to the corrosion resistance of superferritic Fe-29Cr-4Mo-2Ni with similar behaviour observed by Scheers et al.[193] using boiling phosphoric acid. Potgieter and Brookes[171] also found that corrosion rates positively correlated with increased concentration of H_2SO_4 up to the maximum concentration studied: 50%.

Surface Alloyed

Even when low amounts of PGMs are used in bulk alloying, the PGM content can account for the majority of the cost of the alloy[194]. To decrease costs, cathodic modification by surface alloying has been researched. Of the 13 articles analysed that use surface alloying to achieve cathodic modification, austenitic SS are the most widely studied (Figure 2.30 (a)), likely because austenitic grades are the most commonly used SS[10].

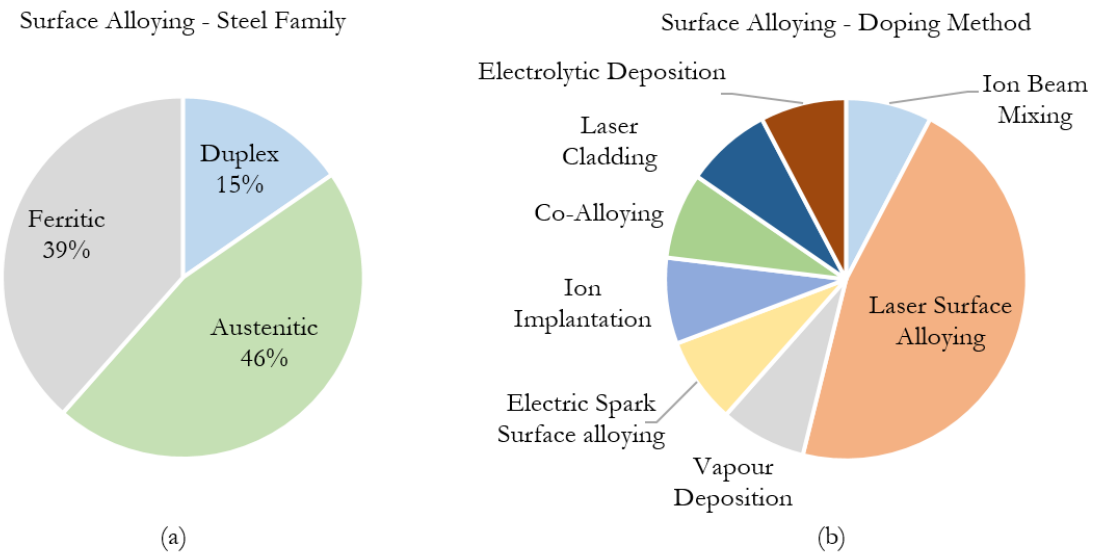

Figure 2.30: Analysis of research articles relating to surface alloyed cathodic modification of SS showing (a) steel families studied and (b) PGM doping methods used

Potgieter et al.[16] compared electron beam vapour deposited and bulk alloyed duplex SS modified with Ru and found both were effective at improving corrosion resistance. However, exposure to H_2SO_4 for 210 minutes caused spalling of the deposited coating which was not improved by annealing. Moyo et al.[9] suggests spalling may be caused by stresses generated by hydrogen evolution during corrosion making the avoidance of such a mechanism difficult to achieve. Similar behaviour was observed by Chernova et al.[195] who electrolytically deposited and electric spark alloyed Pd on ferritic and austenitic SS. Both materials' resistance to corrosion in H_2SO_4 was improved, though after one hour the 0.001 µm coatings dissolved. Annealing was found to improve the longevity of thicker coatings for the duration of the 50-hour tests, but annealing the 0.001 µm coating increased corrosion rates. Chernova et al.[195] conclude that this is because annealing caused the diffusion of Pd into the material decreasing its concentration on the surface.

Tjong et al.[22] compared bulk alloyed ferritic SS with 0.2 wt.% Ru with samples possessing a 0.1 mm Ru coating deposited by laser surface alloying (LSA). The bulk alloyed sample was found to outperform the LSA sample. Lekala et al.[196] reported similar findings, attributing this behaviour to the high cooling rates inherent to LSA resulting in grain refinement. It has been reported that grain refinement can lead to increased corrosion due to the increase in the area available for grain boundary corrosive attack[9,146].

Powder Metallurgically Processed

A relatively small body of literature is concerned with the cathodic modification of powder processed stainless steel. To the best of the author's knowledge, this research was conducted exclusively by Peled and Itzhak[18,23,24], who studied the corrosion behaviour of sintered bulk alloyed PGM-doped 316 stainless steel in 1 N sulphuric acid. In their work, however, Peled and Itzhak did not address parameter optimisation despite its established impact on corrosion behaviour. Additionally, the corrosion behaviour of the sintered samples was not compared to cast equivalents. This renders it challenging to assess the degree the processing approach and the PGM doping affected corrosion performance.

Despite the lack of parameter optimisation, Peled and Itzhak[23] found that pressed and sintered 316 SS doped with 2 wt.% Pt passivated in the 1 N H_2SO_4 solution. In the same study, it was found that doping with less than 2 wt.% Pt was insufficient to cause passivation in acidic media. However, since parameters were not optimised it is impossible to tell whether the corrosion behaviour could have been improved by enhancing density for example without the need for additional Pt content.

In 1990, Peled and Itzhak[18] built on their powder processed cathodically modified stainless steel research by investigating the effect of pore morphology of Pt and Pd doping on passivation behaviour. The findings were positive in terms of corrosion performance since they found that the doped samples showed passive behaviour and outperformed undoped samples regardless of whether pores were open or closed. Later investigations by Peled and Itzhak[24] into the thickness of the passive layer revealed that the doped samples had a passive layer five times thicker than the undoped samples.

The findings of Peled and Itzhak were generally positive and suggest that PGM doping may improve the corrosion performance of powder processed stainless steel. The current study aims to address the identified gaps in the literature by exploring parameter optimisation in the process of producing cathodically modified powder processed stainless steel.

2.6 Chapter Findings

While stainless steels are considered corrosion resistant materials, studies have confirmed that exposure to sulphuric acid and chloride solutions can lead to metal dissolution. Existing literature on the corrosion of powder processed stainless steel established that materials produced by this technique tend to underperform compared to their wrought and cast equivalents. The inferior performance of PM stainless steel is typically attributed to the impact of porosity or undesirable inclusions. A large volume of published studies describe the role of PGM additions in improving the corrosion performance of stainless steels. However, the vast majority of these studies focus only on bulk and surface alloyed materials. Bulk alloying, despite its effectiveness in improving corrosion performance, is inherently high cost. Surface alloying to achieve cathodic modification, though more economical, has exhibited degradation during exposure to corrosive media. An alternative approach to producing cathodically modified stainless steels is via powder metallurgy. However, the research reviewed here revealed that little attention has been paid to this particular topic. Moreover, gaps exist in the studies which did focus on PGM-doped steels produced by powder metallurgical approaches.

This EngD is concerned with producing functionally graded PGM-doped stainless steels using powder metallurgical processing. By addressing the gaps identified in the literature, this study aims to contribute towards a better understanding of powder processed cathodically modified stainless steels. This study also provides the first examination of the corrosion behaviour of functionally graded PM PGM-doped stainless steel.

CHAPTER

3 Materials and Experimental Methods

3.1 Metal Powders

3.1.1 Chemical Composition

In this study, seven different 316L and 17-4PH stainless steel powders were used to produce sintered specimens. Their chemical compositions are listed in Tables 3.1 - 3.4. All powders were supplied by Johnson Matthey and produced by water atomisation (WA) by Atomising Systems Limited, except for one 316L powder which was produced by vacuum induction gas atomisation (VIGA) by Liberty Steel. The PGM-doped powders were prealloyed by adding 0.5 wt.% Pd or Ru to the 316L and 17-4PH melts before atomisation. Residual unatomised metals were removed from the tundish of the atomiser following the production of the Ru- and Pd-doped 316L (see Figure 2.6). These samples were treated as cast metallurgical equivalents and were used to benchmark the powder processed samples.

Table 3.1: Chemical compositions of as-received 316L stainless steel powders, determined by inductively coupled plasma spectroscopy by Johnson Matthey

Composition (wt.%)								
Material	Fe	Cr	Ni	Mo	Mn	Si	Ru	Pd
316L (VIGA)	67.1	15.9	10.3	2.06	1.45	0.75	NA	NA
316L (WA)	68.8	16.4	10.7	2.21	0.49	0.71	NA	NA
316L with Ru (WA)	68.5	16.4	10.5	2.16	0.41	0.58	0.58	NA
316L with Pd (WA)	69.3	16.7	10.5	2.19	0.44	0.66	NA	0.51

Table 3.2: Oxygen, nitrogen and hydrogen content of the as-received 316L stainless steel powders, determined using combustion elemental analysis

Material	O (wt.%)	N (wt.%)	C (wt.%)	H (ppm)
316L (VIGA)	0.036	0.018	0.062	8
316L (WA)	0.388	0.069	0.077	9
316L with Ru (WA)	0.441	0.088	0.067	7
316L with Pd (WA)	0.371	0.083	0.065	11

Table 3.3: Chemical compositions of as-received 17-4PH stainless steel powders, determined by inductively coupled plasma spectroscopy by Johnson Matthey

	Composition (wt.%)								
Material	Fe	Cr	Ni	Mo	Mn	Nb	Cu	Ru	Pd
17-4PH (WA)	78.8	14.4	4.69	0.12	0.40	0.24	2.93	NA	NA
17-4PH with Ru (WA)	76.7	14.5	4.72	0.12	0.47	0.25	2.99	0.47	NA
17-4PH with Pd (WA)	77.2	14.7	4.93	0.12	0.49	0.26	3.10	NA	0.50

Table 3.4: Oxygen, nitrogen and hydrogen content of the as-received 17-4PH stainless steel powders, determined using combustion elemental analysis

Material	O (wt.%)	N (wt.%)	C (wt.%)	H (ppm)
17-4PH (WA)	0.495	0.033	0.06	12
17-4PH with Ru (WA)	0.504	0.039	0.07	5
17-4PH with Pd (WA)	0.526	0.037	0.06	11

3.1.2 Morphology

A Tescan Vega3 LMU scanning electron microscope was used to study the precursor powders. An operating voltage of 15 kV with a 60 µm aperture size was used at 500x magnification. To perform the analysis, conductive adhesive carbon tape was attached to a mounting stub. Around 1 g of the metal powder was distributed onto a piece of paper. The carbon tape-mounting stub assembly was pressed into the powder and placed into the SEM for analysis. Any remaining unmounted powder was returned to the powder container.

3.1.3 Particle Size Analysis

The particle size distribution of the powders used in this study was analysed using a Malvern Mastersizer 3000. The analysis was performed using water dispersion and the Mie scattering model. According to Du[197], the Mie model enables the accurate measuring of size distribution for all particle sizes. This approach does however require that the optical properties of the material being analysed are known. The Fraunhofer approximation was not used since it can lead to the inaccurate measurement of particles with diameters below 50 µm[198]. Three sub-samples from each powder composition were used and then ten powder size measurements were taken for each sub-sample. Mean and standard deviation of the powder size for the D_{10}, D_{50} and D_{90} percentiles were calculated.

3.2 Synthesis of Samples by FAST

3.2.1 Introduction

Sintering was carried out using a FCT HP D25 field assisted sintering furnace situated in the Royce Discovery Centre at the University of Sheffield. Sintering was performed with graphite tooling since they can be reused. However, due to the brittle nature of graphite, rough handling during sample removal can damage it. To ensure the tooling didn't fail during sintering, the die assembly was inspected for cracks before each cycle. Once the preliminary tooling checks were complete, graphite foil was placed along the inside walls of the 20 mm diameter cylindrical graphite die.

Additionally, graphite foil was placed between the punches, wear pads and metal powder

to ease the removal of the sintered parts and prevent damage to the die (illustrated in Figure 3.1). Fifteen grams of powder was then manually loaded into the die. A carbon felt jacket was wrapped around the die assembly to reduce heat losses. Next, to ensure good compaction, 20 MPa pressure was applied to the powder using a desktop hydraulic press. Following this, the assembly was placed into the sintering chamber which was subsequently evacuated. The sintering program was then entered into the computer, uploaded to the sintering apparatus and the sintering cycle started. A uniaxial pressure of 50 MPa was applied alongside a pulsed direct current. The sintering equipment modulated temperature using proportional–integral–derivative (PID) feedback control. An optical pyrometer measured the temperature and subsequently compared this value to the user-defined temperature. If the measured temperature differed from the user-defined temperature, the applied power was adjusted as a corrective measure. At the end of the sintering cycle, the samples were water-cooled by the punches, the sintering vessel was repressurised to atmospheric pressure and the die assembly was removed. The samples were disassembled from the die and any residual graphite foil was scraped off using a craft knife.

3.2.2 Bulk Alloyed Samples

Before FGM samples could be manufactured, it was first necessary to optimise the sintering parameters for each of the powder compositions studied. To do this, bulk alloyed samples were produced and the sintering temperature and hold time were varied as shown in Table 3.5. These conditions were varied as these are the sintering parameters with the greatest influence on density and, therefore, corrosion[98]. The sintering temperature was not increased above 1100°C, as sintering above this temperature was found to cause melting of the powder and destruction of the die in the process of sample removal. All other parameters were kept constant: a uniaxial force of 16 kN (equivalent to a pressure of 50 MPa) and a heating rate of 100°C/min was used in the production of each sample under a vacuum atmosphere. The resulting cylindrical samples were 20 mm in diameter and approximately 6 mm in depth.

The density, porosity, hardness and corrosion behaviour of the bulk alloyed samples were assessed. The combination of parameters most suited to each composition was selected based on these criteria. The selected parameters were then used to produce the functionally graded samples.

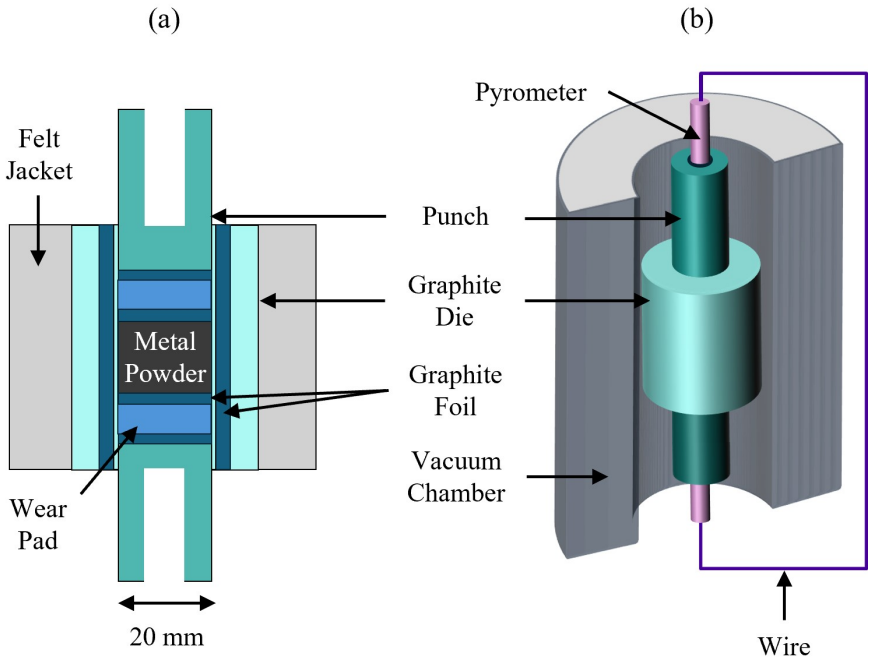

Figure 3.1: Schematics of the die assembly and FAST apparatus used to sinter stainless steel powders. Diagram (a) shows a cross-section of the die assembly before insertion in the vacuum chamber. Diagram (b) shows the die assembly when in the vacuum chamber. The felt jacket was omitted from diagram (b) to improve diagram clarity

Table 3.5: Sintering temperature and hold time combinations used to produce samples usinf FAST

Hold time (s)	Sintering Temperature (°C)
600	1000
600	1050
600	1100
300	1100
900	1100

3.2.3 Functional Grading

The layering approach was used to produce FGMs using field assisted sintering. In producing FGMs, the graphite dies were lined with graphite foil and assembled using wear pads, felt jackets and punches in the same manner used in producing the bulk alloyed samples.

Layering Approach

The layering approach involved the placement of the PGM-doped stainless steel powder into the graphite die (Figure 2.14 (a)). The die assembly was then tapped several times on a level surface to ensure the powder surface was level. Following this, the undoped stainless steel powder was poured into the die, on top of the doped composition. The process of levelling the powder was repeated, the top punch was added and the powders were sintered using the same procedure as with the bulk alloyed samples. A mass of 7.5 g of the undoped and 7.5 g of the PGM-doped powder was used to produce the layered FGMs.

3.3 Heat Treatment

The H1075 heat treatment was performed on the 17-4PH samples. The conditions used are detailed in Table 3.6 and illustrated in Figure 3.2. Heat treatment was performed in an Ar atmosphere. Air cooling was the selected quench as the sample dimensions were small enough to enable sufficiently high cooling rates in air[199].

Table 3.6: Description of the H1075 two-step heat treatment cycle applied to the 17-4PH stainless steel samples

Heat Treatment Condition	H1075	
Heat Treatment Step	Solution Anneal	Precipitation Hardening
Time (Hours)	0.5	4
Temperature (°C)	1050	579
Quench	Air cool	

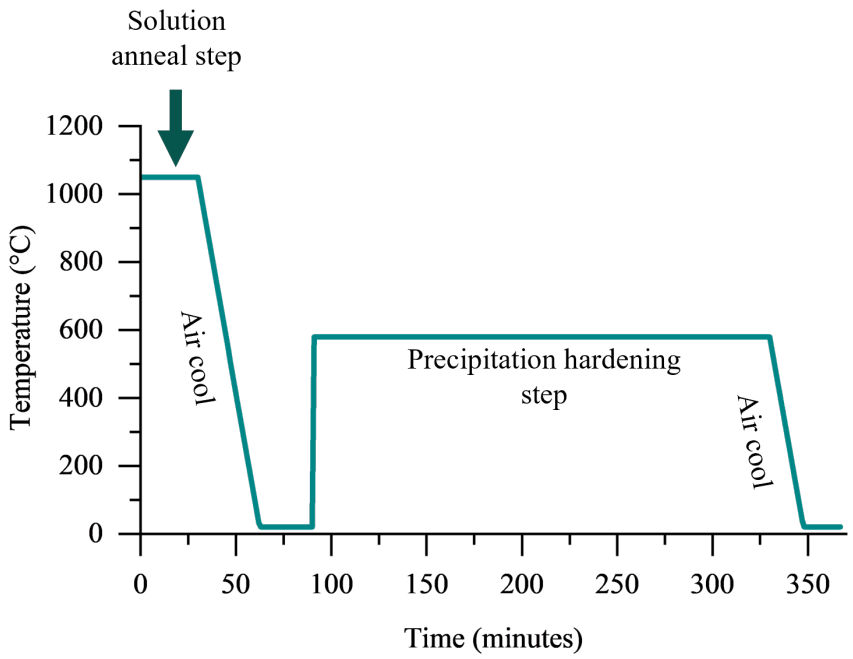

Figure 3.2: Schematic diagram illustrating the solution anneal and precipitation hardening steps in the thermal processing of sintered 17-4PH under H1075 conditions[200]

3.4 Alloy Characterisation

3.4.1 Metallographic Preparation

The cylindrical as-sintered samples were initially sectioned into two pieces using a Secotom-50 manufactured by Struers and a ferrous cut-off wheel. Figure 3.3 presents the sample dimensions and how they were sectioned along their depth. One half was mounted in conductive Bakelite using the Buehler SimpliMet 1000 Mounting Press while the other half was set aside for use in density measurements. A Buehler AutoMet 250 Grinder-Polisher was used to mechanically grind and polish mounted samples with water as the lubricant. Table 3.7 presents the steps used in grinding and polishing the mounted samples. Between each grinding/polishing step, the samples were cleaned using tap water and isopropanol before being dried using hot air. It was ensured that the samples were reoriented by 90° for each consecutive grinding and polishing step. This enabled the easy identification of residual scratches from previous metallographic preparation steps so that grinding or polishing repeats can be performed if needed[201]. The samples produced using the described steps were then used in optical and scanning

electron microscopy and immersion testing.

In order to determine the ideal etching procedure, several different etchant compositions were tested (Table 3.8). Figure 3.4 illustrates the microstructures resulting from unsuccessful etching procedures. Out of the etchants explored, use of Kalling's No.1 was the most successful and so was selected for use in this project.

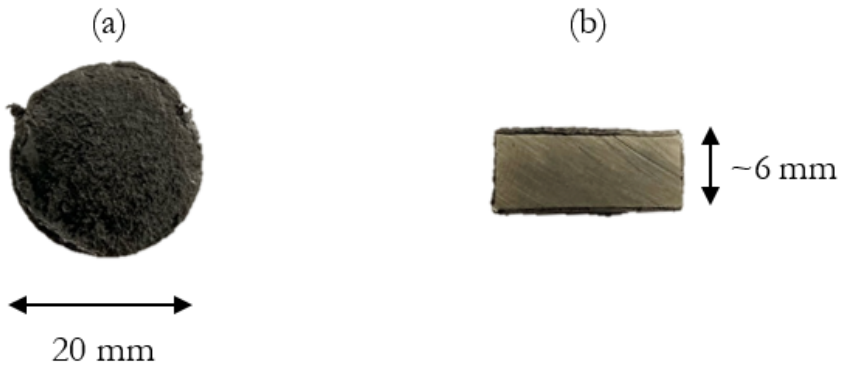

Figure 3.3: Longitudinal view of the as-sintered sample before sectioning (a) and transverse view of the sample after sectioning (b). Residual graphite foil can be seen covering the outer surfaces of the sintered sample. This was removed in subsequent grinding steps

Table 3.7: Metallographic preparation steps

Grinding/Polishing Media Used	Force Applied (N)	Head Speed (rpm)	Platen Speed (rpm)	Time (Minutes)	Head Rotation Direction Relative to Platen Rotation
220 Grit SiC	27	305	60	1	Same
320 Grit SiC	27	305	60	1	Same
400 Grit SiC	27	305	60	1	Same
600 Grit SiC	27	305	60	1	Same
6 µm Monocrystalline Diamond Suspension	27	150	60	5	Opposite
3 µm Monocrystalline Diamond Suspension	27	150	60	3	Same
1 µm Monocrystalline Diamond Suspension	27	150	60	3	Opposite

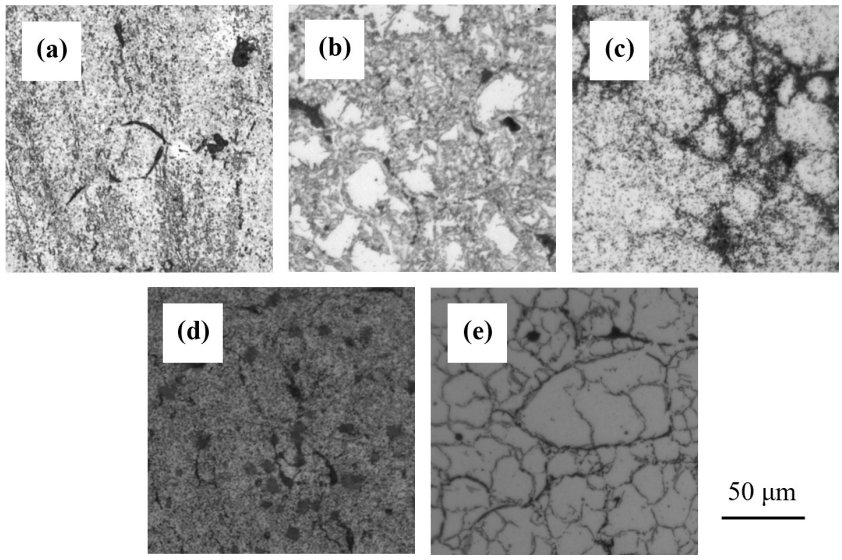

Figure 3.4: Micrographs showing the unsuccessful etching of (a) Pd-doped 316L using Kalling's No.2, (b) Ru-doped 17-4PH using 10% Nital and Kalling's No. 1, (c) Pd-doped 17-4PH using Fry's, (d) Ru-doped 316L using Marble's and the successful etching of (e) Ru-doped 17-4PH etched using Kalling's No.1. Micrographs were captured at x50 magnification

Table 3.8: List of etchants tried in the preparation of stainless steel samples

Etchant	Composition	Methodology	Source
Kalling's No.2 (Waterless Kalling's)	• 2 g $CuCl_2$ • 40 mL HCl • 40 - 80 mL ethanol (95%)	Swabbed for a few seconds	ASTM[202]
Nital 10% and Kalling's No.1	**Nital 10%** • 10 mL HNO_3 • 90 mL ethanol (95%) **Kalling's No. 1** • 2 g $CuCl_2$ • 40 mL HCl • 40 - 80 mL ethanol (95%) • 40 mL water	Immersed in Nital 10% for several seconds then swabbed with Kalling's No.1	Tried combination upon advice from University of Sheffield technicians
Fry's Reagent	• 5 g $CuCl_2$ • 40 mL HCl • 30 mL distilled water • 25 mL ethanol (95%)	Swabbed for a few seconds	Sun et al. (2018)[77]
Marble's Reagent	• 10 g $CuSO_4$ • 50 mL HCl • 50 mL distilled water	Swabbed for a few seconds	ASTM[202]
Kalling's No.1	• 2 g $CuCl_2$ • 40 mL HCl • 40 - 80 mL ethanol (95%)	Swabbed for a few seconds	ASTM[202]

3.4.2 Microscopy

Optical microscopy was carried out on unetched and etched samples using a Nikon Eclipse microscope operating in bright field mode. Micrographs of the unetched samples were used in the image analysis of porosity.

A Keyence X200K 3D laser confocal microscope was used to image unetched and etched samples to produce micrographs and topography maps. MultiFileAnalyzer 1.3.1.120 and VK Analyzer 3.8 software were used to process data.

Scanning electron microscopy and EDS was performed on the sintered and cast samples using the Tescan Vega3 LMU and Zeiss Ultra operating at 15 - 20 kV with 60 µm aperture size at magnifications ranging between 500 – 20,000x.

3.4.3 Grain Size Measurements

The Heyn lineal intercept method (standardised in ASTM E112-13(2021)[203]) was used to calculate grain size. The analysis was conducted on micrographs of etched samples, ensuring that a minimum of 400 grains were measured across at least four micrographs. The mean and standard deviation for each sample were then calculated for the density and hardness tests in addition to the grain size measurements.

3.4.4 Porosity Measurements

Porosity measurements were calculated by image analysis using ImageJ. A total of five micrographs, taken at x20 and x50 magnification using optical microscopy (OM), were used in the analysis of porosity in this study. These were then opened in ImageJ, the scales set using the scale bar, the image was then cropped so that the scale bar was no longer a part of the image. Next, the image was converted to 32-bit file type and thresholded so that the image became black and white, with porous areas appearing black and everywhere else appearing white. The ImageJ *Analyze* tool was used to determine the percentage area cover and mean area of pores in the micrographs. Using the data gathered, the mean and standard deviation of the percentage area cover and mean area of pores were determined for each sample. A total of five micrographs, taken at x20 and x50 magnification, were used in the analysis of porosity in this study.

3.4.5 Density Measurements

Following initial sectioning, the samples were further sectioned into smaller parts to remove any residual graphite foil using a Buehler IsoMet 5000 Linear Precision Saw and a ferrous cut-off wheel. The density of the sintered samples was determined using a Mettler Toledo NewClassic Balance at room temperature using distilled water as the auxiliary liquid. Ten repeat measurements were carried out for each sample. Subsequently, the mean and standard deviation of the density for each sample was calculated.

3.4.6 Indentation Hardness Testing

Indentation testing was performed as a preliminary examination of the mechanical properties of the sintered parts. Vickers indentation testing was carried out at room temperature on as-polished samples using a Durascan Microhardness Tester and Ecos Workflow software with an applied load of 9.81 N and a dwell time of 15 s. Five indentation tests were carried out for each sample following ASTM guidelines[204]. The mean and standard deviation for each sample was then calculated.

3.5 Focused Ion Beam Implementation

SEM studies confirmed that the sample was homogeneous microstructurally in the longitudinal (direction of applied pressure) and transverse (perpendicular to direction of applied pressure) directions. Focused ion beam (FIB) (Zeiss Gemini 2) was used to prepare the 17-4PH with 0.5 wt.% Pd sample for TEM analysis. First an area of interest was identified in the sideview of the sample (Figure 3.5 (a)). A protective carbon film was applied to the area of interest to protect it from the Ga ion beam during milling (Figure 3.5 (b)). A 30 kV voltage and 300 pA current ion beam was used for a duration of five minutes to deposit a 2 µm thick, 15 x 3 μm^2 carbon film. A Ga ion beam was used to mill the specimen surface. First a rectangular trench (15 x 15 μm^2 and 10 µm deep) on either side of the area of interest was milled (Figure 3.5 (c)). To do this, two coarse milling steps using 30 nA and 15 nA were used, followed by a further fine milling step, which utilised a lower current of 7 nA. For the cross sectioning, an accelerating voltage of 30 kV was used. The milled lamella was 2 µm thick, 15 µm wide and 10 µm deep. The sample was then tilted by 54° and the lamella joined to the probe by the application of a 1 x 1 μm^2 carbon weld. Next the undercut was performed using a 30 kV

voltage and 3 nA current to remove the lamella from the trench (Figure 3.5 (d)). The lamella was then welded to the posts of a Mo grid (Figure 3.5 (e)). The Ga ion beam was used to produce a 200 nm thick foil 5 x 5 μm^2 for TEM characterisation (Figure 3.5 (f)).

3.6 Transmission Electron Microscopy

The formation of Cu precipitates induced by the H1075 heat treatment was investigated by TEM operated at 200 kV (JEOL JEM 2800 TEM). The specimen was examined using a bright-field detector and EDS. Additionally, high resolution imaging was used to generate electron diffraction patterns. ImageJ software was used to determine the diameter of particles of interest.

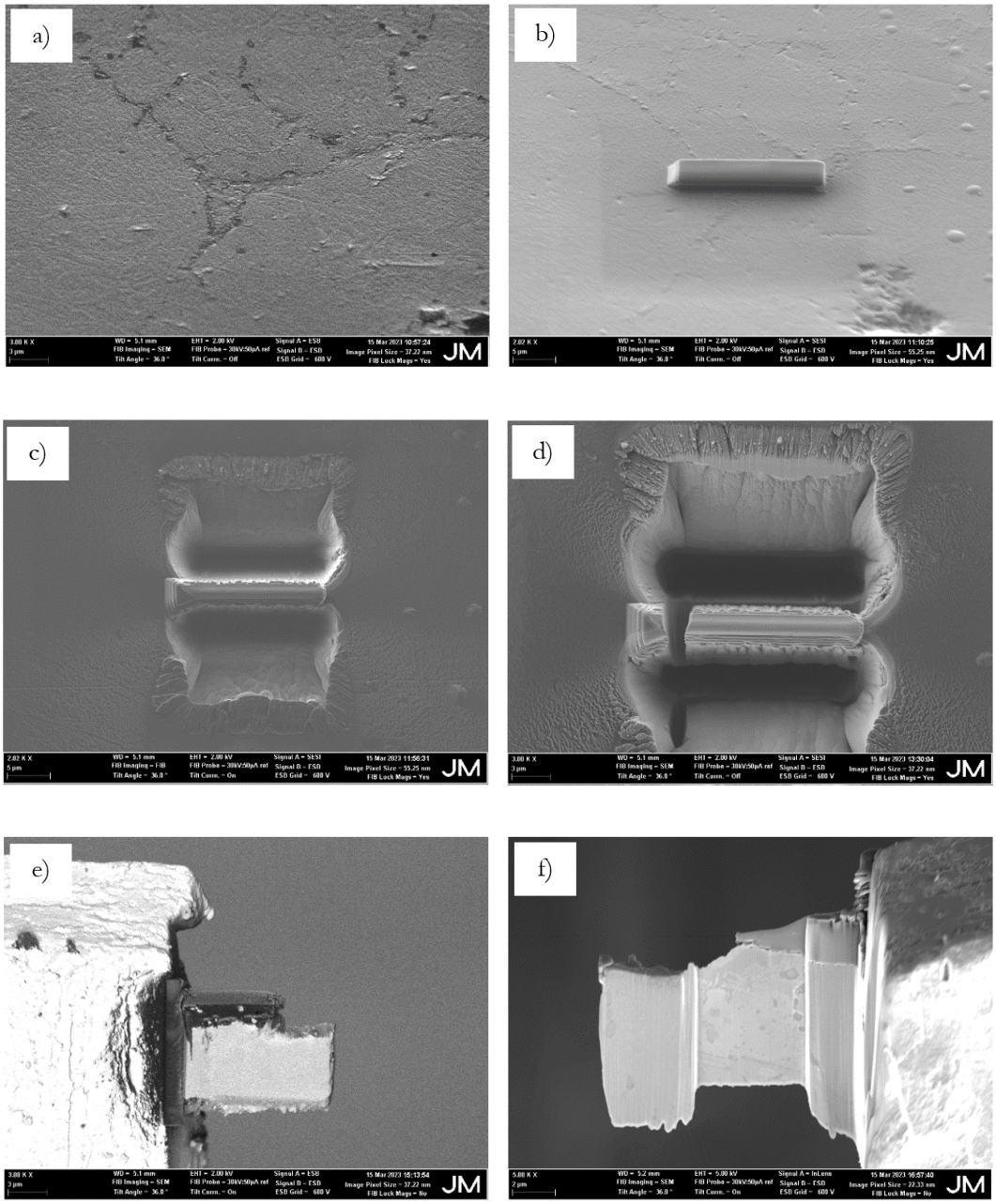

Figure 3.5: Micrographs of the six steps of TEM specimen preparation: (a) area of interest; (b) carbon film deposited on area of interest; (c) milled trenches; (d) undercut lamella; (e) sample welded to post of Mo grid; (f) thinned cross-section

3.7 Corrosion Characterisation

3.7.1 Sample Preparation

Figure 3.6 illustrates the steps taken in preparing samples for corrosion testing. Each cylindrical sample was sectioned and ground using P240 SiC paper to remove any residual graphite from the sintering process. A 1 mm gauge stainless steel wire was then spot welded to the surface. An acrylic tube with 2 mm wall thickness and 8 mm outer diameter was joined to each sample using Araldite 2-Part Instant Epoxy. This was done so that the tube surrounded the stainless steel wire and protected the spot weld from damage due to handling. The samples were then degreased in acetone. MetPrep Epo-Set two-part resin and hardener was used to mount the samples in 30 mm diameter silicon moulds. This particular cold mounting compound was selected for its excellent edge retention, reducing the likelihood of the development of crevice corrosion. To quantify the sample surface area to be exposed to the corrosion solution, photographs of the mounted samples were taken and analysed using ImageJ. This was necessary to calculate the corrosion current density. Before electrochemical testing, the testing surface of each sample was abraded using P1200 SiC paper and rinsed with distilled water and isopropanol alcohol before being dried using hot air. Following this, a heat gun was used to make the acrylic tube more malleable, then the sample was bent by 90°. This was done so that the sample surface could be vertically aligned, facing the reference and counter electrode. Hoyle and Taylor[130] found that horizontal surface orientation can affect corrosion measurements by inhibiting the formation of the oxide film by the build-up of particulates on the sample surface in addition to disturbing the already formed oxide film. A vertical sample orientation was therefore selected for use in the current study to ensure that sample orientation was not influencing the observed corrosion behaviour.

To enable the formation of the protective oxide film, a period of 2 hours between the final polishing step and the commencement of the corrosion test was allowed to elapse. Immediately before specimen testing, the surface was rinsed using deionised water and dried using lint-free paper towel.

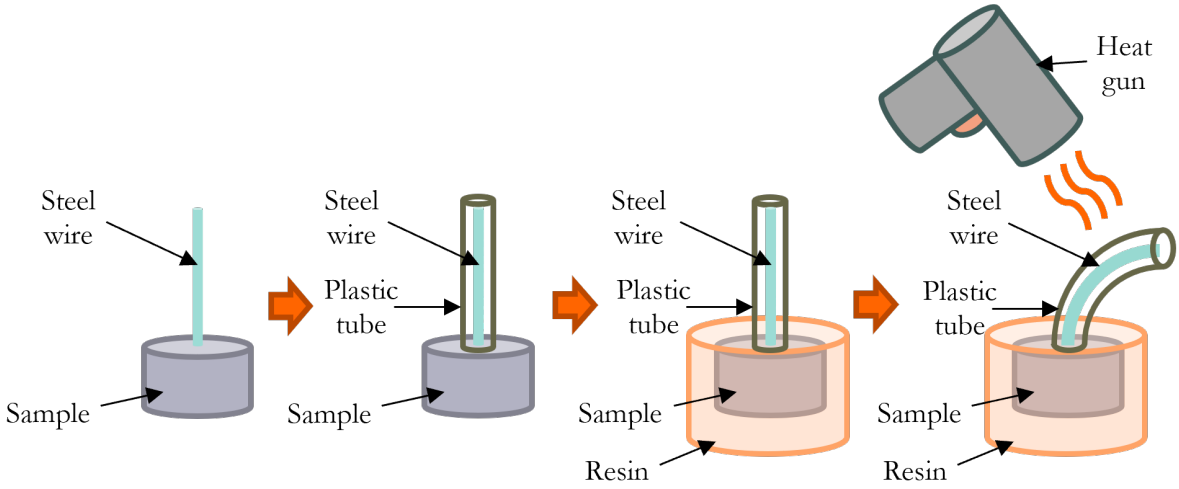

Figure 3.6: Diagram illustrating the steps taken in producing samples for electrochemical corrosion testing

3.7.2 Electrochemical Cell Set-Up

The corrosion performance of the bulk alloyed samples was evaluated by OCP and potentiodynamic polarisation testing. The corrosion tests were performed in 0.05 M H_2SO_4. To create the desired solution, deionised water was used to dilute concentrated H_2SO_4. A three-electrode set-up was used which consisted of the stainless steel sample as the working electrode, an AgCl reference electrode and a graphite counter electrode, connected to an IviumSoft potentiostat (Figure 3.7) and controlled using IviumSoft 4.1109 software. The test solutions were deaerated for at least 0.5 hours before the start of electrochemical testing and throughout the corrosion experiments by bubbling N_2 through them.

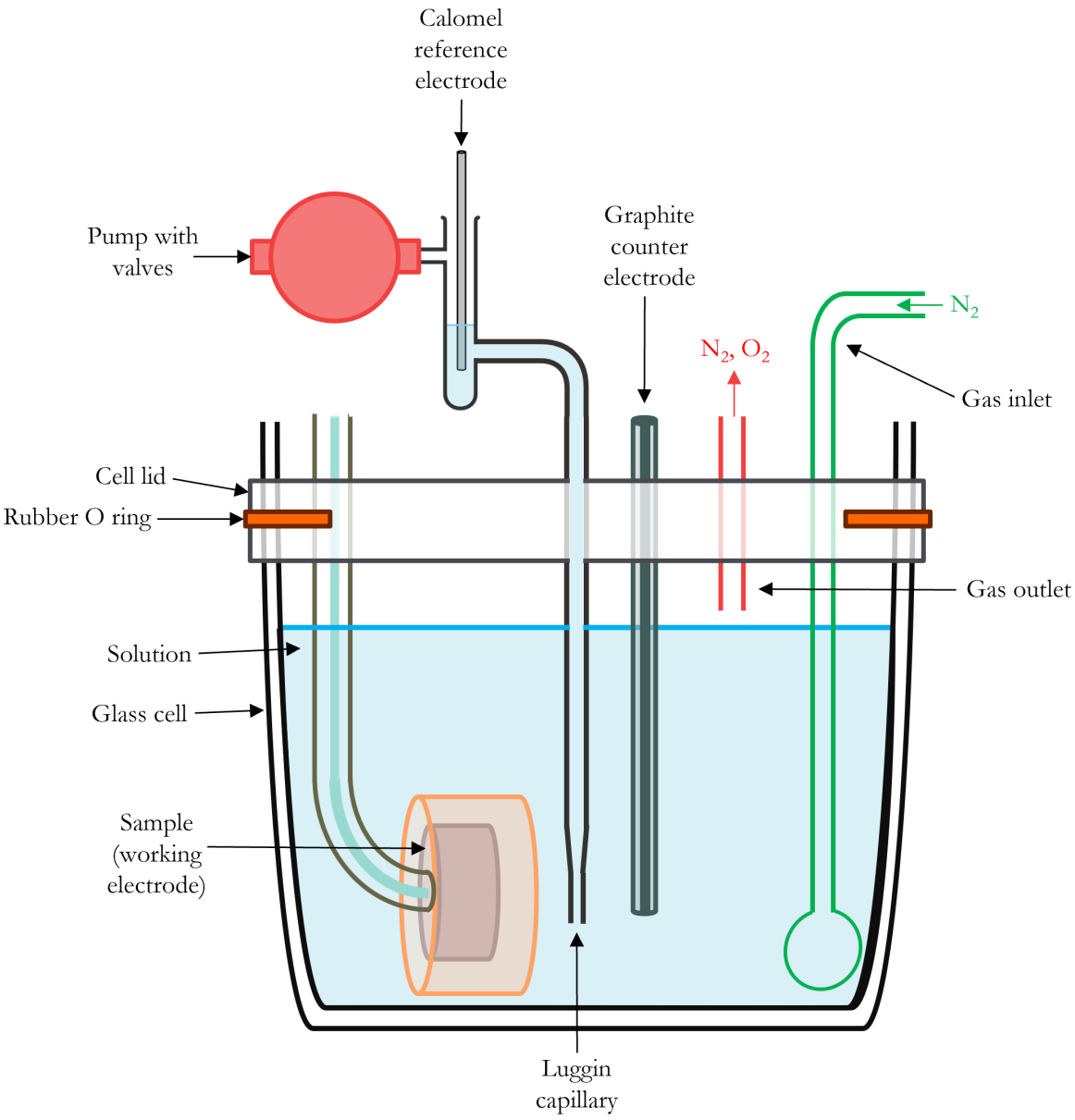

Figure 3.7: Schematic diagram of the three-electrode cell set-up used to corrosion test samples. Please note that the diagram is not to scale

3.7.3 Open Circuit Potential

OCP tests measure the potential of the sample when no external potential is applied. The OCP measurements were carried out for a maximum of 3600 s. If the sample achieved a stable potential before 3600 s, characterised by a <5 mV variation for >600 s, then the OCP test was stopped prematurely.

3.7.4 Potentiodynamic Polarisation

Immediately following the OCP test, the potentiodynamic polarisation scan was performed. The applied potential was varied from 200 mV below the OCP up to 1100 mV. A scan rate of 0.5 mV/s was used.

3.7.5 Immersion Tests

Immersion tests were performed for a total of 24 hours following ASTM B895-16 guidance[205]. The tests were performed in sealed beakers in solutions of 5% NaCl or 0.05 M H_2SO_4 at room temperature. In preparation for the immersion tests, the samples were ground to P1200 using SiC paper, rinsed with acetone and then rinsed with deionised water and dried using lint-free paper towel. The samples were removed from the solution at time intervals of 0.5, 1, 2, 4, 8 and 24 hours and photographed to evaluate the progression of corrosion. At each evaluation point, the sample was removed from the immersion solution, rinsed with deionised water and dried using lint-free paper towel.

3.7.6 Post-Corrosion Test Characterisation

Following corrosion testing, samples were characterised by microscopy. Samples were investigated before and after cleaning by optical microscopy as described in Section 3.4.2. Cleaning the samples post-corrosion testing involved a mild abrasive and a soft bristled brush and rinsing with tap water. The topography of the samples following corrosion testing and cleaning was investigated using confocal microscopy by the method stated in Section 3.4.2. Higher magnification micrographs were taken using SEM using the apparatus and process listed in Section 3.4.2. Characterisation of pitting by analysing number of pits and pit area was investigated using ImageJ.

3.8 Statistical Analysis

To study the correlation between the sintering parameters and sintered part properties the Pearson's R value was calculated. OriginPro 2022b 9.9.5.171 was used to plot density, hardness and grain size against the sintering parameters at which the samples were produced. The *Linear Fit* function was employed which tabulates the R value of the data set. The R values for each sample composition were then presented in a heat map to aid comparison between the effects of the sintering parameters on the measured parameters.

CHAPTER

4

Results and Discussion: Powder Characterisation

An essential step in powder metallurgical processing is the characterisation of the feedstock powder. The selected atomisation method, operational parameters and feedstock material impact the resulting metal powders, affecting characteristics such as morphology, size distribution and chemical composition[79]. It is imperative to investigate these qualities as they influence powder usage in later processes and can impact the sintered part's properties and performance[84]. In this study, a total of seven different 316L and 17-4PH stainless steel powders were utilised. This chapter presents their chemical composition, powder morphology and powder size distribution.

4.1 Chemical Composition

To better understand the powders used in this study, their elemental contents were compared to the compositional requirements outlined in ASTM A666-23[206] and A693-22[207] and presented in Table 4.1[206,207]. Tables 3.1 - 3.4 detail the compositions of the 316L and 17-4PH SS powders. Where variations arise between the standardised compositions and the elemental concentrations identified in this study, the possible causes and ramifications will be examined.

Table 4.1: Chemical compositions 316L and 17-4PH stainless steel obtained from ASTM standards[206,207]. Where an elemental composition is not listed in the standard the entry in the table below is instead filled with '...'. The compositions presented here are maximums unless stated as a range

Composition (wt.%)								
Material	Cr	Ni	Mo	Mn	Si	Cu	Nb	C
316L	16.0 - 18.0	10.0 - 14.0	2.00 - 3.00	2.00	0.75	...	...	0.030
17-4PH	15.0 - 17.5	3.00 - 5.00	...	1.00	1.00	3.00 - 5.00	0.15 - 0.45	0.07

4.1.1 Chromium

The 17-4PH powders contain Cr below the range designated in ASTM A693-22 (15.0 - 17.5 wt.%)[207]. As the 17-4PH alloys used in this study have a Cr content exceeding 10.5 wt.%, a chromium oxide passive film is expected to form[2]. However, since the Cr content of the studied 17-4PH alloys is lower than the standardised composition, the former may possess worse corrosion resistance, greater film instability and poorer self-healing characteristics than an alloy which meets the ASTM specifications[2]. The discrepancy between the Cr content of the powders studied and that described in the ASTM standards is small ($\sim$ 0.5 wt.%). It is unlikely that the change in the relative proportions in alloying elements is due to the presence of PGM dopants since the same trend is observed in both the doped and undoped 17-4PH powders. Another possible ramification of lower Cr amounts than expected could be that the formation of δ-ferrite is suppressed to a greater degree compared to a material that meets chemical specification (discussed in Section 2.1.1). Typically, δ-ferrite is desired to be suppressed due to its negative reported effects on mechanical and corrosion behaviour[51–53].

4.1.2 Molybdenum

A minimum amount of Mo in 17-4PH is not stated in the standards and the Mo content of 17-4PH is rarely reported in the literature. However, where reported, the amounts observed match that in the current study[208]. The amount of Mo present in the 316L alloys used in this study adheres to the concentrations outlined in the relevant standard[206].

4.1.3 Manganese

The 17-4PH WA powders studied contain considerably less Mn than is listed in ASTM A693-22[207]. Similarly, the WA 316L powders used in this study possess around 75% lower Mn than the maximum amount specified in the standard[206]. As explained in Section 2.1.1, the limits on Mn content are more stringent in powder metallurgy than in cast materials. Mn is a strong oxidising element and since oxygen can be detrimental to material behaviour, it is desirable to limit its presence in stainless steel. During the processing of cast stainless steel, deoxidation can be used to remove some oxygen pick-up. However, the same process cannot be used in atomisation. Therefore efforts must be made to limit the total amount of oxygen pick-up since it cannot easily be subsequently removed in atomisation. One way of achieving this is by reducing the Mn content.

It was also observed that the WA powder in this study contained 66% less Mn than the VIGA 316L powder. Similar discrepancies between the Mn content of GA and WA were found by Jandaghi et al.[61], Lou et al.[62] and Tobar et al.[63]. The amount of oxygen pick up is typically higher in WA than in GA. Therefore, more stringent Mn limits are required in the former to minimise the total amount of oxygen.

4.1.4 Silicon

The Si content of VIGA 316L powder is at the limit prescribed by the standard (0.75 wt.%) while all other 316L powders studied are below this limit. Though listed in the ASTM standards, the Si content of the 17-4PH samples was not provided by the supplier of the powder used in this study.

4.1.5 Copper

The concentration of Cu in 17-4PH samples is slightly below the limit outlined in the standard and so is unlikely to have a large impact on the hardenability of the material.

4.1.6 Carbon

The C content of the 316L alloys studied exceeds the ASTM standards. This can be detrimental to corrosion behaviour because a higher C content means greater susceptibil-

ity to the formation of chromium carbides and the mechanism of intergranular corrosion. The C content of the 316L alloys may be higher than expected due to the pickup of C during melting; because these powders were water atomised, they were melted in air. Dunkley[83] states that it is very difficult to avoid the pickup of C when melting in air. Much of the C present in the wrought feedstock used in atomisation will also be present in the final powder produced since the process offers little opportunity for decarburisation[60].

4.2 Powder Morphology

The WA stainless steel powders used in this study were of irregular morphology (Figure 4.1 (a)). Contrastingly, the VIGA 316L powder used in this study possesses a spherical morphology with evidence of some satellites (Figure 4.1 (b)). These powder morphologies are typical for WA and GA powders[62,134]. Powder morphology is especially important in sintering techniques which rely on high compressibility of powders[102]. However, since FAST is a versatile technique capable of consolidating a range of different feedstock morphologies and sizes to high densities, the influence of powder morphology may be less than compared with a technique such as MIM where packing behaviour is a greater concern[102,134].

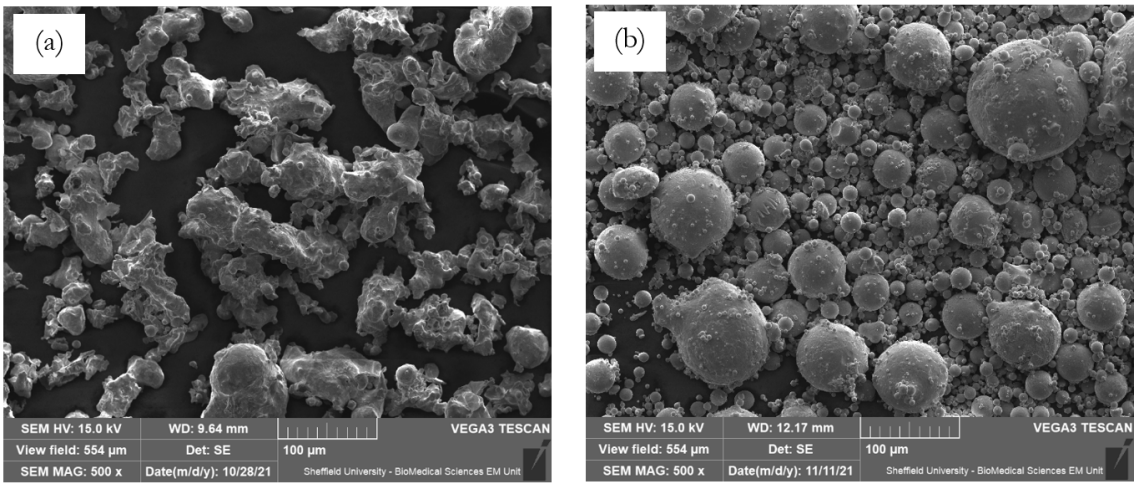

Figure 4.1: Scanning electron micrographs of (a) WA 17-4PH and (b) VIGA 316L stainless steel powder. Owing to the morphological similarities between the WA powders and the need for brevity, further WA powder micrographs are not presented here

4.3 Powder Size Analysis

Relative span (Equation 4.1) is a measure of particle size distribution about the median size[102]. The undoped 316L produced by VIGA has a smaller median particle size but a larger relative span to all other WA samples (Table 4.2). The WA powders are all approximately the same in size meaning that comparisons can be made between them.

$$Relative\ Span = \frac{D_{90} - D_{10}}{D_{50}} \tag{4.1}$$

Table 4.2: Particle size distribution of the 316L and 17-4PH stainless steel powders used in this study

Material	D_{10}(µm)	D_{50}(µm)	D_{90}(µm)	Relative Span
17-4PH (WA)	16.8±0.83	50.5±2.21	113±2.31	2.10
17-4PH with Pd (WA)	12.9±1.08	39.1±2.36	106±3.69	2.37
17-4PH with Ru (WA)	13.8±0.43	40.5±1.46	106±3.17	2.28
316L (WA)	18.3±0.54	51.2±2.34	123±5.93	2.04
316L with Pd (WA)	18.4±0.58	50.2±1.80	119±3.96	2.00
316L with Ru (WA)	15.4±0.34	41.9±1.20	104±3.61	2.11
316L (VIGA)	7.58±0.57	20.9±0.57	73.5±6.53	3.16

4.4 Chapter Findings

The seven stainless steel powders used in this study were characterised. Some discrepancies between the chemical composition of the studied powders and the ASTM standards were observed. It was found that the WA powders were irregular in morphology while the GA powder was spherical in morphology. This finding is in good agreement with the literature.

CHAPTER

5

Results and Discussion: Sample Synthesis and Microstructural, Physical and Elemental Analysis

One of the objectives of this study was to assess the feasibility of using FASTto produce graded cathodically modified stainless steels. To achieve this it was first necessary to determine near-optimal sintering parameters for each of the compositions considered. This chapter presents an investigation of the impact of sintering temperature and times on the properties of the bulk alloyed (i.e. non-FGM) samples. Comparisons are made between the chemical and physical characteristics of the FAST-processed and the cast samples. Also explored here is the influence of atomisation technique on sintered sample characteristics, focusing specifically on the properties evolving from water atomisation and vacuum inert gas atomisation. The final part of this chapter also presents the assessment of the functionally graded PGM-doped stainless steel that was synthesised. The corrosion behaviour of both the bulk alloyed and functionally graded samples is detailed later in Chapter 7.

5.1 Bulk Alloyed Samples

Optimising the sintering parameters is an imperative step in powder metallurgy as it ensures your material will perform satisfactorily. In the current study, different combinations of sintering temperature and time were explored to ascertain near-optimal FAST sintering conditions (Table 3.5). The samples produced were then characterised in terms of their microstructure, elemental distribution and physical properties.

5.1.1 Microstructure and Elemental Mapping

The first set of water atomised (WA) 316L and 17-4PH stainless steel samples was sintered at 1000°C for 600 s. Micrographs of these samples revealed dark and typically

crescent-shaped features (Figure 5.1 (a) and 5.2 (a)). Irregular morphological features such as these are typically attributed to porosity along prior powder particles[62,134,209]. Visible powder boundaries and pores can result from under-sintering, a phenomenon associated with either sintering at too low a temperature or too short a time[210]. During the early stages of sintering, necking between particles should form to ensure good mechanical behaviour of the compacted part and annihilate residual porosity between powder particles[210]. Therefore, in an attempt to reduce the presence of these powder particle boundary features, different sintering temperature and time combinations were used (Table 3.5). The samples produced by expanding the production parameters used are illustrated in Figure 5.1 (b-e) and 5.2 (b-e).

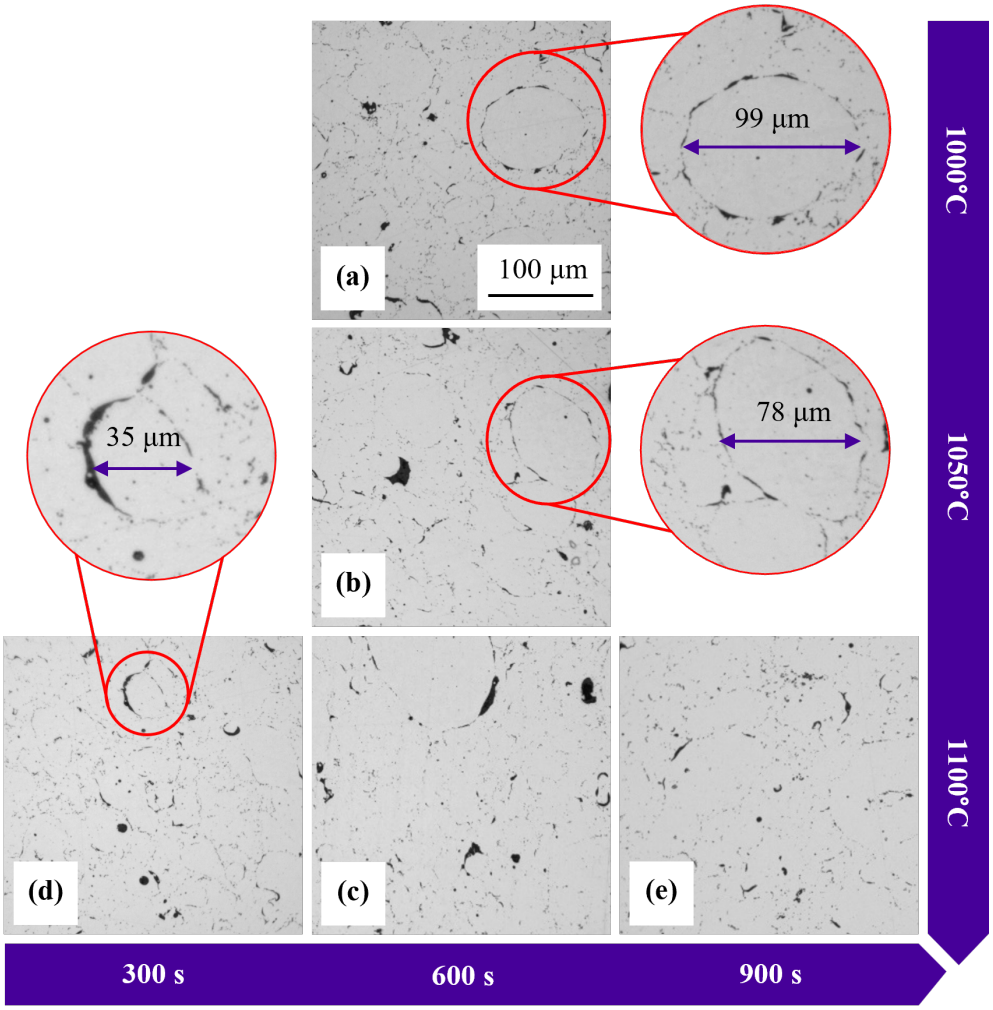

Figure 5.1: Matrix of optical micrographs of unetched WA 316L with Pd sintered at differing temperatures (a-c) and differing sintering times (d-e) (x20). The size of selected prior powder particles are measured

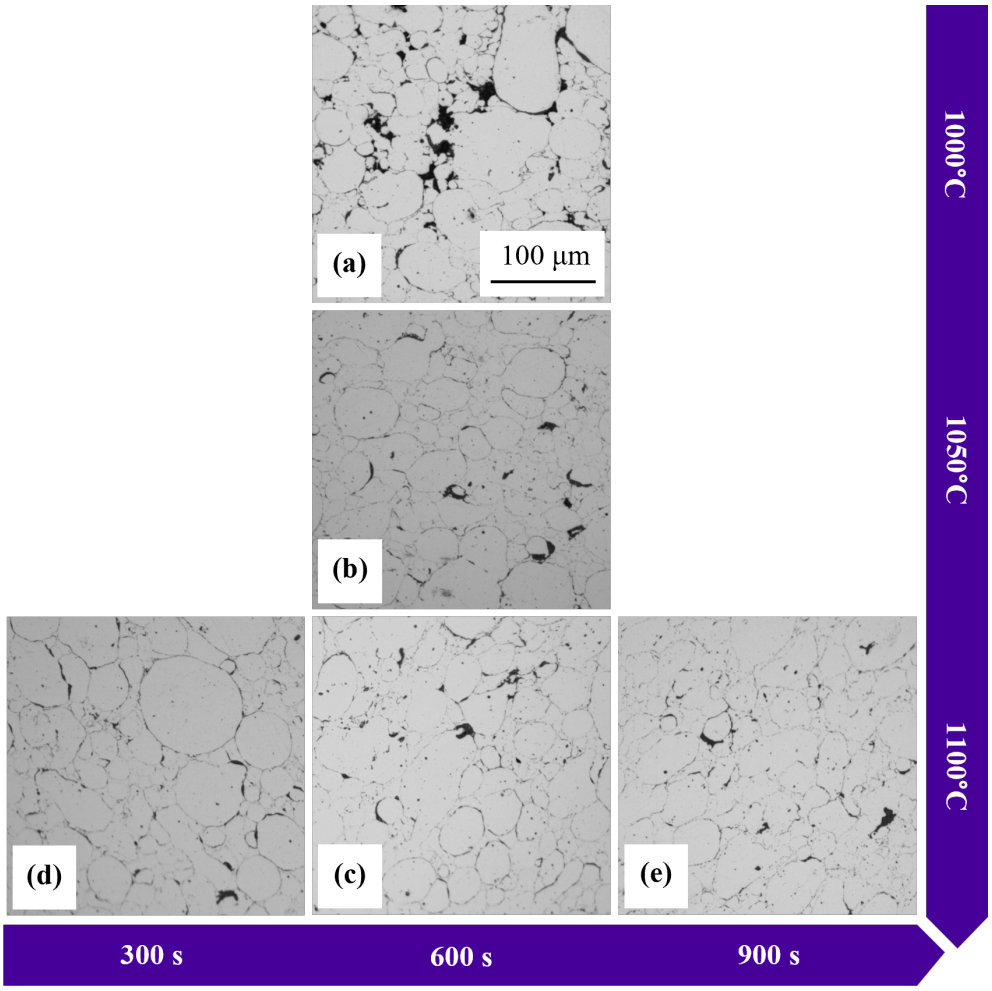

Figure 5.2: Matrix of optical micrographs of unetched WA 17-4PH with Pd sintered at differing temperatures (a-c) and differing sintering times (d-e) (x20)

Increasing the sintering temperature reduced but didn't eliminate the appearance of the dark features at the powder particle boundaries in the 17-4PH samples (Figure 5.2 (b-e)). In contrast, varying the sintering parameters yielded fewer microstructural changes in the 316L samples, with all micrographs exhibiting a similar distribution of powder particle boundary features (Figure 5.1 (b-e)). Further investigation revealed increasing the sintering temperature improved the relative density to near-full density and reduced the porosity of the sintered samples (Figure 5.9). Despite this, the features at the prior particle boundaries were still visible. This suggests that porosity alone does not fully account for the presence of the powder particle boundary features.

The presence of oxide inclusions is an alternative explanation for the dark features seen in Figures 5.1 and 5.2. As explained in Chapter 2, the surface of water atomised powders typically possesses silicon-rich oxides. Kozub et al.[69] state that these oxide compounds can be reduced. This can be achieved in a vacuum by thermal decomposition but this is dependent on sintering temperature and time being adequately high[67,69]. SiO_2 is the most difficult of the surface oxides found in powder processed SS to reduce and can obstruct the formation of necking between particles if not removed[67]. According to the Ellingham diagram (Figure 2.24), silicon oxides thermally decompose at temperatures exceeding those used in this study[141]. As a result, this suggests that any oxide inclusions originating from the atomisation process will remain in the sintered samples studied here.

EDS mapping and laser confocal imaging were used to characterise the chemical composition and morphology of the samples to further investigate the nature of the unknown features in the WA specimens. As Figure 5.3 illustrates, these features were confirmed to be oxides rich in Si, Mn and Cr and topographic mapping gave further support to the conclusion that these features are not wholly pores. Specifically, the topographic analysis indicated that the crescent-shaped particle boundary features exhibited minimal height variation relative to surrounding areas (Figure 5.4). Instead, smaller and rounder features (as shown in Figure 5.4 (ii)) were found to possess greater peak-to-valley height profile which signifies porosity. Therefore, EDS and topographic mapping demonstrated that the irregular features surrounding sintered water atomised powder particles are oxides rich in Si, Mn and Cr rather than pores. The current study shows good agreement to the literature whereby multiple studies have reported the presence of oxide inclusions in atomised stainless steel[62,211–213].

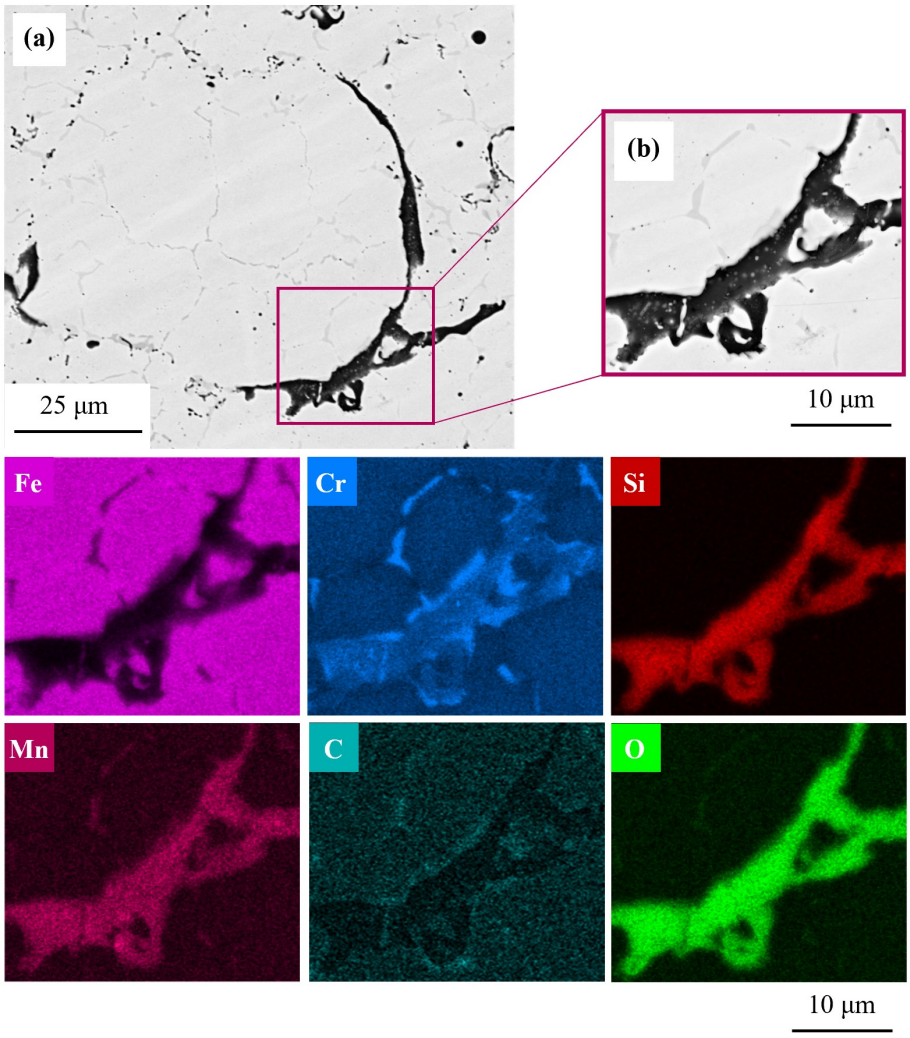

Figure 5.3: Scanning electron micrographs and EDS maps of inclusions surrounding prior powder particles found in WA 316L with Ru sintered at 1100°C for 600 s. Micrograph (a) was taken at x3000 magnification while the inset micrograph (b) and the corresponding EDS maps were captured at x10,000 magnification

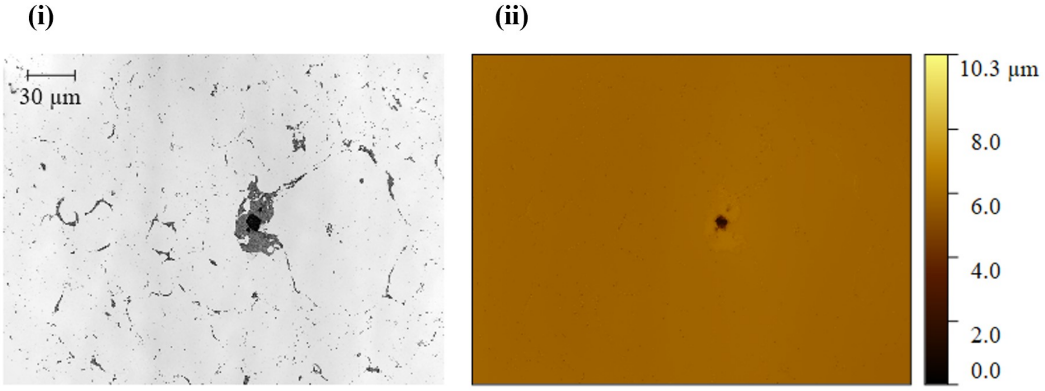

Figure 5.4: Confocal laser micrographs of a pore found in a sample of WA 316L with Ru sintered at 1100°C for 600 s. Micrograph (i) shows the light microscopy image and (ii) shows the topographic map of the same area. Darker hues in the topographic map represent greater depths. Both images were captured at x50 magnification

While the results reported in Figures 5.3 and 5.4 concern 316L stainless steel, the same observations were made for the sintered 17-4PH specimens. EDS mapping was used to confirm that the 17-4PH samples also possessed silicon-rich oxide inclusions at powder particle boundaries (Figure 5.5). This is to be expected as both the 316L and 17-4PH powders examined here are water atomised. The inclusions found in both alloys consisted of O in addition to Si, Mn and Cr, showing good agreement with the work of Yang et al.[213] and Riabov et al.[212].

The chemical composition and thickness of the oxide inclusions on powder particles are of interest to the current study because of the detrimental effect that these oxide inclusions can have on the sinterability of the SS powders in addition to the corrosion resistance[73,74,214]. Similar to the current study, Tunberg and Nyborg[73] and Hedberg et al.[139] found that water atomised stainless steel particles were covered with Mn, Fe, Cr and Si oxides. An area where differences can be found between the current study and earlier findings lay in the oxide thickness. Tunberg and Nyborg[73] and Hedberg et al.[139] determined that the oxide thickness was between 5 to 30 nm. A measurement of the oxide layer in the current study revealed that the oxide inclusions are two to three orders of magnitude larger than those observed by Tunberg and Nyborg[73] and Hedberg et al.[139] (Figure 5.5).

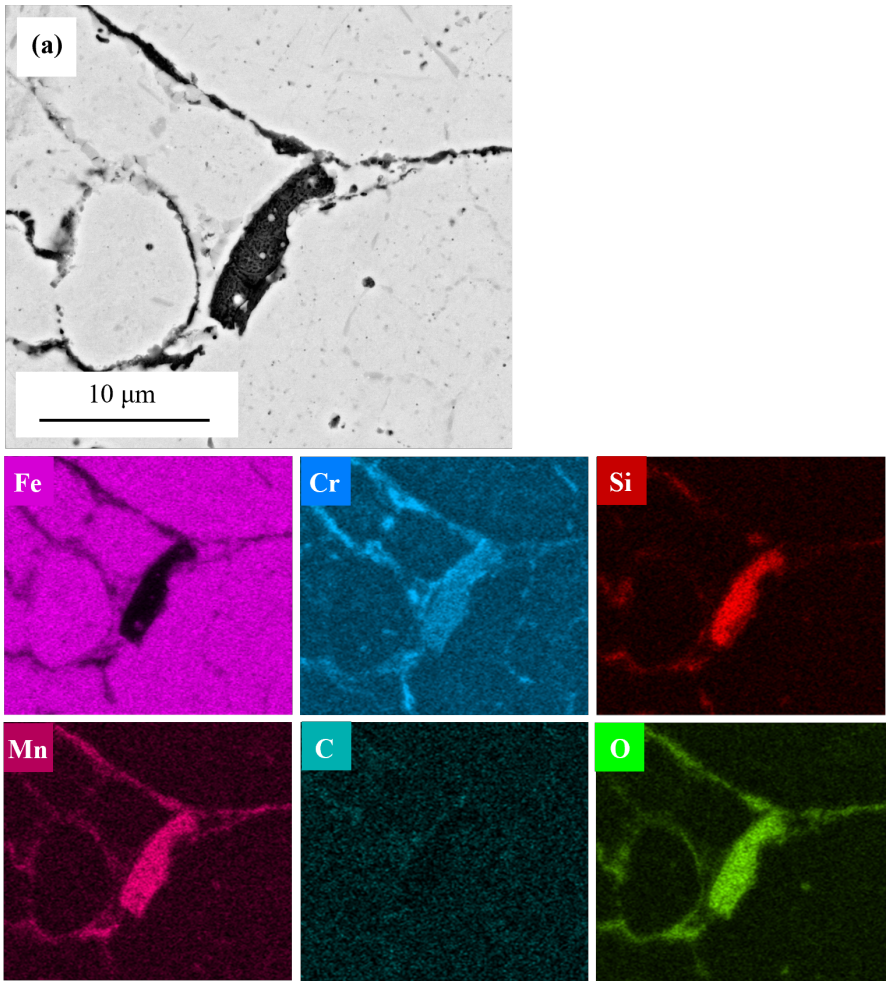

Figure 5.5: Scanning electron micrographs and EDS maps of inclusions surrounding prior powder particles found in WA 17-4PH sintered at 1100°C for 300 s. All micrographs were captured at x10,000 magnification

Several factors affect the thickness and chemical composition of the oxide inclusions on atomised SS powders, these include: particle size, cooling rates, oxygen content of the atomising atmosphere and powder chemical composition[61,73]. Oxide thickness and powder particle size are also linked: smaller particles cool more rapidly therefore less time is available for oxide film formation leading to thinner oxides[73]. Since the powders studied by Tunberg and Nyborg[73] and Hedberg et al.[139] were produced by water atomisation, it is expected that the cooling rates in the current study are of the same order of magnitude. Therefore, variation in the cooling rates is an unlikely explanation for the differences in oxide thickness. A factor more likely to have contributed to the inconsistencies in oxide thickness is the chemical composition. Schade and Dunkley[215] explains that the oxide content of water atomised stainless steel is a function of the arithmetic difference between the Si and Mn content (illustrated in Figure 5.6). Si oxide films are more protective against further oxidation than Mn oxide films are. This suggests a higher content of Si relative to Mn therefore will result in a thinner oxide film. The arithmetic difference of the current study and the work of Tunberg and Nyborg[73] and Hedberg et al.[139] is presented in Table 5.1. A larger arithmetic difference between Si and Mn is exhibited by the stainless steel powders investigated in the current work compared with those reported in previous studies (Table 5.1). The large thickness of the oxides in the current study may therefore be attributed to the relative Si and Mn contents of the stainless steel powders. Another potential cause for the differences in the measured oxide thickness in the current study compared with literature may be owing to the investigative technique utilised. The current study analysed the thickness visually using SEM micrographs while Tunberg and Nyborg[73] and Hedberg et al.[139] used Auger electron spectroscopy. While the experimental approach likely impacted the measured oxide thickness it is probable that the relative Si and Mn content also contributed.

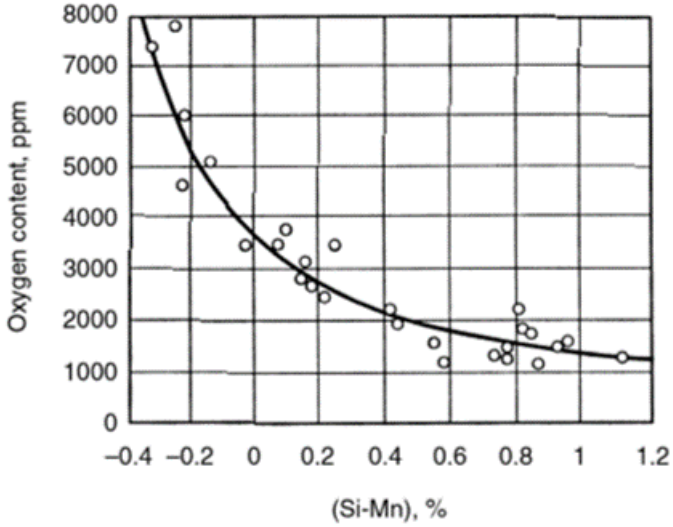

Figure 5.6: Graph showing the effect of Si and Mn content on the O content of 304L stainless steel powders. As the difference between Si and Mn content increases the oxygen pick-up during atomisation decreases. This graph was used with permission of ASM International, from Powder Metallurgy, Atomization; permission conveyed through Copyright Clearance Center, Inc[215]

Table 5.1: Arithmetic difference between Si and Mn contents of the water atomised stainless steels powders used in this study compared with that reported in the literature

Source	Alloy	Si - Mn (wt.%)
Current Study	316L SS	0.22
	316L SS with Ru	0.17
	316L SS with Pd	0.22
Tunberg and Nyborg[73]	304L SS	0.77
	304L SS	0.70
Hedberg et al.[139]	316L SS	0.75

Figure 5.7 presents the microstructure of two representative etched sintered samples. The grains were found to be of same order of magnitude and several grains found to make up a single powder particle. Owing to their similarity, the microstructures of other etched samples is not included here.

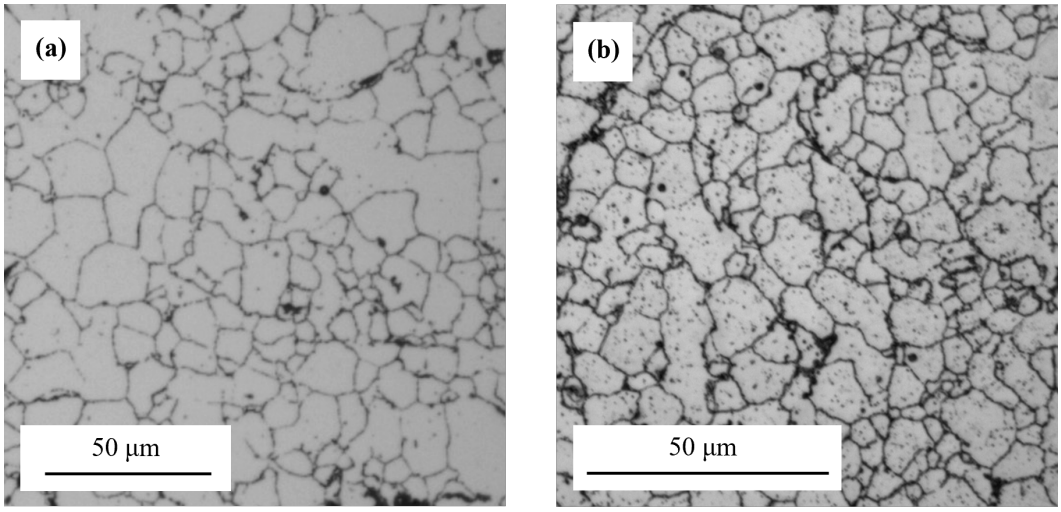

Figure 5.7: Micrographs of sintered (a) Ru-doped 316L (x20 magnification) and (b) Pd-doped 17-4PH demonstrating the microstructural similarities in the two alloys in their as-sintered state. Images were captured at x50 magnification. Both samples were sintered at 1100°C for 600 s and were etched using Kalling's No.1 solution

5.1.2 Density and Grain Size

Density and grain size are important to consider when regarding powder processed stainless steels. Higher densities and smaller grains are typically associated with enhancing corrosion resistance[25,146]. As explained in Section 2.2.3, density and grain size are interconnected characteristics. Consequently, these two material characteristics will be presented and discussed here together.

For the 316L samples, a positive correlation was identified between the density and both sintering temperature and time, as illustrated in Figures 5.8 (a), 5.9 (a-b) and 5.10 (a-b)). Note that a stronger positive correlation exists between sintering temperature and density compared to that between sintering time and density (Figure 5.8 (a)). The grain size and the sintering parameters exhibited a similar trend: a weaker positive correlation was found between sintering time and grain size compared to sintering temperature and grain size. In contrast, the 17-4PH samples exhibited a strong positive correlation

between the sintering parameters and both density and grain size (Figures 5.8 (b), 5.9 (c-d) and 5.10 (c-d)).

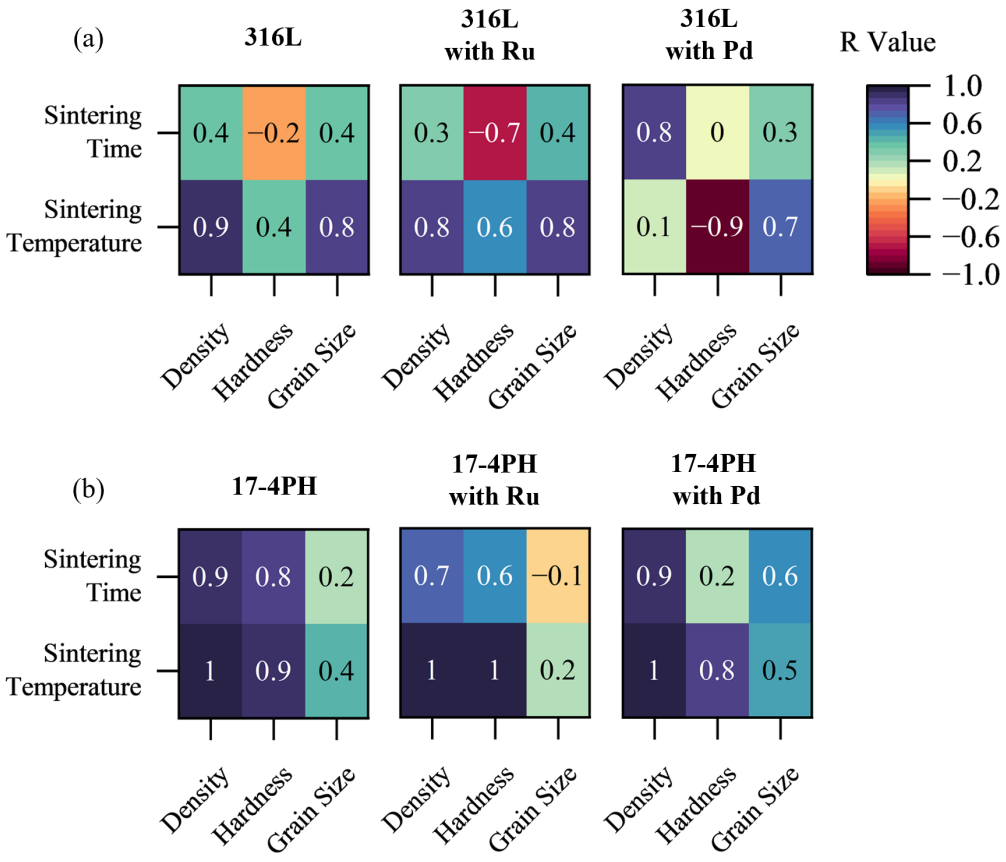

Figure 5.8: Correlation matrix presenting the relationship between sintering temperature and time against the relative density, grain size and hardness for the (a) 316L and (b) 17-4PH samples. A positive R value suggests a positive correlation, the opposite is true for a negative R value. It is worth noting that correlation does not imply causation

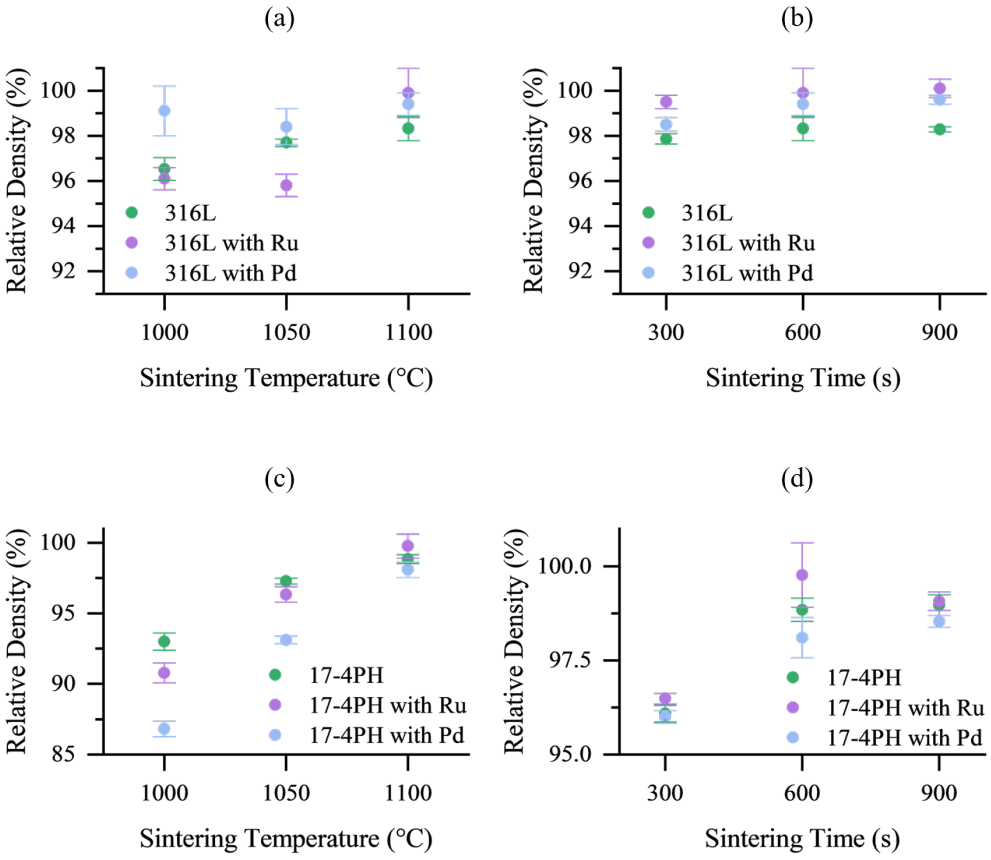

Figure 5.9: Graphs comparing the relative density of sintered WA 316L and 17-4PH stainless steel samples. Graphs (a) and (c) show the effect of varying the sintering temperature while sintering for 600 s. Graphs (b) and (d) illustrate the effects of varying the sintering time on hardness while maintaining the sintering temperature at 1100°C

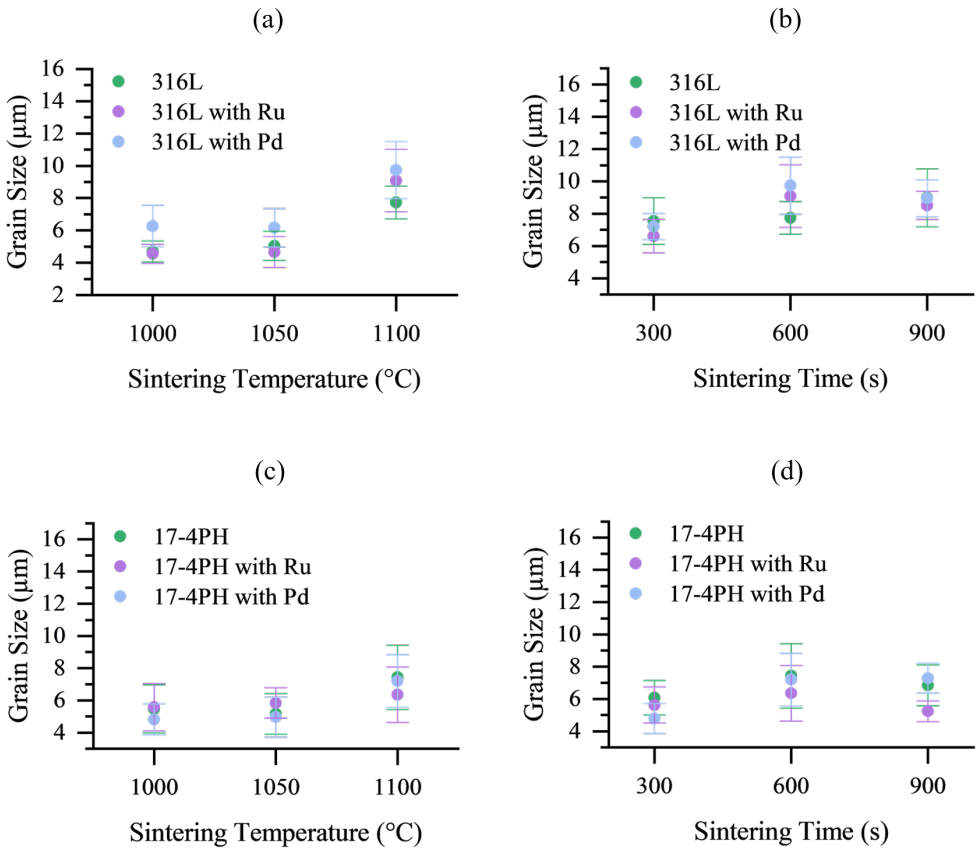

Figure 5.10: Graphs comparing the grain size of sintered WA 316L and 17-4PH stainless steel samples. Graphs (a) and (c) show the effect of varying the sintering temperature while sintering for 600 s. Graphs (b) and (d) illustrate the effects of varying the sintering time on hardness while maintaining the sintering temperature at 1100°C

The data suggest increasing sintering time was less effective at improving 316L sample density than sintering temperature. However, the sintering time variation tests were performed at 1100°C - a temperature at which the samples all had near-full density - therefore, the opportunity for further densification is limited by the nearing of maximum attainable density (Figure 5.9 (b)).

Contrastingly, the 17-4PH samples show an improvement in density with both the increase in sintering temperature and the increase in sintering time (Figure 5.9 (b) and (d)). A reason for the difference in the trends exhibited by the two alloys in this study may be their physical differences. Sintering temperature is proportional to melting temperature[216]. Since 17-4PH has a higher melting temperature than 316L SS[48], it is expected that 17-4PH will have a higher ideal sintering temperature than 316L SS. This may explain why sintering at 1000°C resulted in lower relative densities in the 17-4PH samples compared to the 316L samples (Figure 5.9 (a) and (c)). Meanwhile, at a sintering temperature of 1100°C, both the 316L and 17-4PH stainless steel samples in this study possessed near-full density. Consequently, it could be described that the sintering parameters approached an optimal combination. Given the relatively low sintering temperatures and times examined, along with the high densities achieved, the sintering process can be considered successful and efficient.

It is important to note that while the samples investigated here exhibited relative densities approaching theoretical values, full density was not achieved. One potential reason for this is the presence of trapped gases within pores which can limit full densification[93]. These gases are difficult to remove and can, if the pores with trapped insoluble gas, result in the coarsening of pores if the gas pressure increases. Consequently, the density can decrease while porosity increases[93]. Such findings were reported in the work of Thangamani et al.[217], who found that the pores in sintered parts made from WA powders became trapped and remained as closed pores, limiting the final density of the sintered part. Another possible explanation for the lack of full densification is that the methodology requires further optimising, a process which could involve varying other sintering conditions which were not explored in the current study, such as applied pressure.

The processing times used in FAST are short compared to conventional sintering techniques such as HIP[102]. This feature of FAST limits the opportunities for grain growth, consequently providing a possible explanation for why the grains in this study are

smaller than that typically reported elsewhere using other sintering techniques[218–221]. An additional reason for the small grain size in this study is the silicon-rich oxide inclusions identified in Section 5.1.1. These oxides can inhibit sintering rates by restricting grain coarsening mechanisms[103].

A potential impact of the relatively small grain size exhibited by samples in this study is the improvement of corrosion behaviour. A review by Ralston et al.[146] states that corrosion rates decrease with grain size reduction in materials which exhibit passivity. This phenomenon was attributed to oxide film growth rates positively correlating with grain boundary density. This finding suggests that the small grain size of the samples in this study relative to other powder processed stainless steels could have a positive effect on their corrosion performance.

As shown in Figure 5.10 (a) and (c), the mean grain size of samples sintered at 1100°C was larger than those sintered at 1000°C. This observation agrees with established findings whereby higher sintering temperatures promote grain coarsening[99,222]. Increasing sintering time resulted in a similar trend (Figure 5.10 (b) and (d)). However, note the overlap in the spread of grain size data obtained from the samples produced under different sintering conditions. This suggests that the trends may not be statistically significant.

This study finds sintering at 1100°C for 600 s to be the most optimal parameter combination where maximising sample density and minimising processing time is concerned. While sintering at 1100°C for 900 s yields the highest density for both the 316L and 17-4PH SS samples, the difference in density for samples sintered for 600 s and 900 s is marginal. Since sintering for prolonged time facilitates grain coarsening and can provide opportunities for the formation of unwanted secondary phases, it is desirable to limit hold times to 600 s.

5.1.3 Hardness

Though not a primary focus of this study a rudimentary understanding of the mechanical properties of the samples produced in this study is desirable. Since it is well established that hardness is proportional to strength, hardness testing is explored in the current study to understand the relationship between the processing parameters and mechanical behaviour[223].

Regarding sintered materials, strength increases are associated with the higher densities and lower porosities which are typically achieved by sintering at higher temperatures and for longer times[94,96–99]. The strength, and therefore hardness, of sintered materials is dependent on the densification and grain coarsening mechanisms[94]. Mechanical strength is developed during sintering by the formation of necking at particle contact points which increase in size as sintering proceeds and strengthen the material[93]. However, over-sintering (sintering at higher temperatures and/or for extended time) can lead to excessive grain coarsening or over-burning which can be detrimental to mechanical properties[224]. Stanley and Perrotta[101] report that grain growth occurs in 316 SS at temperatures of 1037.8°C and above. The Hall-Petch relationship, shown in Equation 5.1[225], can be used to describe the influence of grain size on hardness, where H_v is the hardness in a polycrystalline metal, d is grain size, H_{v_0} and k_{Hv} are constants. By Equation 5.1, grain growth will result in a decrease in hardness.

$$H_v = H_{v_0} + k_{H_v} d^{-1/2} \tag{5.1}$$

In the current study, sintering time and hardness exhibited a negative correlation for both undoped 316L and Ru-doped 316L (Figure 5.8 (a)). Meanwhile, for the same two alloys, a positive correlation exists between sintering temperature and hardness. Contrastingly, Pd-doped 316L exhibits the opposite trends. The trends observed in 316L and Ru-doped 316L may be explained by grain coarsening phenomena. Sintering at 1100°C for 600 s resulted in near-full density, sintering the sample for an additional 300 s did not lead to further densification but instead facilitated a slight increase in grain size and therefore a decrease in hardness according to Equation 5.1 (Figures 5.9 and 5.10).

For all 17-4PH samples used in this study, a positive correlation was found between sintering time and temperature and hardness (Figure 5.8 (b)). This is likely due to the density improvements which were achieved by increasing the sintering temperature and time (Figure 5.9). Lower density sintered materials typically have more porosity which can be detrimental to hardness because it reduces the area via which forces are transmitted. By increasing density, porosity is reduced which in turn improves mechanical properties. However, the overlap in the data suggests that the results and any conclusions made from them may not be significant (Figure 5.11 (c-d)).

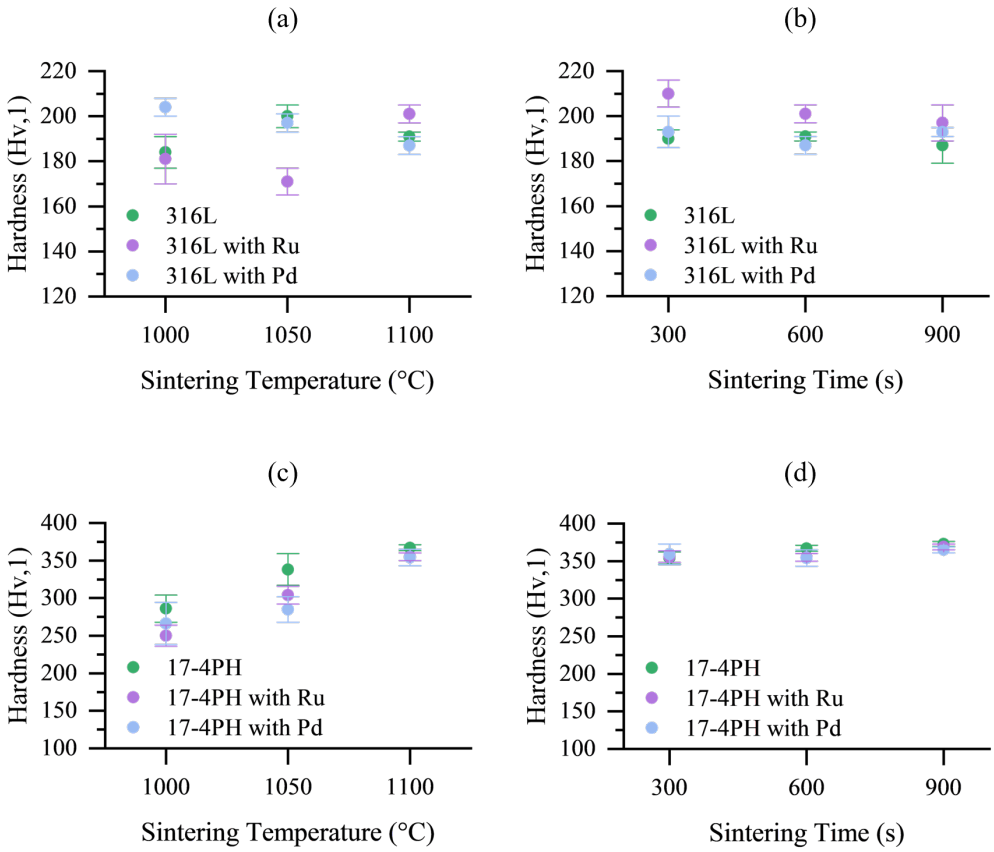

Figure 5.11: Graphs comparing the hardness of sintered WA 316L and 17-4PH stainless steel samples. Graphs (a) and (c) show the effect of varying the sintering temperature while sintering for 600 s. Graphs (b) and (d) illustrate the effects of varying the sintering time on hardness while maintaining the sintering temperature at 1100°C

In this study, the hardness of the sintered 316L samples was found to vary between 184 and 200 Hv which is lower than what ASTM reported for bar 316L: 220 Hv (Figure 5.11). Owing to the porosity inherent to powder metallurgical processing, the mechanical

properties of sintered parts are typically poorer than that of cast equivalents[218,226]. Pores are a microstructural feature often characteristic of sintered parts. Pores can be detrimental to mechanical properties since they limit the effective load-bearing cross-sectional area and introduce stress concentrators to the material[95,227]. Therefore the findings of this study show good agreement with the literature. Typically, the mechanical properties of sintered parts are enhanced by increased sintering temperature due to improved densification and the resulting reduction in porosity[98,99]. However, the conditions which permit densification also facilitate microstructural coarsening mechanisms and so grain growth remains an unavoidable feature of sintering[95].

The hardness of the undoped as-sintered 17-4PH varied between 286 and 373 Hv. These values show good agreement with values reported for powder metallurgy 17-4PH specimens in the literature. Huber et al.[221] sintered AM 17-4PH specimens at temperatures between 1270 and 1360°C for times between 0.5 and 3 hours, they achieved hardness measurements between 275 and 350 Hv. Irrinki et al.[228] also reported similar hardness values to the current study, with values ranging from 258 to 332 Hv for the different build conditions in as-built LPBF 17-4PH specimens. Suri et al.[229] sintered 17-4PH by the cold isostatic pressing technique and found that the as-sintered samples possessed a hardness of 262 Hv, again a value which shows good agreement to the observations made in the current study. In another study, Pandya et al.[226] sintered 316L stainless steel at between 1200 and 1400°C and measured a maximum hardness of 126 Hv, which is substantially lower than that measured in this study. However, this is likely due to the relative densities achieved by Pandya et al.[226] (83 - 90%) which is lower than that found in the current study, which ranged between 96.5 - 98.3%. These findings highlight the efficiency by which FAST can achieve comparable hardness to other powder metallurgy techniques. The maximum processing time used in this study, including heating and cooling, was around 1 hour, which is substantially shorter than the processing times used by Huber et al.[221] and Suri et al.[229] to achieve similar hardness values, 5 - 7.5 hours and 10 hours respectively.

With regard to the effect of the PGM additions on hardness, it is known that doping with small amounts of elements can lead to an enhancement of mechanical properties by solid solution strengthening. Solid solution strengthening enhances mechanical performance of metals by impeding the motion of dislocations in the material[138]. Solution strengthening can be substitutional or interstitial in its nature. Given the relative size of Fe, Ru

and Pd atoms, Ru and Pd atoms will be present within the stainless steel crystal lattice as substitutional solutes. The mechanism of solid solution strengthening is dependent on the size of the solute atoms and their concentration within the parent metal matrix[1]. In stainless steel, the larger the solute atom relative to Fe atoms the greater the strengthening effect[138]. Few studies explore the effect of PGM doping on stainless steel mechanical properties however those that do found that it does not have a significant impact. For example, Lekala et al.[196] found that laser alloying Ru to 316L substrates increased the hardness by 40 Hv compared to the unmodified substrate. However, this change was partly attributed to the laser alloying process, a technique which causes microstructural refinement that improves hardness via the Hall-Petch mechanism (Equation 5.1)[196,230]. This finding was confirmed by van der Merwe and Nelwalani[180], who investigated the hardness of 304L stainless steel which had been laser surface alloyed with Ru at varying laser parameters. Their study found that the hardness was influenced by the laser parameters and not dependent on Ru presence nor increasing Ru content. This was established by comparing the hardness of the substrate when modified with undoped and doped powders of varying Ru contents.

In the current study, no clear trend emerged from the PGM doping of the stainless steels. With only two Ru-doped and one Pd-doped sample showing a small increase in the hardness relative to the undoped sample. For all other samples the presence of the PGMs either had no statistically significant effect or had a detrimental affect on the hardness. These results are not surprising as the PGM additions are not expected to have a positive hardening effect on the alloys in this study. Given the location of Ru and Pd relative to Fe in the periodic table, their atomic sizes are similar. Additionally, the amounts of Ru and Pd added to the 316L and 17-4PH stainless steels explored in this study are small. These factors combined mean PGM presence will not have a strong solid solution strengthening effect on the alloys studied here.

5.1.4 Pore Analysis

Pores are an inherent feature of PM parts and their complete removal is typically not attainable. As a result, though the samples in this study were of near-full density, some porosity remained (Figures 5.12 and 5.13). Pores can remain in powder processed parts because gases can become trapped and pressurised in pores during densification preventing further sintering from occurring[95].

A comparison of the 316L and 17-4PH samples revealed differences in geometry of pores when sintered under the same conditions (Figures 5.12 and 5.13). The pores in the 17-4PH samples were of greater irregularity, size and depth than those in the 316L sample. Insufficient sintering (sintering for too short a time and/or at too low a temperature) can produce specimens in possession of sharp, angular pores[103]. Porosity is expected to decrease during sintering due to the elimination of pores via grain boundary and volume diffusion[134]. Simultaneously, pore size may increase due to the low pressure in the sintering chamber causing trapped air in the closed pores to expand and due to Ostwald ripening causing growth of pores within grains[96,134,231]. The presence of silicon-rich oxides can also impact sinterability causing the remnants of residual porosity[95]. Additionally, these inclusions can affect pore morphology in a negative way since they can inhibit sinter bonds and prevent pore rounding[103]. This may offer an explanation for the presence of the residual angular porosity in the WA samples.

Mean pore size has been found by Verlee et al.[97] to be dependent on mean particle size since smaller particles can be packed closer together. Verlee et al.[97] describes that the primary driving force during sintering is surface energy and since driving force is higher for smaller particles, they will achieve higher densification more easily than coarse particles. However, the D_{50} particle size of the 316L and 17-4PH stainless steel powders used in this study are broadly similar (Tables 3.1 and 3.3). Therefore, particle size is an unlikely factor contributing to the differences in pore size and depth observed in the 316L and 17-4PH stainless steel samples.

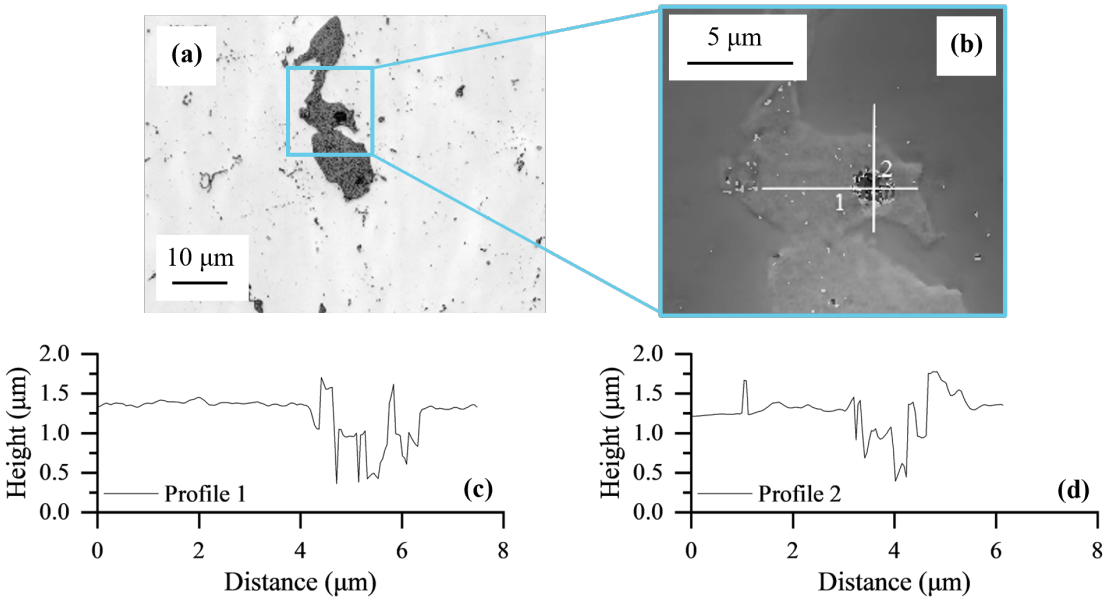

Figure 5.12: Confocal laser micrographs of a pore observed in a sample of WA 316L with Pd sintered at 1000°C for 600 s. Micrograph (a) shows the light microscopy image and the inset image (b) shows a close up topographic map of the highlighted pore. Darker hues in the topographic map represent greater depths. Line graphs (c) and (d) show the corresponding height profiles for Lines 1 and 2 depicted in image (b). Both micrographs were captured at x150 magnification

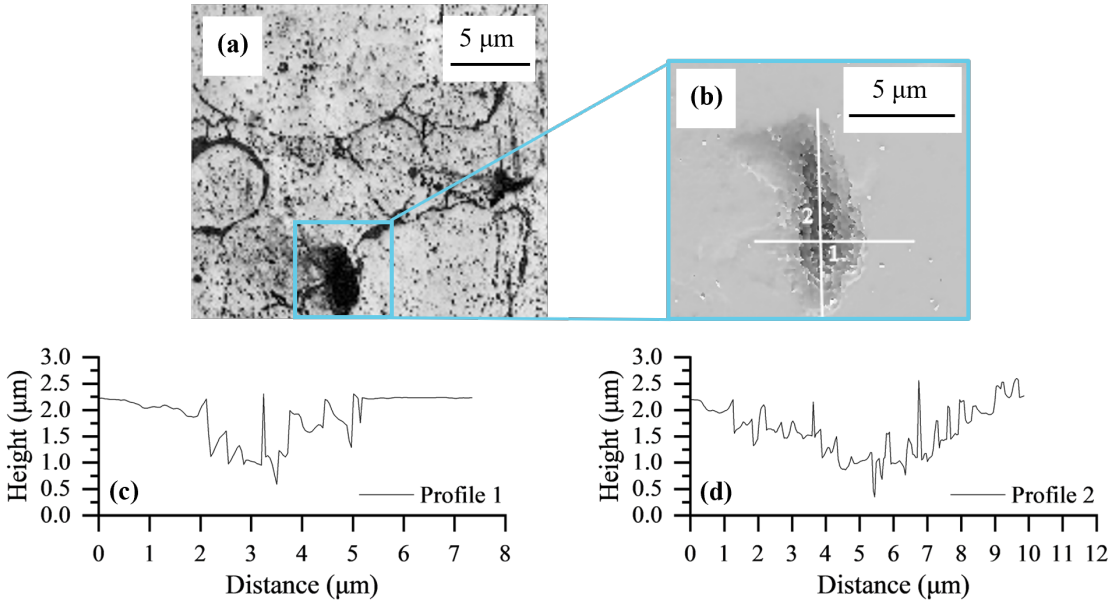

Figure 5.13: Confocal laser micrographs of WA 17-4PH sintered at 1000°C for 600 s. Micrograph (a) shows the light microscopy image and the inset image (b) shows a close up topographic map of the highlighted pore. Darker hues in the topographic map represent greater depths. Line graphs (c) and (d) show the corresponding height profiles for Lines 1 and 2 depicted in image (b). Both micrographs were captured at x150 magnification

5.1.5 Summary

It was concluded that sintering the 316L and 17-4PH samples at 1100°C for 600 s produced near-optimal properties. Shorter hold times are preferred to reduce processing time and grain growth opportunities[99,232]. Additionally, minimising hold time reduces the likelihood of the reactions between the powder and die and the formation of unwanted phases[28]. In this study, increasing hold time had a less dramatic effect on relative density and hardness than increasing sintering temperature (Figures 5.9 and 5.11). Ji et al.[219] reported similar findings: small increases in sintering temperature resulted in significant increases in the part density with the effect of time being significantly smaller. Both increasing sintering temperature and increasing hold time had a more pronounced effect on the relative density of 17-4PH samples compared with 316L samples. Increasing hold time had no significant effect on the hardness of 316L samples and improves the hardness of 17-4PH samples by a small degree. This may be because, for the investigation into the effect of hold time, the sintering temperature was maintained at 1100°C, a temperature at which even at 300 s hold time, relative densities above 96% were achieved for all samples. The extent by which the relative density, and therefore the hardness, could be improved by increased hold time was therefore limited.

5.1.6 Effect of Metal Processing Technique on Microstructure, Physical Properties and Elemental Distribution

This section compares the properties of the cast Ru- and Pd-doped 316L stainless steels to their sintered equivalents evaluating the effect of processing route on microstructure, density and hardness.

Microstructure and Elemental Mapping

Figure 5.14 shows the microstructure of the etched cast Ru-doped sample. Due to its similarity to the Ru-doped sample, micrographs of the Pd-doped sample are not presented here. The cast samples possess coarse grains with a columnar dendritic structure. This is in contrast to the sintered samples which possess an entirely equiaxed microstructure (Figure 5.7). The grains found within the cast samples are also more coarse than those in the sintered samples. The difference in the microstructures is likely owing to the difference in cooling rates. Fast cooling rates are known to result in more refined microstructures because they restrict the amount of grain coarsening which can occur[233]. In cast metallurgical processing cooling can proceed at rates of 0.5 Ks^{-1} while the cooling rates associated FAST processing can be around 1.3 Ks^{-1} [234]. The fine grain structures in the sintered samples relative to the cast samples is because of the faster cooling rates associated with FAST. In their studies, Mesquita and Barbosa[235] and Bartolomeu et al.[236] also observed finer microstructures in PM steel compared with cast. Cast metals commonly possess dendritic microstructures since the anisotropic surface energy facilitates dendritic growth in certain directions[237].

Figures 5.15 - 5.18 present the elemental distribution of the FAST processed and cast PGM-doped 316L stainless steel samples. These figures confirm the PGMs are homogeneously distributed in both the FAST processed and cast samples. The homogeneous distribution of PGMs is desirable in this study. This is because one of the ways in which cathodic modification leads to the enhancement of corrosion performance is through the noble alloying additions blocking anodic sites in the crystal lattice, reducing rates of anodic dissolution[238]. The other way in which cathodic modification can contribute to lower corrosion rates is by the modifying elements acting as a catalyst for the hydrogen evolution reaction, which shifts the corrosion potential into the passive region[9]. The literature suggests that a non-uniform distribution of PGMs in the SS matrix leads to electrochemical inhomogeneities and can contribute to worsened corrosion performance.

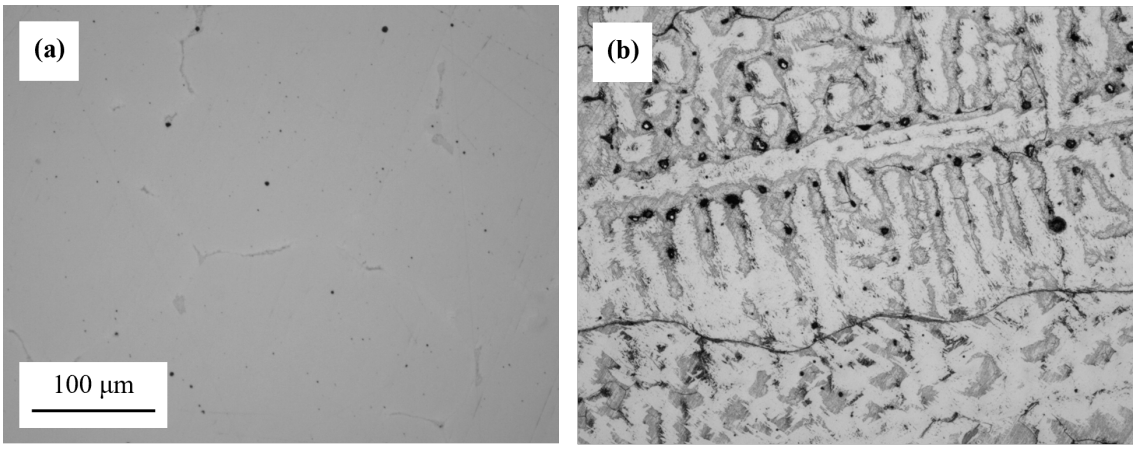

Figure 5.14: Optical micrographs of (a) unetched and (b) etched cast Ru-doped 316L (x20 magnification). The sample was etched using Kalling's No.1 solution. Etching revealed a dendritic microstructure

For example, when Peled and Itzhak [23] alloyed 316 SS with 1 wt.% Ag the Ag was present as inclusions in the austenitic matrix. Corrosion testing revealed the cathodic activity of the inclusions in this sample led to the breakdown of the passive film. Meanwhile, they found that when alloying with 2 wt.% Pt a solid solution was formed with the austenitic matrix and the resulting sample was passive for the duration of the immersion tests. Lekala et al. [196] observed that 316L SS laser alloyed with 5.6 wt.% Ru resulted in the dissolution and homogeneous distribution of Ru, enhancing corrosion behaviour. Contrastingly, it was found that undissolved Ru particles attributed to the poor corrosion performance of 9.6 wt.% Ru laser surface alloyed 316L SS. By taking into account the literature, the achievement of even distribution of PGMs in both the FAST and cast samples in this study bode well for their corrosion performance.

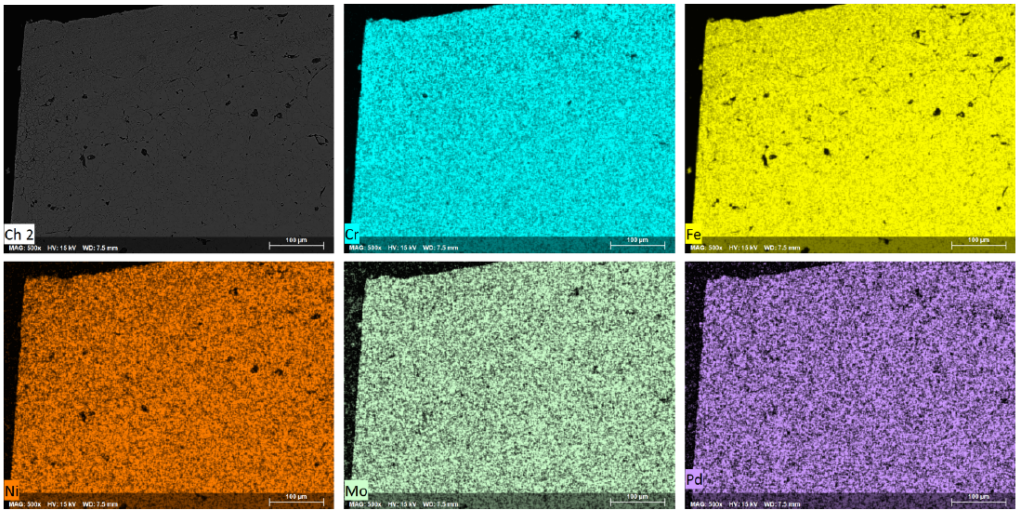

Figure 5.15: EDS map of Pd-doped 316L stainless steel sintered at 1000°C for 600 s showing the distribution of selected primary alloying elements alongside the PGM dopant (x500 magnification)

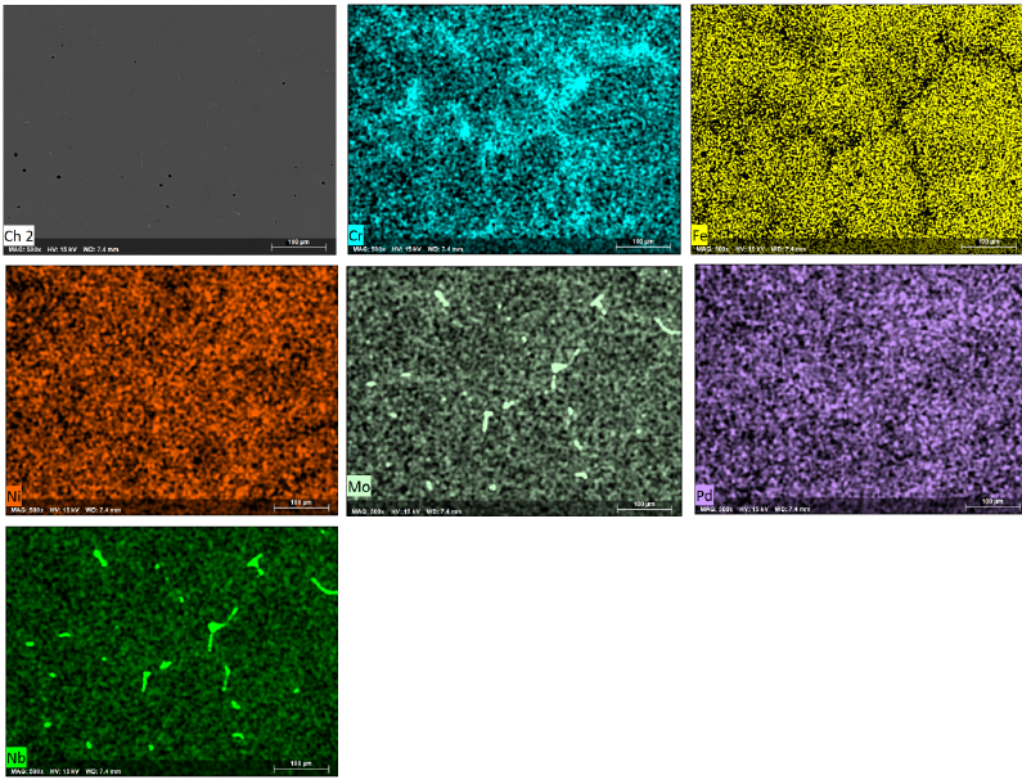

Figure 5.16: EDS map of cast Pd-doped 316L stainless steel showing the distribution of selected primary alloying elements alongside the PGM dopant (x500 magnification)

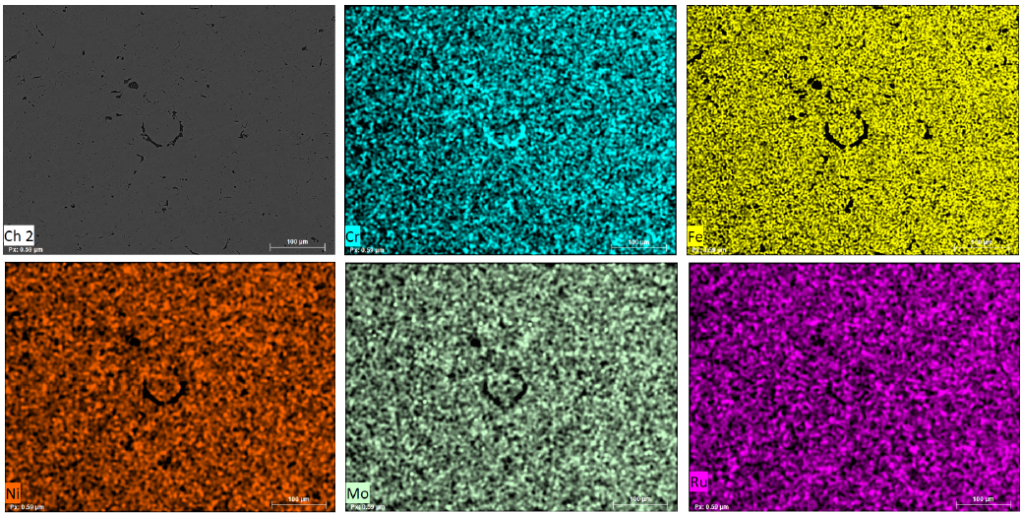

Figure 5.17: EDS map of Ru-doped 316L stainless steel sintered at 1000°C for 600 s showing the distribution of selected primary alloying elements alongside the PGM dopant (x500 magnification)

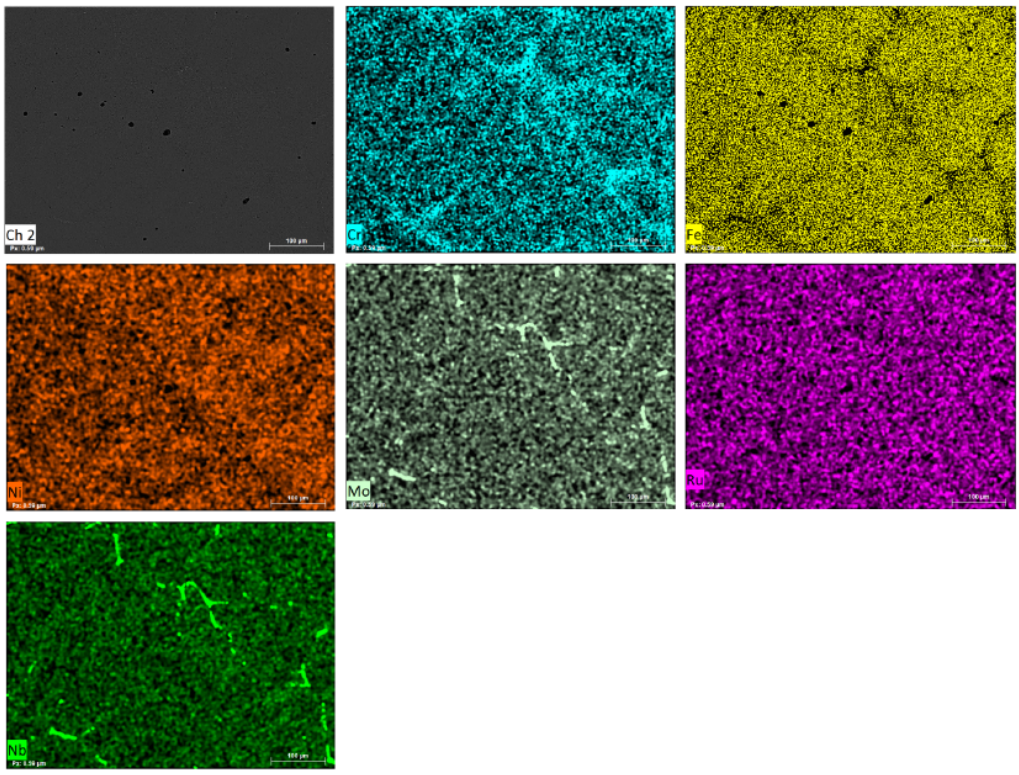

Figure 5.18: EDS map of cast Ru-doped 316L stainless steel showing the distribution of selected primary alloying elements alongside the PGM dopant (x500 magnification)

Other elements exhibited some inhomogeneity. The cast samples showed a greater degree of enrichment of elements, for example, with regions enriched in Nb, Mo and Cr observed (Figures 5.16 and 5.18). Nb is a strong carbide-forming element present in 316L for stabilisation purposes[1]. This means it will preferentially form, minimising the chance of Cr depletion by the formation of $M_{23}C_6$ precipitates which can lead to intergranular corrosion[1]. As a result, the presence of the Nb-rich regions in the cast samples in this study is likely not a cause for concern.

Figures 5.15 and 5.17 illustrate that Mo is evenly distributed throughout the sintered samples. Contrastingly, their cast equivalents (Figures 5.16 and 5.18) present areas enriched in Mo. This observation may be due to the atomisation process finely dispersing any formed precipitates resulting in the homogeneous distribution of alloying elements. Mo is present in stainless steels to improve resistance to pitting corrosion by increasing the stability of the passive film, reducing the number of point defects in the passive film and limiting pit growth rates[239]. Mo will readily react to form undesirable carbides[1,7]. Therefore, the formation of Mo-rich regions in these samples may lead to inhomogeneous pitting resistance across the exposed surface of the SS, leaving some regions more susceptible to this corrosion phenomenon. The distribution of Mo in the cast samples suggest that its pitting resistance may be detrimentally affected.

Hardness

The mean hardness for the Ru- and Pd-doped cast samples was 222±10 Hv and 223±7 Hv, respectively (Figure 5.19). For the sintered samples, which were produced at a range of sintering temperature and times, the obtained mean hardness was 187 - 204 Hv for the Ru-doped samples and 171 - 210 Hv for the Pd-doped samples. A comparison of the hardness of the highest hardness sintered samples and their cast equivalents revealed a difference of 6% and 9% for the Ru-doped and Pd-doped samples, respectively. The mean hardness of PGM-doped 316L cast samples explored here is slightly higher than the values reported by Bartolomeu et al.[236] and Sun et al.[240], which was 165 and 185 HV respectively, in undoped cast 316L. It was ascertained in the literature review (Section 2) that PGMs will not impact the hardness of the sample through solid solution strengthening. Therefore, the differences between the hardness observed here and that reported in the literature are due to reasons other than the PGM content. This study does however show good agreement with the ASTM standards, which report a hardness of 220 Hv for conventionally processed 316L stainless steel[206]. Many differences can arise

during the casting process which may affect the hardness, these include the presence of residual porosity, microsegregation or the formation of coarser grains due to slower cooling rates[237]. These factors provide a potential explanation for the range of different values of the hardness of cast 316L stainless steel reported in the literature.

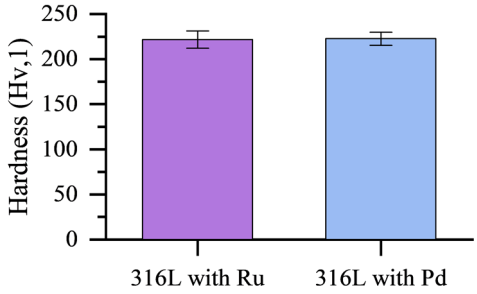

Figure 5.19: Bar graph comparing the hardness values of the two PGM-doped 316L stainless steel cast samples

The variation in the hardness was small for both the cast and the sintered samples. Homogeneous mechanical properties in the samples suggest the microstructure of both the sintered and cast Ru-doped and Pd-doped 316L samples are uniform.

In terms of the absolute values, the hardness of the cast samples was higher than the sintered samples. While enhanced hardness is associated with lower grain size, as given by the Hall-Petch equation (Equation 5.1), the opposite trend is observed here: the more coarsely grained cast samples have hardness values which exceed that of the more finely grained sintered counterparts. Porosity, rather than grain size, is a more probable cause of the difference in the hardness values of the cast and PM specimens in this study. Sintered samples are often reported to have lower hardness than their conventionally produced counterparts[62,220,226,229]. Additionally, studies show that with decreasing porosity sintered samples have higher hardness[220,226]. Such findings suggest the presence of porosity, though comparatively minimal in the current study (since relative densities were >86%), may be responsible for the differences in the hardness of the sintered and cast samples.

5.1.7 Effect of Atomisation Route on Microstructure, Physical Properties and Elemental Distribution

Vacuum inert gas atomisation (VIGA) and water atomisation (WA) are two techniques commonly used to produce metal powders. They differ primarily in terms of the atomisation fluid used and atomisation atmosphere. These differences lead to variations in powder morphology, size and chemistry, which in turn impact how the powder behaves in subsequent processing.

Often, the choice of atomisation technique is dictated by specific application requirements. For example, within the aerospace sector, where stringent oxygen limits are specified, VIGA atomisation is preferred due to its ability to produce low oxygen content powders[86]. In comparison to VIGA powders, WA powders have higher oxygen contents but are considerably lower in cost and so where their use is feasible, they are preferred[84]. FAST is a versatile powder processing technique capable of successfully consolidating a range of metallic feedstock types, including VIGA and WA powders[102]. The current study assesses whether FAST can produce samples using powders produced by the cheaper WA approach which possess comparative characteristics to those produced from the more expensive VIGA powders. Specifically, how the atomisation route impacts the microstructure and physical properties of the sintered compacts will be studied.

Microstructure and Elemental Mapping

Silicon oxide inclusions are detrimental to the corrosion performance of stainless steels as they have a negative effect on the passive film stability[60,103]. As explained in Chapter 2, the silicon-rich oxides on the surfaces of water atomised powders are typically absent from gas atomised powder. Silicon oxide inclusions form during water atomisation due to silicon being a strong oxidiser. Silicon has a greater propensity to oxidise during water atomisation when compared to VIGA because of the availability of greater oxygen in the system. The crescent-shaped features found in sintered WA stainless steel samples which were proven to be silicon-rich oxides in the previous section are present in a different form in the VIGA samples (Figure 5.20 (a)). The inclusions in the gas atomised samples have a smaller particle size (around 1 µm) than that found in the WA samples (Figures 5.20 and 5.21).

Similar to the current study, Riabov et al.[212] and Lindstedt and Karlsson[70] found that VIGA powders possessed a lower degree of particle surface coverage by oxide compounds compared with WA powders. This observation is attributed to the lower amount of oxygen available during the atomisation process to facilitate oxidation. In terms of the composition of the inclusions, the WA samples possessed oxide inclusions which were rich in Si, Cr and Mn. Meanwhile, the oxide inclusions found in the VIGA samples were not enriched in Cr and Mn but instead were primarily Si-rich oxides. This is despite the Si contents of the two powders being similar and the VIGA powder containing almost three times as much Mn (Table 3.1). The oxides found in the VIGA powder consisted of primarily Si-rich oxides likely because Si, being an element with a high affinity for oxygen, will preferentially oxidise in the low O_2 vacuum environment[212].

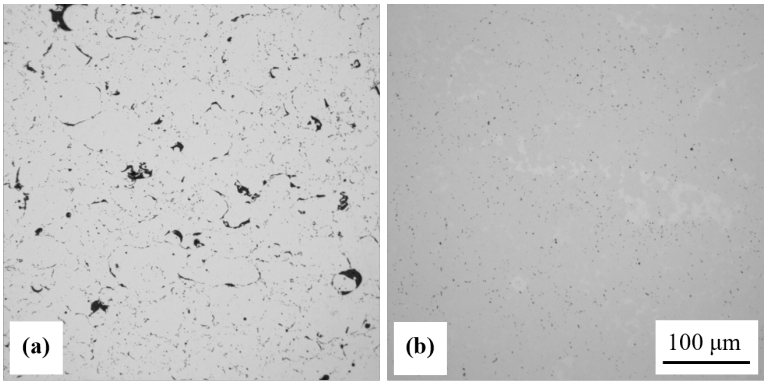

Figure 5.20: Optical micrographs showing the microstructure of consolidated (a) water atomised and (b) vacuum inert gas atomised 316L stainless steel. Both samples were sintered at 1100°C for 600 s. Prior powder particle boundaries can be observed in (a) but cannot in (b). A finer distribution of inclusions is found in (b) compared with (a)

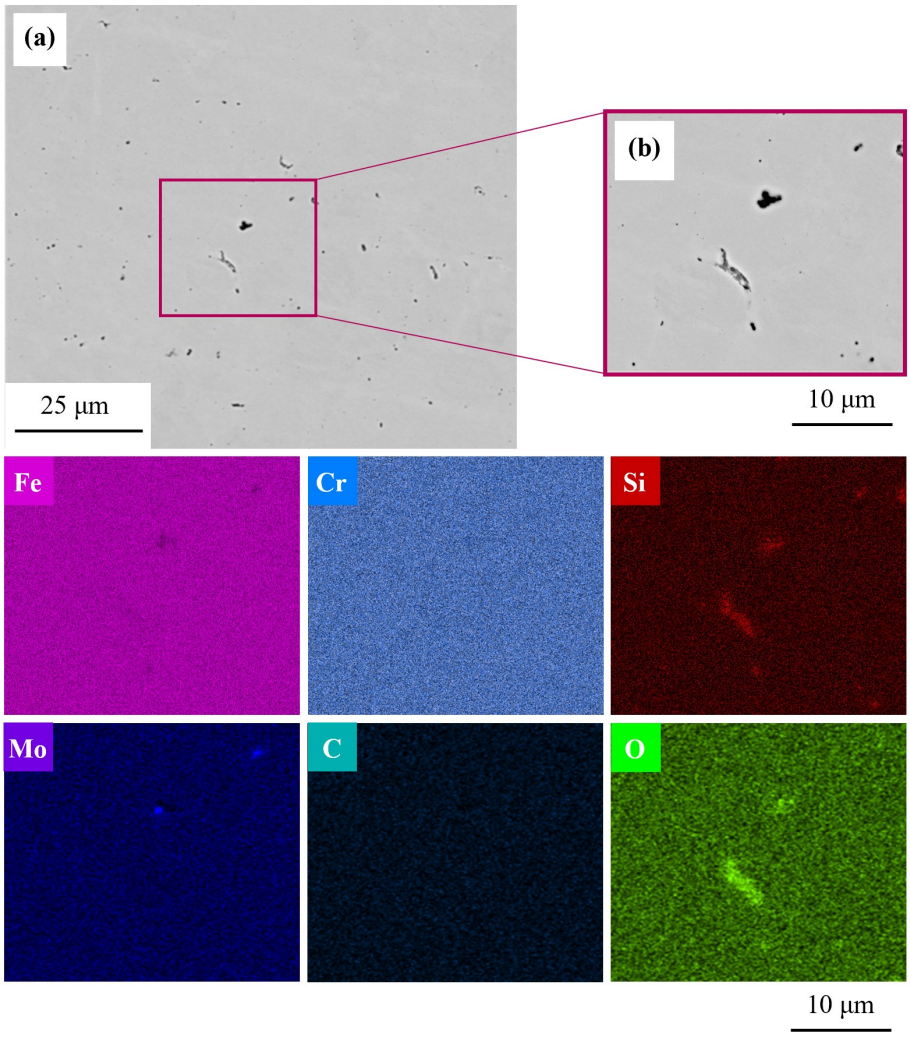

Figure 5.21: Scanning electron micrographs and EDS maps of inclusions observed in VIGA 316L stainless steel sintered at 1100°C for 300 s. Micrograph (a) was taken at x3000 magnification while the inset micrograph (b) and the corresponding EDS maps were captured at x10,000 magnification

Density and Grain Size

As Figure 5.22 demonstrates, the relationship between density, hardness and grain size and the varied sintering parameters showed alike trends for both the WA and VIGA samples. The close resemblance in the trends suggest that parameter variation has similar effects on the sintering behaviour of both powders. The main differences in the trends emerge concerning hardness. While the WA samples show a positive correlation between sintering temperature and hardness and a negative correlation between sintering time and hardness, the opposite relationship is exhibited by the VIGA samples.

Figure 5.23 compares the relative density of undoped VIGA and WA 316L powders sintered at varying temperatures (a) for varying times (b). Both the gas and water atomised samples in this study were sintered to near-full density at temperatures of 1100°C. However, at the lower sintering temperature of 1000°C, the GA sample achieved higher relative density. Increasing the sintering temperature to 1100°C eliminated the density disparity between the two sample sets. At this temperature, relative densities of $\sim$ 98.5% were achieved.

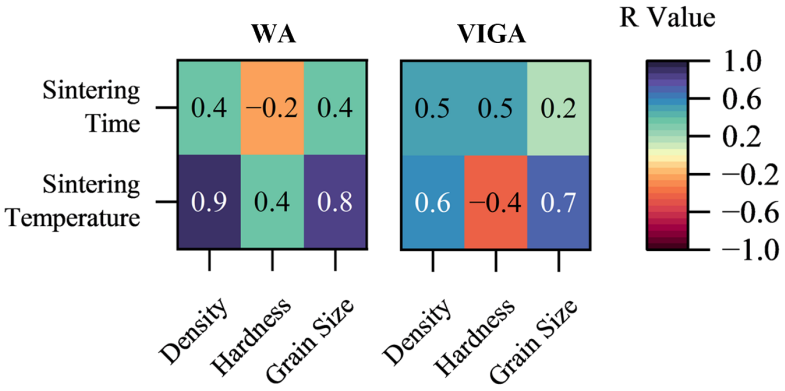

Figure 5.22: Correlation matrix presenting the relationship between sintering temperature and time against the relative density, grain size and hardness for the (a) WA and (b) VIGA 316L stainless steel samples

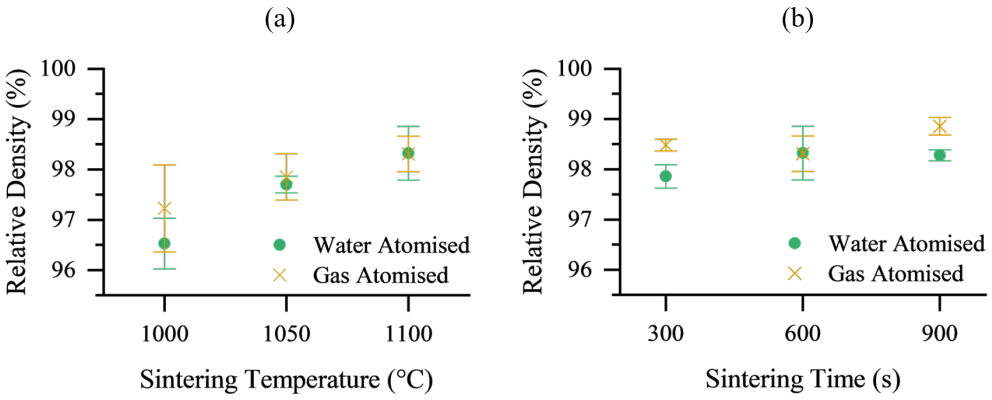

Figure 5.23: Graphs comparing the relative density of sintered WA and GA 316L stainless steel samples produced under varied sintering conditions. The effect of varying sintering temperature while maintaining a sintering time of 600 s is shown in (a). Graph (b) shows the effect of varying the sintering time while keeping sintering at a temperature of 1100°C

Regarding grain size, for all sintering temperature and time combinations explored in this study, the GA samples possessed higher mean grain size than the WA equivalents. The primary driving force for grain growth is the interfacial surface energy[95]. Smaller particles will have a higher total surface energy for a given volume than larger particles[97]. This means that grain growth mechanisms will be more efficient where smaller particles are concerned. The VIGA 316L powder used in this study has smaller particle size than the WA equivalent (Table 4.2). The disparity in the grain size may therefore be due to the difference in the powder size of the two feedstocks.

Grain growth mechanisms are also influenced by powder morphology. The VIGA powder used has spherical morphology (Figure 4.1). Such particles typically have higher packing efficiency and, therefore, more particle-particle contacts per unit volume than more irregular particles, such as those produced by WA[87]. Additionally, smaller particles have more particle-particle contacts per unit volume than larger particles[88]. Particle-particle contacts are where sinter bonds are formed and these features can then form grain boundaries. These contacts are required for sintering to proceed. Therefore, more particle-particle bonds mean sintering can proceed with greater efficiency. Consequently, grain growth may occur at higher rates in the VIGA powder used in this study, thus explaining why grains were larger in the VIGA samples.

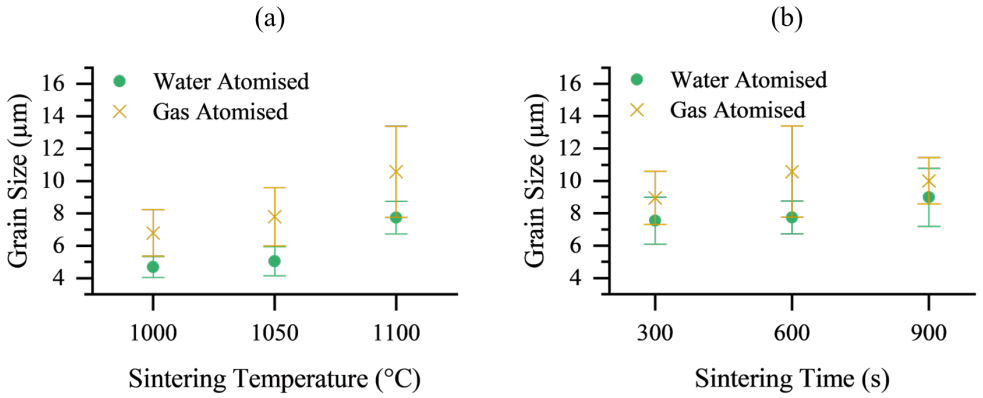

Figure 5.24: Graphs comparing the grain size of sintered WA and GA 316L stainless steel samples produced under varied sintering conditions. The effect of varying sintering temperature while maintaining a sintering time of 600 s is shown in (a). Graph (b) shows the effect of varying the sintering time while keeping sintering at a temperature of 1100°C

As observed in Figures 5.3 and 5.21, the VIGA samples exhibit a lower concentration of silicon oxides compared with the WA samples. Grain coarsening and densification mechanisms can be restricted due to the presence of silicon oxides as they can can prevent the bond formation required for necking[103]. The lower Si-oxide content of the VIGA samples provide another explanation for their larger grains and why sintering at 1000°C yields higher relative densities.

Hardness

The samples produced from the VIGA powders had between 18 - 26% lower hardness than those produced from the WA powders. The relatively low hardness of the VIGA 316L samples may be due to its slightly wider particle size distribution (Table 4.2). Ma and Lim[89] investigated the influence of particle size distribution of submicron alumina on sintering behaviour. During the intermediate stages of sintering, compacts formed from broad particle size distributions demonstrated enhanced grain growth but reduced densification rates compared with compacts formed from narrow particle size distributions. As suggested by Equation 5.1, enhanced grain growth will lead to a reduction in hardness.

Powder morphology may also be playing a role in the low hardness of the VIGA 316L sample when compared to other samples prepared using WA powders. As explained in

Section 5.1.7, the spherical nature of the VIGA powder may have enhanced sintering efficiency, leading to increased rates of densification and grain coarsening mechanisms. The particle size and size distribution in combination with the particle morphology of the VIGA 316L powder may be contributing to increased grain coarsening and its knock-on effect on hardness as described by Equation 5.1.

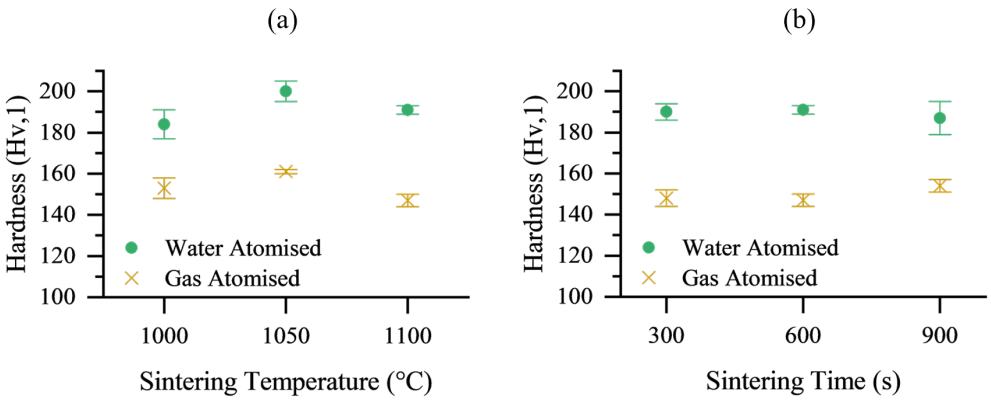

Figure 5.25: Graphs comparing the hardness of sintered WA and GA 316L stainless steel samples produced under varied sintering conditions. The effect of varying sintering temperature while maintaining a sintering time of 600 s is shown in (a). Graph (b) shows the effect of varying the sintering time while keeping sintering at a temperature of 1100°C

Pore Analysis

To compare the pores found within the WA and VIGA sintered parts topographic maps were produced using confocal light microscopy. This investigation revealed the pores in the VIGA samples were morphologically distinct from those in the WA specimens. Specifically, the pores found in the VIGA samples were more rounded and smaller in general (Figures 5.26 and 5.12). The inner pore morphology of the samples produced by VIGA were smoother in their profile than those produced by WA (Figure 5.26 (iii-iv)). Several factors can affect pore morphology, for example[25]:

- Powder morphology
- Particle size distribution

Irregular pore morphologies are associated with sintered WA stainless steel while spheroidal pores are associated with sintered GA stainless steel owing to the typical powder shape resulting from these two atomisation methods[136]. Using smaller

powders can contribute to more efficient sintering since they can contribute to the formation of more particle-particle bonds which facilitate the surface diffusion of material leading to the spheroidisation of pores[28,88]. The combination of powder morphology, powder size distribution and sintering efficiency enhancement likely contributed to the pore morphology of the VIGA specimens.

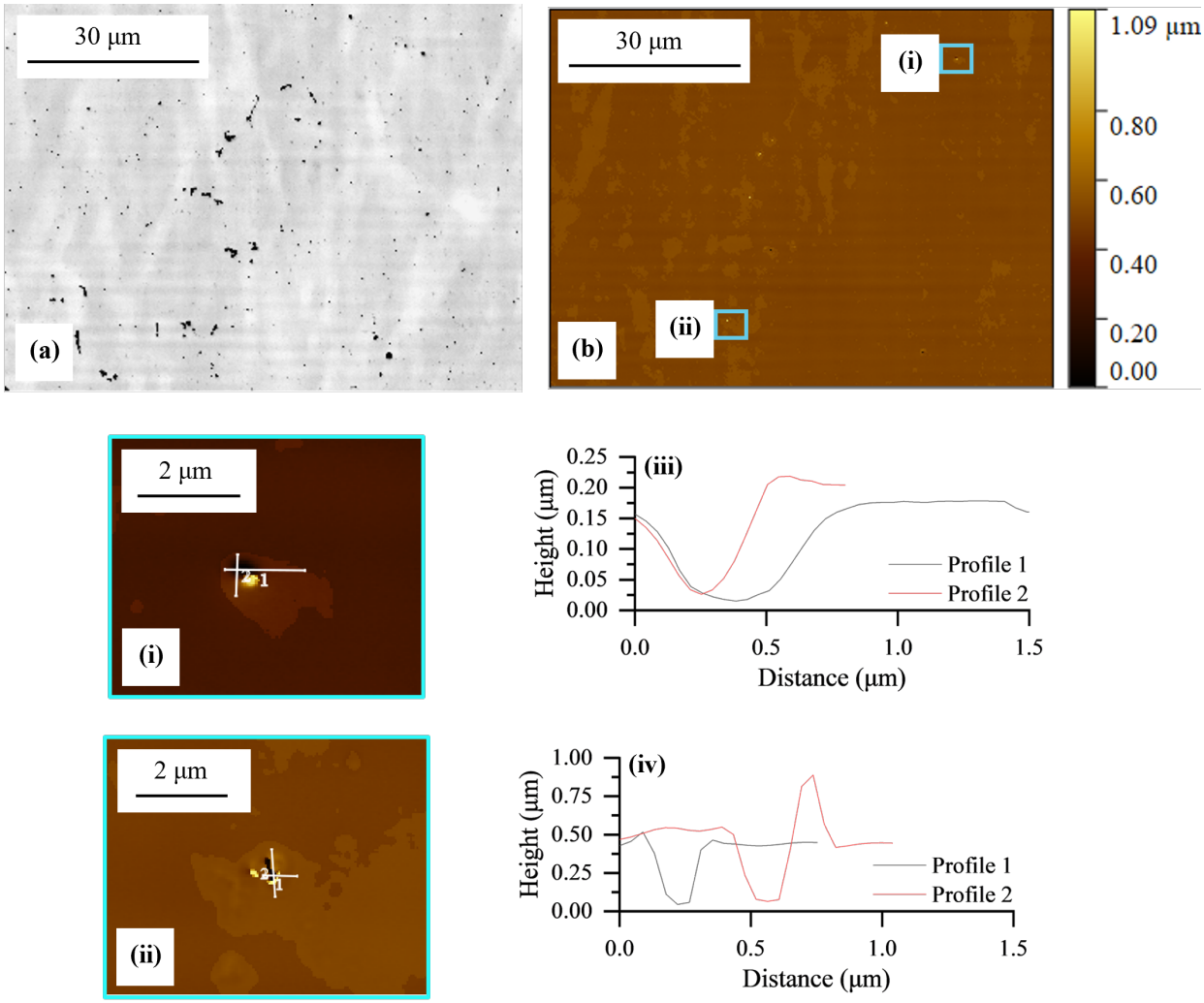

Figure 5.26: Confocal laser micrographs of WA 316L stainless steel sintered at 1000°C for 600 s. Micrograph (a) shows the light microscopy image and the inset image (b) shows a close up topographic map of the highlighted pore. Darker hues in the topographic map represent greater depths. Lines (c) and (d) show the corresponding height profiles for Lines 1 and 2 depicted in image (b). Both micrographs were captured at x150 magnification

Summary

This investigation has found that FAST can be used to consolidate both WA and VIGA 316L stainless steel powders to high densities. The comparative analysis of the two sample sets revealed notable microstructural and physical dissimilarities. The VIGA samples exhibited inclusions that were smaller in size and differed in size compared to those in the WA samples. Additionally, VIGA samples were characterised by coarser grains and lower hardness. The pores of the two sample sets also differed, with the VIGA samples possessing finer but more numerous pores. Despite these differences, once sintered at 1100°C for times at or exceeding 600 s both powder types achieved comparable, near-full densities.

This study has demonstrated the profound effect that atomisation technique can have on the microstructure, elemental distribution and physical properties of sintered 316L stainless steels. The differences between the two sample sets were attributed to factors such as feedstock powder size, morphology and chemistry having a knock-on effect on sintering efficiency then leading to discrepancies in features such as grains and pores. Chapter 7 gives further consideration as to the effects of atomisation route on the corrosion performance of sintered stainless steel.

5.2 Functionally Graded Samples

5.2.1 Introduction

FGM samples were successfully produced using field assisted sintering and WA PGM-doped and undoped 316L and 17-4PH stainless steel powders. This section discusses the characterisation of these specimens. These functionally graded materials were produced by layering PGM-doped stainless steel powder on undoped stainless steel powder and sintering the two powder compositions together. As summarised in the preceding paragraphs, sintering at a temperature of 1100°C for 600 s produced bulk alloyed samples of near-full density. As a result, these parameters were used to produce the FGM samples.

5.2.2 Microstructure and Elemental Mapping

A study of the PGM-doped and undoped layers in the FGM samples revealed microstructures and elemental distributions that resemble the compositionally equivalent bulk alloyed samples. For the sake of brevity these are not presented here. The samples showed no signs of cracking. Though this was to be expected owing to the good match between the coefficients of thermal expansion for the compositions examined here. Though observed elsewhere[187,241,242], a microstructurally distinct diffusion layer representing the region where the two compositions meet was not observed in this study (Figure 5.27). This is likely owing to the compositional similarity in the powders used to produce the FGMs resulting in two identical microstructures.

5.2.3 Hardness

As with the microstructure, the hardness of the FGM samples did not differ to that of the bulk alloyed samples. Again for the sake of brevity the specific results will not be presented here. The results however are as expected as it was not expected for the FGM layered approach to have any effect on the hardness. Within the bonding zone, no hardness variation was observed which contrasts the findings of Firouzdor and Simchi[241]. The homogeneity of hardness throughout the depth of the FGM samples in this study suggest microstructural uniformity, agreeing well with the findings of the microstructural study discussed above.

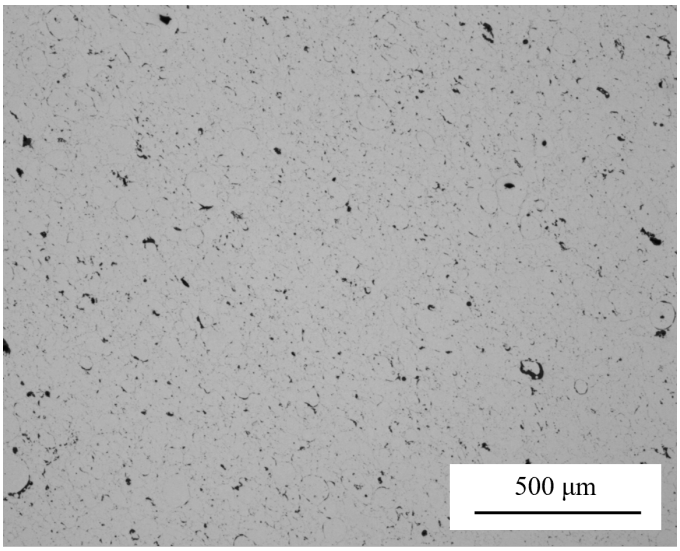

Figure 5.27: Micrograph of the centre of a functionally graded material made from 316L and Pd-doped 316L. The layers in the FGM are aligned vertically in this image. This micrograph was captured at x5 magnification

5.3 Chapter Findings

This chapter has detailed the successful progress made towards optimising the sintering parameters for the production of near-fully dense PGM-doped 316L and 17-4PH stainless steel samples. Sintering at 1100°C for 600 s was identified as the most ideal combination of temperature and time, yielding high density samples while minimising sintering time. Therefore, excessive grain growth was prevented and the formation of undesirable secondary phases minimised.

Also considered in this chapter was the influence of atomisation technique on the microstructure, elemental distribution and physical properties of 316L stainless steel. Specifically, the effect of vacuum induction gas atomisation (VIGA) and water atomisation (WA) on sintered samples was examined. There were notable differences between the two sample sets highlighting the profound effect of the atomisation technique of the properties of the sintered materials. Despite these differences, both sample types achieved near-full densities when sintered at 1100°C for at least 600 s.

Finally, this chapter demonstrated the feasibility of using the field assisted sintering technique for the production of PGM-doped stainless steel functionally graded samples, successfully meeting one of the aims of this EngD project.

CHAPTER

6

Results and Discussion: Heat Treatment of Sintered 17-4PH Stainless Steel

Heat treating 17-4PH stainless steel results in the formation of Cu-rich precipitates. The heat treated state of this alloy is industrially used since it maximises mechanical properties and expands the number of applications it can be used in.

As the over-arching focus of this EngD project is the effect of PGMs on the corrosion resistance of sintered stainless steels, the heat treatment of PGM-doped sintered stainless steel was not optimised. The task of optimising a heat treatment for a particular material is a time-consuming process. To ensure the focus of this project was maintained on corrosion, the scope of this chapter was limited to exploring the impact of the standard H1075 heat treatment on sintered 17-4PH stainless steel.

The main purpose of this chapter is to evaluate whether this heat treatment performs as intended and causes the precipitation of Cu-rich particles. The presence of Cu-rich particles is imperative to enable corrosion testing to be carried out on samples which are analogous to the in-service material state. This approach ensures the findings of this study are directly relevant to industrial applications. Within this chapter, the microstructure, elemental distribution and hardness of as-sintered and heated treated FAST-processed 17-4PH stainless steel was investigated to assess the effect of the H1075 heat treatment. Meanwhile, the relationship between the heat treatment and the corrosion performance of 17-4PH stainless steel is presented and discussed in Chapter 7.

6.1 Microstructure and Elemental Mapping

The heat treatment did not cause any discernible changes to the appearance of the unetched 17-4PH samples in terms of the silicon oxide inclusions at powder particle boundaries - which can be identified by their dark colour and crescent shape (Figure 6.1). Given the heat treatment was carried out in an Ar atmosphere at maximum temperatures of 1050°C, this observation is in agreement with expectations. Such temperatures and atmospheres are insufficient to facilitate the reduction of the silicon oxides identified in Section 5.1.1[141]. Sun et al.[77] and Lashgari et al.[243] also observed that HT had no noticeable effect on the presence of silicon oxide inclusions in SLM 17-4PH stainless steel specimens

Upon cooling, the heat treatment of 17-4PH stainless steel is expected to result in a fully martensitic microstructure[45]. Etching the heat treated samples revealed varying microstructures across the different specimens (Figure 6.1). In some samples, such as those illustrated in Figure 6.2 (b) and (c), the grains transformed from a spherical morphology representative of austenite to the needle-like microstructure characteristic of martensite. Other samples, however, such as that shown in Figure 6.2 (a), did not possess a martensitic microstructure despite the H1075 heat treatment. Instead, the microstructure appeared predominantly austenitic. This suggests the heat treatment may need to be tailored to the specific sintering conditions used to produce the desired fully martensitic microstructure. This is in agreement with Lashgari et al.[243] who also found that conventional heat treatments were not directly applicable to 17-4PH specimens that were not produced by conventional means.

Figure 6.3 presents a summary of the microstructure of the samples following heat treatment and etching as determined by visual examination. Following heat treatment, the 17-4PH specimens possessed a variety of different microstructures which ranged from fully martensitic to fully austenitic. Heat treating the samples produced at the shorter sintering time of 300 s resulted in microstructures which were fully austenitic or a mixed microstructure, comprising predominantly of austenitic with some martensite. Meanwhile, following heat treatment, those samples sintered for the longer time of 900 s exhibited fully martensitic microstructures, as exemplified in Figure 6.2 (c). This trend suggests that small changes in the thermal processing of powder metallurgy parts can impact the material's response to heat treatment.

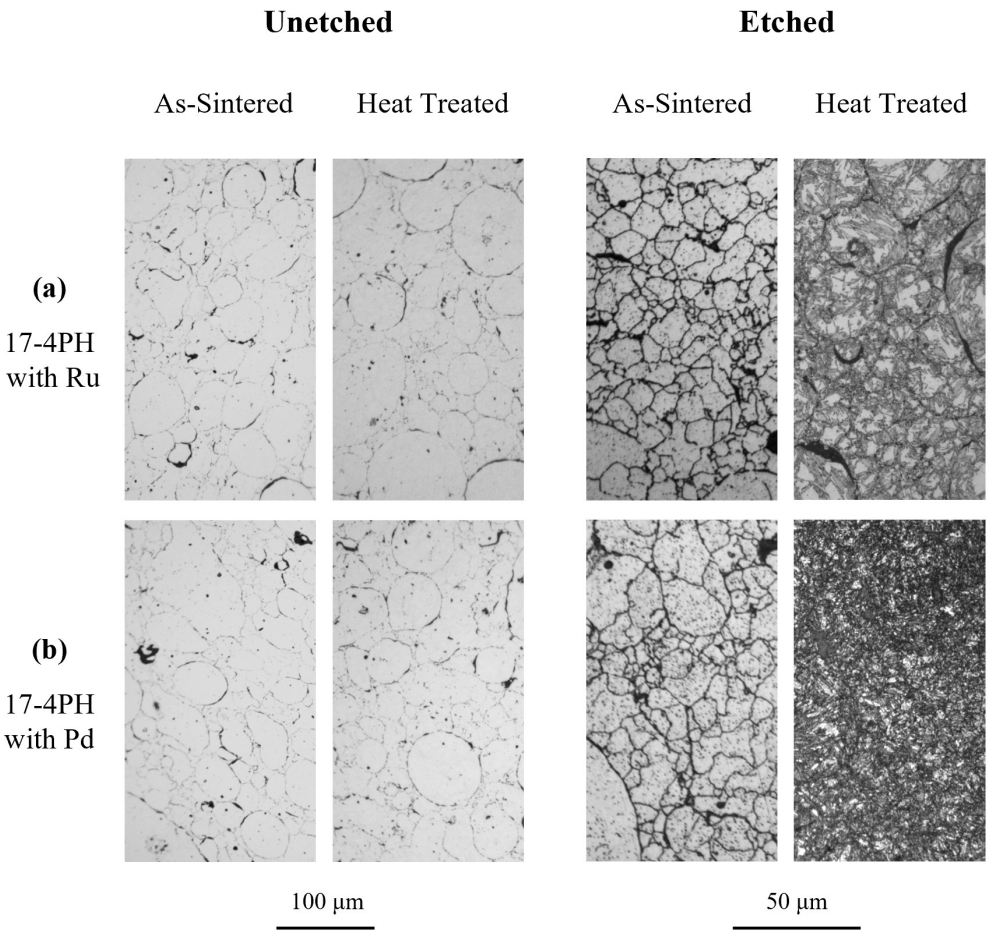

Figure 6.1: Optical micrographs of (a) 17-4PH with Ru and (b) 17-4PH with Pd stainless steel in their as-sintered and heat treated conditions both before and after etching. Samples were sintered at 1100°C for 600 s. The unetched micrographs were collected at x20 magnification while x50 magnification was used to collect the etched micrographs shown. Kalling's No.1 was used to etch the samples and revealed the fine microstructures evolved by heat treatment

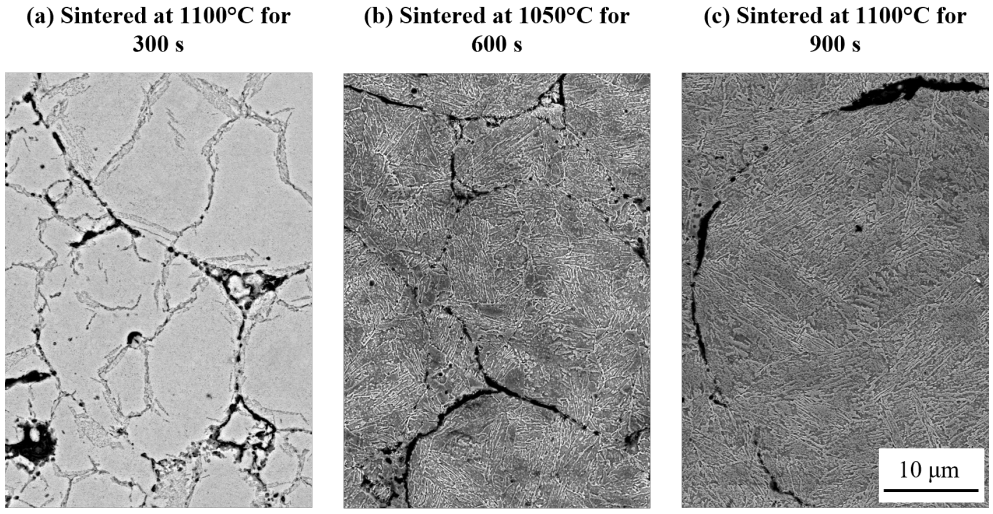

Figure 6.2: Scanning electron micrographs of heat treated and etched 17-4PH stainless steel showing the impact of different sintering conditions on the heat treatment response. The micrographs presented here were at collected at x5000 magnification and 20 kV acceleration voltage. Kalling's No.1 was used to etch the samples

Several different factors can affect the heat treatment response of precipitation hardening stainless steels. For example, elemental inhomogeneities can act as nucleation sites for martensite formation because martensite transformation temperatures are influenced by alloy chemistry[1]. As a result microstructural inhomogeneities can result. However, as observed here and elsewhere, atomised stainless steels have a generally even elemental distribution[61,244]. Additionally, sintering can have a minor homogenising effect on elemental distribution[245]. As a result, homogeneous elemental distribution was expected in the sintered samples in this study. Indeed, EDS maps revealed the samples produced at different sintering temperature and time combinations all possessed even elemental distributions, with the exception being the regions of inclusions rich in Si, Mn, Cr and O (with a typical elemental distribution shown in Figure 5.5). While inclusions themselves can act as sites for the heterogeneous nucleation of austenite[243], the current study observed that they too were evenly distributed in all the samples considered. For these reasons, it is unlikely that elemental heterogeneities are due to the differences in the heat treatment response among the studied samples.

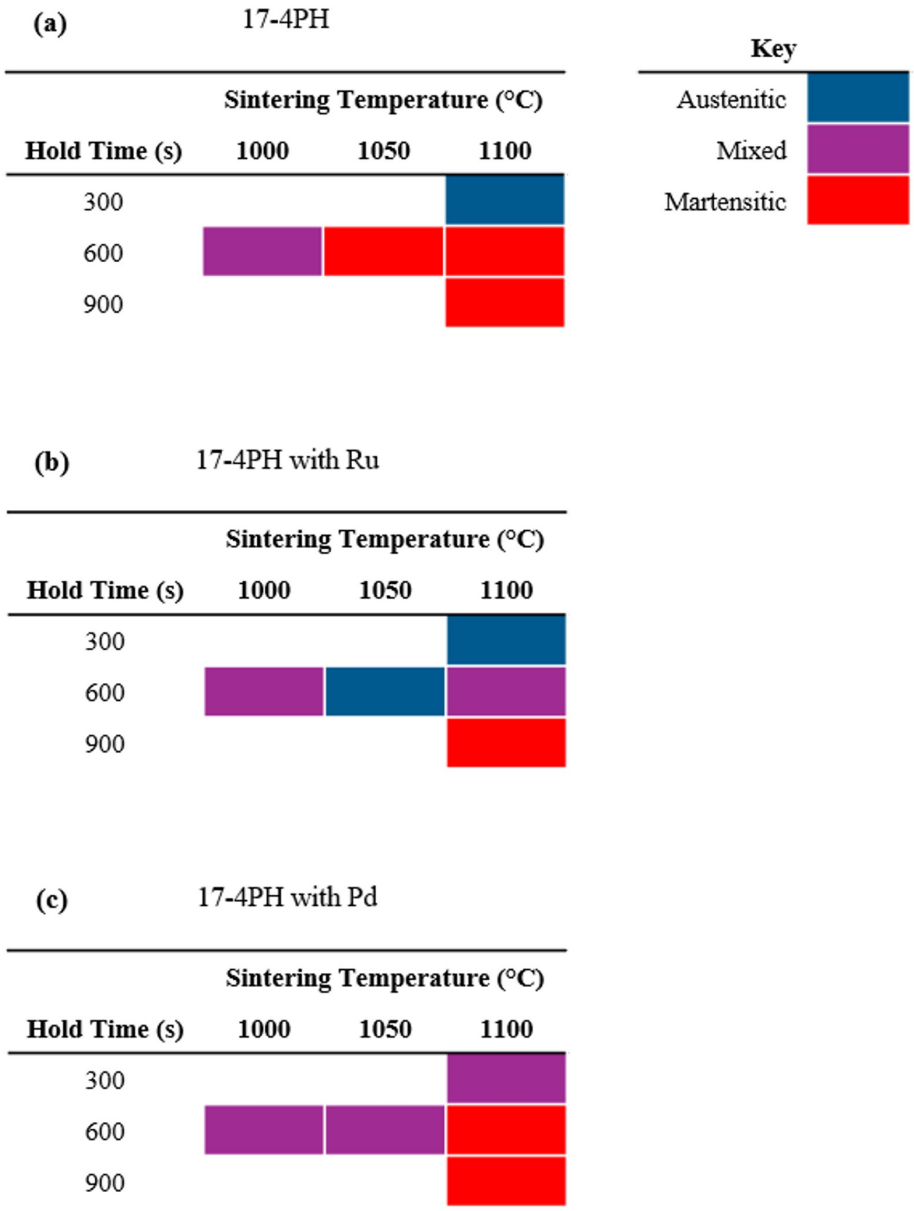

Figure 6.3: Summary of the microstructure types of the undoped and doped 17-4PH samples produced at varying sintering temperatures and times following the H1075 heat treatment. Each colour represents a microstructure as designated by the key. "Mixed" refers to both austenite and martensite being identified in the sample

Sintering for too short a time can lead to temperature gradients in the sample leading to lower than expected temperatures within the sample. This can then lead to microstructural gradients developing within the samples. However, this phenomenon is more common in larger samples and is exacerbated where a high heating rate is applied[246,247]. Since the samples produced in this study are considered small and the grain size was uniform, it suggests that, if present, any temperature gradients were minimal.

The specific reasons for the behaviour of the heat treated samples in this study remain unclear. A review of the literature found the impact of sintering parameters on the response to heat treatment is not a topic that has been explored elsewhere to the best of the author's knowledge. The literature that considers the heat treatment of sintered steels is typically focused on exploring the effect of different heat treatments on samples produced using a single set of processing parameters. While various factors can impact a material's response to heat treatment, such as phase distribution, further investigation is required to pinpoint the responsible underlying characteristics.

Martensite grain size can be analysed using electron backscatter diffraction (EBSD) but due to the time-sensitive nature of this project, this technique was not employed. The grain size analysis technique used in this project, the lineal intercept method, is inappropriate for use in determining martensite grain size. As a result, only the grain size of the three samples whose microstructures determined to be fully austenitic in the heat treated condition were analysed here. In these samples, the H1075 heat treatment did not affect grain size in a statistically significant way (Figure 6.4).

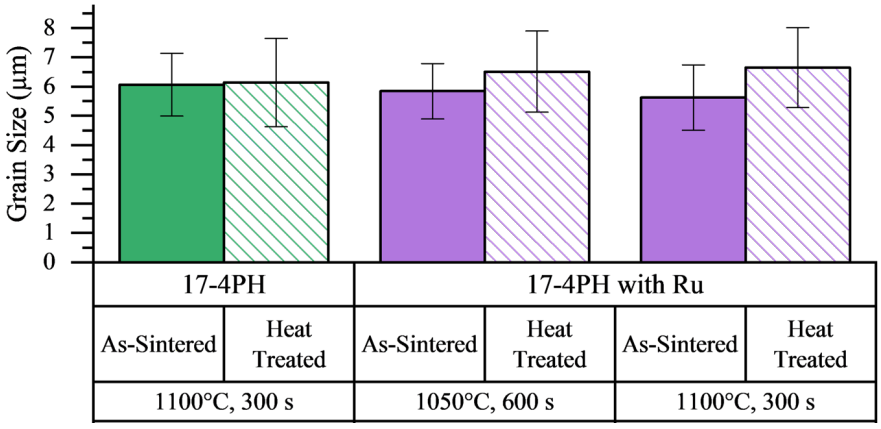

Figure 6.4: Bar graphs comparing the grain size of sintered 17-4PH samples in the as-sintered and HT condition. Samples of different compositions and different production methods are shown here

6.2 Cu-Rich Precipitates

The heat treatment of 17-4PH stainless steel is designed to precipitate nano-sized Cu-rich particles. The precipitation hardening effect is influenced by the size, type and number density of Cu precipitates which in turn is affected by the phase from which the particles precipitate[248].

Owing to the nano-scale size of the Cu-rich particles found in heat treated 17-4PH stainless steel and the resolution limits of SEM EDS, this mapping technique is not able to characterise them. In this study, high resolution elemental mapping was carried out alongside TEM analysis to assess the precipitates. Owing to the time-intensive nature of this technique, only one sample was investigated: a 17-4PH with Ru sample which was sintered at 1100°C for 900 s. The TEM EDS characterisation revealed Cu-rich precipitates, as expected, in the heat treated sample of Ru-doped 17-4PH (Figure 6.5). The formation of Cu-rich precipitates in this sample suggests the 0.5 wt.% Ru addition did not hinder the ability of these particles to form. This study of elemental distribution also confirmed that Ru is uniformly distributed even at magnifications considerably higher than those used in EDS analysis (Figure 6.5).

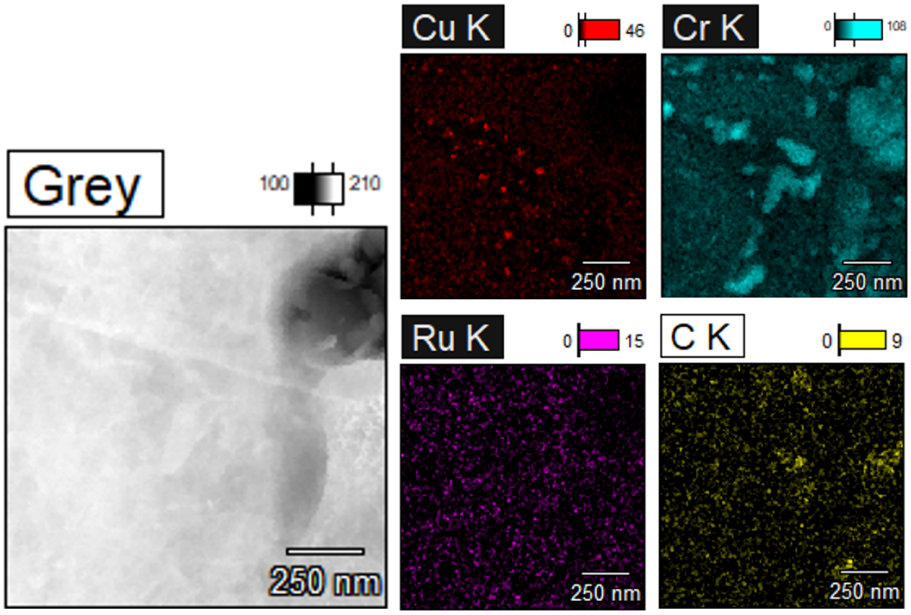

Figure 6.5: High resolution TEM EDS of heat treated sintered 17-4PH with Ru showing the presence of nano-sized Cu-rich precipitates and finely distributed Ru and C

In the literature, Cu-rich particles of a range of different morphologies and size have been observed in precipitation hardening stainless steel. For example, Xiao et al.[249] found Cu-precipitates in a heat treated 15-5PH sample that ranged from 40 nm long and rod-shaped, small and spherical (around 1.6 nm diameter) to particles which were large and spherical (4 nm in diameter). With each shape particle being associated with different phases within the material. The size of CRPs is important since it impacts their hardening effect. In the current study, the CRPs were determined to be spheroidal in terms of morphology and 10 - 40 nm in size, with a mean length of 20 nm. It is reported that ageing time and temperature plays a role in the size of the CRPs which form following heat treatment. Increasing ageing time is known to contribute to the coarsening of CRPs[78,250–252]. For example, Yeli et al.[252] found that ageing 17-4PH for longer times at 480°C and 590°C increased the mean radius of CRPs. The coarsening was enhanced when performing the ageing treatment at 590°C. The coarsening of CRPs should be controlled since their size increase is associated with a decrease in hardness Li et al.[253]. Despite ageing for two hours longer but at a similar temperature, Yeli et al.[252] observed Cu-rich precipitates with a mean size of 5.5 nm, representing a 114% difference compared to the larger precipitates observed in this study. This suggests the ageing time and temperature used in this study may need to be minimised to better control Cu-rich precipitate coarsening and maximise the enhancement of mechanical properties.

6.3 Hardness

It is expected that heat treatment will increase the hardness of the 17-4PH samples due to the precipitation of CRPs which strain the lattice, impede the motion of dislocations and produce a hardening effect[45,77]. In current study, the HT generally had this effect on hardness (Figure 6.6).

Almost all of the samples hardness increased as a result of the heat treatment (Figure 6.6. The highest and greatest percentage change in hardness was in the undoped 17-4PH sample sintered at 1100°C for 600 s following HT, with a 40% increase resulting in a hardness of 514 Hv. The heat treated samples typically exhibited a greater hardness range than the as-sintered samples, despite the same hardness testing procedure being used. This suggests that mechanical properties are less homogeneous in the heat treated samples compared with the as-sintered samples. The wide standard deviation in the hardness in the heat treated samples could be due to two or more phases with different

hardness being measured. However, comparing the standard deviation in the hardness values and assessing the corresponding microstructures did not reveal the expected trend. Instead, for the microstructures determined to be a mix of austenite and martensite the data spread was smaller ($<\pm 50$) suggesting greater hardness consistency. Meanwhile, those microstructures which were either fully austenitic or fully martensitic had greater variability in their hardness (up to ± 98 Hv).

Though a correlation was not found between hardness variability and microstructure, a trend was observed between the microstructure and the absolute hardness values. Namely, the four samples with hardness exceeding 450 Hv were all determined to be martensitic. For the lowest hardness samples in this study, no clear trend emerged correlating hardness with microstructure.

The effectiveness of the heat treatment in improving the hardness of 17-4PH samples was enhanced by increasing the sintering temperature. For example, the absolute change in hardness following HT for samples sintered at 1100°C for 900 s was 135, 106 and 111 Hv for the undoped, Ru-doped and Pd-doped samples, respectively. While at the lower sintering time of 300 s the changes in hardness brought about by HT for these compositions was 6, 73 and 68 Hv, respectively. This same trend was observed in both the undoped 17-4PH alloys and the PGM-doped ones, though to a lesser degree in the latter. Although less pronounced, a similar relationship was also found with increased sintering time.

In this study and elsewhere, sintering temperature and time have been found to improve relative density and decrease the porosity of sintered samples (Chapter 5)[99,209,220,226]. As increasing the density increases the load bearing area it is associated with improved mechanical properties[62,99,220,226]. In the current study, for example, it was found in the as-sintered 17-4PH samples that where relative density increased by 6.2% the hardness increased by 28.3%. Therefore, a likely reason for effectiveness of the heat treatment improving with increased sintering temperature and time is the associated enhancement of sample density.

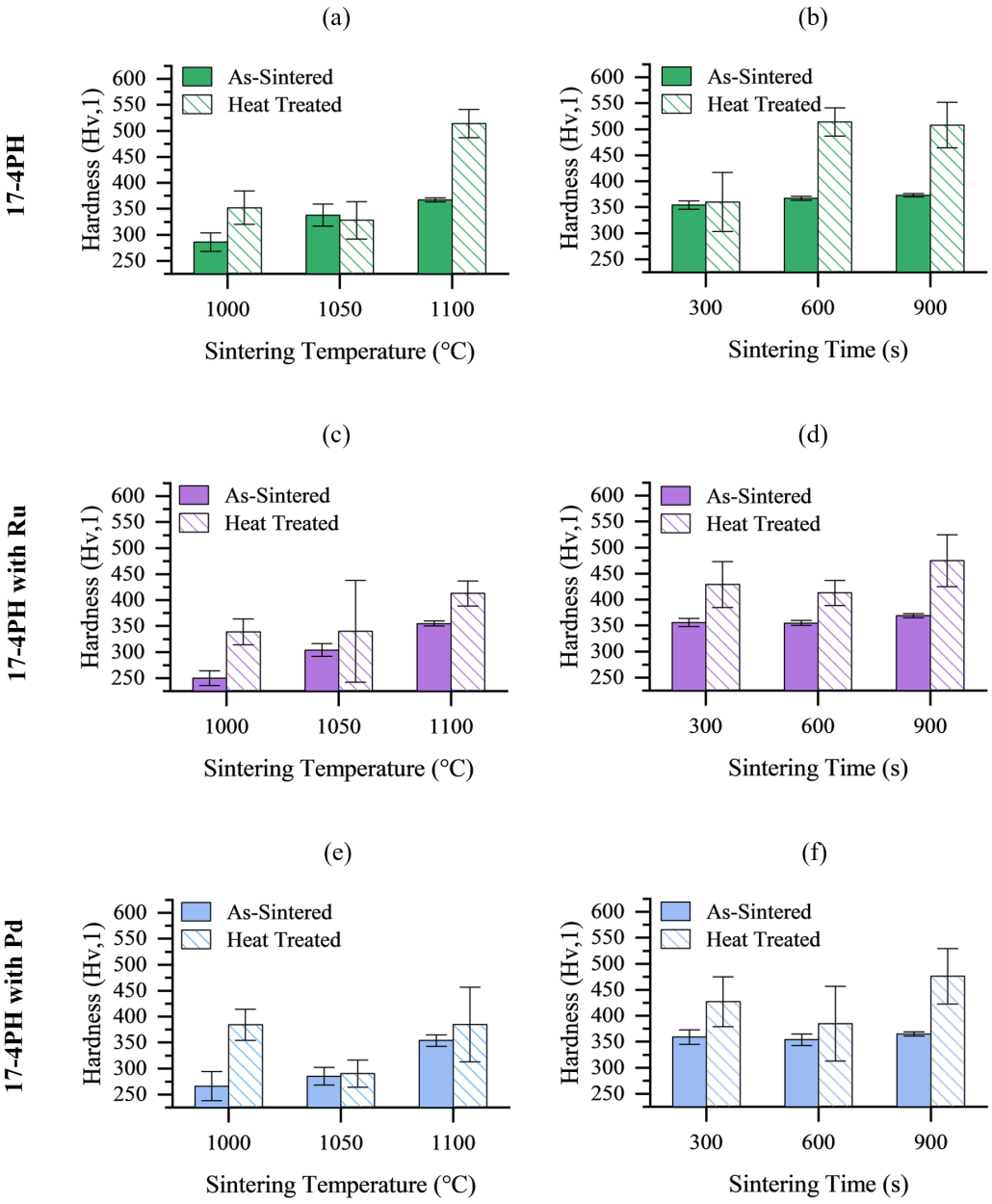

Figure 6.6: Graphs illustrating the influence of the H1075 heat treatment and sintering parameters on the hardness of undoped (a-b), Ru-doped (c-d) and Pd-doped (e-f) 17-4PH SS

When indentation hardness tests are performed on sintered materials the volume measured will be impacted by porosity. By increasing the relative density, a greater proportion of the test volume will be the solid material itself and a smaller proportion will be voids, thereby reducing the impact of porosity on the hardness measurement. In the context of precipitation hardening heat treatment, with some of the test area being occupied by voids, this volume will obviously not benefit from the hardening effect of the heat treatment. As a result, increasing the density amplifies the perceived effectiveness of the heat treatment since it constitutes an increased volume of CRP-containing material being tested.

The hardness values reported in the technical specification produced by Allegheny Technologies Incorporated[254] for the H1075 heat treatment are between 311 - 376 Hv. The standardised hardness values published by ASTM are similar: 277 - 361 Hv[207]. In all but one sample, the hardness values in this study meet or exceed these ranges. In fact, nine out of the fifteen samples examined in this study possess a hardness which exceed these ranges. The higher hardness values in the current study is likely owing to the selected metallurgical processing approach, with the values reported by ATI[254] and ASTM[207] pertaining to wrought samples while the current study explores sintered PM samples.

As presented in Table 6.1, producing and heat treating precipitation hardening alloys via different techniques results in a large range of hardness values. The hardness values exhibited by these samples are attributed to several different factors, such as inclusions. Sun et al.[77] observed that AM 17-4PH samples had 16% higher hardness than their wrought counterpart following heat treatment. This observation was attributed to the presence of inclusions in the AM samples which originated from the atomisation process. These inclusions can pin grain boundaries and result in a more refined grain structure, which as known from the Hall-Petch relationship (Equation 5.1), enhances hardness. As the samples in this study were found to possess Si-rich inclusions these particles may have contributed to the high hardness values.

Table 6.1: Comparison of the hardness of heat treated 17-4PH stainless steel produced by various methods

Synthesis Method	Solution Anneal Conditions	Ageing Conditions	Hardness (Hv)	Source
Wrought	1066°C, 0.5 hours	579°C, 4 hours	277 - 361	ASTM[207]
Wrought	1066°C, 0.5 hours	579°C, 4 hours	311 - 376	ATI[254]
Wrought	1038°C, 4 hours	482°C, 1 hour	450±9	Sun et al.[77]
Selective Laser Sintering	1100°C, 1 hour	480°C, 1 hour	405 - 440	Leo et al.[153]
Sintered	1020 - 1040°C, 0.5 hours	480 - 500°C, 1 hour	325 - 355	Szewczyk-Nykiel and Kazior[255]
Sintered	1066°C, 0.5 hours	482°C, 1 hour	393	Suri et al.[229]
AM	1038°C, 4 hours	482°C, 1 hour	525±6	Sun et al.[77]

Another factor which can effect the hardness of heat treated precipitation hardening stainless steel is Cu content. Sun et al.[77] identified this as a contributing factor for the hardness of an AM 17-4PH part exceeding that of a wrought part. Specifically, the Cu content of the powder used to produce AM parts was found to be 30% higher than the Cu content of the wrought parts. In the current study, the Cu content was around 3 wt.%, a value which is at the lower limit of the Cu content designated by ASTM standards[207]. As a result, this factor is unlikely to have contributed to the high hardness of the sintered samples studied here.

Suri et al.[229] produced 17-4PH samples by cold isostatic pressing, sintering and the H900 heat treatment. The resulting specimens exhibited a hardness of 393 Hv, a value that aligns well with the standardised value reported by ASTM International[207] for the same heat treatment. This hardness value is below the maximum hardness in each of the heat treated compositions studied here. The H900 heat treatment used by Suri et al.[229] is expected to result in higher hardness than the H1075 heat treatment which was used in this study[254]. Despite this, the opposite trend was observed when comparing the results of the current study and that of Suri et al.[229]. Grain size differences are unlikely to explain the discrepancy, as Suri et al.[229] reported a grain size of < 10 µm, a value which shows good agreement to the grain size observed here. An alternative reason for the observed disagreement is variations in the Cu content. However, since Cu content was not alluded to in the work of Suri et al.[229] it is impossible to assess whether elemental content account for the differences in hardness in this study and that of Suri et al.[229].

Despite the residual porosity and the Cu content of the sintered samples studied here, several samples exceeded the hardness specifications[207,254]. Sintering at 1100°C resulted in the best heat treatment response, a finding likely due to the minimal porosity in these samples.

6.4 Chapter Findings

This chapter assessed the effect of the H1075 heat treatment on the microstructure, physical properties and chemical composition of FAST-processed 17-4PH stainless steel. While the heat treatment did result in the precipitation of nano-sized Cu-rich precipitates its impact on microstructure varied depending on the applied sintering conditions. Those specimens sintered for shorter times remained austenitic following heat treatment whereas those samples sintered for 900 s were martensitic following heat treatment. This suggests that conventional heat treatments should be applied with care to sintered 17-4PH specimens. The effect of heat treatment on hardness also varied with sintering conditions with samples sintered for 900 s at 1100°C generally exhibiting a more pronounced hardness response than those sintered at shorter times and lower temperatures. The improved response is likely due to the presence of martensite in the microstructure and the absence of porosity in the samples sintered at higher temperatures for longer times.

The achievement of higher hardness values following heat treatment is limited by the residual porosity present in the sintered samples. Despite this factor, many of the samples examined here exhibited hardness values that exceed those reported elsewhere for wrought and sintered samples. Several factors are likely responsible for the enhanced hardness. For example, the refined microstructure and inclusions resulting from the powder metallurgy process.

CHAPTER

7

Results and Discussion: Corrosion Characterisation

7.1 Introduction

This chapter presents and evaluates the findings of the corrosion characterisation study. Samples were evaluated by open circuit potential (OCP) and potentiodynamic polarisation testing in 0.05 M H_2SO_4 at room temperature. Separate samples were also subjected to 24 hour immersion in 5 wt.% NaCl. This chapter aims to assess:

- The impact of the sintering parameters on the corrosion performance
- The influence of PGM presence on the corrosion resistance of 316L and 17-4PH stainless steel
- The comparative cathodic modification efficiency of the 316L and 17-4PH stainless steel alloys
- The differences in the corrosion behaviours of sintered water atomisation (WA) and vacuum induction gas atomisation (VIGA) 316L powder
- The effect of sample processing approach by contrasting the corrosion performance of tundish and FAST-processed samples
- The feasibility of FAST to produce PGM-doped functionally graded stainless steel materials

7.2 Effect of Sintering Parameters

This section evaluates the impact of varying the sintering temperature and time on the corrosion performance of the sintered materials. Due to the time-sensitive nature of an EngD, only samples presented in Table 7.1 were evaluated by electrochemical means.

Table 7.1: Matrix detailing which samples were electrochemically tested in the evaluation of processing parameter impact where 'X' denotes that a sample was corrosion tested

		Temperature (°C)	
		1000	1100
Time (s)	600	X	X
	900		X

7.2.1 Effect of Sintering Temperature

The impact of sintering temperature on the OCP of the 316L and 17-4PH stainless steel alloys was mixed. For the 316L samples, increasing sintering temperature had either a small impact or no statistically significant effect (Figure 7.1). Specifically, increasing the sintering temperature decreased the OCP for the Pd-doped compact by 4 mV while Ru-doped 316L exhibited a 4 mV increase in OCP (Figure 7.1 (a-c)). Increasing the sintering temperature did not impact the OCP of undoped 316L stainless steel in a statistically significant way. Conversely, the changes in OCP were more dramatic in magnitude in the 17-4PH samples. For example, the OCP decreased by 65, 737 and 50 mV for the undoped, Ru-doped and Pd-doped samples, respectively (Figure 7.1 (d-f)). No overlaps in data of these OCP values were detected, as such the differences are considered statistically significant. Sintering temperature has little effect on the time taken for potential stability as this was attained within the 3600 s OCP test for all samples considered. Both stainless steel grades tested showed good stability throughout the duration of the OCP test with no potential fluctuations characteristic of instability observed. As exemplified in Figure 7.3 (f), some samples exhibited small perturbations in the OCP, however, such features are attributed to experimental noise.

As shown in Figure 7.2, increasing the sintering temperature increased i_{crit} for undoped and Ru-doped 316L by 615 and 263 µA cm^{-2}, respectively. Contrastingly, the opposite trend was observed for Pd-doped 316L, which showed a decrease in i_{crit} by 744 µA cm^{-2}. Increasing the sintering temperature increased i_{crit} for undoped 17-4PH by 763 µA cm^{-2}. Contrastingly, i_{crit} decreased by 221 µA cm^{-2} in Pd-doped 17-4PH. Owing to the shape of the polarisation curve, a value for i_{crit} couldn't be determined for Ru-doped 17-4PH produced at 1000°C. The polarisation curves indicate that none of the samples experienced metastable pitting as sharp fluctuations of the measured current were not observed[10].

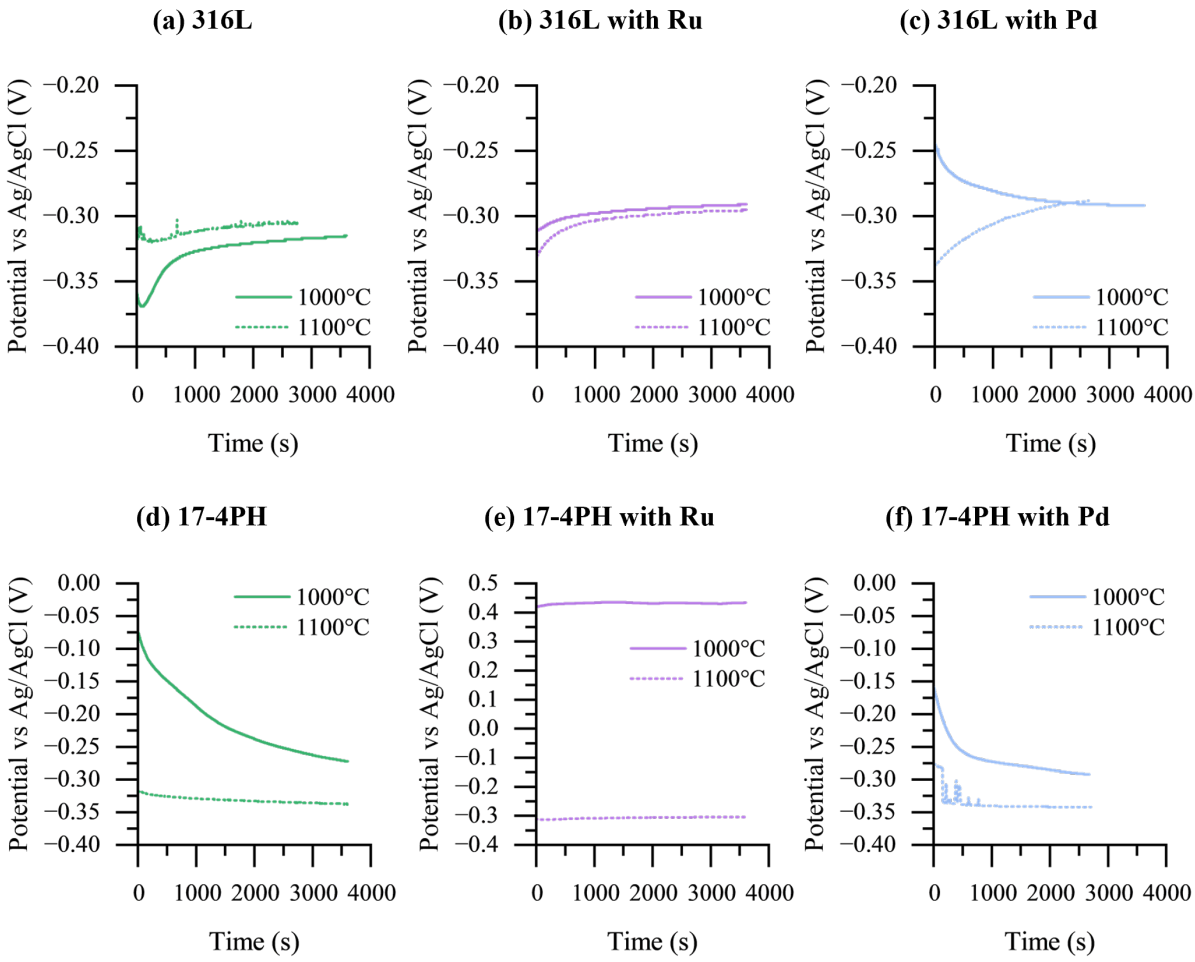

Figure 7.1: OCP curves showing the effect of sintering temperature on (a) 316L, (b) 316L with Ru, (c) 316L with Pd, (d) 17-4PH, (e) 17-4PH with Ru and (f) 17-4PH with Pd exposed to 0.05 M H_2SO_4 for 3600 s

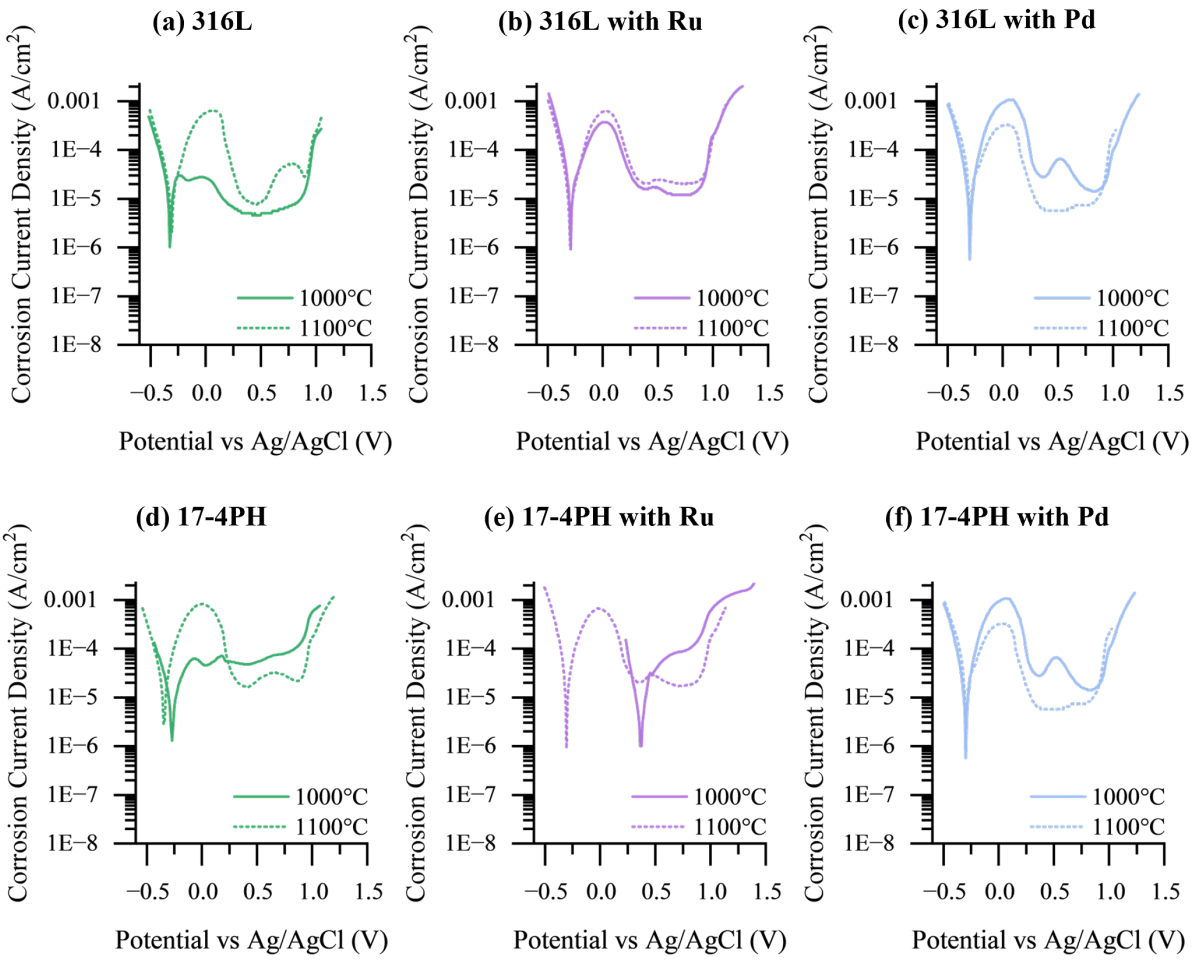

Figure 7.2: Potentiodynamic polarisation curves showing the effect of sintering temperature on (a) 316L, (b) 316L with Ru, (c) 316L with Pd, (d) 17-4PH, (e) 17-4PH with Ru and (f) 17-4PH with Pd exposed to 0.05 M H_2SO_4

As Figure 7.2 illustrates, different samples possessed differing passive region shapes - with some being a single flat plateau and others consisting of multiple plateaus. No clear trend arose between sintering temperature, composition and passive region shape. The passivation current, i_{pass}, exhibited correlation trends with sintering temperature identical to those observed in i_{crit}. The passivation range trends also correlated to the i_{crit} and i_{pass}: where i_{crit} and i_{pass} increased with sintering temperature the passivation range was narrower. Conversely, where these parameters decreased the passivation range was broader.

The OCP of a material gives an indication of the thermodynamic stability of its passive film within the test solution. Where cathodic modification is concerned, an increase in OCP is associated with an improvement in corrosion behaviour as it suggests the sample is more stable in that environment[10]. Additionally, Klar and Samal[25] summarises that it is generally expected that higher porosities will cause greater passive film instability in stainless steels. This is owing to the lack of passivation that occurs within pores contributing to poor corrosion behaviour with studies by Raghu et al.[135,142] corroborating this statement. As presented in Chapter 5, increasing sintering temperature increased sample density, therefore corrosion performance is expected to improve. Unexpectedly, the 17-4PH samples sintered at higher temperatures had higher relative densities but lower OCP values which is unexpected considering previous work[135,142]. This suggests, despite possessing reduced porosity, those samples had greater passive film instability. The trivalent species of Cr responsible for the passivity of stainless steel is stable at potentials between -200 mV and 600 mV[10]. With the OCP of the 17-4PH samples sintered at 1100°C all falling below -200 mV, film dissolution is expected. Instead, the potentiodynamic polarisation curves revealed those samples showed electrochemical behaviour suggestive of improved corrosion resistance compared with samples produced at lower sintering temperatures (Figure 7.2). For example, the samples produced at 1100°C had lower passivation currents. Both the undoped and PGM-doped samples showed this same behaviour, suggesting that it is not cathodic modification dependent. Similar to the current study, the work of Peled and Itzhak[23] and Szewczyk-Nykiel et al.[256] also observed that despite OCP being lower than the potential at which trivalent Cr is stable, the samples showed passivity during the polarisation test.

It is worth noting here the initial gradient of the OCP curve immediately after the sample has been immersed in the solution is not indicative of corrosion characteristics

and many different shaped curves have been observed elsewhere which do not correlate with corrosion behaviour[10]. The nature of the initial gradient is determined by the state of the electrodes prior to the test initiation and so this stabilisation region of the curve is ignored.

Significant corrosion behaviour changes were observed in Ru-doped 17-4PH as a result of sintering temperature (Figures 7.2 (e) and 7.1 (e)). When sintered at 1000°C, the alloy did not possess the active-passive behaviour characteristic of stainless steel. The sample also lacked an anodic peak, a characteristic typically indicative of the desirous spontaneous passivation behaviour[10,22] (Figure 7.2 (e)). Such polarisation behaviour of PGM-doped steels has been observed by researchers elsewhere[10,19,22,257]. Tjong et al.[22] states spontaneous passivation occurs when, due to selective dissolution and the diffusion of Ru to defect sites, the surface concentration of PGMs reaches a critical value. Selective dissolution may be enhanced in this particular sample due to the degree of porosity in this sample (the sample was determined to have the second lowest relative density of all samples studied - 90.8%). Pores may have led to unstable passive film initially, meaning more material dissolution occurred before stable passivation was achieved causing greater degree of Ru-enrichment at that surface. Despite the suggestion of spontaneous passivation this sample does not exhibit a stable passive film, as indicated by the continually decreasing potential after the attainment of minimum corrosion current density at around 300 mV. With increased sintering temperature, however, this alloy assumed typical stainless steel corrosion behaviour with a clear passive region indicating an improvement of corrosion performance.

Most of the samples exhibited multiple plateaus in the passive region of the polarisation curve which is indicative of a change in the nature of the passive film (Figure 7.2). This feature did not appear to be affected by sintering temperature as it was identified in samples produced at both the high and low sintering temperatures (for example, Figure 7.2 (f)). Multiple plateaus in the passive region were observed elsewhere by Peled and Itzhak[23] and Raghu et al.[142] but no comments were made attributing any significance to such features.

7.2.2 Effect of Hold Time

Hold time had a similar effect on both the 316L and 17-4PH samples. Increasing the sintering time had either a small or statistically insignificant effect on the OCP of the 316L samples (Figure 7.3 (a-c)). The OCP of undoped 316L increased by 1 mV by increasing the sintering time, meanwhile, the OCP of the PGM-doped samples did not change by a statistically significant degree. Similarly, for the 17-4PH samples, increasing hold time led to a 12 mV increase in the OCP for the Pd-doped sample (Figure 7.3 (f)). For the undoped and Ru-doped samples, however, the change in OCP was determined to not be statistically significant (Figure 7.3 (d and e)). As observed with increasing sintering temperature, increasing hold time had no notable effect on the stability of the samples. The OCP curves of samples produced at both hold times were stable for the duration of the tests (Figure 7.3).

The trends in critical corrosion current i_{crit} varied across the 316L samples. Sintering for longer times resulted in lower i_{crit} for undoped 316L and Ru-doped 316L but higher i_{crit} in Pd-doped 316L (Figure 7.4 (a-c)). Conversely, Figure 7.4 (d-f) shows that in all the 17-4PH compositions a longer sintering time led to a higher critical corrosion current. As critical corrosion current gives an indication of the ease with which passivation can be achieved, the data suggests passivation was harder to achieve for 17-4PH samples which had been sintering for prolonged times.

The passivation current and passivation range trends mirror that observed with i_{crit}. A higher passivation current was exhibited by all 17-4PH alloys and Pd-doped 316L when sintered for longer, suggesting these samples experienced greater corrosion rates when the passive film was present. Similarly, the passivation range was narrower for these four alloys when sintered for 900 s. This indicates these samples resist corrosion over a smaller range of potentials. Additionally, these samples exhibited the onset of passivation, characterised by a rapid decrease in current, at a lower potential than those sintered for a longer duration. As indicators of corrosion behaviour, the i_{crit}, passivation current and passivation range data suggests that increased sintering time is a a detriment to corrosion performance where the Pd-doped 316L and the three 17-4PH samples are concerned.

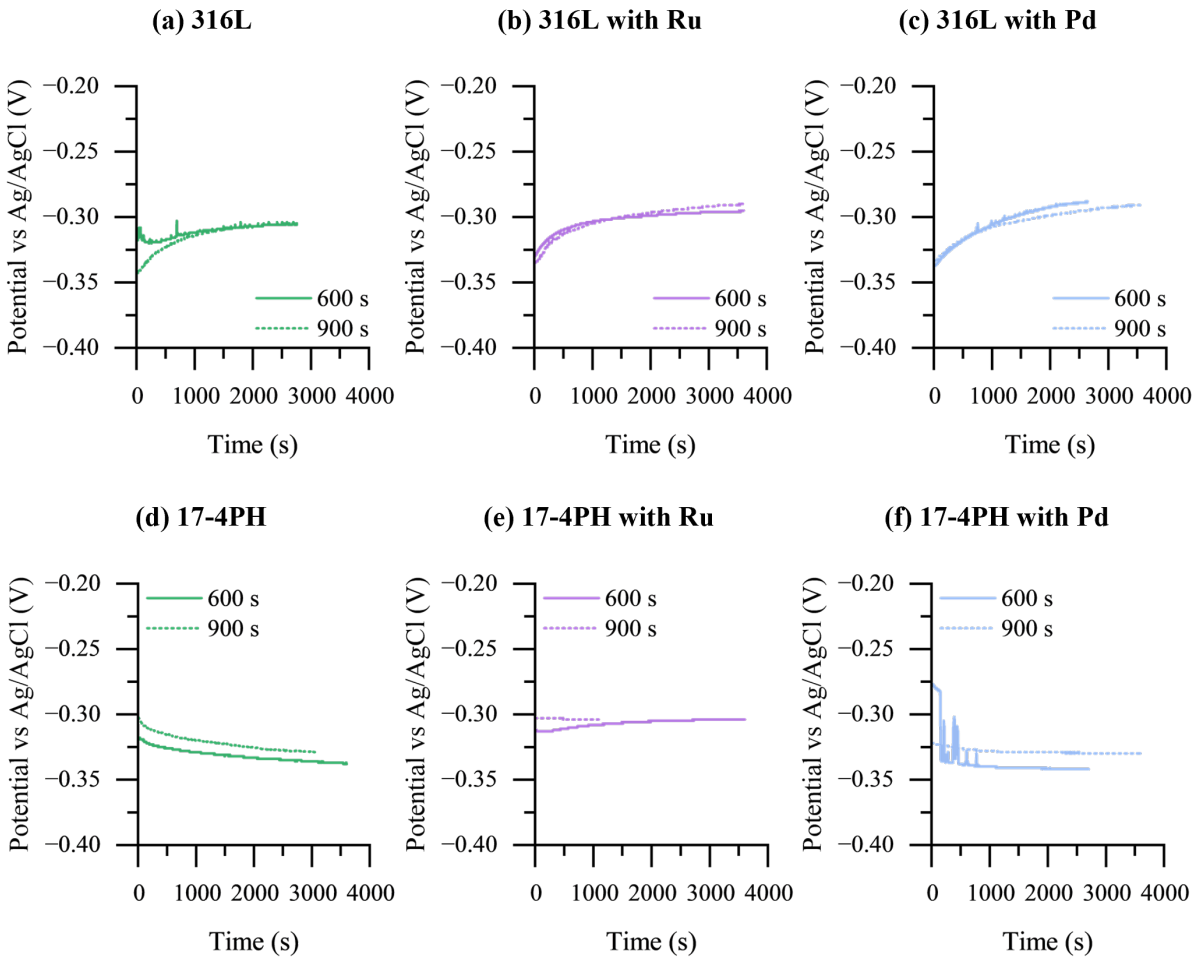

Figure 7.3: OCP curves showing the effect of sintering time on (a) 316L, (b) 316L with Ru, (c) 316L with Pd, (d) 17-4PH, (e) 17-4PH with Ru and (f) 17-4PH with Pd exposed to 0.05 M H_2SO_4 for 3600 s

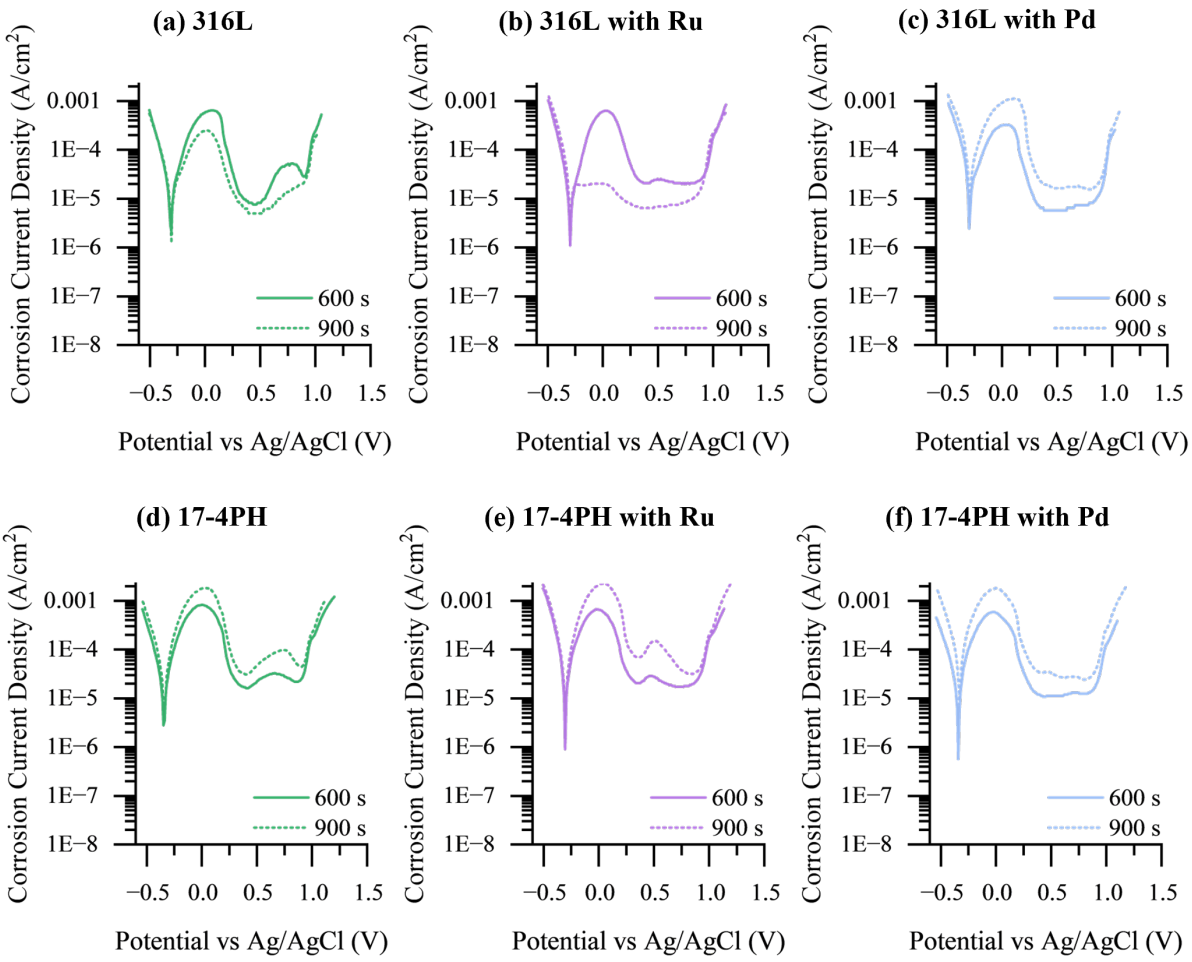

Figure 7.4: Potentiodynamic polarisation curves showing the effect of sintering time on (a) 316L, (b) 316L with Ru, (c) 316L with Pd, (d) 17-4PH, (e) 17-4PH with Ru and (f) 17-4PH with Pd exposed to 0.05 M H_2SO_4

Increasing sintering duration and temperature enables more time for grain growth but also gives more opportunities for procession of unwanted reactions and the formation of unwanted secondary phases. For these reasons among others, sintering time is kept to a minimum. Grain size is of interest as larger grains can contribute to higher corrosion rates[146]. However, the investigation into grain size presented in Chapter 5 revealed increasing sintering time had no significant impact on grain size of the 17-4PH samples. EDS mapping also did not reveal any noticeable changes in elemental distribution caused by increased sintering time. Density can also impact corrosion resistance, however, no significant change in this property was observed by increasing sintering time. It is therefore likely that another unknown factor is responsible for the observed changes.

7.3 Effect of PGM Doping

It is expected the presence of PGMs will shift the OCP in the positive direction, indicating successful cathodic modification: the PGMs have catalysed the hydrogen evolution reaction and blocked active sites in the crystal lattice[9]. The current study found the opposite to be true for the 316L samples sintered at 1000°C for 600 s, whereby PGM doping led to a decrease in the OCP (Figure 7.5 (a)i). The samples produced at the higher sintering temperature of 1100°C however did exhibit the expected behaviour, namely, the OCP was shifted in the noble direction (Figure 7.5 (b)i and (c)i).

The data collected for the 17-4PH samples agrees with the literature more comprehensively compared with the 316L samples. It was found that PGM doping shifted the OCP in the noble direction for all the sintering parameter combinations whose corrosion properties were characterised (Figure 7.6).

This study revealed that in all sintering parameter combinations investigated the Ru additions were most effective at enhancing corrosion behaviour and causing the OCP to increase. This is in agreement with the general statement presented by Potgieter[258], who listed the PGMs in decreasing order of effectiveness in terms of their ability to enhance corrosion resistance in H_2SO_4:

Ir > Rh > Ru > Pt > Pd > Os

The improved cathodic modification efficiency of Ru compared to Pd was also found by Chernova et al.[259] who attributed this behaviour to Ru being more effective at reducing the hydrogen overvoltage, a primary mechanism behind cathodic modification. Chernova et al.[259] also found Ru more effective at reducing i_{crit}, a decrease in which indicates passivation is easier to achieve.

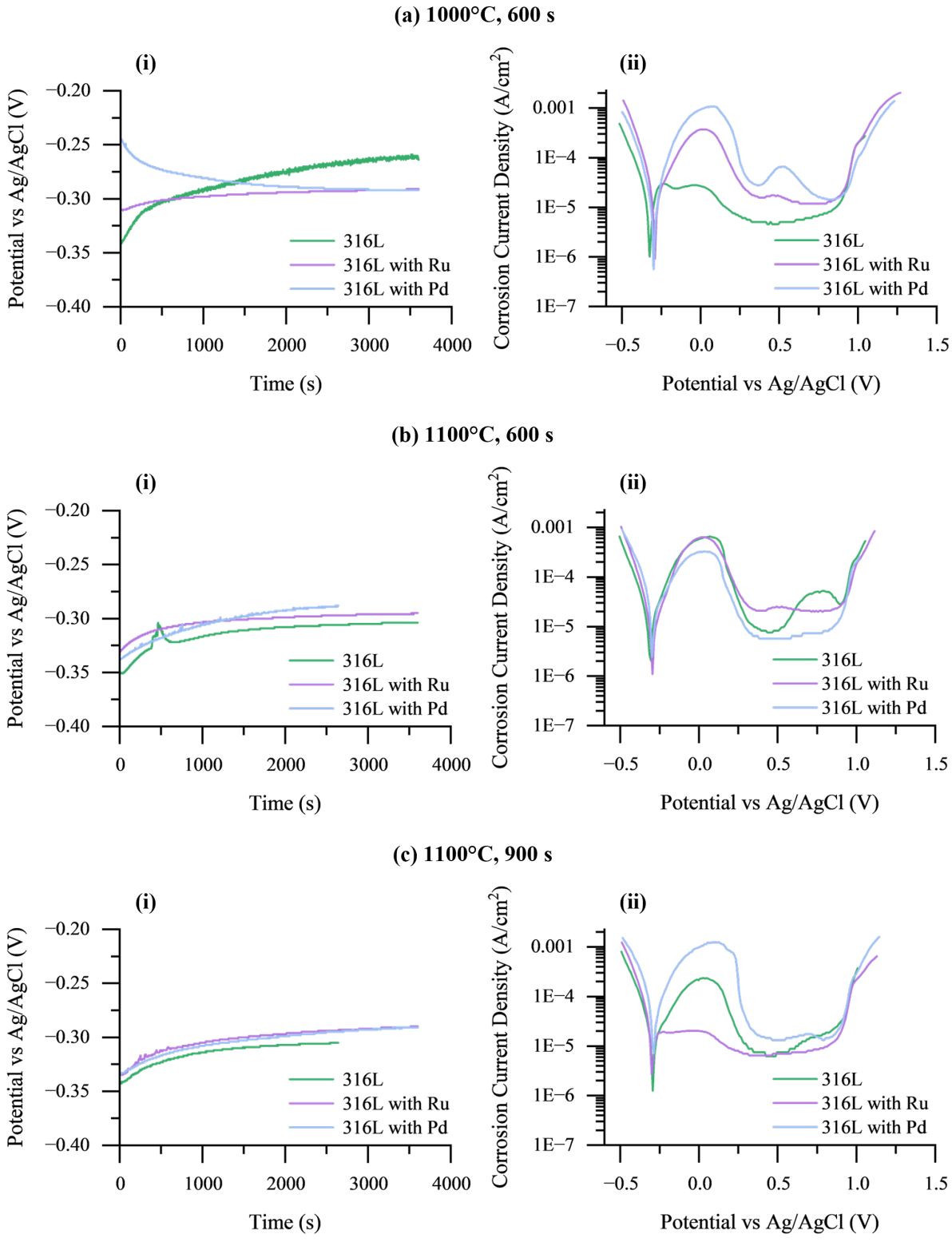

Figure 7.5: OCP (i) and potentiodynamic polarisation (ii) curves showing the effect of PGM doping on 316L stainless steel samples produced at (a) 1000°C for 600 s, (b) 1100°C for 600 s and (c) 1100°C for 900 s exposed to 0.05 M H_2SO_4

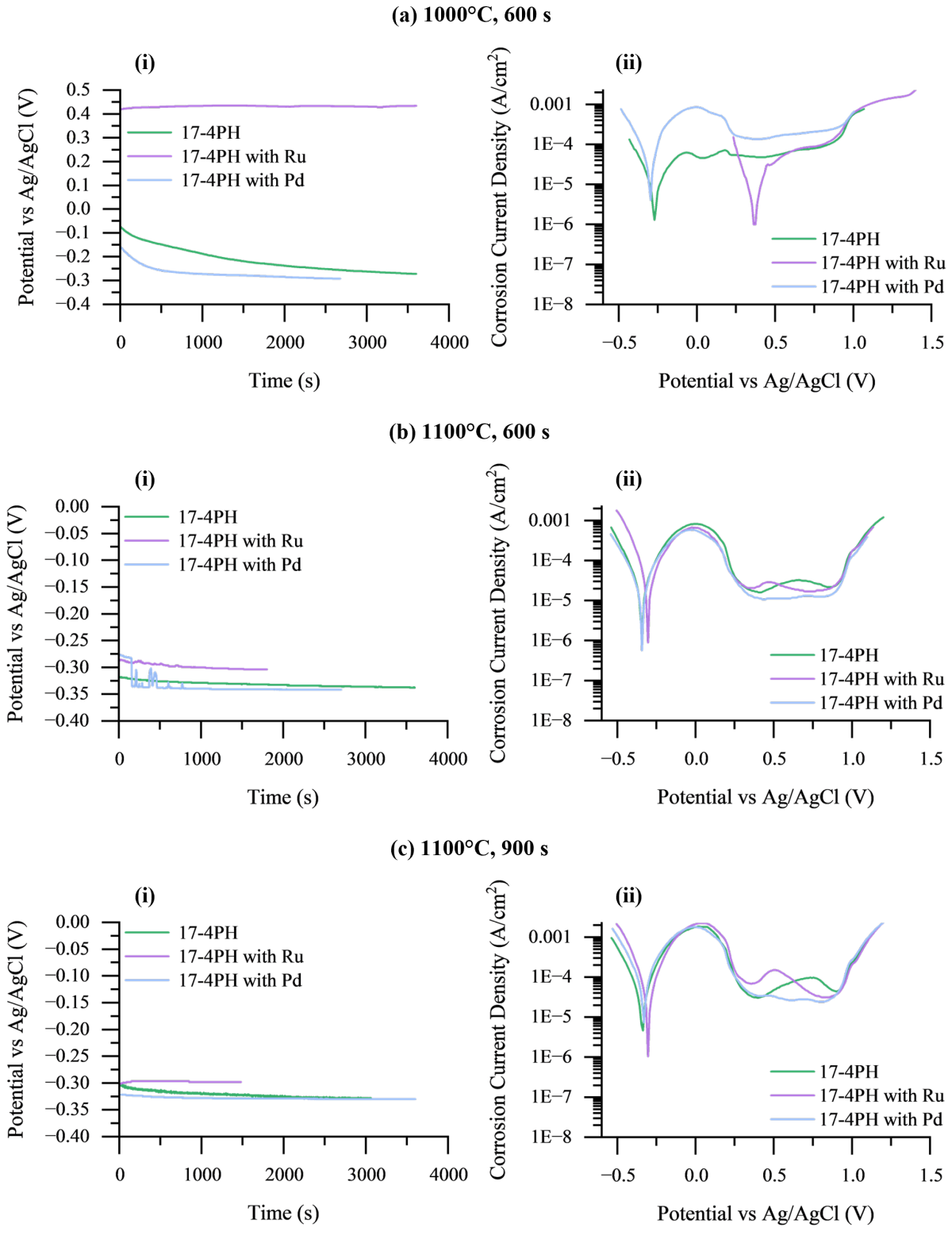

Figure 7.6: OCP (i) and potentiodynamic polarisation (ii) curves showing the effect of PGM doping on 17-4PH stainless steel samples produced at (a) 1000°C for 600 s, (b) 1100°C for 600 s and (c) 1100°C for 900 s exposed to 0.05 M H_2SO_4

Studies have consistently demonstrated cathodic modification can result in an increase of the OCP. If this increase is particularly significant, the potential will fall within the passive range and spontaneous passivation has been observed to occur as a result [10,22,165,257]. In this study, this behaviour was exhibited by the Ru-doped sample shown in Figure 7.6 (a)ii. This sample also possesses the most noble OCP of all samples at a value of 0.45 V and in fact the only electropositive value (Figure 7.6 (a)i). Repeats of the OCP test confirmed this was not a random error.

An examination of the polarisation curves (Figures 7.5 and 7.6) confirmed that both undoped and doped samples exhibited the expected active-passive behaviour characteristic of stainless steel and were characterised by stable passive regions, with the exception of Ru-doped 17-4PH produced at 1000°C.

The critical corrosion current, i_{crit}, gives an indication of the ease with which passivation occurs, with lower values suggesting passivation occurred more easily. Other researchers found the presence of PGMs resulted in the reduction of i_{crit} [10,15,165,196]. In the current study, the composition which exhibited the lowest i_{crit} depended on the sintering conditions used. Regarding i_{crit} specifically, at the baseline parameters, 316L exhibited the lowest i_{crit}, however, sintering at 1100°C for 600 s resulted in Pd-doped 316L possessing the lowest i_{crit}, while sintering at 1100°C for 900 s resulted in Ru-doped 316L exhibiting the lowest i_{crit} value (Figure 7.5). Similar trends were observed when considering the passivation current. Undoped 316L produced at baseline parameters possessed the lowest passivation current (4.6 µA/cm^2), closely followed by Ru-doped 316L (6.4 µA/cm^2) produced at higher sintering temperature and time of 1000°C and 900 s respectively. Contrastingly, Moyo [10] consistently found that 304L doped with Ru exhibited significantly lower current densities. The observations in the current study suggest that multiple compounding factors affect the efficiency of cathodic modification. The powder metallurgical processing is a possible source for the additional complexities.

Within the passive region, some samples exhibited multiple plateaus (see Ru- and Pd-doped 316L in Figure 7.5 (a)ii). The same behaviour was observed by van der Merwe and Tharandt [181], van der Merwe et al. [183], Lekala et al. [196] in PGM-doped stainless steel in sulphuric acid. The variation in current in the passive region is explained by a change in chemical or structural composition of the passive film [10]. Regarding 316L sintered at 1100°C for 600 s (Figure 7.5 (b)ii), starting at 0.55 V, a large decrease in the passive current is observed before stabilising at a higher current density. This

signifies the passive film which formed on this sample was less stable than the other samples. Contrastingly, in the Pd-doped sample which also presented multiple plateaus in the passive region (Figure 7.5 (a)ii), the passive current decreased with the increase in potential. This behaviour suggests an improvement in the stability of the passive film. The difference between the polarisation behaviour of these two multiple plateau samples may be owing to the action of the PGMs. The perturbation in the centre of the passive region of the PGM-doped 316L samples was also observed by van der Merwe and Nelwalani [180] who suggested it may be caused by the activation of the hydrogen reaction owing to the cathodic modification mechanism.

To further explore the effect of PGM doping on pitting resistance specifically, samples were immersed in a 5 wt.% NaCl solution for a total of 24 hours and photographed to track the progression of corrosion. The photographs taken during this study are presented in Figure 7.7. As Figure 7.7 demonstrates, the sintered Ru-doped and Pd-doped samples showed some signs of crevice corrosion occurring at the interface between the sample and the resin in which it was mounted. As the crevice corrosion resulted from the methodology since the resin did not bond with the metal. As a result, the detected crevice corrosion was not considered a reflection of the corrosion performance of the samples and was ignored when analysing these samples under the microscope. Further testing was conducted with PTFE tape applied to the sample-resin interface (as shown in the tundish Ru-doped sample in Figure 7.7 (a)) to reduce the degree of crevice corrosion.

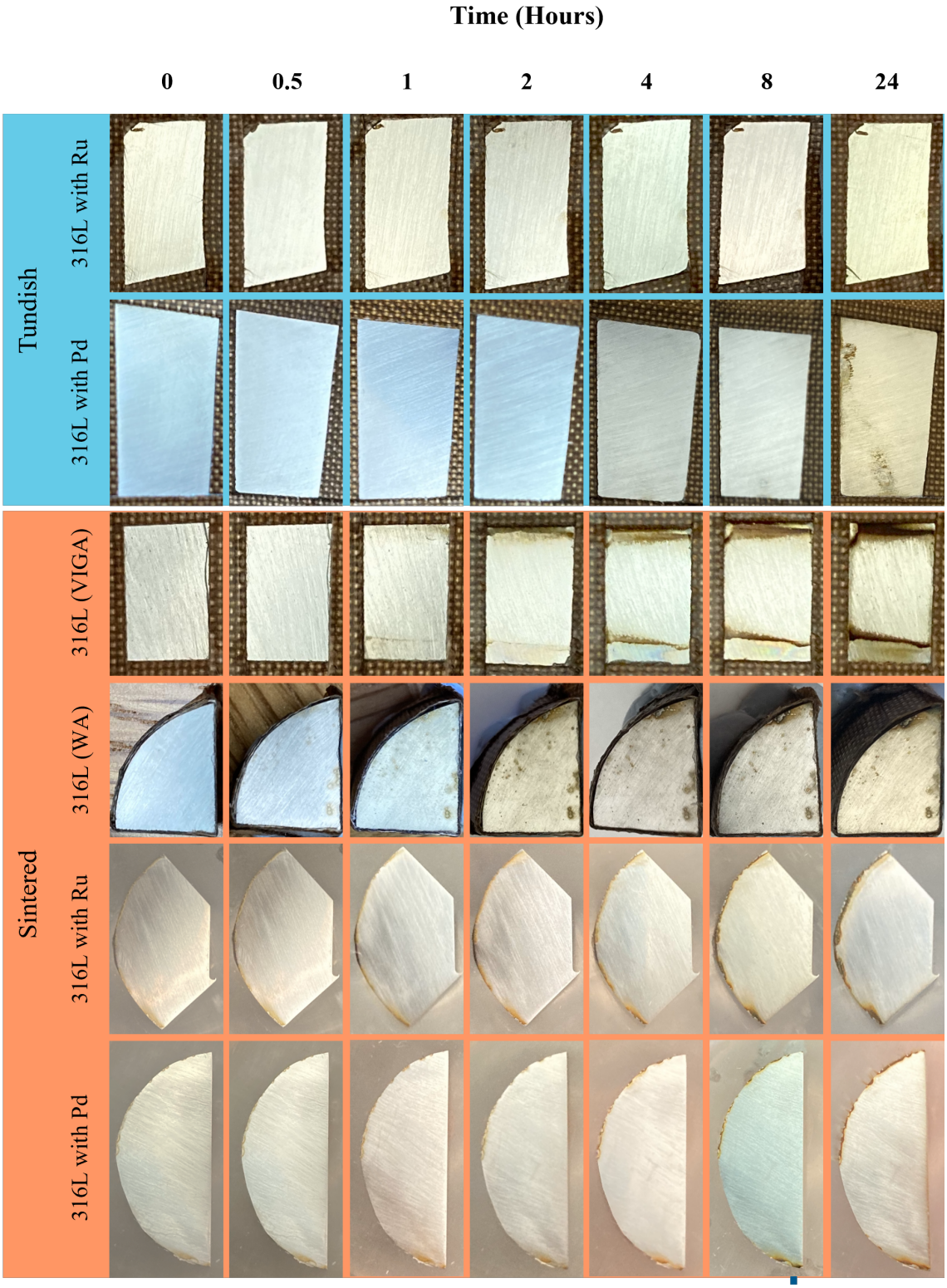

Figure 7.7: Photographs of 316L stainless steel samples taken during the 24 hour immersion test in 5 wt.% NaCl solution at room temperature. The sintered samples presented here were sintered at 1100°C for 600 s

Another point worth noting is since these samples were photographed immediately after being removed from the NaCl solution and rinsed with deionised water, corrosion products can also be seen on the surfaces of the samples, for example in Figure 7.7 (b-c). As a result, the features observed in sintered WA 316L may be partly owing to visible corrosion products and partly owing to the formation of pits. In the VIGA 316L and tundish Pd-doped 316L samples (shown in Figure 7.7 (b-c)), the path of corrosion product deposited on the surface which travelled down the sample in the direction of gravity can be observed. While these features indicate that corrosion has occurred the amount of corrosion product visible does not necessarily correlate to worse material degradation.

The photographs obtained during the immersion test revealed no obvious pitting corrosion in the tundish and sintered Ru- and Pd-doped samples (Figure 7.7 (a-b, e-f)). The most significant changes were observed in the WA 316L sample, illustrated in Figure 7.7 (d), with the appearance of spheroidal features which appeared after only 0.5 hours of immersion. Similarly, Figure 7.7 (c) presents the signs of degradation which appeared in the VIGA 316L sample following one hour of immersion. The differences in the appearance of the PGM-doped samples and the undoped samples may be due to the presence of the cathodic modifying elements in the former. Wolff et al.[184] also reported Ru additions have a positive effect on the pitting potential of Fe-Cr alloys. Similarly, Zuo et al.[260] found the presence of Pd as a film on 304 stainless steel improved corrosion resistance in NaCl solutions.

To further investigate the impact of immersion testing on the samples SEM characterisation was conducted. The analysis revealed pits of various morphologies. Spheroidal as well as elongated pits of varying sizes were observed across the different samples (Figure 7.8).

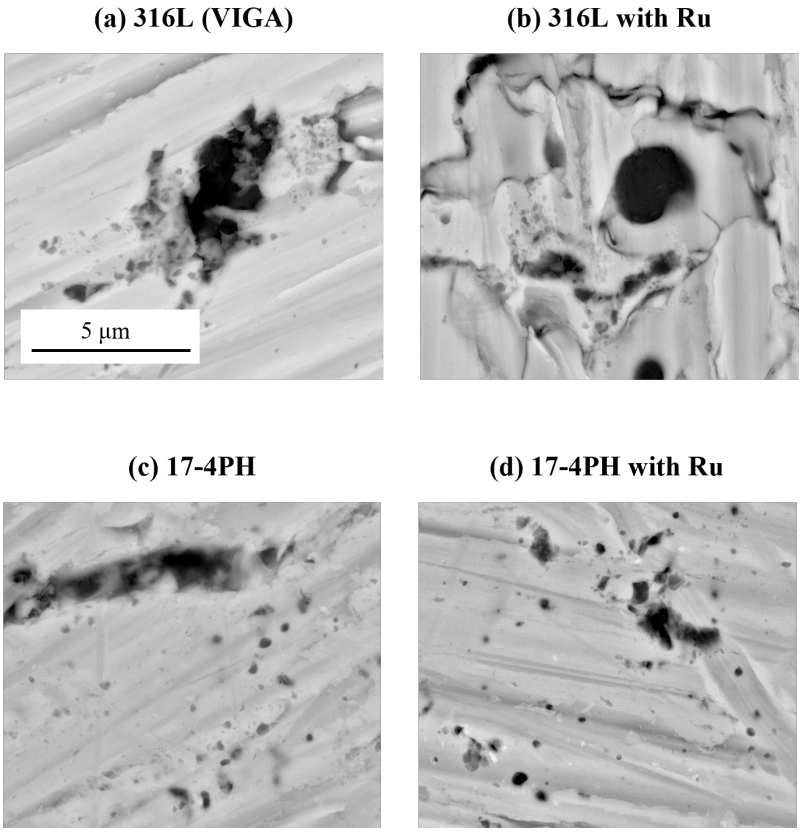

Figure 7.8: SEM micrographs of sintered (a) 316L (VIGA), (b) 316L with Ru (WA), (c) 17-4PH and (d) 17-4PH following immersion in 5 wt.% NaCl for 24 hours. Specimens were sintered at 1100°C for 600 s

Undoped 17-4PH exhibited signs of severe pitting (Figure 7.8 (c)). The pits observed were of larger dimension and less spherical than those observed in the PGM-doped samples (Figure 7.8 (b) and (d)). In their study of the pitting behaviour of FAST-processed 316L SS, Saito et al.[147] found that both pores and inclusions formed pit initiation sites. While the silicon oxide particles identified in Chapter 5 possess high aspect ratios reminiscent of the pits observed in Figure 7.8 (c) it is unlikely that their dissolution is the sole reason for these pits. The reason being that silicon oxides inclusions were found throughout both undoped and doped stainless steel samples in this study. As a result, it is expected that the silicon oxide dissolution and therefore similar pit morphology would occur across all sample compositions studied. Instead, the large and high aspect ratio pits were found primarily in undoped 17-4PH stainless steel.

While pits were found dispersed throughout the sample some pits appear to concentrate around SiO_2 inclusions (Figure 7.9). This suggests the passive film is less effective in this region. The silicon-rich oxides were also enriched in Cr relative to the surrounding areas. The depletion of Cr in the surrounding areas may be a reason for the passive film in this region being less effective, though quantitative elemental characterisation is needed to confirm that the concentration of Cr here is low enough to lead to passive film instability.

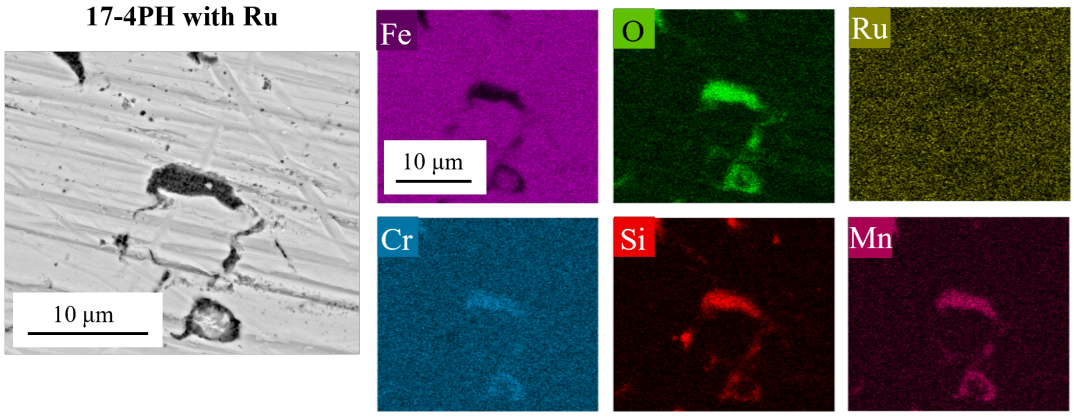

Figure 7.9: Scanning electron micrograph and EDS maps of Ru-doped 17-4PH stainless steel following immersion in 5 wt.% NaCl for 24 hours. Images were captured at x10k magnification. The micrograph illustrates the fine pits which develop in the vicinity of inclusions while the EDS maps show the elemental composition of the inclusions

Comparing 316L and 17-4PH

Based on chemical differences between the two stainless steel grades studied different synergistic alloying effects were expected. 17-4PH stainless steel contains little Mo, in contrast to 316L, which contains around 2% (Tables 3.1 and 3.3). Previous studies have found that Mo acts in synergy with PGMs in cathodically modifying stainless steels[261,262]. While it is reported that Mo promotes the cathodic evolution of hydrogen the reason for its synergistic effect alongside PGMs is unknown[258]. Another synergistic effect has been observed between Ni and Ru by Streicher[263] whereby it was found that Ni and Ru additions were more beneficial to corrosion resistance in boiling H_2SO_4 than either of the additions alone. The 316L SS used in this study have around 10 wt.% Ni content meanwhile the Ni content of the 17-4PH alloys is around 5 wt.%. Therefore, this synergistic behaviour is more likely to be exhibited in the 316L samples than the 17-4PH samples. However, this study observed similar OCP and potentiodynamic polarisation behaviour for both the 316L and 17-4PH stainless steel alloys with no clear synergistic effects being exhibited. This shows good agreement with the work of Sobral et al.[264] who found powder processed 316L and 17-4PH possessed similar electrochemical behaviour when evaluated in a H_2SO_4 solution.

7.4 Effect of Alloy Synthesis Technique

This section presents an investigation into the effect of the sample synthesis technique on corrosion behaviour. Water atomised samples of Ru- and Pd-doped 316L are compared with their cast equivalents. Also presented here is a comparison of undoped 316L stainless steel samples produced by two different atomisation techniques: water atomisation (WA) and vacuum induction gas atomisation (VIGA). Finally, bulk alloyed and functionally graded samples are compared to assess how the processing approach affects corrosion resistance.

7.4.1 Powder Metallurgy vs Cast

The OCP graphs were similar for cast and sintered Ru-doped 316L samples and the potential values were not found to deviate significantly for the duration of the test (Figure 7.10 (a)i). A constant OCP is suggestive of the passive film being present and stable[142]. Regarding the Pd-doped alloys, the OCP of the sintered samples converged at approximately the same OCP towards the end of the test. Conversely, the OCP of the cast sample was 0.05 V lower at the end of the test and appeared to be continually decreasing for the duration of the test (Figure 7.10 (b)i). Such behaviour is indicative of the sample becoming electrochemically active (i.e. corroding) within the test solution[142].

Unlike the current study, Raghu et al.[142] found that wrought 316L stabilised in sulphuric acid faster than the sintered samples. The absolute time for the wrought sample to stabilise was approximately 50 hours while the sintered samples did not stabilise for the duration of the 100 hour test. The discrepancies between this study and that of Raghu et al.[142] may be because the solution strength used in the study of Raghu et al.[142] was higher than that used in this study (0.5 M vs 0.05 M H_2SO_4) and that the sintered samples were of higher porosity than used in this study (29 - 63% vs 1 - 18%). These factors may explain why the sintered samples in this study appeared to outperform those tested by Raghu et al.[142]. It is unlikely the PGMs are responsible for the differences between this study and that of Raghu et al.[142] since the behaviour of the samples in this study, both undoped and doped, is broadly similar which therefore suggests that alternative factors are responsible.

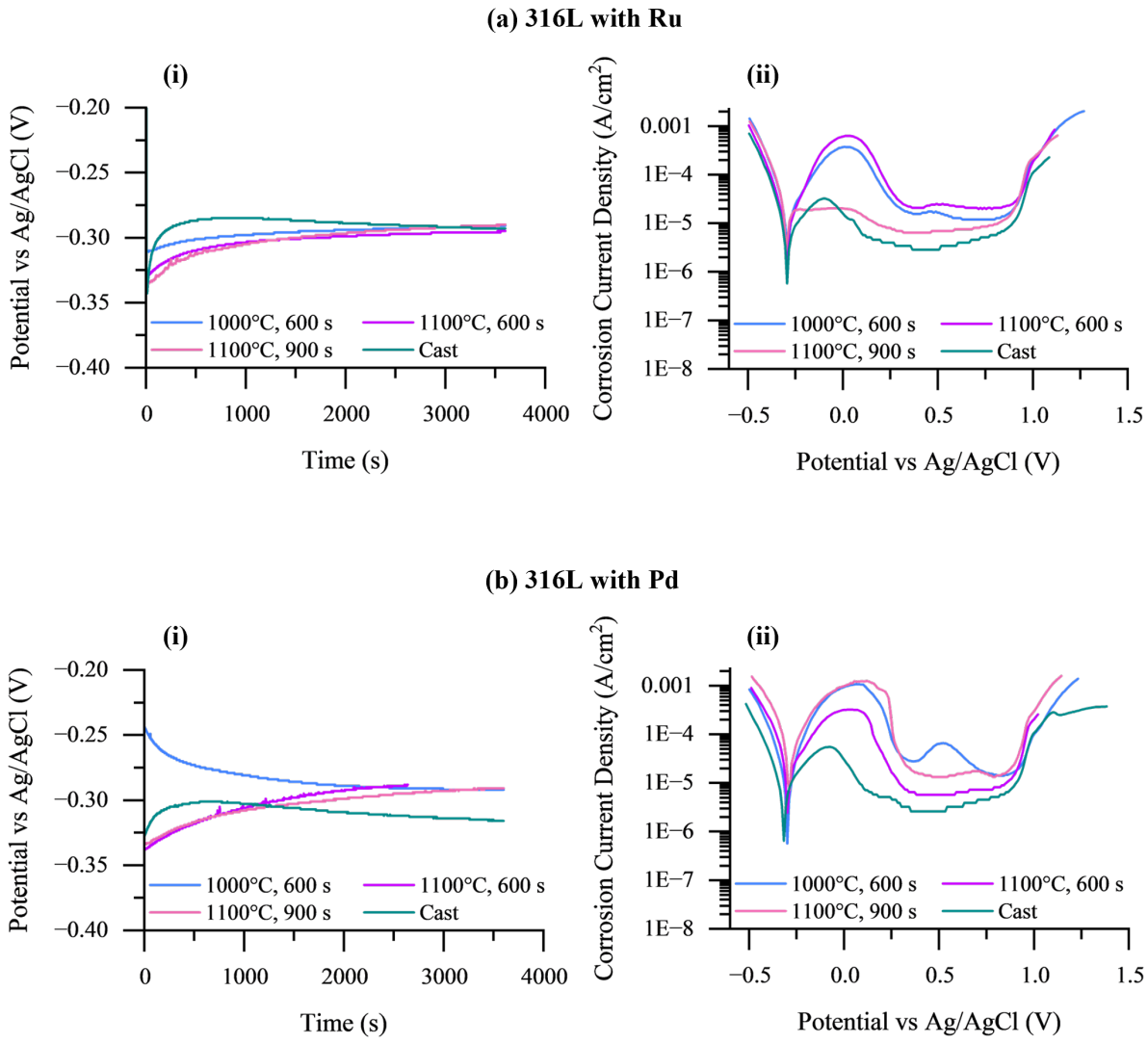

Figure 7.10: OCP (i) and potentiodynamic polarisation (ii) curves comparing PGM-doped 316L stainless steel samples produced by sintering and their cast equivalents exposed to 0.05 M H_2SO_4. Graphs (a)i-ii show Ru-doped samples while (b)i-ii present the Pd-doped samples

As shown in Table 7.2, passivation was generally easier to achieve in the cast samples as indicated by their low i_{crit}. Similar to what was found by Raghu et al.[142], the current study found that both the cast samples possessed lower i_{pass} than their PM equivalents (Table 7.2). The Ru-doped sintered samples sintered at 1100°C for 900 s, however, achieved the same order of magnitude i_{crit} and i_{pass} values as their cast equivalents. Contrastingly, the Pd-doped sample produced under the same conditions did not. This suggests the cast samples are more effective at inhibiting the anodic dissolution of the stainless steel. A reason for the increased i_{crit} and i_{pass} in the sintered samples may be due to the presence of pores. Raghu et al.[142] states that discontinuities and pores interfere with passive film formation increasing the active-to-passive transition current. Despite the presence of segregation in the cast samples identified in Section 5.1.6 these samples outperform the PM samples. This suggests that porosity is more detrimental to corrosion resistance than the presence of elementally enriched regions.

In the current study, the difference in i_{crit} between the cast and sintered samples was a maximum of one order of magnitude for the Ru-doped samples, while the spread of data for the Pd-doped samples was two orders of magnitude. The absolute values of i_{crit} for the Ru-doped samples was also generally lower than the Pd-doped. This is despite the Ru-doped and Pd-doped samples possessing similar densities when produced under the same sintering conditions. The passivation currents for both the Ru- and Pd-doped samples were within the same orders of magnitude. From this trend it can be deduced that the type of PGM addition impacts different corrosion parameters differently. While Ru doping more efficiently improved the ability with which passivation can be achieved both Ru and Pd doping had similar effects on inhibiting the anodic dissolution of the stainless steel.

Both the cast samples in the current study also exhibited wider passive ranges than their sintered counterparts. This was also found by Raghu et al.[142] and Geenen et al.[143]. All samples, both cast and sintered experienced the breakdown in passivation at around 1.0 V, a similar value to what is found in the literature[142,143].

Table 7.2: Summary of corrosion parameters extracted from potentiodynamic polarisation graphs of cast and sintered Ru- and Pd-doped 316L stainless steel

		Ru-Doped	Pd-Doped	Ru-Doped	Pd-Doped
Processing Technique		i_{crit} (µA cm^{-2})		i_{pass} (µA cm^{-2})	
Tundish		32	56	2.9	2.6
Sintered	1000°C, 600 s	370	1060	12	16
	1100°C, 600 s	630	320	21	5.7
	1100°C, 900 s	19	1240	6.4	13

7.4.2 Water Atomisation vs Gas Atomisation

This study revealed the GA 316L samples achieved more noble OCP than the WA sintered samples across the sintered parameters explored (Figure 7.11). Stability was also achieved substantially faster in VIGA samples than in the WA samples. This suggests that passivation was easier to achieve in the samples made using VIGA feedstock compared with those produced using WA powder. A comparison of the polarisation graphs revealed the i_{pass} for VIGA was lower than the samples made from WA 316L powder. Additionally, in the samples produced at 1100°C for 600 s, it was revealed the i_{crit} was lower for the VIGA.

This study shows good agreement with the work of Tobar et al.[63] and Jandaghi et al.[61] who also observed that GA 316L stainless steel possessed more noble OCP than the WA equivalents. The shorter time to potential stability exhibited by the samples produced from VIGA powders may be due to the impact of pore morphology on the stability and the ease with which the passive film forms[142,148]. This reasoning can also be used to explain why the passivation currents for the samples produced by VIGA powders are lower than that obtained by the samples produced by WA powders.

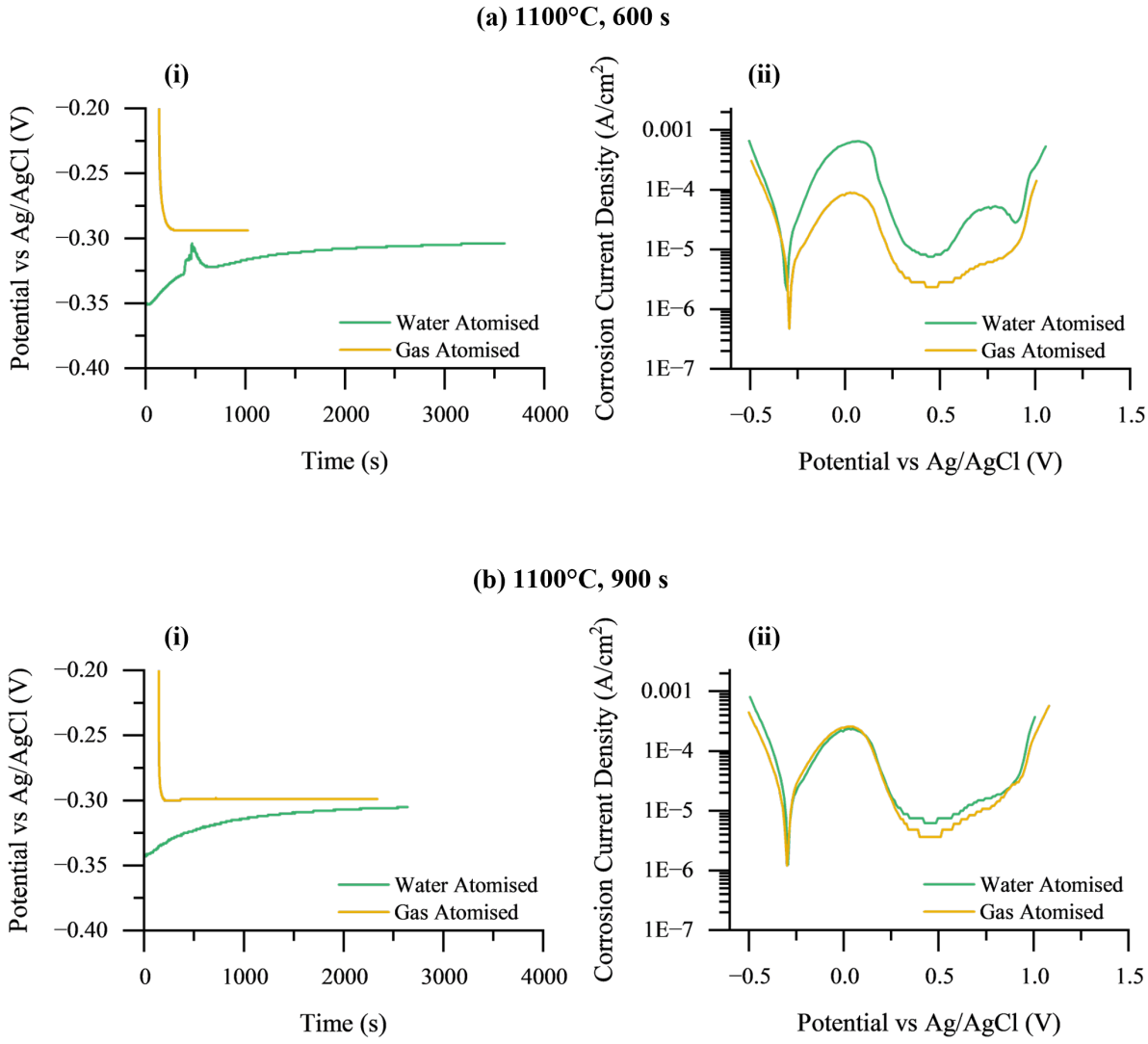

Figure 7.11: OCP (i) and potentiodynamic polarisation (ii) curves comparing sintered water and gas atomised 316L powders exposed to 0.05 M H_2SO_4. Graphs (a) (i-ii) present the samples produced by sintering at 1100°C for 600 s while (b) (i-ii) illustrate the behaviour of the samples produced by sintering at 1100°C for 900 s

In published research, porosity is sometimes attributed to the differences in the corrosion behaviour of WA and GA stainless steels. Specifically, poorer corrosion resistance is ascribed to higher porosity[144,148,149]. However, since the relative densities of the samples in this study are similar, between 96.5 - 99%, it suggests that total porosity is unlikely to explain the differences in the corrosion performance of the VIGA and WA samples studied. Conversely, dissimilarities were observed in the pore sizes, with finer pores being observed in the VIGA samples. Fine and widely distributed surface pores have been found to cause more rapid corrosion. This relationship is ascribed to passivation being harder to achieve because finer pores represent more interruptions in the passive film[62,142,148]. Since the VIGA samples have higher numbers of fine pores this indicates the corrosion behaviour will be worse (Figure 5.20). However, the opposite was found to be true in the current study with the VIGA possessing better corrosion characteristics. This suggests that an alternative factor is contributing to the observed corrosion behaviour. The difference between the data and this study may be owing to the electrolyte used. The polarisation studies in this investigation were carried out in H_2SO_4 while the literature reporting on the effects of pore size on corrosion properties were studied in chloride containing environments (NaCl and HCl). The differences in the observations in this study and those presented in the literature may be owing to the presence of chlorides affecting the corrosion mechanism that proceeds. Stainless steels are highly susceptible to pitting corrosion in the presence of chlorides while it is expected that only general corrosion will occur when exposed to H_2SO_4.

In other research, higher Mn contents have been attributed to worse corrosion resistance when comparing WA and VIGA powders due to their contributions in forming MnS inclusions which are highly detrimental to pitting corrosion[58,61,265]. In the current study, though the VIGA powder has 99% more Mn than the WA powder, the VIGA samples outperformed those produced from WA powders. However, it is worth noting that MnS inclusions were not detected in either the VIGA nor WA samples during the chemical characterisation. This suggests that in this particular study, an alternative factor is the primary contributor to the observed corrosion behaviour.

An additional factor reported to negatively impact the corrosion behaviour of sintered parts is Si-rich oxides which represent areas of local Cr depletion[74]. In the current study, the degree of Si-rich oxide surface coverage was higher in the WA samples, agreeing with previously made observations[72,150]. The discrepancy in the Si-oxide content of compacts

made from the two powder types may be a factor contributing to their differing corrosion behaviours.

Immersion Testing

As illustrated in Figure 7.12, both WA and VIGA samples showed signs of pitting corrosion following immersion in NaCl solution. Analysis of the low magnification (x5 and x10) OM images using ImageJ revealed the mean pit area was higher in the VIGA sample but the overlap in the data means that this difference in the data may not be statistically significant (Table 7.3). The area covered by pits in the micrographs was determined to be similar for both the WA and VIGA samples. However, it should be stressed that since only low magnification micrographs were analysed here, smaller pits which are beyond the resolution capable at x5 and x10 magnification will not be captured here.

The differences in pore morphology in the two samples (as shown in Figure 5.4 and 5.26) appears to make no discernible impact on the resistance to pitting. Optical microscopy revealed both 316L samples were susceptible to pitting corrosion, which is to be expected of stainless steels exposed to a chloride containing environment.

Table 7.3: Summary of pit area analysis of WA and VIGA 316L stainless steel samples sintered at 1100°C for 600 s following immersion in 5 wt.% NaCl for 24 hours. Measured by image analysis of x5 and x10 magnification micrographs

Sample	Mean Pit Area (μm^2)	Area Coverage (%)
WA	15.4 ± 10.95	0.56 ± 0.17
VIGA	20.42 ± 11.78	0.46 ± 0.30

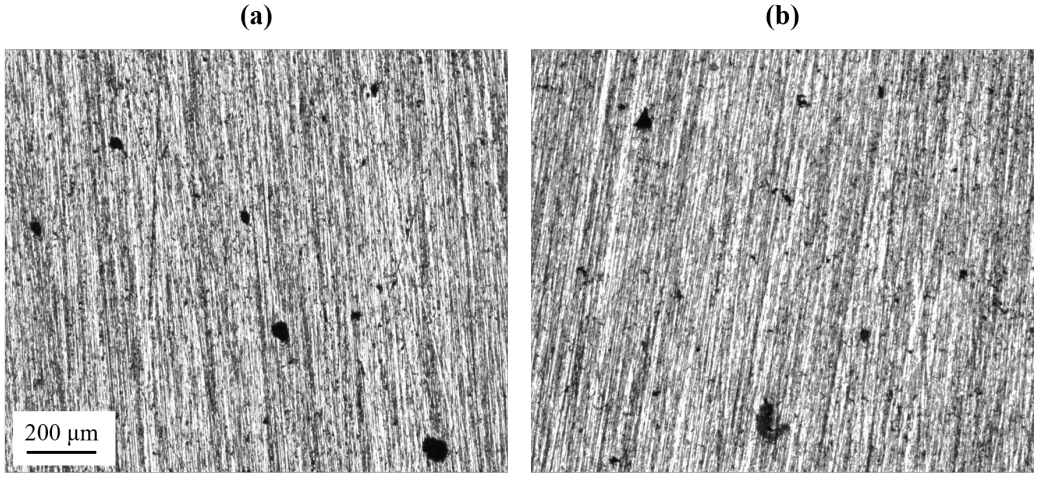

Figure 7.12: Optical micrographs of cleaned (a) WA and (b) VIGA specimens sintered at 1100°C for 600 s following immersion in 5 wt.% NaCl for 24 hours. Images captured at x5 magnification. The visible striations are caused by the final P1200 polish performed before corrosion testing

7.5 Functionally Graded Samples

Selected areas in the undoped and PGM-doped regions of the 17-4PH/Pd-doped 17-4PH FGM were characterised following immersion in 5% NaCl. Visual inspection by SEM revealed no clear differences in the two regions (Figure 7.13). The pits were further investigated by image analysis. This characterisation revealed the mean pit area in the two layers of the FGM was not statistically different from one another (Table 7.4). Plotting the distribution of the pit area revealed the data skewed left for both regions of the FGM meaning both regions exhibit a greater proportion of smaller pits. However, differences can be observed in the number of pits detected, with that figure being greater in the undoped region. Similarly, the upper range of measured pit area is higher in the undoped region. As previously discussed, pits can represent interruptions in the passive film, in which case, greater pit numbers are detrimental to corrosion resistance[62,142,148]. The data suggests the presence of a PGM had a small effect on the pitting corrosion resistance of the stainless steel in chloride environment. This shows good agreement with the corrosion behaviour observed in the bulk alloyed samples whereby undoped 17-4PH exhibited greater signs of pitting attack than its PGM-doped counterparts (Figure 7.8). Additionally, it indicates a material's corrosion resistance is not impacted by whether it is bulk alloyed or functionally graded.

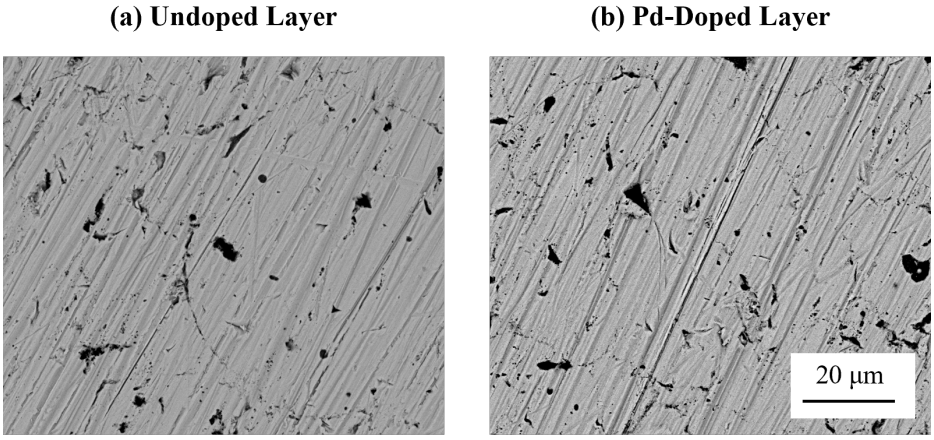

Figure 7.13: SEM micrographs of the 17-4PH/Pd-doped 17-4PH FGM following immersion in 5 wt.% NaCl for 24 hours. Micrograph (a) presents the undoped layer while (b) presents the Pd-doped layer. The visible striations are caused by the final P1200 polish performed before corrosion testing

Table 7.4: Summary of pit area analysis of 17-4PH/Pd-doped 17-4PH stainless steel FGM sample following immersion in 5 wt.% NaCl for 24 hours

Layer	Mean Pit Area (μm^2)
Undoped 17-4PH	0.11 ± 0.41
Ru-doped 17-4PH	0.15 ± 0.47

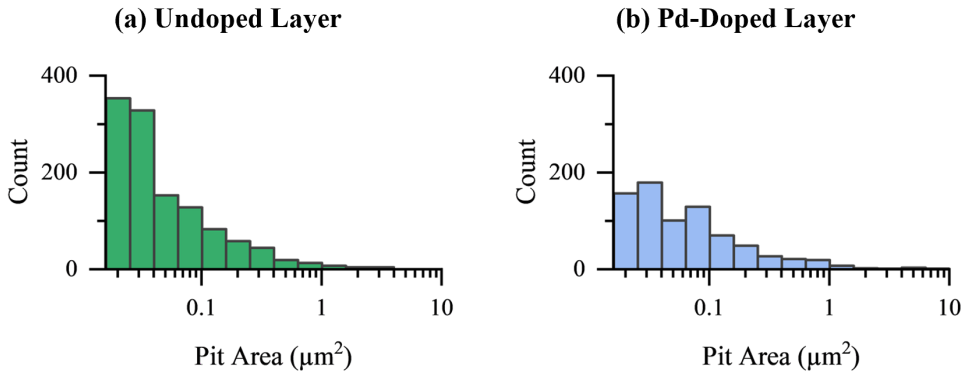

Figure 7.14: Histogram illustrating the distribution of pit areas in the 17-4PH/Pd-doped 17-4PH FGM following immersion in 5 wt.% NaCl for 24 hours. Graph (a) illustrates the data from the undoped layer and (b) presents the findings from the Pd-doped layer

7.6 Effect of Heat Treatment

As previously explained, 17-4PH is a stainless steel which is typically utilised in its heat treated condition to exploit the enhanced mechanical properties which evolve. For the corrosion testing in this study to yield industrially relevant results, it was desirable to perform corrosion studies of the material in this condition. The sintered undoped and doped 17-4PH specimens were subjected to the H1075 heat treatment. This involved solution treatment at 1050°C for 0.5 hours followed by air cooling. The samples were then aged by holding them at 579°C for 4 hours. Subsequently, the samples were exposed to 0.05 M H_2SO_4 for OCP and potentiodynamic polarisation testing.

The effect of the heat treatment on the OCP was variable, with no clear trend emerging (Figure 7.15). In terms of the time taken to achieve stability, the potential of some heat treated samples did not plateau during the entire OCP test (Figure 7.15 (c) and (i)). These samples showed a slight decrease in OCP during the exposure time which suggest passive film dissolution and activation of the metal surface leading to increased corrosion[25,256]. Raghu et al.[142] and Kazior[266] also observed the decrease of OCP with time when analysing sintered stainless steel. This change was accompanied by the penetration in the pores and the stagnation of the electrolyte. While the potential decrease observed by Raghu et al.[142] was greater than that observed in the current study, Raghu et al.[142] observed a decrease from 0 mV to -280 mV, it was observed over a greater time frame (40 hours). The current study analysed the samples over a 1 hour time period. It may be the test was not carried out for long enough to observe the degree of change in OCP that was found by Raghu et al.[142]. Additionally, the samples explored in this study are less porous than those investigated by Raghu et al.[142] and so less electrolyte pore penetration is expected here.

The undoped heat treated samples exhibited lower OCP values than the undoped as-sintered samples (Figure 7.15 (a-c)). This was also observed by Kazior[266] in solution annealed and aged at 490 and 500°C sintered 17-4PH stainless steel when exposed to 0.5 M NaCl. However, the same study found ageing at the slightly lower temperature of 480°C resulted in an improved corrosion resistance. Additionally, solution annealing alone led to the best corrosion performance in the sintered samples. An explanation for why this occurs was not given but these findings suggest that if corrosion resistance is a priority heat treatment should be optimised.

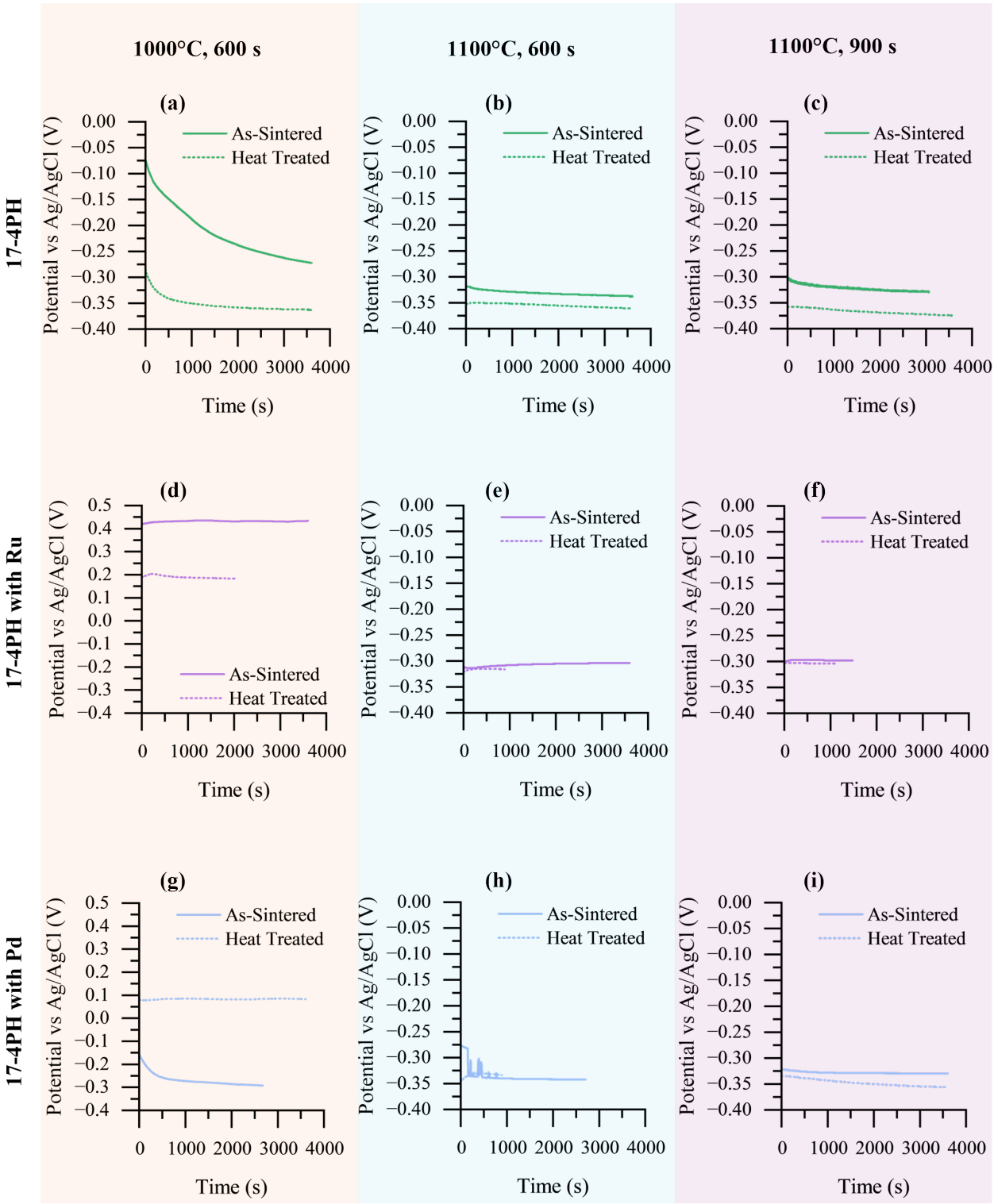

Figure 7.15: OCP curves comparing the as-sintered and the heat treated 17-4PH stainless steel specimens exposed to 0.05 M H_2SO_4 for 3600 s

Heat treatment did not have a consistent effect on the OCP of the PGM-doped samples (Figure 7.15 (d-i)). In the PGM-doped samples sintered at 1100°C for 600 s, the absolute OCP values were similar for the as-sintered and heat treated samples. Meanwhile in the Ru-doped sample produced at 1000°C for 600 s and the Pd-doped sample produced at 1100°C for 900 s both had higher OCP in the as-sintered condition.

With the majority of specimens in this study exhibiting a similar OCP in both the as-sintered and heat treated state it is implied the heat treatment has little impact on the thermodynamic stability of the passive film in this particular test medium. This disagrees with the previous studies which have concluded heat treatment leads to better corrosion performance by solutionising the material leading to a more homogeneous distribution of alloying elements and a more refined microstructure[77,153]. It should be highlighted, however, the data reporting the annealing effect of the heat treatment is concerning wrought, cast and AM samples, which often possess microstructural and elemental inhomogeneities[77,153,155]. Contrastingly, the samples in the current study were produced by sintering and possessed generally homogeneous elemental distribution, as observed in Section 5.1.1. This therefore limits the homogenising potential of heat treatment and its eventual impact on corrosion performance where sintered compacts are concerned.

In addition to chemical influences, microstructure is reported to impact the corrosion performance of martensitic stainless steels[154,267]. The current study found a correlation between the OCP and the microstructure before and following heat treatment. Specifically, samples determined to be fully martensitic following heat treatment were also characterised by a reduction in OCP. The observed trend shows good agreement with what is reported regarding the effect of martensite on corrosion resistance. Austenite retained in martensitic stainless steels is associated with improved corrosion resistance. Wang et al.[154] found heat treated SLM-processed 15-5PH stainless steel samples in possession of more austenite following heat treatment exhibited higher pitting potentials and more stable passive films than those possessing less. With SKPFM analysis confirming austenite has a surface potential 15 mV higher than martensite. Similar findings were reported also by Li et al.[267] in their study of LPBF 17-4PH stainless steel who observed the corrosion resistance of these samples deteriorated following heat treatment owing to the decreased in austenite content.

Spontaneous passivation was exhibited by two of the heat treated samples, as shown

in Figure 7.16 (d and g). In both samples, spontaneous passivation appeared only following HT with this behaviour being absent from the as-sintered specimen. To the best of the author's knowledge, this behaviour has not been observed elsewhere and it is unknown why it is occurring here. Similar to the trends observed in OCP, HT has the effect of slightly increasing i_{crit}. The same effect is observed in the Ru-doped samples. Contrastingly, this trend was observed in only one of the Pd-doped samples.

HT had no observable effect on neither the passivation range nor the breakdown potential of the samples. The findings of this study contrast that reported by Kazior[266] who found both passivation range and breakdown potential were significantly affected by HT. Specifically, the passivation range widened by up to approximately 0.75 V following HT while the breakdown potential was shifted to more noble values. In the same study, Kazior[266] observed variations of plus or minus 0.2 V in the measured OCP resulting from heat treatment. The differences in findings of the current study and that of Kazior[266] may be due to the electrolyte used. While this study performed electrochemical testing in H_2SO_4, testing was carried out by Kazior[266] in NaCl. The differences suggest HT may have a more profound effect on the pitting corrosion resistance of precipitation hardening stainless steels compared to its effect on their resistance to general corrosion.

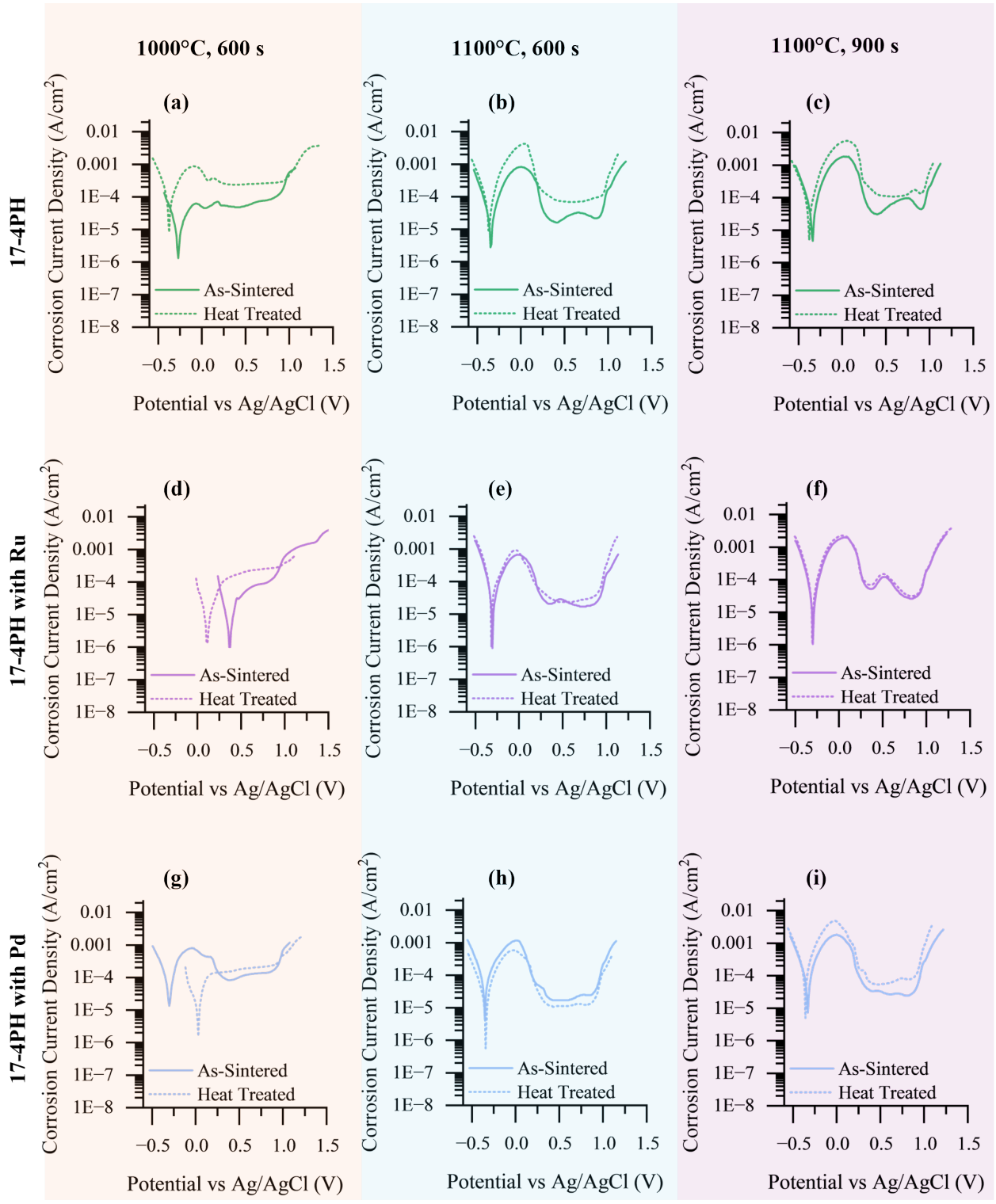

Figure 7.16: Potentiodynamic polarisation curves comparing the as-sintered and the heat treated 17-4PH stainless steel specimens exposed to 0.05 M H_2SO_4

7.7 Chapter Findings

Increasing sintering temperature was more effective than increasing sintering time at improving corrosion resistance. The effect of sintering temperature on corrosion performance was more pronounced in the 17-4PH samples. This trend was attributed to the large increase in density that was exhibited by 17-4PH with the increase in sintering temperature and its beneficial effect on the protective properties of the passive film. For most sintering parameter combinations, the best corrosion corrosion resistance in H_2SO_4 was exhibited by a PGM-doped sample. The presence of PGMs was also determined to improved corrosion behaviour in NaCl solutions. Additionally, showing good agreement with the literature, Ru was determined to be more beneficial to corrosion resistance than Pd. Contrasting the corrosion performance of sintered and cast PGM-doped stainless steel revealed superior resistance capabilities in the latter. This was attributed to the residual porosity observed in the sintered samples and the passive film destabilising effect they have. Comparing the corrosion performance of sintered compacts made from water and vacuum inert gas atomised powders revealed small behavioural differences. Overall, the VIGA compacts outperformed the WA equivalents. This was attributed to the presence of silicon-rich oxides detrimentally affecting the stability of the passive film. The corrosion behaviour of the FGM exposed to NaCl showed good agreement with that of the bulk alloyed samples, indicating that each composition retained its corrosion characteristics despite being incorporated into a graded material. The impact of the H1075 heat treatment on hardness was evaluated here. While previous studies have determined heat treatment benefits corrosion resistance by homogenising elemental distribution, this research revealed the heat treatment did not have a consistent effect on the corrosion behaviour. This lack of correlation was attributed to the elemental homogeneity the as-sintered sample possessed, limiting the further homogenisation, and therefore corrosion resistance enhancement, that heat treatment could facilitate. A relationship between corrosion behaviour and microstructure was identified here. Specifically, a correlation between fully martensitic microstructures and worse corrosion behaviour was found. While martensite is a phase whose presence in heat treated 17-4PH is associated with enhanced mechanical properties, its detrimental impact on corrosion resistance, as detected here and elsewhere, therefore highlights the performance trade-off. In the context of doped precipitation hardening stainless steels the presence of PGM additions had no clear effect on the heat treatment response.

CHAPTER

8

Conclusions and Recommendations

The aim of this work was to use field assisted sintering to produce bulk alloyed and functionally graded Ru- and Pd-doped 316L and 17-4PH stainless steels by powder metallurgical processing. The specific questions which were answered by working towards this aim were:

1. What is the optimal sintering temperature and time combination for the compositions explored?
2. Can field assisted sintering be used to produce a PGM-doped stainless steel functionally graded material?
3. What is the effect of atomisation technique on microstructure, mechanical and corrosion properties?
4. What is the effect of PGM presence on microstructure, mechanical and corrosion properties?
5. What is the effect of processing technique on microstructure, mechanical and corrosion properties?
6. What is the effect of heat treatment on powder processed PGM-doped 17-4PH stainless steel?

Finding 1

The effect of sintering temperature and time was evaluated in Section 5.1. These conditions were varied between 1000 - 1100°C and 300 - 900 s, respectively. The obtained results found with increased sintering temperature the samples were more dense, with this trend being more significant in the 17-4PH samples. Increasing the sintering time had a weaker impact on the density of the samples owing to the fact that sintering temperature was maintained at 1100°C for these tests, a temperature at which all samples had achieved near-full density. Based on density measurements, the optimal combination of processing parameters based on the range of parameters explored here is sintering at 1100°C for 600 s. This combination of parameters resulted in the most time-efficient achievement of near-full density samples. Overall, these sintering parameters also led to better corrosion behaviour.

Finding 2

As presented in Section 5.2, crack-free PGM-doped functionally graded samples were successfully produced by FAST. These were produced by layering the different powder compositions on top of one another prior to sintering. This project has demonstrated the feasibility of FAST in producing PGM-doped functionally graded materials. The FGM samples showed uniform microstructure and mechanical properties throughout their depth.

Finding 3

In Sections 5.1.7 and 7.4.2, the effect of atomisation technique on microstructure, mechanical and corrosion properties was evaluated by comparing sintered water atomisation (WA) and vacuum induction gas atomisation (VIGA) 316L powders. Experimental findings determined both samples could be sintered to near-full density under the sintering conditions explored in the current study. The nature of the porosity in the two samples was observed to differ, with WA samples possessing coarser pores than the VIGA samples. Other studies found VIGA specimens possess a lower degree of oxide inclusions than WA on account of the inert atomisation atmosphere. The current study confirmed this with significantly smaller and less numerous oxide inclusions being observed in the VIGA samples when compared with the WA. The mechanical properties differed between the two sample types with the VIGA samples possessing lower hardness than the WA equivalents. This finding was attributed to the coarseness of the VIGA microstructure compared with the WA sample since grain size impacts mechanical

properties, as illustrated by the Hall-Petch relationship. The VIGA sample exhibited superior corrosion resistance. The lower content of Si-rich oxides in the VIGA samples was established to be a probable cause for its enhanced corrosion characteristics.

Finding 4

The 316L and 17-4PH stainless steel compositions explored in this study were doped with 0.5 wt.% Ru and Pd. Hardness testing confirmed that PGM presence did not effect mechanical properties, as expected. Similarly, the Ru and Pd additions were found to be uniformly distributed in solid solution in the doped samples and had no other impact on microstructure. In terms of corrosion characteristics, consistent with the literature, Ru was determined to be more beneficial to corrosion resistance than Pd. It was observed that across the sintering parameters explored the PGM-doped samples generally outperformed the undoped samples in H_2SO_4 and NaCl.

Finding 5

This study evaluated the impact of processing technique by comparing the properties and behaviour of sintered and cast PGM-doped 316L stainless steel. This study found that the cast sample had the expected dendritic microstructure. Contrastingly, the sintered samples possessed equiaxed grain structures. While the bulk elemental composition of the sintered and cast samples were analogous some differences were observed in terms of elemental distribution. Cast samples were found to be in possession of areas enriched in Cr, Mo and Nb while in the sintered samples these areas were absent. The mean hardness of the cast PGM-doped samples was slightly higher than the sintered equivalents. This difference was attributed to the porosity evolving from the powder metallurgy negatively impacting mechanical properties. In terms of their comparative corrosion resistance, the cast samples exhibited better corrosion performance possessing wider passive ranges, lower i_{crit} and i_{pass} when compared with the sintered samples. This trend was again attributed to the absence of pores in the cast samples.

Finding 6

The sintered 17-4PH samples were subjected to the H1075 heat treatment with the aim of precipitating material hardening Cu-rich precipitates. The H1075 is a typical heat treatment for 17-4PH alloys which involves two steps: the first step is to solution treat the material at 1050°C for 0.5 hours and the second step is to age the sample at 579°C for four hours. Experimentation determined that the heat treatment successfully caused the precipitation of nano-sized Cu-rich particles. Although the hardness enhancing

effect of the heat treatment on the samples was varied the hardness of the sintered samples showed good agreement with or exceeded the hardness values published in literature for similar materials. While it is reported heat treatment can be beneficial to corrosion resistance owing to its homogenising effect this study did not find a clear effect of heat treatment on corrosion resistance. This lack of correlation was attributed to the elemental homogeneity the as-sintered sample possessed, limiting the further homogenising, and therefore corrosion resistance enhancement, that heat treatment could have.

8.1 Industrial Recommendations and Future Work

This study has demonstrated that powder metallurgical processing can be used to produce PGM-doped functionally graded materials. Given the findings of this study, it is plausible that the output corrosion resistance enhancement could be further improved. The author highlights the following areas for future study:

Porosity
Pore size and morphology have an effect on the way in which corrosion proceeds. Characterising pore features in a future study can help to elucidate the relationship between pore characteristics and corrosion performance in the context of PGM-doped stainless steels. Micro-CT is a technique which could be used to understand the nature of pores.

Inclusion Minimisation
This study found that silicon oxide inclusions are detrimental to corrosion behaviour. Alternative approaches that can be used to minimise the presence of silicon oxide inclusions include:

- Different atomisation technique, e.g. vacuum inert gas atomisation or plasma atomisation
- Different sintering conditions, e.g. sintering in a reducing atmosphere

PGM Concentration
The author also recommends exploring doping with higher quantities of PGMs. It may be that due to the deleterious effects of the pores inherent to powder metallurgy that greater proportions of PGMs are required to maximise the cathodic modification effect in sintered specimens.

8.1.1 Summary

This study has demonstrated the feasibility of PM processing in producing cathodically modified functionally graded materials. Such materials have potential applications in electrowinning cells, fuel cells and waste-water treatment fuel cells. The more economic and efficient use of PGMs for cathodic modification when employed using powder metallurgical approaches widen the potential range of applications and industries in which cathodic modification is an appropriate engineering solution. In combination

with the evolving PGM market, where cathodic modification was previously prohibitive economically, it opens up the industries in which cathodic modification can be employed.

Bibliography

[1] H. Bhadeshia and R. Honeycombe. *Steels: Microstructure and Properties*. Butterworth-Heinemann, fourth edition, 2017.

[2] P. K. Samal. *Corrosion Resistance of Powder Metallurgy Stainless Steels*, pages 447–457. ASM International, September 2015.

[3] R. Song, J. Xiang, and D. Hou. Characteristics of Mechanical Properties and Microstructure for 316L Austenitic Stainless Steel. *J. Iron. Steel Res. Int.*, 18(11): 53–59, 2011.

[4] J. K. L. Lai, C. H. Shek, and K. H. Lo, editors. *Stainless Steels - An Introduction and Their Recent Developments*. Bentham Science Publishers, Dubai, United Arab Emirates, 2012.

[5] T. Michler. Austenitic Stainless Steels. In *Reference Module in Materials Science and Materials Engineering*. Elsevier, Amsterdam, the Netherlands, 2016.

[6] G. S. Was and S. Ukai. Austenitic Stainless Steels. In *Structural Alloys for Nuclear Energy Applications*, pages 293–347. Elsevier, Amsterdam, the Netherlands, 2019.

[7] P. A. Schweitzer. *Corrosion Engineering Handbook - Fundamentals of Metallic Corrosion - Atmospheric and Media Corrosion of Metals*. Taylor & Francis, Abingdon-on-Thames, UK, second edition, 2007.

[8] D. T. Llewellyn and R. C. Hudd. Chapter 4 - Stainless Steels. In D. T. Llewellyn and R. C. Hudd, editors, *Steels*, pages 291–379. Butterworth-Heinemann, Oxford, UK, third edition, 1998.

[9] F. Moyo, J. W. van der Merwe, D. Wamwangi, and Y. A. Mgwebi. Cathodic Modification of Stainless Steels with Ruthenium: A Review of Recent Advances in Making the Cheaper Option Cheaper. *Corros. Rev.*, 36(6):495–505, 2018.

[10] F. Moyo. *Using Ruthenium to Modify Surface Properties of Austenitic Stainless Steel for Improved Corrosion Resistance*. PhD thesis, University of the Witwatersrand, 2017.

[11] J. H. Potgieter, A. M. Heyns, and W. Skinner. Cathodic Modification as a Means of Improving the Corrosion Resistance of Alloys. *J. Appl. Electrochem.*, 20(5): 711–715, 1990.

[12] P. Monnartz. Iron-Chromium Alloys with Special Consideration of Resistance to Acids. *Metallurgie*, 8(7), 1911.

[13] E. M. Sherif, J. H. Potgieter, J. D. Comins, L. Cornish, P. A. Olubambi, and C. N. Machio. The Beneficial Effect of Ruthenium Additions on the Passivation of Duplex Stainless Steel Corrosion in Sodium Chloride Solutions. *Corros. Sci.*, 51(6):1364–1371, 2009.

[14] E. M. Sherif. Corrosion Behavior of Duplex Stainless Steel Alloy Cathodically Modified with Minor Ruthenium Additions in Concentrated Sulfuric Acid Solutions. *Int. J. Electrochem. Sci.*, 6:2284–2298, 2011.

[15] O. A. Olaseinde, J. W. van der Merwe, L. A. Cornish, L. H. Chown, and P. A. Olubambi. Electrochemical Studies of Fe-21Cr-1Ni Duplex Stainless Steels with 0.15wt.% Ruthenium at Different Temperatures. *J. South. Afr. Inst. Min. Metall*, 112:535–538, 2012.

[16] J. H. Potgieter, E. Wentzel, and G. Myburg. Effects of Vapour Deposited and Bulk Alloyed Ruthenium on Corrosion Resistance of a Duplex Stainless Steel in Sulphuric Acid. *Surf. Eng.*, 8(4):289–291, 1992.

[17] A. van Bennekom and J. H. Potgieter. Effect of Surface Alloyed Silver on Corrosion Behaviour of Austenitic Stainless Steel in Sulphuric Acid. *Surf. Eng.*, 17(1):71–74, 2001.

[18] P. Peled and D. Itzhak. The Corrosion Behavior of Double Pressed, Double Sintered Stainless Steel Containing Noble Alloying Elements. *Corros. Sci.*, 30(1): 59–65, 1990.

[19] P. A. Olubambi, J. H. Potgieter, and L. Cornish. Corrosion Behaviour of Superferritic Stainless Steels Cathodically Modified with Minor Additions of Ruthenium in Sulphuric and Hydrochloric Acids. *Mater. Des.*, 30(5):1451–1457, 2009.

[20] A. Higginson. Passivation of Cathodically Modified Alloys. *Br. Corros. J.*, 24(4): 297–302, 1989.

[21] N. D. Tomashov, G. P. Chernova, and T. A. Fedoseeva. Cathodic Alloying of the Surface of Titanium, Chromium, and Stainless Steels as a Method of Increasing Their Passivation and Corrosion Resistance. *Corrosion*, 36(4):201–207, 1980.

[22] S. C. Tjong, J. S. Ku, and N. J. Ho. Laser Surface Alloying of Ferritic Fe-40cr Alloy with Ruthenium. *Surf. Coat. Technol.*, 90(3):203–209, 1997.

[23] P. Peled and D. Itzhak. The Effect of Noble Alloying Elements Ag, Pt and Au on the Corrosion Behavior of Sintered Stainless Steel in an H_2SO_4 Environment. *Corros. Sci.*, 28(10):1019–1028, 1988.

[24] P. Peled and D. Itzhak. The Surface Composition of Sintered Stainless Steel Containing Noble Alloying Elements Exposed to a H_2SO_4 Environment. *Corros. Sci.*, 32(1):83–90, 1991.

[25] E. Klar and P. Samal. *Powder Metallurgy Stainless Steels : Processing, Microstructures, and Properties*, chapter Sintering and Corrosion Resistance, pages 59–100. ASM International, Materials Park, Ohio, 2007.

[26] B. A. Obadele, O. S. Adesina, O. P. Oladijo, and E. N. Ogunmuyiwa. Fabrication of Functionally Graded 316L Austenitic and 2205 Duplex Stainless Steels by Spark Plasma Sintering. *J. Alloys Compd.*, 849, 2020.

[27] A. Ruys, O. Gingu, G. Sima, and S. Maleksaeedi. *Powder Processing of Bulk Components in Manufacturing*, pages 1–69. Springer London, 2013.

[28] P. Cavaliere, B. Sadeghi, and A. Shabani. Spark Plasma Sintering: Process Fundamentals. In *Spark Plasma Sintering of Materials*, pages 3–20. Springer International Publishing, 2019.

[29] C. Tan, G. Wang, L. Ji, Y. Tong, and X. Duan. Investigation on 316L/W Functionally Graded Materials Fabricated by Mechanical Alloying and Spark Plasma Sintering. *J. Nucl. Mater.*, 469:32–38, 2016.

[30] E. Jajarmi and S. A. Sajjadi. Fractography of 3YPSZ/316L Functionally Graded Composite Subjected to Indentation And Flexural Bending Tests. *Ceram. Int.*, 43(14):11281–11288, 2017.

[31] S. Z. Jin, H. L. Zhang, J. F. Li, and S. S. Jia. TiB2/AlN/Cu Functionally Graded Materials (FGMs) Fabricated by Spark Plasma Sintering (SPS) Method. *Key Eng. Mater.*, 280-283:1881–1884, 2007.

[32] K. Zarebski and P. Putyra. Iron Powder-Based Graded Products Sintered by Conventional Method and by SPS. *Adv. Powder Technol.*, 26(2):401–408, 2015.

[33] I. F. Machado, L. Girardini, I. Lonardelli, and A. Molinari. The Study of Ternary Carbides Formation During SPS Consolidation Process in the WC–Co–Steel system. *Int. J. Refract. Met. Hard Mater.*, 27(5):883–891, 2009.

[34] Johnson Matthey. PGM Management. Technical report, March 2024.

[35] A. Cowley. Pgm Market Report May 2023. Technical report, Johnson Matthey, 2023.

[36] E. R. Schofield. On the Criticality of Palladium in Organic Synthesis: A Perspective: Palladium-based Catalysis: a Field with Scope for Expansion. *Johnson Matthey Technol. Rev.*, 67(3):285–289, July 2023. ISSN 2056-5135.

[37] European Environment Agency. Trends and Projections in Europe 2023. Technical report, European Union, 2023.

[38] Department of Transport. Zero Emission Vehicle (zev) Mandate Consultation: Summary of Response and Joint Government Response. Technical report, UK Government, 2023.

[39] IEA. Global EV Outlook 2023. Technical report, IEA, 2023.

[40] R. O. Adams. A Review of the Stainless Steel Surface. *Journal of Vacuum Science & Technology A: Vacuum, Surfaces, and Films*, 1(1):12–18, January 1983. ISSN 1520-8559.

[41] G. George and H. Shaikh. Chapter 1 - Introduction to Austenitic Stainless Steels. In H. S. Khatak and B. Raj, editors, *Corrosion of Austenitic Stainless Steels*, pages 1–36. Elsevier, Amsterdam, the Netherlands, 2002.

[42] S. R. Oke, O. O. Ige, O. E. Falodun, A. M. Okoro, M. R. Mphahlele, and P. A. Olubambi. Powder Metallurgy of Stainless Steels and Composites: A Review of Mechanical Alloying and Spark Plasma Sintering. *Int. J. Adv. Manuf. Technol.*, 102(9-12):3271–3290, 2019.

[43] R. L. Plaut, C. Herrera, D. M. Escriba, P. R. Rios, and A. F. Padilha. A Short Review on Wrought Austenitic Stainless Steels at High Temperatures: Processing, Microstructure, Properties and Performance. *Mater. Res.*, 10(4):453–460, 2007.

[44] J. F. Grubb, T. DeBold, and J. D. Fritz. Corrosion of Wrought Stainless Steels. In S. D. Cramer and B. S. Covino, editors, *Corrosion: Materials*, pages 54–77. ASM International, 2005.

[45] L. Li. *Heat Treating of Irons and Steels*. ASM International, 2014.

[46] P. K. Samal. *Alloy Classification and Compositions*, pages 415–420. ASM International, September 2015.

[47] U. K. Mudali and M. G. Pujar. Pitting Corrosion of Austenitic Stainless Steels and Their Weldments. In H. S. Khatak and B. Raj, editors, *Corrosion of Austenitic Stainless Steels*, pages 74–105. Elsevier, 2002.

[48] S. D. Washko and G. Aggen. *Properties and Selection: Irons, Steels and High-Performance Alloys*, chapter Wrought Stainless Steels, pages 841–907. ASM International, January 1990. ISBN 9781627081610.

[49] S. Salahi, M. Ghaffari, A. V. Nemani, and A. Nasiri. Effects of Secondary-Phase Formation on the Electrochemical Performance of a Wire Arc Additive Manufactured 420 Martensitic Stainless Steel under Different Heat Treatment Conditions. *J. Mater. Eng. Perform.*, 30(9):6618–6629, 2021.

[50] A. V. Nemani, M. Ghaffari, S. Salahi, and A. Nasiri. On the Microstructural Characteristics and Corrosion Performance of As-printed and Heat-treated PH 13–8Mo Martensitic Stainless Steel Fabricated by Wire Arc Additive Manufacturing. *Mater. Today Commun.*, 34:105477, 2023.

[51] B. Rho, H. U. Hong, and S. W. Nam. The Effect of δ-ferrite on Fatigue Cracks in 304L Steels. *Int. J. Fatigue*, 22(8):683–690, September 2000. ISSN 0142-1123.

[52] C. C. Tseng, Y. Shen, S. W. Thompson, M. C. Mataya, and G. Krauss. Fracture and the Formation of Sigma Phase, $M_{23}C_6$, and Austenite from Delta-Ferrite in an AISI 304L Stainless Steel. *Metall. Mater. Trans. A*, 25(6):1147–1158, June 1994. ISSN 1543-1940.

[53] S. Roberts. *Martensitic Steels for Cast Components in Ultra-supercritical Power Plants*, pages 121–141. Elsevier, 2017. ISBN 9780081005521.

[54] S. Lampman. *Compressibility and Compactibility of Metal Powders*, pages 171–178. ASM International, September 2015.

[55] K. Hashimoto, K. Asami, and K. Teramoto. An X-Ray Photo-Electron Spectroscopic Study on the Role of Molybdenum in Increasing the Corrosion Resistance of Ferritic Stainless Steels in HC1. *Corros. Sci.*, 19(1):3–14, January 1979. ISSN 0010-938X.

[56] N. D. Tomashov, G. P. Chernova, and O. N. Markova. Influence of Palladium on the Corrosion Resistance of 0Kh25M3T Steel in Dilute Soluions of HCl. *Zashch. Met.*, 9(6):616–618, 1973. ISSN 0033-1732.

[57] T. Voisin, R. Shi, Y. Zhu, Z. Qi, M. Wu, S. Sen-Britain, Y. Zhang, S. R. Qiu, Y. M. Wang, S. Thomas, and B. C. Wood. Pitting Corrosion in 316L Stainless Steel Fabricated by Laser Powder Bed Fusion Additive Manufacturing: A Review and Perspective. *JOM*, 74(4):1668–1689, March 2022. ISSN 1543-1851.

[58] M. A. Baker and J. E. Castle. The Initiation of Pitting Corrosion at MnS Inclusions. *Corros. Sci.*, 34(4):667–682, April 1993. ISSN 0010-938X.

[59] J. Stewart and D. E. Williams. The Initiation of Pitting Corrosion on Austenitic Stainless Steel: On the Role and Importance of Sulphide Inclusions. *Corros. Sci.*, 33(3):457–474, March 1992. ISSN 0010-938X.

[60] R. T. Warzel. *Manufacture of Stainless Steel Powders*, pages 421–426. ASM International, September 2015.

[61] M. R. Jandaghi, H. Pouraliakbar, L. Iannucci, V. Fallah, and M. Pavese. Comparative Assessment of Gas and Water Atomized Powders for Additive Manufacturing of 316L Stainless Steel: Microstructure, Mechanical Properties, and Corrosion Resistance. *Materials Characterization*, 204:113204, October 2023. ISSN 1044-5803.

[62] J. Lou, Y. M. Li, H. He, and L. J. Li. Effect of Atomisation Medium on Sintering Properties of Austenitic Stainless Steel by Eliminating Influence of Particle Shape and Particle Size. *Powder Metall.*, 53(2):112–117, 2010.

[63] M. J. Tobar, J. M. Amado, J. Montero, and A. Yáñez. A Study on the Effects of the Use of Gas or Water Atomized AISI 316L Steel Powder on the Corrosion Resistance of Laser Deposited Material. *Physics Procedia*, 83:606–612, 2016. ISSN 1875-3892.

[64] L. Holappa. *Secondary Steelmaking*, pages 301–345. Elsevier, 2014.

[65] M. Kemp, A. van Bennekom, and F.P.A. Robinson. Evaluation of the Corrosion and Mechanical Properties of a Range of Experimental Cr Mn Stainless Steels. *Mater. Sci. Eng. A*, 199(2):183–194, August 1995. ISSN 0921-5093.

[66] H. Ha, C. Park, and H. Kwon. Effects of Misch Metal on the Formation of Non-metallic Inclusions and the Associated Resistance to Pitting Corrosion in 25 *Scr. Mater.*, 55(11):991–994, December 2006. ISSN 1359-6462.

[67] C. Chang, P. Chen, and K. Hwang. Enhanced Mechanical Properties of Injection Molded 17-4PH Stainless Steel through Reduction of Silica Particles by Graphite Additions. *Mater. Trans.*, 51(12):2243–2250, 2010.

[68] C. Schade and J. J. Dunkley. Atomization. In *Powder Metallurgy, Vol 7*, pages 58–71. ASM International, 2015.

[69] B. Kozub, J. Kazior, and A. Szewczyk-Nykiel. Sintering Kinetics of Austenitic Stainless Steel AISI 316L Modified with Nanographite Particles with Highly Developed BET Specific Surface Area. *Materials*, 13(20):4569, 2020.

[70] U. Lindstedt and B. Karlsson. Microstructure and Mechanical Behaviour of Single Pressed and Vacuum Sintered Gas and Water Atomised 316L Stainless Steel Powders. *Powder Metallurgy*, 41(4):261–268, January 1998. ISSN 1743-2901.

[71] P. Bracconi and G. Gasc. Surface Characterization and Reactivity of a Nitrogen Atomized 304L Stainless Steel Powder. *Metall. Mater. Trans. A*, 25(3):509–520, March 1994. ISSN 1543-1940.

[72] L. Nyborg and I. Olefjord. Surface Analysis of PM Martensitic Steel Before and After Consolidation: Part 1: Surface Analysis of Powder. *Powder Metallurgy*, 31 (1):33–39, January 1988. ISSN 1743-2901.

[73] T. Tunberg and L. Nyborg. Surface Reactions During Water Atomisation and Sintering of Austenitic Stainless Steel Powder. *Powder Metall.*, 38(2):120–130, 1995.

[74] D. H. Ro, E. Klar, and C. I. Whitman. Corrosion-Resistant Powder-Metallurgy Stainless Steel Powders and Compacts Therefrom, 1980.

[75] S. J. Rosenberg and J. H. Darr. Stabilization of Austenitic Stainless Steel. *J. Res. Natl. Inst. Stand. Technol*, 41:1261, 1949.

[76] A. S. Murthy. *Role of Alloy Additions on Strengthening in 17-4PH Stainless Steel*. phdthesis, Missouri University of Science and Technology, 2012.

[77] Y. Sun, R. J. Hebert, and M. Aindow. Effect of Heat Treatments on Microstructural Evolution of Additively Manufactured and Wrought 17-4PH Stainless Steel. *Mater. Des.*, 156:429–440, 2018.

[78] R. Prakash Kolli and David N. Seidman. *Heat Treatment of Copper Precipitation-Strengthened Steels*, pages 188–203. ASM International, October 2014. ISBN 9781627081689.

[79] F. Lemoisson and L. Froyen. Understanding and Improving Powder Metallurgical Processes. In *Fundamentals of Metallurgy*, pages 471–502. Elsevier, Amsterdam, the Netherlands, 2005.

[80] H. Danninger and C. Gierl-Mayer. Chapter 7 - Advanced Powder Metallurgy Steel Alloys. In I. Chang and Y. Zhao, editors, *Advances in Powder Metallurgy*, Woodhead Publishing Series in Metals and Surface Engineering, pages 149–201. Woodhead Publishing, 2013.

[81] D. A. Levina, L. I. Chernyshev, and N. V. Mikhailovskaya. Contemporary Powder Metallurgy: Achievements and Problems. *Powder Metall. Met. Ceram.*, 46(3-4): 202–205, 2007.

[82] P. Ramakrishnan. *Automotive applications of powder metallurgy*, pages 493–519. Elsevier, 2013. ISBN 9780857094209.

[83] J. J. Dunkley. Advances in Atomisation Techniques for the Formation of Metal Powders. In *Advances in Powder Metallurgy*, pages 3–18. Elsevier, Amsterdam, the Netherlands, 2013.

[84] A. Lawley. Atomization. In *Encyclopedia of Materials: Science and Technology*, pages 387–392. Elsevier, Oxford, UK, 2001.

[85] E. Akca and A. Gürsel. A Review on Superalloys and IN718 Nickel-Based INCONEL Superalloy. *Period. Eng. Nat. Sci*, 3(1), 2015.

[86] S. Fanmin, C. Suiyuan, W. Mingwei, L. Jing, and L. Changsheng. The Structure and Properties of Inconel 718 Superalloy Powder Prepared by Vacuum Induction Melting Gas Atomization for Laser Direct Metal Deposition. *Mater. Res. Express*, 6(2), 2018.

[87] J. J. Dunkley. Metal Powder Atomisation Methods for Modern Manufacturing. *Johnson Matthey Technol. Rev.*, 63(3):226–232, 2019.

[88] R. M. German. Chapter 1 - Powders for Metal Injection Molding (MIM). In D. F. Heaney, editor, *Handbook of Metal Injection Molding*, pages 50–63. Elsevier, Amsterdam, the Netherlands, 2012.

[89] J. Ma and L. C. Lim. Effect of Particle Size Distribution on Sintering of Agglomerate-free Submicron Alumina Powder Compacts. *J. Eur. Ceram. Soc.* , 22(13):2197–2208, 2002.

[90] B. Flipon, C. Keller, L. Garcia de la Cruz, E. Hug, and F. Barbe. Tensile Properties of Spark Plasma Sintered AISI 316L Stainless Steel with Unimodal and Bimodal Grain Size Distributions. *Mater. Sci. Eng. A*, 729:249–256, 2018.

[91] M. Pellizzari, A. Fedrizzi, and M. Zadra. Influence of Processing Parameters and Particle Size on the Properties of Hot Work and High Speed Tool Steels by Spark Plasma Sintering. *Mater. Des.*, 32(4):1796–1805, 2011.

[92] W. B. James. Powder Metallurgy Methods and Applications. In P. Samal and J. Newkirk, editors, *Powder Metallurgy, Vol 7*, pages 9–19. ASM International, 2015.

[93] M. N. Rahaman. Sintering Theory and Fundamentals. In *Powder Metallurgy*, pages 205–236. ASM International, 2015.

[94] R. M. German. Sintering Trajectories: Description on How Density, Surface Area, and Grain Size Change. *JOM*, 68(3):878–884, 2016.

[95] R. M. German. Coarsening in Sintering: Grain Shape Distribution, Grain Size Distribution, and Grain Growth Kinetics in Solid-Pore Systems. *Crit. Rev. Solid State Mater. Sci.*, 35(4):263–305, 2010.

[96] M. I. Ramli, A. B. Sulong, N. Muhamad, A. Muchtar, A. Arifin, F. M. Foudzi, and M. S. H. Al-Furjan. Effect of Sintering Parameters on Physical and Mechanical Properties of Powder Injection Moulded Stainless Steel-hydroxyapatite Composite. *PLoS One*, 13(10), 2018.

[97] B. Verlee, T. Dormal, and J. Lecomte-Beckers. Density and Porosity Control of Sintered 316L Stainless Steel Parts Produced by Additive Manufacturing. *Powder Metall.*, 55(4):260–267, 2012.

[98] C. Keller, K. Tabalaiev, G. Marnier, J. Noudem, X. Sauvage, and E. Hug. Influence of Spark Plasma Sintering Conditions on the Sintering and Functional Properties of an Ultra-fine Grained 316L Stainless Steel Obtained from Ball-Milled Powder. *Mater. Sci. Eng. A*, 665:125–134, 2016.

[99] G. Marnier, C. Keller, J. Noudem, and E. Hug. Functional Properties of a Spark Plasma Sintered Ultrafine-Grained 316L Steel. *Mater. Des.*, 63:633–640, 2014.

[100] S. Y. Chang, S. Oh, M. Suk, and C. S. Hong. Spark Plasma Sintering of Stainless Steel Powders Fabricated by High Energy Ball Milling. *J. Korean Powder Metall. Inst.*, 21(2):97–101, 2014.

[101] J. K. Stanley and A. J. Perrotta. Grain Growth in Austenitic Stainless Steels. *Metallography*, 2(4):349–362, 1969.

[102] N. S. Weston, F. Derguti, A. Tudball, and M. Jackson. Spark Plasma Sintering of Commercial and Development Titanium Alloy Powders. *J. Mater. Sci.*, 15(14): 4860–4878, 2015.

[103] P. A. dePoutiloff and P. K. Samal. *Sintering of Stainless Steels*, pages 433–439. ASM International, September 2015.

[104] J. Yang, J. Trapp, Q. Guo, and B. Kieback. Joining of 316L Stainless Steel by Using Spark Plasma Sintering Method. *Mater. Des.*, 52:179–189, 2013.

[105] L. Zhu, Y. Zhu, X. Ren, P. Zhang, J. Qiao, and P. Feng. Microstructure, Properties and Oxidation Behavior of MoSi2-MoB-ZrO2 Soating for Mo Substrate Using Spark Plasma Sintering. *Surf. Coat. Technol.*, 375:773–781, 2019.

[106] F. Nozahic, C. Estournès, A. L. Carabat, W. G. Sloof, S. van der Zwaag, and D. Monceau. Self-Healing Thermal Barrier Coating Systems Fabricated by Spark Plasma Sintering. *Mater. Des.*, 143:204–213, 2018.

[107] A. H. Pakseresht, A. H. Javadi, M. Bahrami, F. Khodabakhshi, and A. Simchi. Spark Plasma Sintering of a Multilayer Thermal Barrier Coating on Inconel 738 Superalloy: Microstructural Development and Hot Corrosion Behavior. *Ceram. Int.*, 42(2):2770–2779, 2016.

[108] A. Almathami and M. Brochu. Microstructure and Transformation of Al-Containing Nanostructured 316L Stainless Steel Coatings Processed Using Spark Plasma Sintering. *J. Mater. Process. Technol.*, 210(15):2119–2124, 2010.

[109] M. Tokita. The Potential of Spark Plasma Sintering (SPS) Method for the Fabrication on an Industrial Scale of Functionally Graded Materials. *Adv. Sci. Tech.*, 63:322–331, 2010.

[110] Prasa K. Samal, Roland Warzel, and Suresh O. Shah. *Powder Metallurgy Stainless Steels Applications*, pages 480–487. ASM International, September 2015.

[111] B. Saleh, J. Jiang, R. Fathi, T. Al-hababi, Q. Xu, L. Wang, D. Song, and A. Ma. 30 Years of Functionally Graded Materials: An Overview of Manufacturing Methods, Applications and Future Challenges. *Compos. B: Eng*, 201:108376, November 2020. ISSN 1359-8368.

[112] M. Tokita. Large-Size-WC/Co Functionally Graded Materials Fabricated by Spark Plasma Sintering (SPS) Method. *Mater. Sci. Forum*, 423-425:39–44, 2003.

[113] H. Feng, Q. Meng, Y. Zhou, and D. Jia. Spark Plasma Sintering of Functionally Graded Material in the Ti–TiB2–B System. *Materials Science and Engineering: A*, 397(1–2):92–97, April 2005. ISSN 0921-5093. Defense, TiB has extreme hardness, high melting point, high electrical conductivity, good thermalshock resistance and chemical inertness.

[114] Y. Watanabe, Y. Iwasa, H. Sato, A. Teramoto, and K. Abe. Fabrication of Titanium / Biodegradable-Polymer FGM for Medical Application. *Materials Science Forum*, 631–632:199–204, October 2009. ISSN 1662-9752.

[115] Y. Makino, K. Mizuuchi, M. Tokita, Y. Agari, M. Kawahara, and K. Inoue. Synthesis of new structural and functional materials by sps processing. *Materials Science Forum*, 638–642:2091–2096, January 2010. ISSN 1662-9752. Electronics - Al/diamond metal matrix. Al - . Diamond - high thermal conductivity, Al helps with ease of fabrication.

[116] X. Tang, H. Zhang, D. Du, D. Qu, C. Hu, R. Xie, and Y. Feng. Fabrication of W–Cu Functionally Graded Material by Spark Plasma Sintering Method. *International Journal of Refractory Metals and Hard Materials*, 42:193–199, January 2014. ISSN 0263-4368.

[117] B. N. Popov. *Corrosion Engineering : Principles and Solved Problems*. Elsevier, Amsterdam, Netherlands, 2015. ISBN 0-444-62727-8.

[118] J. W. Larson. Introduction to Corrosion of Ferrous Metals. In S. D. Cramer and B. S. Covino, editors, *Corrosion: Materials*, pages 3–4. ASM International, 2005.

[119] P. Marcus. Introduction to Fundamentals of Corrosion Thermodynamics. In S. D. Cramer; B. S. Covino, editor, *Corrosion: Fundamentals, Testing, and Protection*, page 5. ASM International, 2003.

[120] E. Protopopoff and P. Marcus. Electrode Processes. In S. D. Cramer and B. S. Covino, editors, *Corrosion: Fundamentals, Testing, and Protection*, pages 6–7. ASM International, 2003.

[121] M. J. Schofield. *Corrosion*, pages 961–985. Elsevier, 2001. ISBN 9780750673280.

[122] Y. Huang and J. Zhang, editors. *Thermodynamics of Materials Corrosion*. De Gruyter, Berlin, Germany, 2018.

[123] K. Elayaperumal and V. S. Raja. *Corrosion Failures*, chapter Thermodynamics and Kinetics of Electrochemical Corrosion, pages 9–28. John Wiley & Sons, Inc, may 2015.

[124] A. B. Kale, B. Kim, D. Kim, E. G. Castle, M. Reece, and S. Choi. An Investigation of the Corrosion Behavior of 316L Stainless Steel Fabricated by SLM and SPS Techniques. *Mater. Charact.*, 163:110204, 2020.

[125] G. S. Frankel. *Corrosion: Fundamentals, Testing, and Protection*, chapter Pitting Corrosion, pages 236–241. ASM International, 2003. ISBN 9781627081825.

[126] G. L. Patrick. *Organic Chemistry*. CRC Press, 2003.

[127] E. H. Phelps and D. C. Vreeland. Corrosion of austenitic stainless steels in sulfuric acid. *CORROSION*, 13(10):21–26, October 1957. ISSN 1938-159X.

[128] S. Ningshen and U. Kamachi Mudali. Chapter 2 - Uniform Corrosion of Austenitic Stainless Steels. In H. S. Khatak and B. Raj, editors, *Corrosion of Austenitic Stainless Steels*, Woodhead Publishing Series in Metals and Surface Engineering, pages 37–73. Woodhead Publishing, 2002. ISBN 978-1-85573-613-9.

[129] Corrosion Atlas Series. pages 97–151. Elsevier, 2020. ISBN 9780128187609.

[130] R. A. S. Hoyle and D. E. Taylor. *Surface Engineering Volume II: Engineering Applications*, chapter Effect of chlorinated hydrocarbons on the corrosion resistance of austenitic stainless steels in chloride solutions. Royal Society of Chemistry, Cambridge, 1993.

[131] P. Liao, J. Jian, and L. Tsay. The corrosion and wear-corrosion of the iron-base amorphous coating prepared by the hvof spraying. *Metals*, 13(6):1137, June 2023. ISSN 2075-4701.

[132] E. Otero, A. Pardo, M. V. Utrilla, E. Sáenz, and J. F. Álvarez. Corrosion behaviour of aisi 304l and 316l stainless steels prepared by powder metallurgy in the presence of sulphuric and phosphoric acid. *Corros. Sci.*, 40(8):1421–1434, August 1998. ISSN 0010-938X.

[133] I. Costa, C. V. Franco, C. T. Kunioshi, and J. L. Rossi. Corrosion Resistance of Injection-Molded 17-4PH Steel in Sodium Chloride Solution. *Corrosion*, 62(4): 357–365, 2006.

[134] P. Suri, R. P. Koseski, and R. M. German. Microstructural Evolution of Injection Molded Gas- and Water-Atomized 316L Stainless Steel Powder during Sintering. *Mater. Sci. Eng. A*, 402(1-2):341–348, 2005.

[135] T. Raghu, S. N. Malhotra, and P. Ramakrishnan. Corrosion Behavior of Porous Sintered Type 316L Austenitic Stainless Steel in 3 *CORROSION*, 45(9):698–704, September 1989. ISSN 1938-159X.

[136] C. Moral, A. Bautista, and F. Velasco. Aqueous Corrosion Behaviour of Sintered Stainless Steels Manufactured from Mixes of Gas Atomized and Water Atomized Powders. *Corros. Sci.*, 51(8):1651–1657, August 2009. ISSN 0010-938X.

[137] R. K. Dayal. Chapter 4 - Crevice Corrosion of Stainless Steel. In H. S. Khatak and B. Raj, editors, *Corrosion of Austenitic Stainless Steels*, pages 1–36. Elsevier, Amsterdam, the Netherlands, 2002.

[138] H. Bhadeshia and R. Honeycombe. *Steels: Microstructure and Properties*. Elsevier Science, third edition, 2006.

[139] Y Hedberg, M Norell, J Hedberg, P Szakálos, P Linhardt, and I Odnevall Wallinder. Surface Characterisation of Fine Inert Gas and Water Atomised Stainless Steel 316L Powders: Formation of Thermodynamically Unstable Surface Oxide Phases. *Powder Metallurgy*, 56(2):158–163, April 2013. ISSN 1743-2901.

[140] Harb S. Nayar. *Powder Metallurgy*, chapter Sintering Atmospheres, pages 237–246. ASM International, September 2015. ISBN 9781627081757.

[141] S. R. Pillai. Chapter 11 - High Temperature Corrosion of Austenitic Stainless Steels. In H. S. Khatak and B. Raj, editors, *Corrosion of Austenitic Stainless Steels*, pages 1–36. Elsevier, Amsterdam, the Netherlands, 2002.

[142] T. Raghu, S. N. Malhotra, and P. Ramakrishnan. Corrosion behaviour of sintered austenitic stainless steel filters in sulphuric acid solutions. *British Corrosion Journal*, 23(2):109–116, January 1988. ISSN 0007-0599.

[143] K. Geenen, A. Röttger, and W. Theisen. Corrosion Behavior of 316L Austenitic Steel Processed by Selective Laser Melting, Hot-isostatic Pressing, and Casting. *Materials and Corrosion*, 68(7):764–775, January 2017. ISSN 1521-4176.

[144] H. Irrinki, T. Harper, S. Badwe, J. Stitzel, O. Gulsoy, G. Gupta, and S. V. Atre. Effects of Powder Characteristics and Processing Conditions on the Corrosion Performance of 17-4 PH Stainless Steel Fabricated by Laser-powder Bed Fusion. *Progress in Additive Manufacturing*, 3(1–2):39–49, May 2018. ISSN 2363-9520.

[145] W. Fredriksson, D. Petrini, K. Edström, F. Björefors, and L. Nyholm. Corrosion Resistances and Passivation of Powder Metallurgical and Conventionally Cast 316L and 2205 Stainless Steels. *Corrosion Science*, 67:268–280, February 2013. ISSN 0010-938X.

[146] K. D. Ralston, N. Birbilis, and C. H. J. Davies. Revealing the Relationship between Grain Size and Corrosion Rate of Metals. *Scr. Mater.*, 63(12):1201–1204, December 2010. ISSN 1359-6462.

[147] H. Saito, M. Nishimoto, and I. Muto. Pitting Corrosion Characteristics of Sintered Type 316 L Stainless Steel: Relationship between Pores and Mns. *npj Materials Degradation*, 8(1), June 2024. ISSN 2397-2106.

[148] S. N. Malhotra, M. Ashok, and P. Ramakrishnan. Effect of Sintering Parameters on Pore-morphology and Corrosion Behaviour of Sintered 316L Stainless Steels. *Transactions of Powder Mettalurgy Association of India*, 17:33–42, 1990. ISSN 0377-9416.

[149] M. M. Bonato, W. da Silveira, Wido H. Schreiner, Paulo A. P. Wendhausen, and P. C. Borges. *On the Use of Stainless Steel Water Atomized Powders for Injection Molding Regarding Corrosion Resistance*, pages 164–172. Trans Tech Publications Ltd., November 2005.

[150] Y. Hedberg, M. Norell, P. Linhardt, H. Bergqvist, and I. Odnevall Wallinder. Influence of surface oxide characteristics and speciation on corrosion, electrochemical properties and metal release of atomized 316l stainless steel powders. *International Journal of Electrochemical Science*, 7(12):11655–11677, December 2012. ISSN 1452-3981.

[151] L. Wang, C. Dong, C. Man, Y. Hu, Q. Yu, and X. Li. Effect of Microstructure on Corrosion Behavior of High Strength Martensite Steel—A Literature Review. *Int. J. Min. Met. Mater.*, 28(5):754–773, May 2021. ISSN 1869-103X.

[152] S. Yin, D. Y. Li, and R. Bouchard. Effects of Strain Rate of Prior Deformation on Corrosion and Corrosive Wear of AISI 1045 Steel in a 3.5 Pct NaCl Solution. *Metall. Mater. Trans. A*, 38(5):1032–1040, May 2007. ISSN 1543-1940.

[153] P. Leo, R. Nobile, J. Barreiro, S. Bagheri, and C. Mele. Precipitation Hardening Stainless Steel Samples Processed by Additive Manufacturing: Process Parameters

and Thermo Mechanical Treatments Effects on Microstructure and Corrosion Resistance. *Opt. Laser Technol.*, 156:108547, 2022.

[154] L. Wang, C. Dong, C. Man, D. Kong, K. Xiao, and X. Li. Enhancing the Corrosion Resistance of Selective Laser Melted 15-5PH Martensite Stainless Steel Via Heat Treatment. *Corros. Sci.*, 166:108427, 2020.

[155] W. Chen, L. Xu, K. Hao, Y. Zhang, L. Zhao, Y. Han, Z. Liu, and H. Cai. Effect of Heat Treatment on Microstructure and Performances of Additively Manufactured 15-5PH Stainless Steel. *Optics & Laser Technology*, 157:108711, January 2023. ISSN 0030-3992.

[156] F. Malaret. Exact Calculation of Corrosion Rates by the Weight-loss Method. *Exp. Res.*, 3, 2022.

[157] W. J. Lorenz and F. Mansfeld. Determination of Corrosion Rates by Electrochemical DC and AC Methods. *Corros. Sci.*, 21(9-10):647–672, jan 1981.

[158] S. Papavinasam. Electrochemical Polarization Techniques for Corrosion Monitoring. In *Techniques for Corrosion Monitoring*, pages 49–85. Elsevier, 2008.

[159] X. L. Zhang, Z. H. Jiang, Z. P. Yao, Y. Song, and Z. D. Wu. Effects of Scan Rate on the Potentiodynamic Polarization Curve Obtained to Determine the Tafel Slopes and Corrosion Current Density. *Corros. Sci.*, 51(3):581–587, 2009.

[160] ASTM International. ASTM G59-23: Standard Test Method for Conducting Potentiodynamic Polarization Resistance Measurements. Technical report, ASTM International, ASTM International, West Conshohocken, PA, 2023.

[161] G. J. Biefer. Effects of Alloying on Polarization and Corrosion of Type 430 Stainless Steel. *Can. Metall. Q.*, 9(4):537–550, 1970.

[162] M. A. Ehsan, A. M. Kumar, R. K. Suleiman, and A. S. Hakeem. Fabrication of Thickness-Controlled NiPd Nanoalloy Thin Films As Anticorrosive Coatings on 316L SS Substrates for Application in Marine Environment. *Surf. Coat. Technol.*, 418:127253, 2021.

[163] X. Gao, J. Tang, Y. Zuo, Y. Tang, and J. Xiong. The Electroplated Palladium-Copper Alloy Film on 316L Stainless Steel and Its Corrosion Resistance in Mixture of Acetic and Formic Acids. *Corros. Sci.*, 51(8):1822–1827, 2009.

[164] P. Ju, Y. Zuo, J. Tang, Y. Tang, and Z. Han. The Characteristics of a Pd-Ni/Pd-Cu Double Coating on 316L Stainless Steel and the Corrosion Resistance in Stirred Boiling Acetic and Formic Acids Mixture. *Mater. Chem. Phys.*, 144(3):263–271, 2014.

[165] M. B. Lekala and J. W. van der Merwe. Effects of Ruthenium and Nickel on the Microstructure and Corrosion Properties of a Laser Alloyed AISI 316L Stainless Steel Surface. *Surfaces and Interfaces*, 8:163–169, 2017.

[166] S. C. K. Banda and J. van der Merwe. Effect of Small Additions of Ruthenium on Pitting Corrosion Resistance of LDX2101 Duplex Stainless Steel. *Corros. Eng. Sci. Technol.*, 49(1):32–38, 2013.

[167] J. H. Potgieter. The Effect of Ruthenium on the Corrosion Behaviour of a 22 Mass *Journal of Materials Science Letters*, 15(16):1408–1411, 1996.

[168] S. Li, Y. Zuo, Y. Tang, and X. Zhao. The Electroplated Pd-Co Alloy Film on 316L Stainless Steel and the Corrosion Resistance in Boiling Acetic Acid and Formic Acid Mixture with Stirring. *Appl. Surf. Sci.*, 321:179–187, dec 2014.

[169] F. Moyo, J. W. van der Merwe, and D. Wamwangi. Corrosion Performance of Pulse Plated Ruthenium: Dependence on Pulse-off Time. *Surf. Coat. Technol.*, 307:971–977, 2016.

[170] J. H. Potgieter, J. Thomson, F. V. Adams, and A. S. Afolabi. Effect of Additions of Ru and Pd on the Electrochemical Behaviour of Austenitic Stainless Steel in Organic Acids. *Int. J. Electrochem. Sci.*, 9(11):6451–6463, 2014.

[171] J. H. Potgieter and H. C. Brookes. Corrosion Behavior of a High-Chromium Duplex Stainless Steel with Minor Additions of Ruthenium in Sulfuric Acid. *Corrosion*, 51(4):312–320, 1995.

[172] J. H. Potgieter and M. U. Kincer. An Electrochemical Investigation of the Effect of Nickel and Ruthenium on the Dissolution of a High Chromium Super-Ferritic Stainless Steel in Reducing Acid Media. *S. Afr. J. Chem.*, 44(2):47–50, 1991.

[173] J. H. Potgieter, P. Ellis, and A. Van Bennekom. Investigation of the Active Dissolution Behaviour of a 22% Chromium Duplex Stainless Steel with Small Ruthenium Additions in Sulphuric Acid. *ISIJ Int.*, 35(2):197–202, 1995.

[174] E. M. Sherif, J. H. Potgieter, J. D. Comins, L. Cornish, P. A. Olubambi, and C. N. Machio. Effects of Minor Additions of Ruthenium on the Passivation of Duplex Stainless-steel Corrosion in Concentrated Hydrochloric Acid Solutions. *J. Appl. Electrochem.*, 39(8):1385–1392, 2009.

[175] J. Tang and Y. Zuo. Study on Corrosion Resistance of Palladium Films on 316L Stainless Steel by Electroplating and Electroless Plating. *Corros. Sci.*, 50(10): 2873–2878, 2008.

[176] J. Tang, Y. Zuo, Y. Tang, and J. Xiong. The Preparation of Corrosion Resistant Palladium Films on 316L Stainless Steel by Brush Plating. *Surf. Coat. Technol.*, 204(9-10):1637–1645, 2010.

[177] J. Tang, Y. Zuo, Y. Tang, and J. Xiong. Composition and Corrosion Resistance of Palladium Film on 316L Stainless Steel by Brush Plating. *Trans. Nonferrous Met. Soc. China*, 22(1):97–103, jan 2012.

[178] J. Tang, Z. Zhang, Y. Wang, P. Ju, Y. Tang, and Y. Zuo. Corrosion Resistance Mechanism of Palladium Film-plated Stainless Steel in Boiling H_2SO_4 Solution. *Corros. Sci.*, 135:222–232, 2018.

[179] S. C. Tjong. Electrochemical and Surface Analysis of the Fe-Cr-Ru System in Non-Oxidizing Acid Solutions. *Appl. Surf. Sci.*, 44(1):7–15, 1990.

[180] J. W. van der Merwe and N. B. Nelwalani. The Corrosion Resistance of Low Concentration Ruthenium Laser Alloyed 304L Stainless Steel Exposed to Sulphuric Acid at 25°C. *Anti-Corros. Methods Mater.*, 65(3):263–270, 2018.

[181] J. van der Merwe and D. Tharandt. Corrosion Resistance of Laser-cladded 304L Stainless Steel Enriched with Ruthenium Additions Exposed to Sulphuric Acid and Sodium Chloride Media. *J. South. Afr. Inst. Min. Metall.*, 115(6):499–505, 2015. ISSN 0038-223X.

[182] J. van der Merwe and D. Tharandt. Corrosion Resistance of Laser Cladded 304L Stainless Steel Enriched with Ru in Hydrochloric Acid. *Corros. Eng. Sci. Technol.*, 52(1):54–60, 2016.

[183] J. W. van der Merwe, F. Moyo, and E. M. Phetla. Corrosion Behaviour of Ruthenium Laser Surface Alloyed Austenitic Stainless Steel in Sulphuric Acid and Sodium Chloride Solutions. *Mater. Corros.*, 68(8):815–823, 2017.

[184] I. M. Wolff, L. E. Iorio, T. Rumpf, P. V. T. Scheers, and J. H. Potgieter. Oxidation and Corrosion Behaviour of Fe-Cr and Fe-Cr-Al Alloys with Minor Alloying Additions. *Mater. Sci. Eng. A*, 241(1-2):264–276, 1998.

[185] L. Xu, Y. Zuo, J. Tang, Y. Tang, and P. Ju. Chromium-Palladium Films on 316L Stainless Steel by Pulse Electrodeposition and Their Corrosion Resistance in Hot Sulfuric Acid Solutions. *Corros. Sci.*, 53(11):3788–3795, 2011.

[186] Yu Zuo, Junlei Tang, Chongzhi Fan, Yuming Tang, and Jinping Xiong. An Electroless Plating Film of Palladium on 304 Stainless Steel and Its Excellent Corrosion Resistance. *Thin Solid Films*, 516(21):7565–7570, 2008.

[187] R. D. Pütz, Y. Pratesa, L. Oster, R. Sharma, U. Reisgen, and D. Zander. Microstructure and Corrosion Behavior of Functionally Graded Wire Arc Additive Manufactured Steel Combinations. *steel research international*, 92(12), October 2021. ISSN 1869-344X.

[188] T. S. Senthil, M. Puviyarasan, S. Ramesh Babu, and T. Ram Prabhu. Pitting corrosion studies on functionally graded inconel 825-ss316l wall manufactured by wire arc additive manufacturing. *Engineering Research Express*, 4(3):035013, July 2022. ISSN 2631-8695.

[189] P. F. Jiang, C. H. Zhang, S. Zhang, J. B. Zhang, J. Chen, and Y. Liu. Microstructure Evolution, Wear Behavior, and Corrosion Performance of Alloy Steel Gradient Material Fabricated by Direct Laser Deposition. *Journal of Materials Research and Technology*, 9(5):11702–11716, September 2020. ISSN 2238-7854.

[190] ASTM International. ASTM G102-89(2015): Standard Practice for Calculation of Corrosion Rates and Related Information from Electrochemical Measurements. Technical report, ASTM International, ASTM International, West Conshohocken, PA, 2015.

[191] G. P. Chernova, L. A. Chigirinskaya, O. D. Agakishiev, and N. D. Tomashov. Corrosion-Resistant High-Chromium, Titanium, Molybdenum, Ruthenium or Palladium Alloyed Steels. *Key Eng. Mater.*, 20-28:1659–1670, 1991.

[192] A. Higginson, R. C. Newman, and R. P. M. Procter. The Passivation of Fe-Cr-Ru Alloys in Acidic Solutions. *Corros. Sci.*, 29(11-12):1293–1318, 1989.

[193] P. V. Scheers, J. J. McEwan, and D. Knight. Development of PGM-Modified Stainless Steels for Reducing Acid Service. *Corros. Coat. SA*, October:4–12, 1994.

[194] J. H. Potgieter. Effect of Minor Ruthenium Additions on the Corrosion Behaviour of Duplex Stainless Steels in Sulfuric Acid. *S. Afr. J. Chem.*, 46(3):82–85, 1993.

[195] G. P. Chernova, T. A. Fedoseeva, L. P. Kornienko, and N. D. Tomashov. Increasing the Passivability and Corrosion Resistance of Stainless Steels by Surface Alloying with Palladium. *Zashch. Met.*, 17(5):513–519, 1981.

[196] M. B. Lekala, J. W. van der Merwe, and S. L. Pityana. Laser Surface Alloying of 316L Stainless Steel with Ru and Ni Mixtures. *Int. J. Corros*, 2012:1–4, 2012.

[197] H. Du. Mie-Scattering Calculation. *Appl. Opt.*, 43(9):1951–1956, 2004.

[198] A. A. Guimarães, T. S. Klein, and R. de Andrade Medronho. Fish-Hook Effect in Dranulometric Efficiency Curves of Hydrocyclones: A Misuse of Laser Diffraction Particle Size Analysers. *Powder Technol.*, 374:185–189, 2020.

[199] ASM International Handbook Committee. *Stainless Steels*, volume 1. ASM International, 1994.

[200] *Specification Sheet: Alloy 17-4PH*. Sandmeyer, 4 2018.

[201] G. F. Vander Voort. *Metallography, Principles and Practice*. ASM international, 1999.

[202] ASTM International. ASTM E407 - 07: Standard Practice for Microetching Metals and Alloys. Technical report, ASTM International, ASTM International, West Conshohocken, PA, 2015.

[203] ASTM International. ASTM E112-13(2021): Standard Test Methods for Determining Average Grain Size. Technical report, ASTM International, ASTM International, West Conshohocken, PA, 2021.

[204] ASTM International. ASTM E92-17: Standard Test Methods for Vickers Hardness and Knoop Hardness of Metallic Materials. Technical report, ASTM International, ASTM International, West Conshohocken, PA, 2017.

[205] ASTM International. ASTM B895-16: Standard Test Methods for Evaluating the Corrosion Resistance of Stainless Steel Powder Metallurgy (PM) Parts/Specimens by Immersion in a Sodium Chloride Solution. Technical report, ASTM International, ASTM International, West Conshohocken, PA, 2020.

[206] ASTM International. ASTM A666-23: Standard Specification for Annealed or Cold-Worked Austenitic Stainless Steel Sheet, Strip, Plate, and Flat Bar. Technical report, ASTM International, ASTM International, West Conshohocken, PA, 2023.

[207] ASTM International. ASTM A693-22: Standard Specification for Precipitation-Hardening Stainless and Heat-Resisting Steel Plate, Sheet, and Strip. Technical report, ASTM International, ASTM International, West Conshohocken, PA, 2022.

[208] A. Barroux, N. Ducommun, E. Nivet, L. Laffont, and C. Blanc. Pitting Corrosion of 17-4PH Stainless Steel Manufactured by Laser Beam Melting. *Corros. Sci.*, 169: 108594, 2020.

[209] A. B. Kale, A. Bag, J. Hwang, E. G. Castle, M. J. Reece, and S. Choi. The Deformation and Fracture Behaviors of 316L Stainless Steels Fabricated by Spark Plasma Sintering Technique Under Uniaxial Tension. *Mater. Sci. Eng. A*, 707: 362–372, 2017.

[210] L. F. Pease and D. L. Pease. Metallography and Microstructures of Powder Metallurgy Alloys. In *Metallography and Microstructures*, pages 994–1020. ASM International, 2004.

[211] T. T. Vollmer. Origin and subsequent behaviour of inclusions in water-atomized low-alloy steel powder. *Powder Metallurgy*, 24(3):146–150, January 1981. ISSN 1743-2901.

[212] D. Riabov, E. Hryha, M. Rashidi, S. Bengtsson, and L. Nyborg. Effect of Atomization on Surface Oxide Composition in 316L Stainless Steel Powders for Additive Manufacturing. *Surf. Interface Anal.*, 52(11):694–706, 2020.

[213] X. Yang, F. Gao, F. Tang, X. Hao, and Z. Li. Effect of Surface Oxides on the Melting and Solidification of 316L Stainless Steel Powder for Additive Manufacturing. *Metallurgical and Materials Transactions A*, 52(10):4518–4532, July 2021. ISSN 1543-1940.

[214] E. Klar and P. K. Samal. *Powder Metallurgy Stainless Steels: Processing, Microstructures, and Properties*, chapter Manufacture and Characteristics of Stainless Steel Powders, page 23–38. ASM International, June 2007. ISBN 9781627083126.

[215] C. Schade and J. J. Dunkley. *Atomization*, pages 58–71. ASM International, September 2015. ISBN 9781627081757.

[216] B. J. Babalola, O. O. Ayodele, and P. A. Olubambi. Sintering of Nanocrystalline Materials: Sintering Parameters. *Heliyon*, 9(3):e14070, March 2023. ISSN 2405-8440.

[217] N. Thangamani, K. Chinnakali, and F. D. Gnanam. The Effect of Powder Processing on Densification, Microstructure and Mechanical Properties of Hydroxyapatite. *Ceram. Int.*, 28(4):355–362, 2002.

[218] N. Kurgan. Effects of Sintering Atmosphere on Microstructure and Mechanical Property of Sintered Powder Metallurgy 316L Stainless Steel. *Mater. Des.*, 52: 995–998, December 2013. ISSN 0261-3069.

[219] C. H. Ji, N. H. Loh, K. A. Khor, and S. B. Tor. Sintering Study of 316L Stainless Steel Metal Injection Molding Parts Using Taguchi Method: Final Density. *Mater. Sci. Eng. A*, 311(1-2):74–82, 2001.

[220] F. Martín, C. García, and Y. Blanco. Effect of Chemical Composition and Sintering Conditions on the Mechanical Properties of Sintered Duplex Stainless Steels. *Mater. Sci. Eng. A*, 528(29-30):8500–8511, 2011.

[221] D. Huber, L. Vogel, and A. Fischer. The Effects of Sintering Temperature and Hold Time on Densification, Mechanical Properties and Microstructural Characteristics of Binder Jet 3D Printed 17-4 PH Stainless Steel. *Addit. Manuf.*, 46:102114, 2021.

[222] T. Borkar and R. Banerjee. Influence of Spark Plasma Sintering (SPS) Processing Parameters on Microstructure and Mechanical Properties of Nickel. *Materials Science and Engineering: A*, 618:176–181, November 2014. ISSN 0921-5093.

[223] Ashby M. F. and Jones D. R. H. *Engineering Materials: An Introduction to Their Properties and Applications*. Pergamon, Oxford, first edition, 1980.

[224] Y. Hu, Y. Li, J. Lou, H. He, and X. Zhang. Effects of Sintering Temperature and Holding Time on Densification and Mechanical Properties of MIM HK30 Stainless Steel. *Int. J. Metall. Met. Phys.*, 3(2), December 2018. ISSN 2631-5076.

[225] M. Hakamada, Y. Nakamoto, H. Matsumoto, H. Iwasaki, Y. Chen, Hiromu Kusuda, and M. Mabuchi. Relationship between Hardness and Grain Size in Electrodeposited Copper Films. *Mater. Sci. Eng. A*, 457(1-2):120–126, 2007.

[226] S. Pandya, K. S. Ramakrishna, A. Raja Annamalai, and A. Upadhyaya. Effect of Sintering Temperature on the Mechanical and Electrochemical Properties of Austenitic Stainless Steel. *Materials Science and Engineering: A*, 556:271–277, October 2012. ISSN 0921-5093.

[227] F. Ternero, L. G. Rosa, P. Urban, J. M. Montes, and F. G. Cuevas. Influence of the Total Porosity on the Properties of Sintered Materials—A Review. *Metals*, 11(5):730, April 2021. ISSN 2075-4701.

[228] H. Irrinki, M. Dexter, B. Barmore, R. Enneti, S. Pasebani, S. Badwe, J. Stitzel, R. Malhotra, and S. V. Atre. Effects of Powder Attributes and Laser Powder Bed Fusion (L-PBF) Process Conditions on the Densification and Mechanical Properties of 17-4 PH Stainless Steel. *JOM*, 68(3):860–868, January 2016. ISSN 1543-1851.

[229] P. Suri, B. P. Smarslok, and Randall M. German. Impact Properties of Sintered and Wrought 17–4 PH Stainless Steel. *Powder Metallurgy*, 49(1):40–47, March 2006. ISSN 1743-2901.

[230] L. Beaunier, C. Pasquier, F. Pillier, and P. Laurens. Stainless steel surface alloying process with molybdenum or ruthenium by high energy excimer laser: Structural, electrochemical and corrosion properties. In *Proceedings of SPIE–the international society for optical engineering.*, volume 3097, pages 443–452, Bellingham, Wash. :, 1997. Society of Photo-optical Instrumentation Engineers.

[231] Y. Lin and K. Hwang. Swelling of Copper Powders during Sintering of Heat Pipes in Hydrogen-Containing Atmospheres. *Mater. Trans.*, 51(12):2251–2258, 2010.

[232] P. S. Liu and G. F. Chen. Making Porous Metals. In *Porous Materials*, pages 21–112. Elsevier, Amsterdam, the Netherlands, 2014.

[233] G. Liang, Y. Ali, G. You, and M. Zhang. Effect of cooling rate on grain refinement of cast aluminium alloys. *Materialia*, 3:113–121, November 2018. ISSN 2589-1529.

[234] M. M. Jabbari Behnam, P. Davami, and N. Varahram. Effect of Cooling Rate on Microstructure and Mechanical Properties of Gray Cast Iron. *Materials Science and Engineering: A*, 528(2):583–588, December 2010. ISSN 0921-5093.

[235] R. A. Mesquita and C. A. Barbosa. High-speed steels produced by conventional casting, spray forming and powder metallurgy. *Materials Science Forum*, 498–499: 244–250, November 2005. ISSN 1662-9752.

[236] F. Bartolomeu, M. Buciumeanu, E. Pinto, N. Alves, O. Carvalho, F.S. Silva, and G. Miranda. 316L Stainless Steel Mechanical and Tribological Behavior - a Comparison between Selective Laser Melting, Hot Pressing and Conventional Casting. *Additive Manufacturing*, 16:81–89, August 2017. ISSN 2214-8604.

[237] S. Louhenkilpi. *Continuous Casting of Steel*, pages 373–434. Elsevier, 2014. ISBN 9780080969886.

[238] J. H. Potgieter. Corrosion of Passive Alloys: The Effect of Noble Metal Additions. In *Shreir's Corrosion*, pages 2224–2249. Elsevier, 2010.

[239] H. Y. Ha, T. H. Lee, J. H. Bae, and D. Chun. Molybdenum Effects on Pitting Corrosion Resistance of FeCrMnMoNC Austenitic Stainless Steels. *Metals*, 8(8): 653, 2018.

[240] Y. Sun, A. Moroz, and K. Alrbaey. Sliding Wear Characteristics and Corrosion Behaviour of Selective Laser Melted 316L Stainless Steel. *Journal of Materials Engineering and Performance*, 23(2):518–526, November 2013. ISSN 1544-1024.

[241] V. Firouzdor and A. Simchi. Co-sintering of M2/17-4PH Powders for Fabrication of Functional Graded Composite Layers. *J. Compos. Mater.*, 44(4):417–435, 2009.

[242] A. Simchi, A. Rota, and P. Imgrund. An Investigation on the Sintering Behavior of 316L and 17-4PH Stainless Steel Powders for Graded Composites. *Mater. Sci. Eng. A*, 424(1-2):282–289, 2006.

[243] H.R. Lashgari, E. Adabifiroozjaei, C. Kong, Leopoldo Molina-Luna, and S. Li. Heat Treatment Response of Additively Manufactured 17-4PH Stainless Steel. *Materials Characterization*, 197:112661, March 2023. ISSN 1044-5803.

[244] R. Groarke, C. Danilenkoff, S. Karam, E. McCarthy, B. Michel, A. Mussatto, J. Sloane, A. O' Neill, R Raghavendra, and D. Brabazon. 316L Stainless Steel Powders for Additive Manufacturing: Relationships of Powder Rheology, Size, Size Distribution to Part Properties. *Materials*, 13(23):5537, December 2020. ISSN 1996-1944.

[245] H. Danninger and C. Gierl. Processes in PM Steel Compacts During the Initial Stages of Sintering. *Materials Chemistry and Physics*, 67(1–3):49–55, January 2001. ISSN 0254-0584.

[246] V. Nečina and W. Pabst. Influence of the Heating Rate on Grain Size of Alumina Ceramics Prepared via Spark Plasma Sintering (SPS). *Journal of the European Ceramic Society*, 40(10):3656–3662, August 2020. ISSN 0955-2219.

[247] T. Voisin, L. Durand, N. Karnatak, S. Le Gallet, M. Thomas, Y. Le Berre, J. Castagné, and A. Couret. Temperature Control during Spark Plasma Sintering and Application to Up-scaling and Complex Shaping. *Journal of Materials Processing Technology*, 213(2):269–278, February 2013. ISSN 0924-0136.

[248] T. Xi, M. B. Shahzad, D. Xu, J. Zhao, C. Yang, M. Qi, and K. Yang. Copper Precipitation Behavior and Mechanical Properties of Cu-bearing 316L Austenitic Stainless Steel: A Comprehensive Cross-Correlation Study. *Mater. Sci. Eng. A*, 675:243–252, 2016.

[249] Y. Xiao, X. Xiong, G. Sun, M. Sun, and W. Liu. Atom Probe Characterization of Cu-Rich Precipitates in Different Phases of 15–5-PH Stainless Steel in Over-aged Condition. *Mater. Charact.*, 191:112184, 2022.

[250] G. Han, Z.J. Xie, Z.Y. Li, B. Lei, C.J. Shang, and R.D.K. Misra. Evolution of Crystal Structure of Cu Precipitates in a Low Carbon Steel. *Materials & Design*, 135:92–101, December 2017. ISSN 0264-1275.

[251] M. Sun, Y. Xu, and J. Wang. Effect of aging time on microstructure and mechanical properties in a cu-bearing marine engineering steel. *Materials*, 13(16):3638, August 2020. ISSN 1996-1944.

[252] G. Yeli, M. A. Auger, K. Wilford, G. D. W. Smith, P. A. J. Bagot, and M. P. Moody. Sequential Nucleation of Phases in a 17-4PH Steel: Microstructural Characterisation and Mechanical Properties. *Acta Mater.*, 125:38–49, 2017.

[253] T. Li, X. Xiong, Q. Shen, X. Wang, J. Li, and L. Wen-Qing. Effect of ni addition on precipitation strengthening of cu-rich precipitates in fe-cu-mn alloy. *Materials Research Express*, 6(10):106510, August 2019. ISSN 2053-1591.

[254] Allegheny Technologies Incorporated. *Technical Data Sheet ATI 17-4™ Precipitation Hardening Stainless Steel*. Allegheny Technologies Incorporated, 2014.

[255] A. Szewczyk-Nykiel and J. Kazior. Effect of Aging Temperature on Corrosion Behavior of Sintered 17-4PH Stainless Steel in Dilute Sulfuric Acid Solution. *J. Mater. Eng. Perform.*, 26(7):3450–3456, 2017.

[256] A. Szewczyk-Nykiel, M. Skałoń, and J. Kazior. Corrosion behaviour of sintered aisi 316l stainless steel modified with boron-rich master alloy in 0.5m nacl water solution. *Archives of Metallurgy and Materials*, 60(3):1795–1800, September 2015. ISSN 2300-1909.

[257] P. Ju, Y. Zuo, Y. Tang, and X. Zhao. The Enhanced Passivation of 316L Stainless Steel in a Simulated Fuel Cell Environment by Surface Plating with Palladium. *Corros. Sci.*, 66:330–336, 2013.

[258] J. H. Potgieter. Alloys Cathodically Modified with Noble Metals. *J. Appl. Electrochem.*, 21(6):471–482, 1991.

[259] G. P. Chernova, L. A. Chigirinskaya, N. D. Tomashov, and E. A. Nasedkina. Special Features of Behaviour of High Chrome Ferritic Stainless Steels Alloyed with Palladium or Ruthenium in Solution of Sulphuric and Hydrochloric Acid. *Prot. Met.*, 22:704–710, 1986.

[260] Y. Zuo, J. L. Tang, Y. M. Tang, and J. P. Xiong. A Palladium Film on Stainless Steels by Brush Plating and Its Excellant Corrosion Resistance in Reducing Mediums. In *17th International Corrosion Congress 2008: Corrosion Control in the Service of Society*, volume 1, pages 416–421, 2008. ISBN 9781615674251.

[261] V. S. Agarwala and G. J. Biefer. Corrosion of Type 430 Stainless Steel: Effects of Mo-Pd and Other Addition Pairs. *Corrosion*, 28(2):64–76, 1972.

[262] K. Govender, F. Scenini, S. Lyon, and A. Sherry. Influence of Pd and Ru Additions on Stress Corrosion Cracking of Austenitic Stainless Steels. *Corros. Eng. Sci. Technol.*, 47(7):507–515, 2012.

[263] M. A. Streicher. Development of Pitting Resistant Fe-Cr-Mo Alloys. *Corrosion*, 30(3):77–91, 1974.

[264] A. V. C. Sobral, C. V. Franco, O. V. Correa, and L. Costa. Corrosion Resistance of Powder Injection Moulded AISI 316L and 17-4PH Stainless Steels in Acid Rain Environments. *Materials Science Forum*, 416-418:64–69, 2003.

[265] M. J. K. Lodhi, A. D. Iams, E. Sikora, and T. A. Palmer. Microstructural Features Contributing to Macroscopic Corrosion: The Role of Oxide Inclusions on the Corrosion Properties of Additively Manufactured 316L Stainless Steel. *Corrosion Science*, 203:110354, July 2022. ISSN 0010-938X.

[266] J. Kazior. Influence of Sintering Atmosphere, Temperature and the Solution-Annealing Treatment on the Properties of Precipitation-Hardening Sintered 17-4 PH Stainless Steel. *Materials*, 16(2):760, January 2023. ISSN 1996-1944.

[267] C. Li, Y. Chen, X. Zhang, T. Liu, Y. Peng, and K. Wang. Effect of Heat Treatment on Microstructure and Mechanical Properties of 17-4PH Stainless Steel Manufactured by Laser-powder Bed Fusion. *Journal of Materials Research and Technology*, 26:5707–5715, September 2023. ISSN 2238-7854.